



Dmitry Gradov

# EXPERIMENTALLY VALIDATED NUMERICAL MODELLING OF REACTING MULTIPHASE FLOWS IN STIRRED TANK REACTORS



Dmitry Gradov

## **EXPERIMENTALLY VALIDATED NUMERICAL MODELLING OF REACTING MULTIPHASE FLOWS IN STIRRED TANK REACTORS**

Dissertation for the degree of Doctor of Science (Technology) to be presented with due permission for public examination and criticism in the Auditorium 1318 at Lappeenranta-Lahti University of Technology LUT, Lappeenranta, Finland on the 12<sup>th</sup> of April, 2019, at noon.

Acta Universitatis  
Lappeenrantaensis 847

Supervisors Professor Tuomas Koiranen  
LUT School of Engineering Science  
Lappeenranta-Lahti University of Technology LUT  
Finland

Docent Arto Laari  
LUT School of Engineering Science  
Lappeenranta-Lahti University of Technology LUT  
Finland

Reviewers Professor Zuoliang Sha  
Department of Chemical Engineering and Technology  
Tianjin University of Science and Technology  
China

D.Sc.(Technology) Pasi Moilanen  
Etteplan Oy  
Finland

Opponent Professor Zuoliang Sha  
Department of Chemical Engineering and Technology  
Tianjin University of Science and Technology  
China

ISBN 978-952-335-352-7  
ISBN 978-952-335-353-4 (PDF)  
ISSN-L 1456-4491  
ISSN 1456-4491

Lappeenranta-Lahti University of Technology LUT  
LUT University Press 2019

# Abstract

**Dmitry Gradov**

**Experimentally validated numerical modelling of reacting multiphase flows in stirred tank reactors**

Lappeenranta 2019

90 pages

Acta Universitatis Lappeenrantaensis 847

Diss. Lappeenranta-Lahti University of Technology LUT

ISBN 978-952-335-352-7, ISBN 978-952-335-353-4 (PDF), ISSN-L 1456-4491, ISSN 1456-4491

Homogenization of reacting flows by mixing is often important in order to achieve high reaction rates. Mechanical agitation is the usual way to homogenize fluids used in industry. When supplied to fluid media, mechanical energy creates turbulence that facilitates mixing. A stirred tank reactor (STR) is a conventional operational unit designed to provide sufficient mixing and suitable conditions for reactions. The design of STRs depend on the operating conditions and properties of the reacting flows. Various types of stirred reactors are used in industry that are different in geometry but share the same principles of multiphase flow, turbulence, interphase mass transfer, and reaction.

Heterogeneous reactions demand extra attention, because the reaction rate is often limited by mass transfer. Mass transfer through interface boundary depends on mass transfer coefficient, interfacial contact area, through which species are transferred, and species concentration gradient. The mass transfer coefficient, on the other hand, depends on the physical properties of the fluid media and mixing rate at micro scale. In turbulent flow, micromixing is driven by a cascade of turbulent Kolmogorov eddies. In turn, the contact area between fluids is greatly dependent on bubble or droplet size distribution.

Empirical correlations, describing the design parameters of mixed multiphase systems, such as gas hold-up, mixing power, volumetric mass transfer etc., in an STR are predominantly based on existing lab- and pilot-scale reactors. Therefore, the design and scale-up of agitated reactors is unreliable, especially for multiphase systems. In order to increase STRs performance, to make reactor design more reliable, to optimize operational conditions, and to improve existing STRs in industry, advanced mathematical tools are required that are capable of examining and testing engineering ideas in detail, preferably before building a laboratory-scale prototype and especially during the scale-up process.

Computational fluid dynamics (CFD) can describe reacting flows in different geometries more accurately than conventional empirical correlations. Detailed information on reacting flows forms a powerful tool in reactor design and scale-up, finding of operational conditions, and studying STR performance under extreme conditions. Due to the nature of Eulerian mathematical approach to fluid flow description and limited spatial and temporal resolutions, CFD software comprises empirical parameters. Therefore, experimental validation of CFD models is crucial. Various intrusive and non-intrusive experimental methods have been invented and presented in literature to provide a



trustworthy insight into fluid hydrodynamics. Each of them has a limited area of application and a combination of several measurement techniques is required to characterize reacting flows sufficiently to verify CFD models.

The aim of this thesis was to develop a set of reliable, experimentally validated models capable to accurately describe multiphase reacting flows in agitated vessels. The modelled physical phenomena were added in a step-wise manner starting from a simple single-phase non-reacting flow in a standard STR and continuing to a multiphase fermentation process in large-scale draft tube OKTOP@9000 reactor. Applicable experimental techniques, such as particle image velocimetry (PIV), electrical impedance tomography (EIT), rheometry, gas hold-up, mixing power, and gas-liquid mass transfer measurements were used to obtain validation data.

Several Reynolds-averaged Navier-Stokes (RANS) turbulence models were tested in a tall, round-bottomed STR equipped with a single Rushton turbine. The  $k-\varepsilon$  Realizable model was found to be the most feasible model for turbulence among the tested two-equation models and it produced the most accurate results in comparison to experiments in single phase mixing.

In the dilute gas-liquid mixing case, bubbles drag force was modelled most accurately by using the Schiller-Naumann's drag force model in combination with Lane's turbulence modification factor. The drag force impact was found to dominate compared to non-drag forces. On the other hand, in the dense gas-liquid flow of spherical bubbles in STR, the dampening effect of the bubble swarms on liquid flow was simulated by the Roghair's modification factor and included into the bubble drag force formula.

The effect of the relative position of impeller blades to baffles on the simulated hydrodynamics via multiple reference frame (MRF) approach was assessed in single and multiphase mixing flows. The effect was found to be less significant in single phase but more evident in gas-liquid mixing. The simulated results at a fixed angular position of an impeller can be improved by averaging the hydrodynamic results simulated at the extreme positions of the impeller.

The three-phase hydrodynamics of a gold concentrate leaching process in a batch STR was modelled. The gold concentrate suspended in agitated liquid flow revealed non-Newtonian rheology, which was used in the simulation. The rheological properties of the agitated suspended solids were mimicked experimentally by in a water solution of carboxymethyl cellulose (CMC), the hydrodynamics of which was measured by particle image velocimetry (PIV). Electrical impedance tomography (EIT) was used to visualize local gas hold-up. Using the assumption of constant bubble size, the local volumetric mass transfer coefficient of oxygen was calculated, which can be used to improve the reliability of the scale-up when designing larger-scale leaching reactors.

An experimental and numerical study of the effect of reagent feed location on the barium sulphate crystallization process was carried out in a semi-batch stirred reactor. The temporal development of crystallization was measured by the EIT technique. CFD modelling was applied to assess local hydrodynamics in a flat-bottomed stirred reactor

equipped with a Rushton turbine. The effect of mixing, considered at macro and meso scales, was found to have a great impact on crystal size because the residence time distribution of the supersaturated concentration is a function of local mixing intensity in the feed area, as well as being a function of the global flow pattern of mixing.

Scale-up of a draft tube reactor was performed from laboratory to industrial scale using CFD modelling. The same number of cells was used in the mesh in both scales to analyze the effect of spatial discretization on the resolved hydrodynamics and gas-liquid mass transfer. An aerobic fermentation process was simulated in the draft tube OKTOP reactor at industrial scale with a known power number. The Newtonian gas-liquid flow, agitated by an impeller of special design, was modelled with an updated drag force that included the effect of bubble swarms. At constant bubble size, the compensation of local volumetric power, which is usually underpredicted by RANS models, increased gas-liquid mass transfer insignificantly (by less than 5 %). However, calculation of the local bubble-size distribution increased the  $k_L a$  value by 15 %. The simulation results of *Pichia pastoris* cell cultivation in industrial batch STR showed reasonable agreement against the experimental data obtained in an identical reactor at laboratory scale. The effect of the oxygenation rate on fermentation was found to increase biomass yield by shifting the metabolism from the fermentative path of sugar consumption to the oxidative path.

Different models available in published literature for turbulence and interphase forces were validated in STRs of different geometries operated over a wide range of operational conditions at both laboratory (14 dm<sup>3</sup>) and industrial (800 m<sup>3</sup>) scales. These models can accurately describe the hydrodynamics and mass transfer, and the coupled reaction kinetics of heterogeneous reacting flows in STRs that are often encountered in chemical processes. Being more flexible than empirical correlations regarding reactor geometry, the CFD models can provide insightful information of great detail. Thus, they can significantly improve the accuracy and reliability of reactor design and scale-up, as well as take the troubleshooting and reactor configuration design to the next level.

**Keywords:** CFD, CSTR, mixing, multiphase flow, mass transfer, scale-up, reacting flows, crystallization, fermentation, PIV, EIT



## Acknowledgements

The research work was carried out in the laboratory of Flow Process in Chemical Engineering in the School of Engineering Science at Lappeenranta University of Technology (LUT).

I am thankful to my first supervisor, Professor Ilkka Turunen, for giving me the chance to start my scientific carrier at LUT. My deepest gratitude goes to my supervisor, Professor Tuomas Koiranen, for his supervision, strong motivation, and active support. I would like to dedicate separate thanks to Docent Arto Laari for his invaluable technical expertise and high scientific standards.

The author appreciates the financial support provided by the Graduate School of Chemical Engineering (GSCE), the Finnish Funding Agency for Technology and Innovation (TEKES), the FERMATRA project, the Centre of Separation Technology (CST), and the Tekniikan Edistämissäätiö fund (TES). During the collaboration, the consultancy on numerical modelling and practical performance of OKTOP®9000 reactor was kindly provided by Outotec Oyj and Neste Jacobs Oy.

I am grateful to my colleagues and friends who made the working environment cheerful and cosy. The atmosphere of comfort and scientific enthusiasm in my research group was maintained by the daily efforts of Demesa Abayneh, Mei Han, Matti Lampinen, Vladimir Zhukov and Esko Lahdenperä.

The trust, support, and patience of my family cannot be overestimated and I am deeply grateful to my beloved wife Kristina and son Mark.

*Dmitry Gradov*

April 2019  
Lappeenranta, Finland



# Contents

<b>Abstract</b>	<b>3</b>
<b>Acknowledgements</b>	<b>7</b>
<b>List of publications</b>	<b>11</b>
<b>Nomenclature</b>	<b>13</b>
<b>1. Introduction</b>	<b>19</b>
1.1. Motivation .....	19
1.2. The objectives.....	20
1.3. The structure of the thesis .....	20
<b>2. Literature Review</b>	<b>23</b>
2.1. Mixing .....	23
2.2. STR.....	24
<b>3. Materials and Methods</b>	<b>27</b>
3.1. The objects of the study.....	27
3.1.1. A flat-bottomed aerated STR .....	27
3.1.2. A tall aerated STR with a rounded bottom .....	28
3.1.3. A draft tube aerated STR .....	29
3.2. Experimental techniques .....	29
3.2.1. Mixing flow hydrodynamics measurements by PIV.....	29
3.2.2. Secondary phase visualization by EIT .....	32
3.2.3. Gas hold-up .....	35
3.2.4. Oxygen mass transfer.....	35
3.2.5. Mixing power .....	37
3.3. CFD .....	37
3.3.1. An introduction to CFD tools for mixing flows.....	37
3.3.2. Agitation.....	39
3.3.3. Multiphase flow .....	40
3.3.4. Turbulence .....	40
3.3.5. Phase Interaction .....	42
3.3.6. Mass transfer .....	44
3.3.7. Species transport and volumetric reactions.....	48
3.3.8. The mesh-size independence test.....	49
3.3.9. The developed CFD modelling on multiphase STR simulation ..	49
<b>4. Results and Discussions</b>	<b>51</b>
4.1. Gas–liquid mixing in a round-bottomed STR .....	51
4.1.1. The research tasks .....	51
4.1.2. The methods and research progress .....	52

4.1.3. The outcomes .....	60
4.2. The effect of stirrer turn angle on resolved hydrodynamics in a baffled STR using MRF.....	61
4.2.1. The research tasks .....	61
4.2.2. The methods and research progress .....	62
4.2.3. The outcomes .....	63
4.3. Leaching hydrodynamics in a batch STR.....	63
4.3.1. The research tasks .....	63
4.3.2. The methods and research progress .....	64
4.3.3. The outcomes .....	66
4.4. The effect of mixing intensity and feeding locations on semi-batch precipitation in STR.....	67
4.4.1. The research tasks .....	67
4.4.2. The methods and research progress .....	67
4.4.3. The outcomes .....	68
4.5. The fermentation process in an industrial draft tube STR.....	69
4.5.1. The research tasks .....	69
4.5.2. The methods and research progress .....	70
4.5.3. The outcomes .....	74
4.6. Discussions.....	74

<b>5. Conclusions</b>	<b>77</b>
-----------------------	-----------

<b>References</b>	<b>79</b>
-------------------	-----------

## **Publications**

## List of publications

The research is based on the following publications in peer-reviewed journals, referred to by the corresponding Roman numerals in the text:

- I. Gradov, D. V., Laari, A., Turunen, I., and Koiranen, T. (2016). Experimentally validated CFD model for gas-liquid flow in a round-bottom stirred tank equipped with Rushton turbine, *International Journal of Chemical Reactor Engineering*, 15(2), 1–17.
- II. Gradov, D. V., Laari, A., and Koiranen, T. (2017). Influence of the relative position of impeller and baffles in multiple reference frame simulation of gas-liquid mixing in stirred tank, *International Journal of Chemical Engineering and Applications*, 18(1), 53–60.
- III. Gradov, D. V., González, G., Vauhkonen, M., Laari, A., and Koiranen, T. (2017). Experimental and numerical study of multiphase mixing hydrodynamics in batch stirred tank applied to ammoniacal thiosulphate leaching of gold, *Journal of Chemical Engineering & Process Technology*, 8(3), 1–17.
- IV. Gradov, D. V., González, G., Vauhkonen, M., Laari, A., and Koiranen, T. (2018). Experimental investigation of reagent feeding point location in a semi-batch precipitation process, *Chemical Engineering Science*, 190, 361–369.
- V. Gradov, D. V., Han, M., Tervasmäki, P., Latva-Kokko, M., Vaittinen, J., Pihlajamäki, A., and Koiranen, T. (2018). Numerical simulation of biomass growth in OKTOP@9000 reactor at industrial scale, *Industrial & Engineering Chemistry Research*, 57(40), 13300–13311.

## The author's contribution

In all the above works, under the active guidance of the supervisors, the author was the main contributor, conducting experimental measurements and computational fluid dynamics modelling, analysing the results, and preparing the manuscripts.





## Nomenclature

### Latin alphabet

$A$	signal amplitude, area	$m^2$
$B$	birth rate	$s^{-1}$
$C$	empirical coefficients in Equation 3.18 and 3.30, coefficients of phases interaction force	-, -
$c$	concentration	$g/l, M/m^3$
$D$	diffusivity, death rate, impeller diameter	$m^2/s, s^{-1}, m$
$d$	particle/droplet/bubble size	$m$
$E$	energy	$J$
$e$	Euler's number	-
$F$	force	$N$
$f$	size group or class	-
$h$	liquid level height	$m$
$g$	gravitational acceleration	$m/s^2$
$K$	consistency index	$Pa \cdot s^n$
$K_i$	saturation coefficient of species $i$ uptake	$g/l$
$K_{in}$	inhibition constant	$g/l$
$K_{pq}$	interphase momentum exchange coefficient	$kg/s$
$k$	turbulence kinetic energy	$m^2/s^2$
$k_L$	mass transfer coefficient	$m/s$
$k_L a$	volumetric mass transfer rate	$s^{-1}$
$m$	moment, mass	-, $kg$
$N$	mixing speed, number of electrodes, number of elements	$s^{-1}$ , -, -
$n$	dimensionless flow behaviour index	-
$\mathbf{n}$	normal vector	-
$\dot{n}$	species flux	-
$P$	mixing power	$W$
$p$	pressure	$Pa$
$q$	specific growth rate	$g_i/(g_{cell} \cdot s)$

$Q$	impeller induced flow	$\text{m}^3/\text{s}$
$R$	net rate of species production	$\text{kg}/(\text{m}^3 \cdot \text{s})$
$S$	source term	$\text{s}^{-1}$
$T$	time scale, reactor diameter	$\text{s}, \text{m}$
$t$	time	$\text{s}$
$\mathbf{u}$	velocity	$\text{m}/\text{s}$
$V$	reactor volume	$\text{m}^3$
$v$	voltage	$\text{V}$
$x$	spatial coordinate	$\text{m}$
$Y$	species concentration	$\text{g}/\text{l}$
$Y_i^{Rj}$	yield coefficient for species $i$ and $j$ in reaction $R$	$\text{g}_i/\text{g}_j$

### Greek alphabet

$\alpha_i$	phase volume fraction, angle	$-, ^\circ$
$\Delta$	delta operator	$-$
$\nabla$	Laplace operator	$-$
$\varepsilon$	turbulence energy dissipation rate, gas hold-up	$\text{m}^2/\text{s}^3, -$
$\eta$	turbulence modification factor	$-$
$\lambda$	Kolmogorov length scale	$\text{m}$
$\mu$	dynamic viscosity	$\text{kg}/(\text{m} \cdot \text{s})$
$\mu_{turb}$	turbulent viscosity	$\text{kg}/(\text{m} \cdot \text{s})$
$\mu_{max}^R$	maximum growth rate of cells in reaction $R$	$\text{s}^{-1}$
$\pi$	mathematical constant	$-$
$\rho$	phase density	$\text{kg}/\text{m}^3$
$\sigma$	surface tension, conductivity distribution, coefficients in Equations 3.17 and 3.18	$\text{N}/\text{m}, -$
$\tau$	torque, particle relaxation time, time constant	$\text{N} \cdot \text{m}, \text{s}, \text{s}$
$\Phi_{f,g}$	cross correlation function of intensity distributions $f$ and $g$	$-$
$\varphi_i$	signal phase, simulation results	$-, -$
$\chi$	interfacial area concentration	$\text{m}^2/\text{m}^3$
$\omega$	angular velocity	$\text{rad}/\text{s}$

$\omega_i$	mass fraction of liquid in cell	-
$\omega_{col}$	frequency of particles collision	s <sup>-1</sup>

**Dimensionless numbers**

CFL	Courant–Friedrichs–Lewy condition = $\frac{u\Delta t}{\Delta x}$
$Da$	Damköhler number = $\frac{\tau_{mixing}}{\tau_{reaction}}$
$E\ddot{o}$	Eötvös number = $\frac{\Delta\rho_{qp}gd_p^2}{\sigma}$
$N_q$	flow number = $\frac{Q}{ND^3}$
$Re$	relative Reynolds number = $\frac{\rho_p u_p-u_q d_p}{\mu_q}$
TR	TR-number = $\frac{\tau_{feed}}{\tau_{meso}}$

**Subscripts**

'	modified
$\Delta h$	level difference method
32	Sauter mean
$B$	breakage
$b$	bubble
$C$	coalescence
<i>coarse</i>	mesh of higher number of elements
<i>crit</i>	critical
$D$	drag force
$D, swarm$	drag force due to swarm of bubbles
<i>drain</i>	drainage
<i>eddy</i>	turbulent eddy
exp	experimental
<i>fine</i>	mesh of lower number of elements
<i>image</i>	imaginary part of measured voltage
<i>imp</i>	impeller

---

$k$	turbulence kinetic energy
$L$	liquid/integral time scale of turbulence/lift force/laminar
$LW$	lubrication wall force
$l$	liquid
meso	mesomixing
$p$	secondary or dispersed phase
$q$	primary phase
$real$	real part of measured voltage
$S$	stagnant flow
$sat$	saturated
$T$	turbulent flow
$t$	turbulence
$VM$	virtual mass force
$w$	wall
$\varepsilon$	energy dissipation rate

### Superscripts

*	compensated energy
$R$	reaction

### Abbreviations

2D	two dimensional
3D	three dimensional
BC	boundary conditions method
BSD	bubble size distribution
CAD	computer-aided design
CCD	charge-coupled device
CFD	computational fluid dynamics
CMC	carboxyl methyl cellulose
CSD	crystal size distribution
CSTR	continuously stirred-tank reactor

---

DNS	direct numerical simulation
EIT	electrical impedance tomography
FEM	finite element method
FVM	finite volume method
IMC	inhomogeneous method of classes
LD	laser diffractometer
LDA	laser Doppler anemometry
MC	method of classes
MOM	method of moments
MRF	multiple reference frame method
Nd:Yag	neodymium-doped yttrium aluminium garnet
NRMSE	normalized root mean square error
PBE	population balance equation
PBM	population balance model
PDE	partial differential equation
PFR	plug flow reactor
PIV	particle image velocimetry
QMOM	quadrature method of classes
RANS	Reynolds-averaged Navier-Stokes turbulence model
RMS	root mean square
RNG	renormalized group
RSM	Reynolds stress model
SEM	scanning electron microscopy
SM	sliding mesh method
SPIV	stereoscopic particle image velocimetry
SST	shear stress transport
STR	stirred-tank reactor
UDF	user defined function



## 1. Introduction

### 1.1. Motivation

Mixing is the mechanical operation of fluids distribution in space, conducted in order to make a heterogeneous system more homogeneous. Mechanical energy supplied to a solution/suspension produces shear stress in a reactor domain, causing fluids to move in space, and thus homogenization occurs. Mixing has found numerous applications in practice, providing blending, dispersion of immiscible fluids, suspension of solids, and promotion of heat and/or mass transfer. A mechanically mixed or stirred tank reactor (STR) is an operational unit widely used in process engineering for diverse applications.

The modelling of the transfer rate of species mass through the interfacial boundary is extremely important in reacting flows modelling. Under the influence of species concentration gradient between phases as the driving force, the species move through the liquid boundary layer at a rate, determined by fluid molecular diffusivity and the rate of outer layer renewal. In turbulent flow, the mass transfer coefficient ( $k_L$ ) is effectively described by the eddy-cell model (Lamont & Scott, 1970), where the rate of bulk fluid engulfment is a function of diffusivity, turbulent energy dissipation rate ( $\varepsilon$ ), and fluid rheology. The overall mass transfer rate, integrated over the domain of reacting flows, is highly dependent on the contact area ( $a$ ) between the phases. In the case of a dispersed phase, droplet or bubble size distribution can influence  $k_L a$  significantly.

An up-to-date, industrial approach to STR design and scale-up relies on overall design parameters that are measured experimentally and correlated to operational conditions and reactor dimensions. Such an empirical approach is robust when constructing well-studied existing reactor types, while the scale-up or design of a novel reactor is complicated. The classical empirical approach consumes much time and resources, therefore a more intelligent approach based on robust mathematical models should be favored.

Numerical methods such as the finite element method (FEM) or the finite volume method (FVM) can simulate the fluid dynamics in an STR reasonably accurately (Joshi et al. 2011a, 2011b; Lindmark et al. 2014; Sajjadi et al. 2012; Wu 2013), which makes them a potential simulation tool. However, direct numerical simulation (DNS) of transport and reaction phenomena requires impractical computational resources (Kaneda & Ishihara 2006; Orszag 1970), which leads to a feasible compromise between available computational power and solution accuracy. Therefore, fluid dynamics is often simulated at a feasible resolution, below which the solution is modelled using empirical parameters that are fair for a great number of cases. However, due to numerical uncertainties arising from spatial and temporal discretization, numerical round offs, and empirical coefficients, experimental validation is required in order to estimate the reliability of simulation results. Thus, experimental techniques to measure local hydrodynamics in an STR—such as particle image velocimetry (PIV) and electrical impedance tomography (EIT), as well as methods of measuring global parameters—are an inevitable part of the application of computational fluid dynamics (CFD) in practice.



CFD has been extensively used in stirred tank simulations during the last couple of decades and achieved a certain level of confidence about its use in practice. Plenty of physical models were proposed by researchers to describe turbulent reacting flows in STRs. Joshi et al. (2011a, 2011b) presented a comprehensive review of the existing CFD models that are suitable for STRs and conducted the comparison studies presented earlier. The summarized results are contradictory and more studies are required to figure out a package of robust and accurate models that can describe turbulent reacting flows in STRs and that are experimentally proved.

Therefore, the aim of this thesis is to model reacting flows in STRs of various geometries with varying scale and fluid properties. The simulation results are to be validated by using relevant experimental measurements. The study consists of developing a series of CFD models that are used for simulating different solutions agitated in different STRs. Thus, the issues connected with suitable models for multiphase flow modelling under different regimes, using CFD for tackling technical problems and scale-up, are considered.

## **1.2. The objectives**

The objectives of this study are as follows:

1. Development of feasible CFD models that accurately describe the turbulent mixing flow in STRs of different geometries, which are then examined experimentally using PIV and torque measurements.
2. Simulation of multiphase mixing flows using CFD, the validation of which is provided by PIV, EIT, torque, and gas hold-up measurements.
3. Modelling of gas–liquid mass transfer in gas–liquid and gas–liquid–solid mixing systems at steady state in a batch STR.
4. Development of process design tool for semi-batch precipitation in an STR based on mesomixing scales, resolved using CFD modelling.
5. Implementation of scale-up, based on CFD modelling, from lab scale to industrial scale using PIV and the torque, measured at both scales.
6. Coupling of reaction kinetics to STR hydrodynamics with a low Damköhler number, allowing direct comparison of fermentation processes at different scales.

## **1.3. The structure of the thesis**

The thesis has the classical structure of a research work: a brief literature review of the background information, which concerns aspects of mixing, and stirred reactor design and operations, is given in Chapter 2. The next chapter starts with a detailed presentation of the STRs studied in the thesis. The experimental and numerical methods used in the work are thoroughly described in Chapter 3. The obtained results and findings that were not included in the publications are presented in Chapter 4 in which the studies are presented in subchapters as separate applications, following in the chronological order of the thesis work development. In each study, CFD simulations were used; therefore, the operational conditions and the used models are summarized in tables at the beginning of each subchapter and the outcomes of each published work are listed at the end of each subchapter. The closing chapter,

Chapter 5, contains the conclusions about the developed CFD models that were validated experimentally in the STRs.



## 2. Literature Review

### 2.1. Mixing

In chemical engineering, mixing is understood as an increase in the volumetric homogeneity of substance property (such as density, phase fraction, species concentration, viscosity, temperature, mass transfer). Depending on the phase of the substances being mixed, mixing has specialized synonyms and definitions. *Blending* is a mixing process of substances of the same phase, while *homogenization* is making the substance properties uniform in space. In turn, distribution is a process of property gradient reduction in space. *Dispersion* and *suspension* are similar actions that are conducted by mechanisms that aim to distribute a secondary phase, which tends to escape the mixing zone by floating or settling under the influence of gravitational force acting upon it due to the density difference between the mixed phases.

The mixing process requires the application of mechanical energy to agitate mixed fluids. The application of the energy of the transported fluid itself has resulted in pipeline reactors and static mixers. A similar mechanism, where one fluid is injected into another one, is used in jet mixers. Gravity-driven reactors, such bubble columns and airlift reactors, are another engineering solution to the mixing problem. Direct mechanical agitation by stirrer is the oldest technological solution for mixing substances and its principle is still widely exploited in practice.

Fluid mixing is promoted by two basic mechanisms, namely diffusion and convection. Naturally, diffusion takes place at the molecular level while convection refers to bulk motion. When being moved, fluid experiences stresses resulting in a relative change of the convection-to-diffusion ratio, typically characterized by a dimensionless Reynolds number ( $Re$ ). At low stress, fluid molecules tend to move uniformly in space without disturbance creating a laminar regime. When the stress reaches some critical value, viscous forces cannot handle the order of the moving molecules and a disturbance starts. A turbulent regime is fully developed after some point when the moving pattern of the flow is stabilized. The described regimes have different impacts on the mixing process. The use of the convective mechanism for mixing is more efficient and rapid compared to molecular diffusion, and thus, the turbulent regime is favorable.

According to the Kolmogorov's theory of the turbulent flow mechanism, mixing is promoted by the diffusion of turbulent vortexes, in addition to molecular diffusion. By scale, turbulent mixing can be classified as *macro* (the length scale of the reactor diameter), *micro* (the length scale of Kolmogorov eddies), and *meso* (the inertial-convective scale, which is intermediate between macro scale and Kolmogorov scale) (Baldyga & Pohorecki 1995). When driven by micromixing, mass transfer determines the product yield in turbulent reacting flows. At interphase boundary, the effective removal of the product and the transport of reactant are controlled by mixing intensity. The Damköhler number ( $Da$ ) defines the ratio of the reaction to the convection mass transfer rates. With a high  $Da$  value, the reaction is mostly over when the reactants and products are transported. In the case of a low  $Da$  value, the reaction is unaffected by the mixing

rate and the reactor can be assumed to be perfectly mixed. The most complicated case is when the rates of the reaction and mixing are similar, which requires that the transport and reaction kinetics are taken into account simultaneously.

## 2.2. STR

A tank with in-tank mechanical agitation is a classical operational unit for mixing. A long history of STR development has produced optimal parameters for reactor design, sizing, and operational conditions. The most typical STR is a cylindrical vessel, often equipped with baffles to prevent solution circulation at high mixing speed. Depending on the application, the bottom of the tank can be of different shapes, such as flat, round, or cone-shaped. Usually, an impeller is mounted in the center, at the height of one third of the reactor diameter. Such clearance produces optimal performance (Kasat & Pandit, 2005). An STR can be also equipped with several impellers if the aspect ratio (the ratio between the liquid height and reactor diameter) of the vessel exceeds 1.

A number of overall design parameters can be used to characterize STR performance:

- ❖ *Volumetric mixing power*  $\frac{P}{V}$  defines the amount of energy spent on mixing.
- ❖ *Critical mixing speed* has its specific meaning in different applications. It can be related to the just suspended solids or completely mixed solids in liquid–solid systems. In aerated solutions, it is related to the minimum mixing speed at which flooding occurs.
- ❖ *Volumetric mean Re* can be used to determine the flow regime in an STR and it is sometimes used in reactor design when empirical correlations are known.
- ❖ *Flow number*  $N_q$  defines the impeller capacity of liquid volume discharge after a single rotation.
- ❖ *Mixing time* denotes the time required to mix the introduced substance well.
- ❖ *Gas hold-up* characterizes the temporal mean overall volume of gas trapped in the liquid.
- ❖ *Mass transfer rate* defines the mass of transferred substance between phases over the reactor volume per time unit.
- ❖ *Shear stress* is important as its disruptive effect can cause bubbles or droplets breakage as well as damage to living organisms in mixed solution.

Historically, in the early stages of mixed reactor modelling, the black box concept was used, considering the reactor as a plug flow reactor (PFR) where the reacting flow moves along the reactor without mixing, or as a perfectly-mixed continuously stirred tank reactor (CSTR) where the substances are mixed as soon as they are introduced. In practice, real reactors are somewhere in between. Nevertheless, those concepts allowed the modelling of reacting flows until the current situation, where computational power has reached the level at which non-ideality in mixing can be resolved in more detail. A crucial part of the

black box concept is the residence time distribution (RTD) of the substance in the reactor, which is usually measured experimentally using tracer injection. The time that the substance stays inside the reactor can be used to find the yield of the product. However, the approach uses mean RTD and does not take the tracers path into account, which is crucial for product yield computation due to local micromixing. Moreover, the experimental measurement of RTD becomes difficult or impossible if the reactor has several reactants injected.

Reacting substances can be introduced into an STR according to three feeding modes. In a batch STR, reagents are fed at once and mixed until the reaction is completed. Alternatively, in a semi-batch mode, reagents can be supplied continuously while the reaction is ongoing, without removing the products. The continuous mode supplies and removes the solution simultaneously, thus several reactors can be operated in series to form a reactor cascade.

When designing an STR on a large scale, it is important to preserve similar process conditions to those tested at laboratory scale. The scale-up procedure depends on prioritized operational conditions, which can be crucial for certain application. Such conditions can be mixing intensity, shear rate, mass transfer, or blending time, which need to be maintained when the scale is changed. Sticking to one criterion inevitably leads to deviation in others, sometimes quite essential deviation, which can lead to a malfunction of an STR or even to disaster. Therefore, deep analysis of all the changes caused by scale-up is important. A method in which reacting flows in a large-scale reactor are studied by imitating the flow conditions at laboratory scale is called *scale-down analysis*. The method allows improvements to be made in large-scale reactor design or reacting flows properties.



### 3. Materials and Methods

#### 3.1. The objects of the study

This work focuses to study mixing of reacting flows in agitated reactors. In general, a stirred reactor is a fluid container with a rotating mixer that can be optionally equipped with supplementary facilities meant to provide a required environment. Studying the numerous aspects of reactor design was not among the objectives of this research. Readers interested in reactor design are referred to the review articles published by Joshi et al. (2011a, 2011b). However, some important characteristics—such as the aspect ratio, scale, impeller clearance, bottom shape, impeller type, draft tube, and baffles—are varied in the applications used to check CFD simulation performance. All the reactors studied have real lab-scale prototypes for experimental verification purposes. A separate subchapter is dedicated to each reactor wherein reactor features and research purposes are described, and physical dimensions, illustrations, and photos are presented.

##### 3.1.1. A flat-bottomed aerated STR

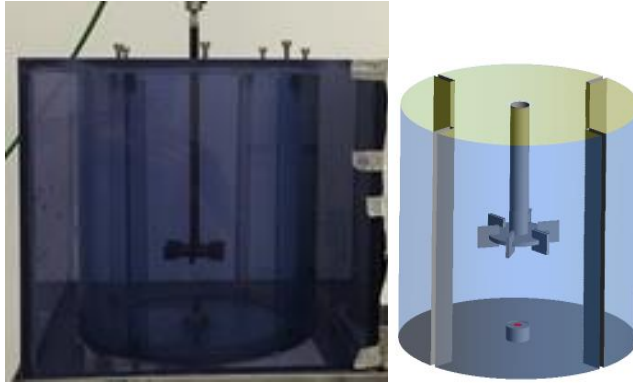


**Figure 3.1. A photo and 3D model of a flat-bottomed STR**

As the first research step, a classical baffled STR ( $T = 0.255$  m) with a flat bottom and a height equal to its diameter (Figure 3.1) is studied. A Rushton turbine ( $D = 0.33T$ ) is centered in the cylindrical vessel with the  $0.33T$  clearance (The dimensions of the reactor can be found in Publications III and IV). A pipe, perforated on one side, is mounted in the bottom and used as a gas sparger. In turn, the pipe is installed in a removable drainage mechanism in the center of the reactor bottom to flush the solution out from the reactor through the opening. The reactor was encapsulated in a Plexiglas rectangular container to prevent optical distortion caused by the reactor wall curvature during PIV measurements.



### 3.1.2. A tall aerated STR with a rounded bottom

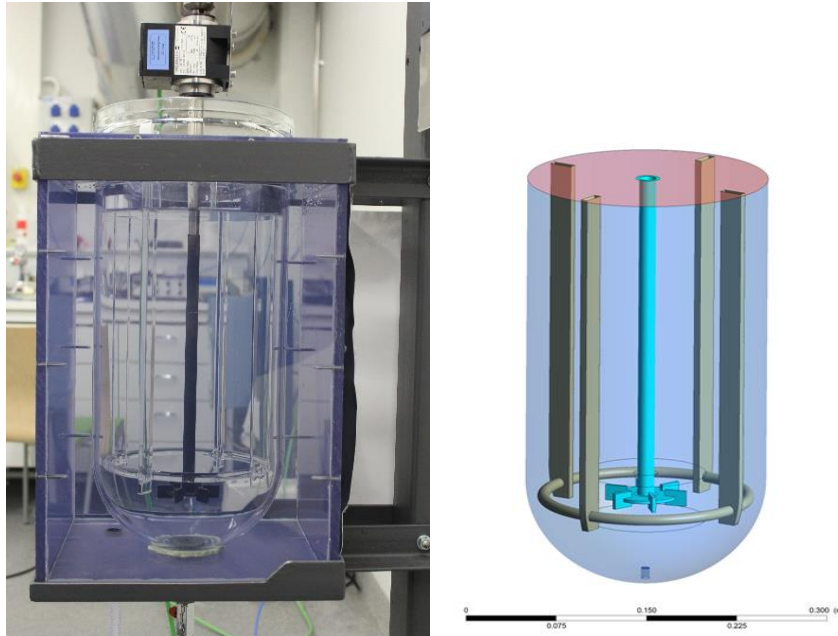


**Figure 3.2. A photo and 3D model of round-bottomed STR of aspect ratio 2**

Usually, industrial-scale reactors are tall vessels with a curved bottom that minimizes plant area and prevents deposits of the heavy fraction. Widely used RANS turbulence models are capable of describing flow hydrodynamics with reasonable accuracy in the relative vicinity of the impeller (Joshi et al. 2011a, 2011b). However, the model performance in distant regions from the impeller is questionable. Therefore, an STR ( $T = 0.2$  m) was made, similar to the flat-bottomed one in the previous subsection, of aspect ratio 2 and round bottomed (Figure 3.2). Four baffles, stabilized by glass rings, do not reach the reactor bottom, leaving an unbaffled space below the Rushton impeller. Detailed information on the sizing of the reactor can be found in Publications I and II.

### 3.1.3. A draft tube aerated STR

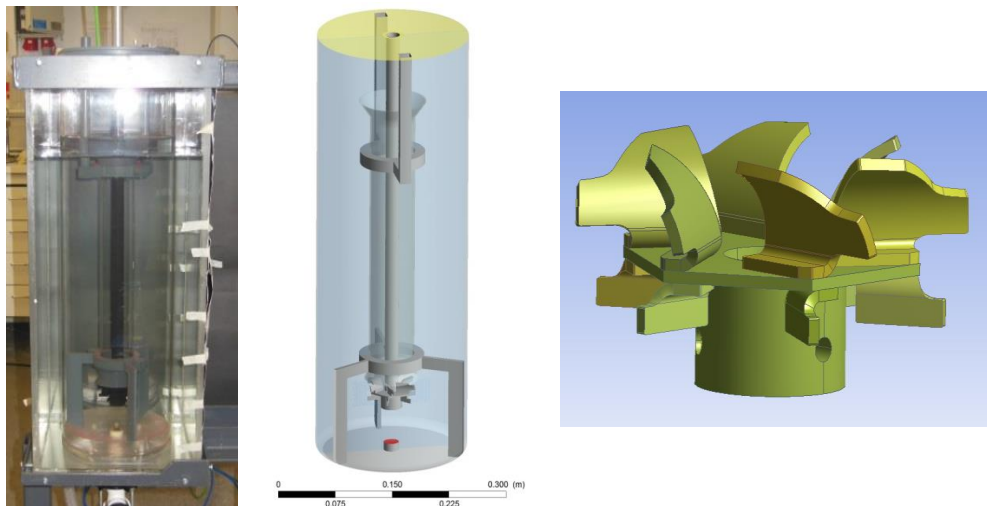


**Figure 3.3. A photo and 3D model of a draft tube OKTOP reactor at lab scale (left and center) and a CAD model of an OKTOP impeller (right)**

An industrial draft tube reactor ( $D = 7.2$  m) of special design was manufactured by Outotec Oyj specifically for the needs of the hydrometallurgical process of atmospheric Zn leaching (Svens 2010). Being in use onsite in Kokkola, Finland, the draft tube STR is meant to provide high mixing efficiency and mass transfer (Kaskiala 2005). The idea of combining the benefits of an STR and a bubble column resulted in a tall reactor with a draft tube installed just above a radial impeller of special design in order to represent a combination of radial and hydrofoil turbines (Figure 3.3). Gas, supplied below the impeller, is dispersed in the lower part of the reactor where homogenization and gas–liquid mass transfer are the highest. Then, the mixed solution spirally rises without active collisions of gas bubbles in the unbaffled middle part of the reactor. Low pressure, created by impeller rotation, sucks the solution into the draft tube together with a portion of gas bubbles. At a certain mixing speed, gas can also be dragged from the liquid surface via the formation of a strong vortex. The supplied gas does not go directly into the draft tube due to the construction of the draft tube and the shape of the upper blades. Thus, high mixing efficiency and mass transfer are provided at the energetic costs of a single impeller. The dimensions of the reactor can be found in Publication V.

## 3.2. Experimental techniques

### 3.2.1. Mixing flow hydrodynamics measurements by PIV

PIV was used to study the hydrodynamics of the single and multiphase mixing flows in the stirred tanks on a 2D plane. This technique measures velocity flow fields by capturing the movement of tracing particles, which are small enough to follow the measured flow without an impact. By penetrating the flow with a laser sheet, stereoscopic PIV (SPIV) can measure the velocity components of the fluid motion within the illuminated 2D plane.

Velocity vectors (Eq. [3.1]) are reconstructed based on the spatial shift of tracer particles between a pair of laser pulses emitted consecutively with a preset time interval between the pulses (Adrian 1991):

$$u(x, t) = \frac{\Delta x(x, t)}{\Delta t}. \quad (3.1)$$

The tangential velocity component is computed according to Raffel et al. (2007) using the following equation:

$$u_{tan} = \frac{OX_1 + OX_2}{\Delta t(\tan \alpha_1 + \tan \alpha_2)}, \quad (3.2)$$

where  $OX_1$  and  $OX_2$  are the projections of particle displacement on the plane,  $\alpha_1$  and  $\alpha_2$  are the camera angles with respect to the object plane, and  $\Delta t$  is the detention time between the laser pulses.

The imaging of tracer shift was carried out by two charge-coupled device (CCD) cameras synchronized with the laser pulsing. Thus, the velocity vector fields of axial and radial components are measured in two-dimensional space. The PIV set-up, schematically presented in Figure 3.4. (on the left), includes a double-pulsed Nd:Yag laser and two CCD cameras with the resolution of  $1600 \times 1200$  pixels. The laser and the cameras were controlled by DaVis 7.2 PIV software (LaVision GmbH, 2006). Detention time between laser pulses was dictated by the maximum flow velocity in a frame.

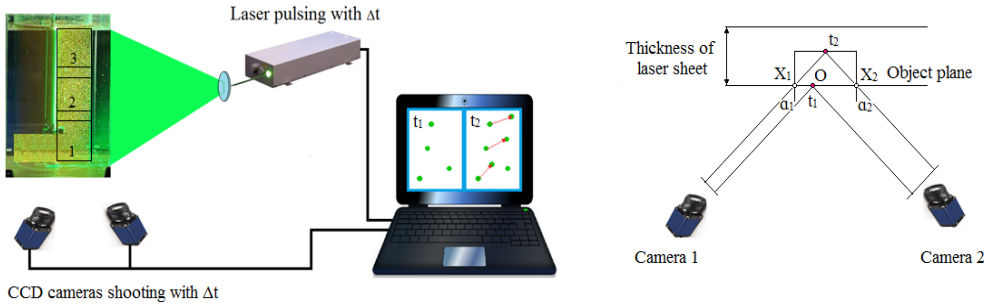


**Figure 3.4. A schematic representation of the stereoscopic PIV set-up (left) and its principle of third component determination (right)**

Clear vision is the key to accurate measurements in PIV techniques. However, providing a clear visual path in complicated objects with highly reflective surfaces and moving parts is challenging. Therefore, all the studied reactors were encased by prismatic chambers filled with water to remove visual distortions. The walls of the prismatic chambers, opposite the laser source and cameras, were covered by matte black paper to minimize reflections. As shown in Figure 3.4 (on the left), the laser sheet was oriented vertically in

all the cases. The laser sheet was positioned vertically at a distance of 20 mm upstream from the baffle, as shown in Figure 3.5 (on the left). This position was selected as a compromise between the reduction of visual obstacles (baffles mainly) and strong reflections. Due to the geometrical similarities of the reactors studied in this work, strong reflections were found at the shaft, the impeller blade, and the opposite wall to the reactor. The flow in the impeller region was masked to remove the influence of incorrect velocity vectors when processing the results. To measure the liquid phase flow, fluorescent particles of the size of 20–50  $\mu\text{m}$ , made of polyamide, were used as tracers. The fluorescent tracers emit light at a wavelength different to that of the laser. This property was used to eliminate unwanted light reflections in the background. High bandpass filters (light red filter: BP635) were installed on the CCD cameras to limit the light to the wavelength range of 615–645 nm in order to filter out the green light coming from the light-reflecting surfaces of the reactor (Schroeder & Willert 2008). The recommended seeding density (Figure 3.6a) of at least 10 tracer particles per processing window was used (Khan 2005). Gas phase motion was recorded using the light reflected from the bubbles. In this case, cameras were equipped with grey filters (B+W, 52 103 ND 0.9 8x) to reduce the intensity of the reflected light.

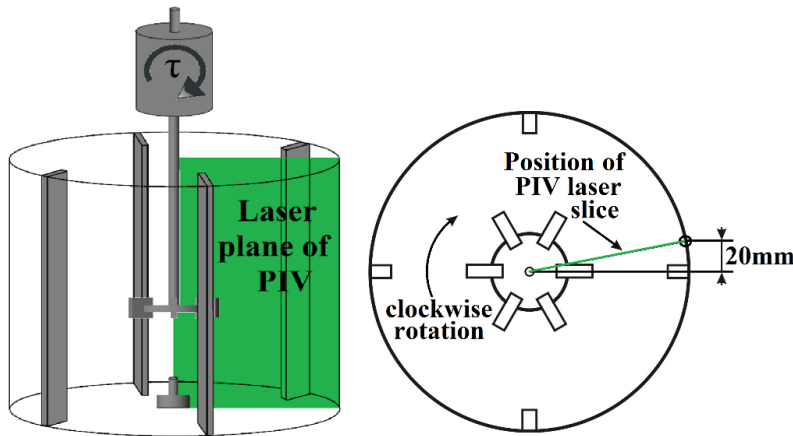


**Figure 3.5. Illustrations of laser plane positioning in an STR seen from the front (left) and above (right).**

The size of a single frame taken (the measurement window) depends on camera resolution, the distance between the camera and the plane of measurement, and the focal length of the objective. The acquired frames were processed by DaVis software (LaVision 2005) twice via a cross-correlation algorithm (Keane & Adrian 1992). The intensity distributions of the two images, separated by  $\Delta t$ , are analysed in order to track the shift of tracing particles using a cross-correlation algorithm (Eq. [3.3]) (Westerweel 1993):

$$\Phi_{fg}(m, n) = \sum_i \sum_j f(i, j) \times g(i + m, j + n), \quad (3.3)$$

where  $f(i,j)$  and  $g(i,j)$  are the image intensity distributions of the two images, and  $m$  and  $n$  are the pixel shift between the two images.

With growing area, the processing time of computing the velocity vectors becomes computationally expensive. An effective solution to overcome the problem is using the fast Fourier transform (FFT; Raffel et al. 2007). Here, using FFT, a multi-pass algorithm was applied in combination with decreasing the resolution of the interrogation window with a 50 % overlap. Then, the interrogation area was decreased and the frame was treated once more in order to search for the shift of tracer particles more accurately. The camera resolution, the size of the interrogation area, and the physical size of the measurement window give a resolution of around 2 mm for the PIV results. When spurious vectors are found, the measured instantaneous velocity fields were processed by computing 2D convolution with a Gaussian kernel equal to 1 in order to filter out any spurious vectors. According to Escudié and Liné (2003), Aubin et al. (2004), Liné et al. (2013), Malik et al. (2016), and Alberini et al. (2017), statistical convergence of the instantaneous velocities averaging happens at around 500 frames in the case of mixing flows in lab-scale reactors. Nevertheless, statistical convergence was tested in each case separately. Examples of a recorded frame (Figure 3.6a), a reconstructed instantaneous velocity vectors field (Figure 3.6b), and an averaged velocity vectors field (Figure 3.6c) are presented below.

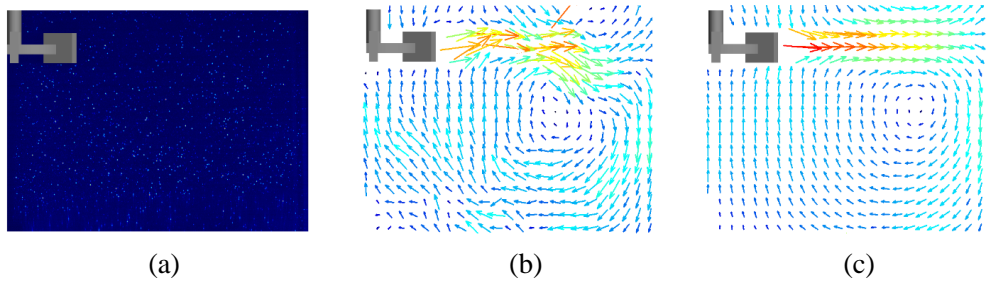


**Figure 3.6. The measurement window and the calculated velocity vector fields near the impeller: (a) the PIV frame, (b) an instant velocity vector field, and (c) an averaged velocity vector field.**

In order to get a full picture of the reactor, it was necessary to combine several frames at different heights along the vertical axis using overlapping (Figure 3.4).

### 3.2.2. Secondary phase visualization by EIT

Unfortunately, PIV application is limited to transparent liquids and other experimental methods should be used when dealing with opaque flows. EIT uses the conductivity difference of phases to enable the visual representation of the dispersed phase volume fraction (Figure 3.7).

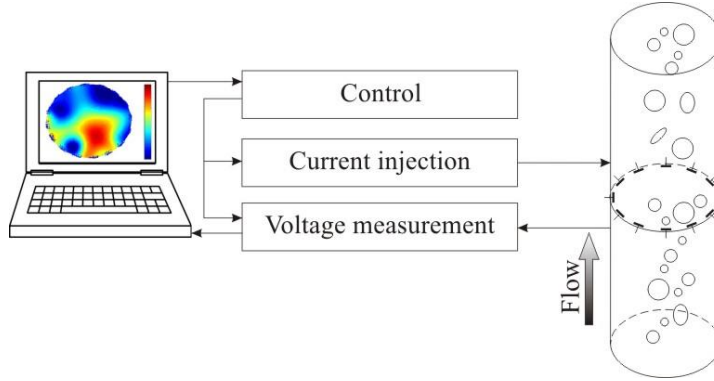


**Figure 3.7. A block diagram of an EIT set-up**

A typical EIT set-up comprises a signal generator, receiver, controller, and processor (Kourunen 2009). Using current injections, response voltages are measured at electrodes placed uniformly around a flow (Figure 3.7). Such a net of electrodes provides a grid of signals that can be systematically processed and visualized. The spatial distribution of the electrodes defines the EIT resolution of object visualization. However, the resolution is not uniform because the measured flow is resolved near walls more accurately than in the center of the flow. Signals of constant voltage are used according to a predefined scheme of pulses pairwise or multiple injections simultaneously. The received signals are forwarded to the demodulation stage where the voltage amplitude and phase are calculated using Equations (3.4–3.7) (Kourunen 2009):

$$v_{real} = \frac{2}{N} \sum_{i=0}^{N-1} v(i) \sin \frac{2\pi i}{N}, \quad (3.4)$$

$$v_{image} = \frac{2}{N} \sum_{i=0}^{N-1} v(i) \cos \frac{2\pi i}{N}, \quad (3.5)$$

$$A = \frac{2}{N} \sqrt{v_{real}^2 + v_{image}^2}, \quad (3.6)$$

$$\varphi = \tan^{-1} v_{image} / v_{real}, \quad (3.7)$$

where  $N$  is the number of electrodes,  $v(i)$  is the measured voltage at the  $i^{th}$  electrode,  $v_{real}$  is the real part of the measured voltage,  $v_{image}$  is the imaginary part of the measured voltage, and  $\varphi$  and  $A$  are the signal phase and amplitude correspondingly.

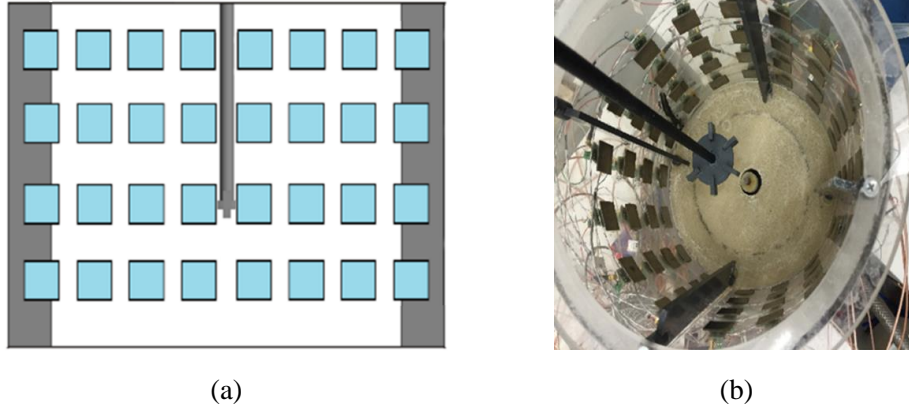


**Figure 3.8. The spatial position of electrodes mounted in a flat-bottomed STR for EIT experiments: (a) a schematic illustration, (b) a photo of the reactor**

The electric conductivity of the studied flow affects the current injections values. The high conductivity of the solution lowers the sensitivity of the EIT technique. Higher current injections may overcome the problem (Kourunen 2009; Aw et al. 2015). However, it imposes limits on the measuring system since the injection level is limited due to generator capacity and creates signal noise.

The EIT technique is based on an inverse problem solution. A small change in voltage may be caused by a significant change of the electric conductivity distribution in the flow domain. The possibility of multiple solutions requires additional information about the studied object, such as the virtual flow domain discretized spatially and reference data. Statistically averaged homogeneous conductivity distribution can be used as reference (Heikkinen 2005; Kourunen 2009). A homogeneous mixed solution is used as a reference in order to get background conductivity distribution. The spatial distribution of the dispersed phase or introduced reagent can be found using Equation (3.8) (Heikkinen 2005):

$$\Delta\sigma = \frac{2(\sigma_1 - \sigma_2)}{2\sigma_1 + \sigma_2}, \quad (3.8)$$

where  $\sigma_1$  and  $\sigma_2$  are the conductivity distributions of homogeneous and non-homogeneous solutions correspondingly.

The difference in conductivity distributions between the homogeneous and the measured solutions are visualized on a constructed 3D mesh of the studied domain. Using FEM, the conductivity difference is distributed among the elements of the mesh. Further conversion of the conductivity into the phase fraction is possible. Non-conductive objects presenting in a studied domain do not require special treatment, because they are removed during the subtraction operation of the conductivity distributions measured in homogeneous and non-homogeneous solutions.

### 3.2.3. Gas hold-up

Surface level variation was detected visually in gas hold-up measurements. The height difference between the liquid surface at non-aerated and aerated modes was determined. A moving liquid surface and foaming can worsen the measuring accuracy. To reduce uncertainties, experimental tips, described by Yawalkar et al. (2002) and Devi and Kumar (2015), were adopted. In particular, the surface level was recorded by a camera at several locations between the baffles with a millimeter scale on the reactor wall. Measurements at each point were repeated 10 times for averaging purposes. The overall gas hold-up in the STR was calculated using Equation (3.9):

$$\varepsilon_{\Delta h} = \frac{h_{gas} - h_l}{h_{gas}}, \quad (3.9)$$

where  $\varepsilon_{\Delta h}$  is the overall gas hold-up, and  $h_{gas}$  and  $h_l$  are the heights of the mixed solutions with and without gas introduction, correspondingly.

### 3.2.4. Oxygen mass transfer

Gas–liquid mass transfer gives the oxygenating capacity of an aerated reactor. Being independent of oxygen concentration in bubbles,  $k_L a$  determines the oxygen flux (Eq. [3.10]) together with the concentration difference:

$$\dot{n} = k_L a (c_{sat} - c_l), \quad (3.10)$$

where  $c_{sat}$  is the saturated oxygen concentration in water in  $M/m^3$ , and  $c_l$  is the oxygen concentration in liquid in  $M/m^3$ .

There are many isothermal techniques proposed to measure  $k_L a$  in gas–liquid stirred reactors (Pinelli et al. 2010). Most of them are based on transient measurements of species concentration in gas and/or liquid phases. Transformed into logarithmic form, the dynamics of the dissolved gas concentration to a step change in gas concentration is represented by a linear equation where the slope is  $k_L a$ . The time lag, or time constant, indicates a time that it takes for the probe to respond to a concentration step change. Accurate results are expected when the time lag is smaller than  $k_L a^{-1}$  (Van't Riet 1979; Ruchti et al. 1981). The response time constant ( $\tau_p$ ) of the probe was measured separately for each solution studied. Some techniques, such as the dynamic pressure method (Linek et al. 1989) and frequency response method (Vardar & Lilly 1982), use a change in the total pressure to cause a change in  $c_{sat}$ . Other methods, such as the batch and feeding steady-state methods (Vasconcelos et al. 1997), and the chemical dynamics method (Havelka et al. 1998), employ oxidation reaction to find the dissolved oxygen concentration based on the reaction products concentration in the liquid phase.

In many cases, liquid can safely be assumed to be perfectly mixed in stirred reactors, so the dissolved gas concentration is constant at any point in the liquid volume. However, the oxygen concentration in bubbles is changing as gas bubbles move in the volume of the reactor. Depending on the application, this can be taken into account via one of the



basic models proposed in literature. The “no depletion model” is suitable for small STRs when pure oxygen and/or low gas residence time are used, meaning that the driving force of gas–liquid mass transfer is constant. In cases of dilute gas, more realistic approaches have to be applied, such as the “perfect mixing model” or the “plug flow reactor model” where the bubbles oxygen depletion is modelled uniformly in all bubbles or dynamically, as a function of an axial coordinate and/or axial dispersion. Additional measurements of the dissolved oxygen dynamics at several axial positions and/or the RTD of gas are then required. However, the models assume a volume averaged gas concentration in a bubble instead of a surface average gas concentration (Linek et al. 1991; Pinelli et al. 2010) and do not consider breakage and coalescence phenomena.

Pinelli et al. (2010) conducted a comparison study of various combinations of the methods and models. They concluded that using the available up-to-date methods and models, gas–liquid  $k_La$  can be found with 20 % confidence. Among the transient measuring techniques, the dynamic pressure method produced the most accurate results. For gas phase modelling, the PF model, both with and without axial dispersion, is recommended for non-coalescent and coalescent systems, correspondingly (Pinelli et al. 2010). Linek et al. (1996) tested the perfect mixing and PF reactor models for the gas phase modelling in combination with the “gas-in” and dynamic pressure methods in water and sodium sulphate solutions. Despite the growing inaccuracy, along with the mixing intensity of the gas-in method in both coalescent and non-coalescent systems, below 200 W/m<sup>3</sup> of total volumetric power (including mixing and aeration), the gas–liquid mass transfer produced by both methods was similar.

Due to simplicity, the gas–liquid volumetric mass transfer coefficient was measured in this work by the dynamic gas-in method using a dissolved oxygen meter (MARVET BASIC). To measure the oxygen dynamics, the oxygen probe was placed in a nitrogenized reactor to track the dynamics of dissolved oxygen concentration when a gas valve was switched from nitrogen to air. Air was supplied until it reached a stable maximum concentration. The value of the  $k_La$  was computed from the measured data by parameter estimation software MODEST (Haario 2001) using Equation (3.11). Additionally, MODEST software was used to determine the baselines of minimum and maximum concentrations before data fitting:

$$\frac{c_{sat} - c_l(t_1)}{c_{sat} - c_l(t_2)} = \frac{e^{(-k_Lat)} - k_La\tau_p e^{-t/\tau_p}}{1 - k_La\tau_p}, \quad (3.11)$$

where  $c_{sat}$  is the saturated oxygen concentration in water in M/m<sup>3</sup>,  $c_l$  is the oxygen concentration in liquid at  $t_1$  and  $t_2$  in M/m<sup>3</sup>, and  $\tau_p$  is the time constant of the probe in s<sup>-1</sup>.

The formulation includes the assumptions of ideal mixing and no oxygen depletion for the liquid and gas phases, correspondingly. The model also assumes that liquid phase

resistance dominates in mass transfer, gas and liquid are mixed perfectly, and the pressure and oxygen concentration in the bubbles are constants.

### 3.2.5. Mixing power

Power draw was measured by a torque transducer installed on the shaft. A reading device was connected to the transducer to monitor agitator speed, torque, and power. Due to impeller-blade interaction with baffles, a slight vibration of the shaft was noticed, as well as fluctuations of the measured values within, at most, 8 % deviation. Theoretically, at steady state, the mechanical energy of mixing, supplied to fluid media in a closed stirred vessel (Eq. [3.12]), goes to friction with the vessel walls and surface. Energy losses at the surface are negligibly small. Therefore, the stress integral over the stirred tank walls, as well as over the impeller, produces the power shown in Equation (3.13) (Lane & Koh 1997).

$$P_\varepsilon = \rho \int \varepsilon dV, \quad (3.12)$$

$$P_\tau = 2\pi n \int \tau dA_{imp}. \quad (3.13)$$

## 3.3. CFD

### 3.3.1. An introduction to CFD tools for mixing flows

The laws of fluid mechanics were well established long ago, and they have proved their consistency in practice. Fluid dynamics in a constrained continuum can be described by the integration of the laws mathematically. However, practical solutions for various industrial tasks in applied engineering have been limited until the recent era of computerization. The rapid growth of computational power has allowed fast calculation of numerical problems that has boosted the development of CFD. The general idea behind the finite volume method (FVM) in CFD is a balance equation, which describes the physical laws of fluid mechanics within the space of an element. The consistency of the balance equation provides results at an unknown boundary when the values at other boundaries are known. Any limited space can be divided to a finite number of geometrical elements where the balance equations are to be solved. Providing boundary conditions creates gradients for variables, so the numerical solution progresses towards balance until a subjectively predefined level of accuracy is reached. Using these methods in practical applications, an engineer can obtain the inherent information of fluids dynamics or chemical reactions.

By *fluids*, engineering science usually refers to a substance, the deformation of which is not constrained by a crystal lattice, such as a liquid, gas, or plasma. CFD can use the finite element method (FEM) or FVM, where the numerical results are stored at the nodes or at the centers of mesh elements, correspondingly. Partial differential equations (PDEs) are solved in each element to resolve fluxes between the elements. Thus, fluid dynamics can be resolved with reasonable accuracy.

In order to tackle an engineering task dealing with fluid flow, an engineer has to go through the following steps:

- ❖ Computer-aided design (CAD) of the fluid domain
- ❖ Generation of a grid or mesh
- ❖ Assignment of boundary conditions (BCs) and making an initial guess
- ❖ Setting a mathematical method to solve a PDE
- ❖ Post-processing
- ❖ Validation of the achieved results

Depending on the custom-made or commercial software used, the listed steps may have specific features and can be treated individually. However, some common practical issues related to STR modelling were distinguished and described by Marshall and Bakker (2004) to save the time spent on trial and error way of learning. It is a good strategy to study the information available in published scientific literature on the object to be modelled. Relevant data, calculated directly, measured experimentally, and/or achieved through simulation results, can be a reasonable guide with which an engineer can make a rough judgment on model adequateness. In the case of an STR, such data are global gas hold-up, mass transfer, tip speed, the power number etc.

The geometrical sizing of a reactor, operational conditions, and the available computing power are used to make an approximate estimation of calculation time. The speed of a transport equation calculation is dependent on the degree of spatial discretization. Therefore, in the case of transient simulation, the approximate size of an easy-to-converge time step can be found from the smallest element in a model where velocity is the highest. The solution, progressing more than one element per time step, is hard to converge. Based on Courant–Friedrichs–Lewy condition (CFL), one can define time-step size and/or adjust the mesh size. Special attention should be paid to grid construction and model simplification not to bias fluid dynamics. It is a widely used practice to reduce the grid size by using symmetry and limiting to a sector of a cylindrical tank. However, care must be taken when doing so, since the number of baffles may differ from the number of impeller blades and such a resolved flow is biased (Versteeg & Malalasekera 2007). A mesh-size independence test is necessary to prove that the grid size is small enough to resolve the variable of interest. Thus, the velocity field can be calculated at a coarser mesh than turbulence energy or (in particular) the energy dissipation rate.

When the equations to be solved are assigned, boundary conditions (BCs) are applied. Unknown values at a BC can be safely approximated with default settings that have been proven to be consistent over a great number of cases. It is important to provide suitable values for the elements of a domain as an initial guess in order to avoid creating false gradients that would most likely cause divergence.

The important issues of solution control in CFD simulations—such as those related to steady or unsteady states, explicit and implicit methods, under-relaxation factors, and multi-grid settings—are not covered in this thesis. Information on these topics and much

more can be found by interested readers in the work of Versteeg and Malalasekera (2007), and Date (2005).

Due to spatial discretization, CFD models are full of empirical parameters that are consistent in many cases, but at the same time, they cause inaccuracy. Therefore, the validation step is crucial for a CFD model and requires accurate experimental data. If such data are not available, simulation results obtained at a highly discretized domain, where the numerical error is at a minimum, can be used with care for validation—for example, as used in direct numerical simulation (DNS).

### 3.3.2. Agitation

Stirrer rotation can be modelled implicitly via a BC, semi-implicitly, using a multiple reference frame (MRF; Luo et al. 1994), or explicitly, by using a sliding mesh (SM; Marshall & Bakker 2004). Schematic illustrations of the approaches are presented in Figure 3.9.

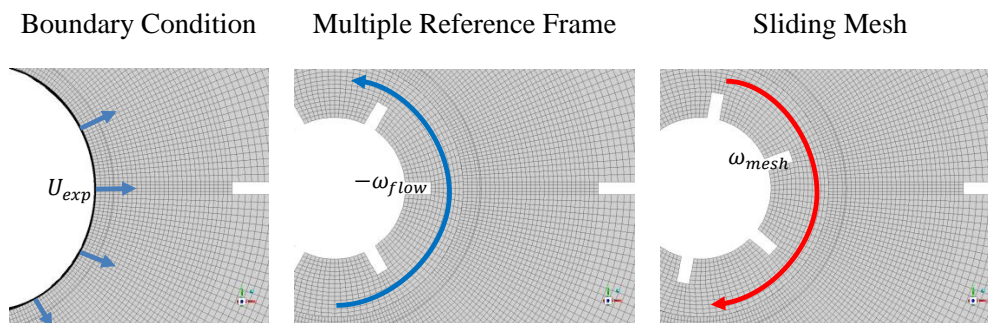


**Figure 3.9. Illustrations of the methods to simulate impeller rotation**

In the first approach, experimental data of a mixer is vital in order to simulate the jet stream created by the impeller by defining the velocity at the BC of a cylindrical domain surrounding the impeller. This approach is useful when computational power is limited and the accurate resolution of the impeller region can be approximated. It is worth mentioning that such multiphase mixing flows simulations should be treated with care because the BC creates flux apart from velocity gradient.

The latest two methods are capable of resolving the flow of impeller geometry accurately. Both the explicit and semi-implicit methods require the reactor domain to be split into a rotating zone (RZ) and a stationary zone (SZ) so that flow is calculated in the RZ and transferred into the SZ at each iteration. SM is the easiest method to understand, wherein the RZ moves relative to the SZ transmitting fluid velocity. The most accurate method, SM, can only be simulated in transient manner, which requires many time steps to be resolved before steady-state mixing is reached. The MRF method has the advantages of a steady-state solution and time efficiency. However, relative positioning of baffles to impeller blades that are “frozen” in space affects the mixing hydrodynamics of the resolved flow. This issue is raised and researched in Publication II. It is worth mentioning

that a combination of the SM and MRF methods was proposed by Lindstedt (2017) to decrease the simulation time significantly, compared to the “pure” SM transient simulation, while counting for baffle-impeller interaction.

### 3.3.3. Multiphase flow

Incompressible inviscid fluids, interacting and immiscible, can be described by the Eulerian method. Any separation caused by the action of body forces, such as gravity or a centrifugal force, can only be captured by treating the fluids with a multiphase model. When such a model is used, each fluid is assigned a separate set of properties. While the primary phase is treated by the Eulerian method, the secondary phase can be described by either an Eulerian model (Volume of Fluid, Eulerian–Eulerian, Eulerian granular models) or the Lagrangian method (a discrete phase model, working at a gas volume fraction below 10 %).

In cases of aerated STRs, the Eulerian–Eulerian multiphase approach is the most used model to simulate mixed immiscible fluids in which the phases are considered to be interpenetrating continua, expressed via the volume fraction per phase. The mass balance is controlled by Equation (3.14):

$$\sum_i \alpha_i = 1 \quad (3.14)$$

and each phase is described by a set of conservation equations (Eqs. [3.15–3.16]):

$$\nabla \bar{u} = 0, \quad (3.15)$$

$$\bar{u} \cdot \nabla \bar{u} = -\nabla \bar{p} + \nabla(\mu \nabla \bar{u}), \quad (3.16)$$

where  $\alpha_i$  is the phase volume fraction,  $\bar{u}$  a phase velocity in m/s,  $\bar{p}$  is the pressure in Pa, and  $\mu$  is the viscosity in Pa·s.

### 3.3.4. Turbulence

Turbulence is the natural mechanism of transmitting the mechanical energy of agitated fluid at macro scale to the molecular level or to heat under viscous forces. When convection surpasses viscous forces ( $Re > 1$ ), the laminar flow is broken by turbulent swirls appearing because of the spatial misbalance of the counteracting forces of convection and molecular friction. As a result, turbulent flow can be considered as a cascade of eddies of characteristic lengths that become smaller as turbulence grows. Anisotropic nature of turbulence and high dependence on spatial resolution is the reason why several different turbulence models have been developed (Wilcox 1994).

Following the statement that “All models are wrong, but some of them are useful,” researchers have produced several turbulence models that are feasible with the available computational power. DNS is capable of resolving turbulence directly. However, the simulations are very time-consuming for even lab-scale cases, not mentioning the scale

of industrial units. The large eddy simulation model resolves turbulence up to the scale of big eddies, below which turbulence is assumed to be homogeneous and turbulence eddies are modelled. However, this highly accurate model still takes a significant amount of computational time and requires averaging if a steady-state flow is wanted. In practice, the Reynolds-averaged Navier-Stokes (RANS) models where flow velocity is decomposed into mean and fluctuating parts are the most used turbulence models. Based on Boussinesque's assumption, they use turbulent viscosity modelling to describe turbulent flow. Turbulence formulation in RANS models is based on statistical analysis of Reynolds stresses rather than on actual physical phenomena (Wilcox, 1994).

Flow in stirred reactors is mostly turbulent, except when highly viscous solutions are being mixed. A solution in an STR experiences jet-like and swirling motion with flow separation that makes it difficult to simulate by the standard  $k$ - $\varepsilon$  model (Marshall & Bakker 2004). Therefore, the renormalized group (RNG) model was developed as an upgrade of the standard  $k$ - $\varepsilon$  model in order to describe highly swirling motions by using renormalization theory (Orszag et al. 1993). However, at high strain, normal stress may become negative, which is not physical. In turn, the  $k$ - $\varepsilon$  Realizable model, developed to overcome the negative strain mathematically, is questionable when it is used in conjunction with the MRF technique because the formulation includes mean rotation (Shih et al. 1995). The  $k$ - $\omega$  shear stress transport (SST) model combines the benefits of the  $k$ - $\varepsilon$  model in free-stream modelling with the near-wall treatment according to the  $k$ - $\omega$  formulation (Menter 1993). Being significantly more computationally expensive, the Reynolds stress model (RSM) includes additional transport equations to describe the Reynolds stresses and produces more accurate results for complex flows (Launder et al. 1975). Due to the pros and cons of the described turbulence models, as well as their incomplete comparative studies and the contradictory results published in scientific literature, another performance assessment study is required. Therefore, in Publication I, four popular models from among the RANS models family were tested in a round-bottomed STR, namely the  $k$ - $\varepsilon$  RNG model, the  $k$ - $\varepsilon$  Realizable model, the SST  $k$ - $\omega$  model, and the RSM. A generalized view of the RANS two-equation models are presented below:

$$\bar{u} \cdot \nabla k = P - \varepsilon + \nabla \cdot \left[ \left( \mu + \frac{\mu_{turb}}{\sigma_k} \right) \nabla k \right], \quad (3.17)$$

$$\bar{u} \cdot \nabla \varepsilon = C_{\varepsilon 1} \frac{\varepsilon}{k} P - C_{\varepsilon 2} \frac{\varepsilon^2}{k} + \nabla \cdot \left[ \left( \mu + \frac{\mu_{turb}}{\sigma_\varepsilon} \right) \nabla \varepsilon \right], \quad (3.18)$$

where  $k$  is the turbulence kinetic energy in  $\text{m}^2/\text{s}^2$ .

In the case of a dilute secondary phase, the dispersed turbulence formulation model can compute fluctuating quantities of the phase as the function of the mean terms of the primary phase. From the primary phase turbulence terms  $k$  and  $\varepsilon$ , the secondary phase turbulence terms are found and the exchange of turbulence momentum between phases is computed based on the Tchen's theory (Tchen 1947; Hinze 1975).

### 3.3.5. Phase Interaction

Surface tension and difference in the density and wettability of the immiscible fluids create interfacial forces that act in multiphase flows, such as drag, lift, turbulence interaction, and wall lubrication. The momentum conservation equation (Eq. [3.19]) includes a cumulative force  $\vec{F}_q$  (Eq. [3.20]) acting on the primary phase:

$$\frac{\partial}{\partial t}(\alpha\rho\vec{u})_q + \nabla \cdot (\alpha\rho\vec{u}\vec{u})_q = \nabla \cdot (\alpha\sigma)_q - \alpha_q\nabla p + \vec{F}_q + \alpha_q\rho_q\vec{g}, \quad (3.19)$$

$$\vec{F}_q = \sum_{p=1}^n (K_{pq}(\vec{u}_p - \vec{u}_q) + \dot{m}_{pq}\vec{u}_{pq} - \dot{m}_{qp}\vec{u}_{qp}). \quad (3.20)$$

An analysis of the contribution of the terms to mixed flow hydrodynamics was assessed by Champagnat et al. (2014), Joshi et al. (2011b), Khopkar and Ranade (2006) Li (2014), Scargiali et al. (2007), and Taghavi et al. (2011). The researchers concluded that drag force is the major influence in an aerated stirred reactor. A single droplet experiences a drag force, which is dependent on bubble shape. Tsamopoulos et al. (2008) showed that droplets have the shape of spheres when sized below 3 mm and are in a gas–liquid solution. The drag force on gas bubbles, droplets, or solid particles of a regular spherical shape, is alike. Therefore, the drag force of sinking solids was studied experimentally at first in laminar flows and then in turbulent flows (Brucato et al. 1998; Schwartzberg & Treybal 1968). Different drag models can be found in published literature. The drag model, proposed by (Schiller & Naumann, 1933), expressed in Equation (3.21), is suitable for rigid spherical particles in laminar flow:

$$K_{pq} = \frac{\rho_p C_D Re}{144\tau_p} d_p A_i, \quad (3.21)$$

where  $\rho_p$  is the particle density in kg/m<sup>3</sup>,  $C_D$  is the drag force coefficient,  $Re$  is the relative Reynolds number, and  $A_i$  is the interfacial area in m<sup>2</sup>. The drag force coefficient is the function of  $Re$  according to the following formulation:

$$C_D = \begin{cases} 24(1 + 0.15Re^{0.687}) & Re \leq 1000 \\ 0.44 & Re > 1000. \end{cases} \quad (3.22)$$

Being distorted, big droplets can have changing cross-sectional area in a normal direction towards the primary phase flow stream, which affects drag force. Several models are available for taking the drag force due to shape change into account.

The drag force model is based on bubble-rise velocity, measured in stagnant fluids, which is higher than the rise velocity in turbulent flow. A model correcting the drag force coefficient for turbulence was first proposed by Brucato et al. (1998). This turbulence modification factor (Eq. [3.23]) changes the stagnant fluid drag force in order to make it suitable for turbulent multiphase flow simulation:

$$K'_{pq} = \eta K_{pq} = \left(1 + K \left(\frac{d_p}{\lambda}\right)^3\right) K_{pq}, \quad (3.23)$$

where  $\eta$  is the turbulence modification factor,  $K = 6.5 \cdot 10^{-6}$ ,  $\lambda$  is the Kolmogorov length scale, m. Later, Lane et al. (2005) suggested a new correlation (Eq. [3.24]) for the turbulence modification factor that is based on the ratio of stagnant terminal velocities to turbulent terminal velocities  $\frac{u_s}{u_T}$ , which is correlated with the ratio of particle relaxation time to integral time scale of turbulence (Eq. [3.24]):

$$\eta = \left(1 - 1.4 \left(\frac{\tau_p}{T_L}\right)^{0.7} e^{\left(\frac{0.6\tau_p}{T_L}\right)}\right)^{-2}, \quad (3.24)$$

$$T_L = 0.135 \frac{k}{\varepsilon}. \quad (3.25)$$

The presence of bubble swarms reduces liquid flow energy, increasing the drag force between the phases. The effect of the gas volume fraction (0.01–0.45) of the dispersed gas on gas–liquid drag force has been modelled by Roghair et al. (2011) in flows of intermediate and high  $Re$ , resulting in the following formulation:

$$C_{D,swarm} = C_D \left(1 + \alpha_p \left(\frac{18}{E\ddot{o}}\right)\right) (1 - \alpha_p), \quad (3.26)$$

where  $E\ddot{o}$  is the Eötvös number, which is a dimensionless number, characterizing the shape of bubbles or droplets moving in fluid.

Acting perpendicularly to flow in the direction of the velocity gradients growth, lift force takes place in shear flow and is proportional to slip velocity (Eq. [3.27]):

$$F_L = -C_L \alpha_p \rho_q (\vec{u}_q - \vec{u}_p) \times (\nabla \times \vec{u}_q), \quad (3.27)$$

where  $C_L$  is the lift force coefficient.

Under strong agitation, bubbles follow the primary phase flow in diluted gas–liquid flow in a turbulent regime that imposes insignificant lift force.

Gas bubbles were observed to be pushed away from a solid wall when moving in liquid, which is caused by liquid wetting the wall. The corresponding *wall lubrication force* is described via the following equation:

$$F_{WL} = C_{WL} \alpha_p \rho_q |\vec{u}_q - \vec{u}_p|^2 \vec{n}_w, \quad (3.28)$$

where  $C_{WL}$  is the wall lubrication force coefficient and  $\vec{n}_w$  is the normal vector to the wall.



Generally, the force acts at the distance of five droplet diameters (Lubchenko et al. 2018). Therefore, in large-scale reactors it is insignificant and requires a fine mesh next to the wall to capture the phenomenon.

Unlike in the Eulerian method, different phases cannot physically occupy the same space in reality. Therefore, the inertia of fluid media caused by the relative acceleration of a droplet is modelled artificially in CFD. The force is called *virtual mass force* or *added mass force* (Eq. [3.29]):

$$F_{VM} = C_{VM} \alpha_p \rho_q \left( \frac{d_q \vec{u}_q}{dt} - \frac{d_p \vec{u}_p}{dt} \right), \quad (3.29)$$

where  $C_{VM}$  is the virtual mass force coefficient.

### 3.3.6. Mass transfer

#### *The mass transfer coefficient in liquid*

The volumetric mass transfer coefficient is the product of the specific interfacial area and the mass transfer coefficient. The specific surface area between fluids is sensitive to bubble-size distribution and gas hold-up. Therefore, in accurate simulations a turbulent multiphase model is used in combination with a population balance model. There are two main approaches to evaluate the interfacial mass transfer coefficient, namely the slip velocity and eddy-cell models. Both of these models are based on the “penetration” theory described by Higbie (1935). According to the theory, a molecular diffusion process takes place through two contacting fluids films at the interphase. In a turbulent flow the diffusion is described by surface renewal models (Frössling, 1938; Higbie, 1935; Lamont & Scott, 1970; Levins & Glastonbury, 1972; Mena, 2005). “Slip velocity” models (Frössling, 1938) describe the liquid film renewal mechanism by the phase velocity difference, which is responsible for moving the old portion of the fluid from the film to the liquid bulk and a new portion to the film. On the other hand, the chaotic flow in turbulent regime has brought the idea of the interface being surrounded by turbulence eddies that are responsible for the diffusion of molecules (Lamont & Scott, 1970). The slip velocity approach is fair in laminar flows while it underestimates  $k_L$  with growing mixing intensity (Linek et al. 2004). Based on the eddy-cell model, Kawase et al. (1992) proposed a correlation for the gas–liquid mass transfer coefficient in power-law viscous fluids:

$$k_L = C \sqrt{D_L} \left( \frac{\varepsilon \rho}{K} \right)^{\frac{1}{2(1+n)}}, \quad (3.30)$$

where  $D_L$  is the gas diffusivity in liquid in  $\text{m}^2/\text{s}$ ,  $\rho$  is the liquid density in  $\text{kg}/\text{m}^3$ ,  $K$  is the consistency index in  $\text{Pa} \cdot \text{s}^n$ ,  $n$  is the dimensionless flow behavior index, and  $C$  is the proportionality coefficient.

The effect of gas bubbles on the mass transfer coefficient is taken into account with the proportionality coefficient. The value of 0.301 for the coefficient, proposed by Kawase et al. (1992), has been tested by Garcia-Ochoa and Gomez (2004) and found to produce accurate results for gas–liquid mass transfer in stirred reactors.

### *Interfacial area concentration*

The specific volumetric surface area of the secondary phase is found as follows:

$$A_p = \frac{6\alpha_p}{d_p}. \quad (3.31)$$

Constant bubble-size approximation can be fairly accepted in many industrial applications where the mixed solutions may contain high concentration of ions and have low surface tension and high mixing power is used. In such cases, bubble size (which is accepted as being uniform in the reactor domain) has to be measured relatively accurately.

### *Population Balance Models*

However, mixing power is generally not uniform in stirred reactors and gas bubbles tend to have different sizes due to coalescence and breakage phenomena. The idea of the population balance model (PBM) is to solve a conservation equation for the number density function (NDF) to compute droplet volume, which changes in space and time. The NDF is defined as  $n(V, t)$  and the conservation equation is as follows:

$$\frac{\partial}{\partial t}(n(V, t)) + \nabla \cdot (\vec{u}n(V, t)) = B_C - D_C + B_B - D_B, \quad (3.32)$$

where  $B_C$ ,  $D_C$ ,  $B_B$ , and  $D_B$  are the rates of the death and birth of bubbles or droplets due to collision and breakage.

### *Breakage and Coalescence*

Suitable breakage and coalescence functions are needed in order to close the PBM equation. Turbulence fluctuation is the dominating mechanism in agitated reactors. The frequency of collision is defined as the sweep of effective volume through space and time (Eq. [3.33]; Figure 3.10):

$$\omega_{col} = \frac{\pi}{4}(d_i + d_j)^2(u_i^2 + u_j^2)^{0.5}, \quad (3.33)$$

where  $d_i$  and  $d_j$  are the bubbles diameters (bubble diameter and the turbulent eddy length scale),  $u_i$  and  $u_j$  are the velocities of the bubbles (bubble and eddy).

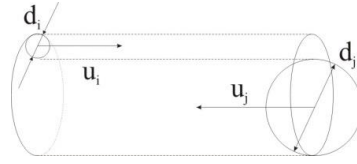


**Figure 3.10. Illustration of effective volume sweep**

In turbulent flow, the bubble surface is attacked by turbulent eddies. The concept of the breakage theory is illustrated in (Figure 3.11, on the left). If the scale of colliding eddy is bigger than the bubble size, the bubble is transported unharmed. A low energy turbulent vortex of the same or smaller scale than the bubble can only distort the bubble while breakage happens when the energy of the colliding eddy is higher than the energy of the bubble surface tension (Luo & Svendsen 1996). The breakage kernel includes the breakage frequency and possible size distribution of the droplets or bubbles produced by breakage. The size distribution before collision and energy dissipation rate affect the resulting BSD after breakage (Luo & Svendsen 1996).

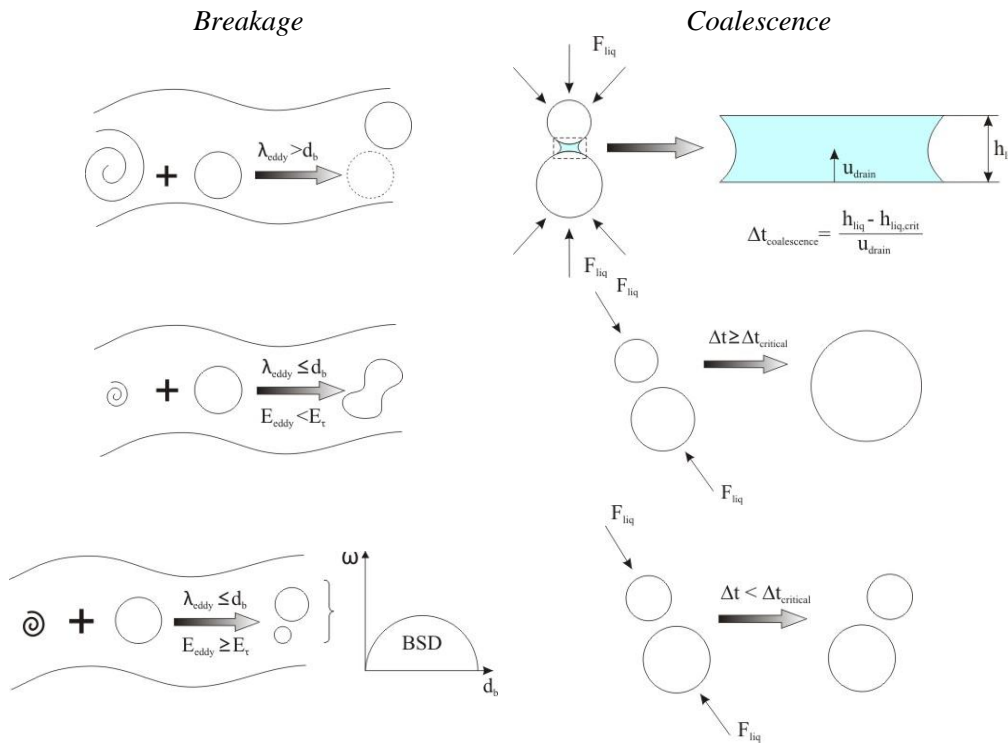


**Figure 3.11. Illustrations of the concepts of droplet breakage (on the left) and coalescence (on the right) theory**

Aggregation kernel mainly depends on the frequency and efficiency of collisions between particles or between particles and turbulent eddies. There are several physical

mechanisms that drag gas bubbles—such as wake entrainment, buoyancy force difference, velocity gradient, eddy capture, and turbulence fluctuation—which result in bubble contact of sufficient time for the intermediate liquid film thickness to reach a critical value, at which it is disrupted and the bubbles coalesce (Figure 3.11, on the right). In case the contact time is smaller, the bubbles are drawn away by the flow without collision (Luo, 1993).

#### *Methods for Classes*

The probability density function can be expressed via a finite number of classes representing the population distribution (Kumar & Ramkrishna, 1996). Then the PBM equation is reformulated in terms of the size fraction (Eq. [3.34]):

$$\frac{\partial}{\partial t}(\rho_p \alpha_p f_i) + \nabla \cdot (\vec{u} \rho_p \alpha_p f_i) = B_C - D_C + B_B - D_B, \quad (3.34)$$

where  $f_i$  is the class  $i$  fraction of all the classes.

It is a robust method, describing relatively narrow BSD with a moderate amount of classes. The higher the accuracy demanded, the more classes are required. When the size groups experience significant velocity difference, they can be assigned to different phases (the inhomogeneous method of classes [IMC]) sharing a common volume fraction, which enables bubbles to migrate between those size groups. However, the high accuracy of the approach demands a significant number of additional equations to be solved, which is highly time consuming.

#### *Methods of Moments*

In order to reduce computational time, the method of moments (MOM) was proposed by Randolph and Larson (1971), wherein the transport equations of number density are replaced with fewer transport equations, those of the moments characterizing distribution. By integrating the number density throughout the particle space, weighted with the particle property raised to its  $i^{th}$  power, a limited set of momentum is defined as follows:

$$m_k(\vec{x}, t) = \int_0^\infty n(L; \vec{x}, t) L^k dL = \sum_{i=1}^N \omega_i L_i^k, k = 0, 1, \dots, N-1, \quad (3.35)$$

where  $\omega_i$  is the weight of the  $i^{th}$  moment and  $L$  is the cumulative length of the particles.

Additional transport equations are solved for the limited amount of moments (3 to 8) in order to effectively describe the BSD (Eq. [3.36]; McGraw 1997):

$$\frac{\partial}{\partial t}(m_k) + \nabla \cdot (\vec{u} m_k) = B_C - D_C + B_B - D_B. \quad (2.36)$$

The moments have no physical meaning, but they have valuable information such as the total number of particles ( $m_0$ ), cumulative length ( $m_1$ ), total surface area ( $\pi m_2$ ), total volume ( $K_v m_3$ ), and Sauter mean diameter ( $m_3/m_2$ ) per unit volume.

As a compromise between reduced computational efforts and accuracy, the quadrature method of moments (QMOM) approach does not describe the size distribution exactly (McGraw, 1997). However, it produces average and total quantities representing the BSD. Analogous to the IMC, the direct quadrature method of moments (DQMOM) uses several quadrature points and has its own momentum (Marchisio & Fox, 2005) in order to overcome the drawback of the QMOM (where the secondary phase has the same momentum for all droplets).

#### *The Interfacial Area Concentration Approach*

To reduce the computational load further, a single transport equation for the gas phase of interfacial area concentration  $\chi$  (Eq. [3.37]) can be solved instead of a number density function (Kocamustafaogullari & Ishii, 1995):

$$\frac{\partial \chi}{\partial t} (\rho_p \chi) + \nabla \cdot (\rho_p \vec{u}_p \chi) = \frac{1}{3} \frac{D\rho_p}{Dt} \chi + \frac{2}{3} \frac{\dot{m}_p}{\alpha_p} \chi + \rho_p (S_C + S_B), \quad (3.37)$$

where  $S_C$  and  $S_B$  are the sink and source terms due to coalescence and breakage, measured in  $s^{-1}$ .

The approach has been successfully applied by Liu et al. (2017) to study gas hold-up and mean bubble size in an STR equipped with a Rushton turbine. However, the method requires additional transport equations to be solved when bubble-size groups experience different velocity.

#### **3.3.7. Species transport and volumetric reactions**

The species transport technique is widely used in reactor engineering to calculate RTD and to simulate reaction kinetics. The general assumption in this technique is that the species follow the phase flow without interaction. The conservation equation of the species transport in turbulent flow is as follows:

$$\frac{\partial}{\partial t} (\rho Y_i) + \nabla \cdot (\rho \vec{u} Y_i) = \nabla \cdot (\rho (D_{i,L} + D_t) \cdot \nabla Y_i) + R_i, \quad (3.38)$$

where  $Y_i$  is the mass fraction of component  $i$ ,  $D_{i,L}$  and  $D_t$  are the diffusivities due to laminar and turbulence diffusion correspondingly, measured in  $m^2/s$ , and  $R_i$  is the net rate of the production of species by the  $i$  chemical reaction in  $kg/(m^3 \cdot s)$ .

### 3.3.8. The mesh-size independence test

Grid resolution influences the results of numerical simulations. Therefore, several grids are usually tested in simulations in order to conduct a grid independency study. Good practice is to make such grids by doubling the mesh size relative to one another. The scaling uniformity should be maintained as much as possible. A variable of interest can differ significantly within the domain of CFD model, therefore several representative points can be sampled. One criterion to estimate grid independence is normalized root mean square error (NRMSE) of CFD predictions (Wang & Zhai 2012), which formulation is as follows:

$$NRMSE = \frac{3}{\left(\frac{N_{fine}}{N_{coarse}}\right)^p - 1} \sqrt{\frac{\sum_{i=1}^n (\varphi_1(i) - \varphi_2(i))^2}{\sum_{i=1}^n (\varphi_2)^2}} 100\%, \quad (3.39)$$

where  $N$  is number of cells in a grid (it is advised to keep grid size ratio above 1.3 [Celik et al. 2008]),  $p$  corresponds to the order of discretization,  $n$  is the number of samples, and  $\varphi_1$  and  $\varphi_2$  are predictions of coarse grids and fine grids accordingly.

### 3.3.9. The developed CFD modelling on multiphase STR simulation

Many efforts were made to develop the CFD modelling of multiphase flow in STR before the start of the doctoral thesis. Joshi et al. (2011) presented a review of the works, related to the CFD simulation of multiphase flow in STR. A year later, Sajjadi et al. (2012) published a review of the works related to multiscale CFD modelling of gas-liquid mixing in STRs.

Apart from the works directed at the improvement of the existing fundamental models, some researches concentrated at improvement of the performance of the models by adding new phenomena, going for higher accuracy of CFD results as well as developing the semi-empirical algorithms to benefit from the accuracy of CFD flow models and reduce computational time.

Accurately resolved turbulence improves the simulation results of gas-liquid mixing. The LES method was used by Zhang et al. (2012) to simulate liquid phase of gas-liquid mixing in a lab scale STR. They studied the effects of tracers feed location, mixing speed and gas flow rate on mixing time. The predicted history of the tracers concentration as well as the mixing times were in good agreement with experimental data, however no hydrodynamics validation was presented. High accuracy of the LES model costed two months to perform one simulation at 830 000 elements mesh and a constant bubble size.

Modelling of gas-liquid interfacial area is the key towards accurate simulation of the mass transfer rate. Ramsey et al. (2019) achieved much accurate results of the gas-liquid mass transfer using PBM compared to constant bubble assumption. The most time-consuming MC approach was used to simulate dispersed gas in STR in many studies, among which are Kálal et al. (2014), Bao et al. (2015), Sarkar et al. (2016), Li et al. (2017), Nauha et

al. (2018), Ramsey et al. (2019). Kálal et al. (2014) performed a comparison of different break-up models using a lab scale STR. The superior model showed good agreement with experimental data. Using the Luo and Svendsen break-up model (Luo and Svendsen, 1996) to simulate gas void fraction in a multiple impeller STR, Bao et al. (2015) achieved less accurate results compared to the local gas hold-up, measured by a conductivity probe. Li et al. (2017) tested several combinations of breakage and coalescence models to predict local gas hold-up in a dual Rushton turbine reactor. They concluded that the constant bubble size assumption produced the local gas fraction value with the accuracy similar to PBM at low gas flow rates. However, at the high gassing rates the application of PBM showed clear advantage. Less accurate, but more effective the CQMOM approach was used by Basavarajappa and Miskovic (2016) in a multiphase STR and a flotation cell modelling. Using Laakkonen's breakage (Laakkonen et al. 2006) and Lane's drag force (Lane, 2006) models the Sauter mean diameter in the STR, studied by Laakkonen experimentally (Laakkonen et al. 2005), was well predicted. Liu et al. (2017) showed a good match between the simulation results of the interfacial area concentration approach and the local gas fraction, measured experimentally in a lab STR. Unfortunately, mean bubbles size wasn't validated. Witz et al. (2016) simulated dispersed gas in three impeller STR at lab ( $0.15 \text{ m}^3$ ) and industrial ( $40 \text{ m}^3$ ) scales using Eulerian-Lagrangian method. Without tuning of empirical coefficients, a fair agreement of local gas hold-up with experimental data was achieved. However, the prediction of the global mass transfer rate was less successful using slip velocity approach to calculate  $k_L a$ . The PBM approaches are to be analysed at a common ground, for instance, by using the same STR, well studied by Laakkonen et al. (2005). No doubt, more experimental data on multiphase mixing flows in STRs of various scale and geometry are needed.

Apart from the development of the gas-liquid hydrodynamics modelling, some researchers concentrated at the simulation of gas-liquid mass transfer. For the mixed solutions with relatively constant average bubbles size Bach et al. (2017) showed an iterative algorithm where they tuned the bubble  $d_{32}$  until the calculated mass transfer matches the experimental data. More time demanding but mechanistic approach was proposed by Sarkar et al. (2016). They tuned initial values of size classes at gas inlet based on experimental value of  $k_L a$ . To overcome the time demanding CFD simulation by reducing calculation accuracy, the CFD results of gas-liquid hydrodynamics were converted by Nauha et al. (2018) into a compartmental model, which was then used to calculate local oxygen mass transfer.

## 4. Results and Discussions

### 4.1. Gas–liquid mixing in a round-bottomed STR

#### 4.1.1. The research tasks

The aim of this work was to examine dilute non-reactive gas–liquid flow agitated in a stirred reactor, both experimentally and numerically. The reviewed literature on the numerical description of mixed flows in STRs is, to some extent, contradictory and deficient. Therefore, some uncertain issues—such as the feasible models for turbulence and gas–liquid phase interaction—requires validation backed by experimental measurements. Firstly, a single-phase flow was modelled via widely used turbulence models (namely the  $k$ - $\varepsilon$  RNG model, the  $k$ - $\varepsilon$  Realizable model, the  $k$ - $\omega$  SST model, and the RSM) for comparison. The accuracy of the examined turbulence models was assessed using PIV and mixing power measurements. The most accurate turbulence model was then used to simulate gas–liquid mixing. Bubbles in the dilute gas–liquid flow in this study are simplified to spherical droplets of average constant size. A comparison of several laminar drag force models, used in conjunction with different correcting factors for turbulence drag force, was conducted. In addition, the effect of non-drag forces—a cumulative effect comprising lift, wall lubrication, and virtual forces—on liquid phase hydrodynamics is examined. Table 4.1 presents the simulated operational conditions, the phenomena modelled, and the models describing the phenomena numerically used in the study.

**Table 4.1. The summarized conditions of mixing simulations**

Phase	Agitation rate, s <sup>-1</sup>	Gas superficial velocity, mm/s	Phenomena	Models
Water	5	-	Turbulence	$k$ - $\varepsilon$ RNG model (Orszag et al. 1993)
				$k$ - $\varepsilon$ Realizable model (Shih et al. 1995)
				$k$ - $\omega$ SST model (Menter, 1993)
				RSM (Launder et al. 1975)
			Near-wall flow	Standard wall function model
Air-water	5	0.83	Primary phase turbulence	$k$ - $\varepsilon$ Realizable model (Shih et al. 1995)
		0.67	Near-wall flow	Standard wall function model



$(d_b = 1 \text{ mm})$			Secondary phase turbulence	Dispersed turbulence model
				Per phase turbulence model
			Drag force in laminar flow	Model of Schiller & Naumann (1933)
				Model of Morsi & Alexander (1972)
				Model of Takamasa & Tomiyama (1999)
			Drag force in turbulent flow	Model of Brucato et al. (1998)
				Model of Lane et al. (2005)
			Lift force	Model of Saffman (1965)
			Wall lubrication force	Model of Tomiyama (1998)
			Turbulence dispersion force	Model of Burns et al. (2004)

#### 4.1.2. The methods and research progress

##### *Water mixing*

The STR chosen in this research represents a typical round-bottomed STR with a Rushton turbine that is used in chemical engineering. Based on the studied literature (Joshi et al. 2011a) on the applicability of turbulence models in an STR, it was not clear which model describes the mixing hydrodynamics most accurately. Therefore, four models from the RANS family were used—namely, the  $k$ - $\varepsilon$  RNG model, the  $k$ - $\varepsilon$  Realizable model, the  $k$ - $\omega$  SST model and the RSM—in single-phase flow agitated in a tall reactor with a single impeller. A regular grid was constructed with such a mesh size for the layer next to walls that the dimensionless  $y^+$  value falls within the applicability limits (30–300) of the standard wall function (Cebeci et al. 2005). To save time, the MRF approach was used instead of the SM approach as the difference between the methods is small (Joshi et al. 2011a). QUICK (quadratic upstream interpolation for convective kinematics) differencing scheme was applied to the dependent variables while the SIMPLE (semi-implicit method for pressure linked equations) pressure–velocity coupling algorithm was used. The convergence criteria were set to  $10^{-6}$  and the single-phase simulation of the mixed flow was run until the flow was resolved and the residuals stabilized below the preset level of convergence.

The qualitative results of the water mixing simulations using different turbulence models are presented in Figure 4.1.

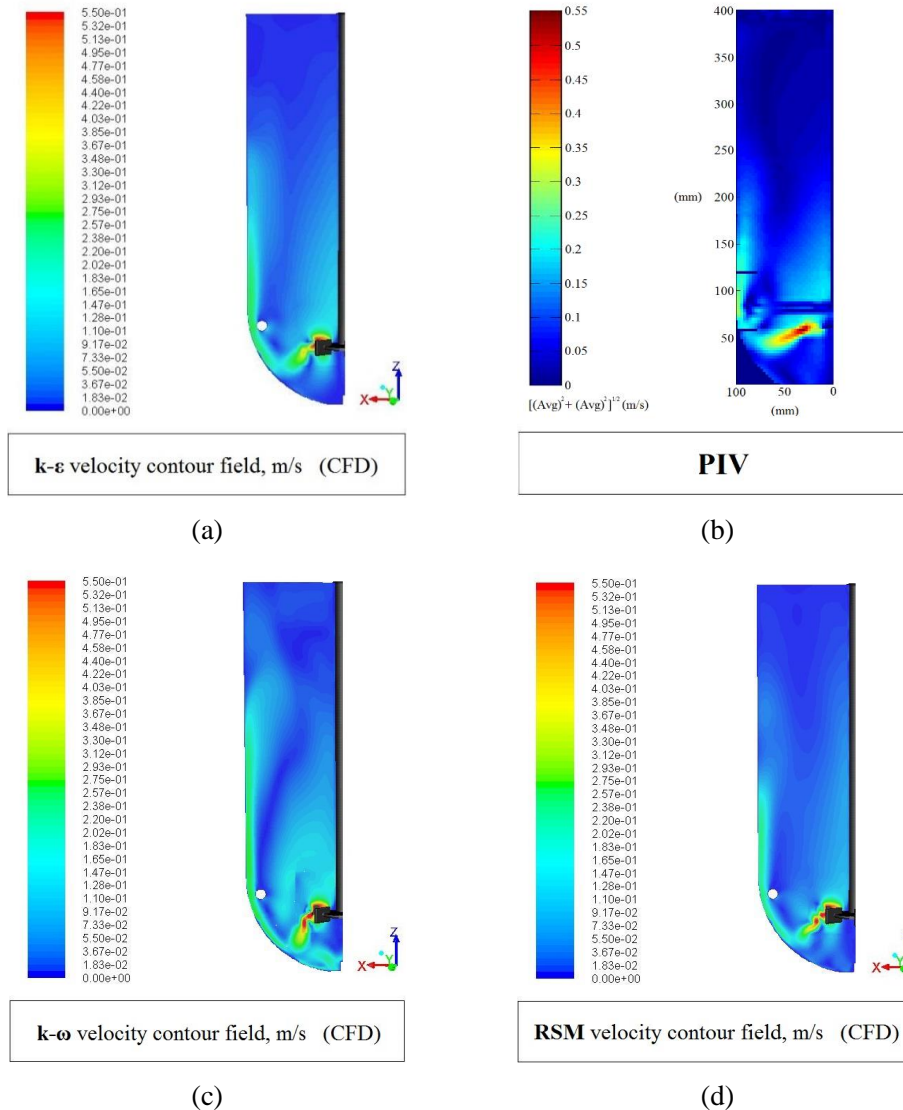


**Figure 4.1. The mean velocity contour fields simulated by CFD using different turbulence models and measured by PIV: (a) the  $k-\epsilon$  Realizable model, (b) PIV, (c) the  $k-\omega$  SST model, and (d) the RSM**

The overall similarity between the simulations and the PIV results is obvious. However, minor differences can be found on a closer look. The jet-stream flow is worst resolved by the  $k-\omega$  SST model. At higher computing costs, the RSM turned out to show the best

accuracy in the stream jet by predicting a higher value and a better overall velocity topology than the  $k$ - $\varepsilon$  Realizable model.

Profiles at different vertical coordinates were sampled in order to assess the simulation results produced by the turbulence models tested against radial and axial normalized velocities, measured by PIV (see Publication I).

Local volumetric power, showing the average amount of mixing energy dissipated in liquid, is an important parameter for multiphase flows and reacting flows in an STR since it controls many phenomena, such as micromixing, breakage and coalescence, reagent supply, and reactant wash-out around reacting bubbles. Therefore, the predictions of  $\varepsilon$  by the turbulence models were estimated (Eq. [3.12]) and compared against the torque (Eq. [3.13]) measured experimentally (Table 4.2).

**Table 4.2. Power draw prediction by the RANS models**

Model	Power( $\tau$ ), W	Power( $\varepsilon$ ), W	Difference, %
$k$ - $\varepsilon$ RNG model	1.39	0.77	45
$k$ - $\varepsilon$ Realizable model	1.38	0.96	31
$k$ - $\omega$ SST model	1.29	0.75	42
RSM	1.30	0.74	43
Measured experimentally	1.38–1.46		-

The results of the comparison indicate that the RSM produces the most accurate results among the RANS models tested in the STR and should be used if a single-phase flow is to be resolved. However, the  $k$ - $\varepsilon$  Realizable model is a compromise between accuracy and computational time when choosing from among the two-equation turbulence models. Therefore, in the following gas–liquid simulations, the  $k$ - $\varepsilon$  Realizable model was used.

### ***Gas–liquid mixing***

In the gas–liquid simulations, the liquid surface was treated as a pressure outlet BC. An air sparger, mounted in the bottom of the reactor, was set as a velocity inlet. Based on the results of the turbulence models comparison, the  $k$ - $\varepsilon$  Realizable model was used in the following gas–liquid mixing simulations. The turbulence characteristics were used as standard values, provided by ANSYS FLUENT 16. The bubble size was assumed to be of constant size of 1 mm at 5 s<sup>-1</sup> and superficial gas flow rates of 0.83 and 1.67 mm/s. The convergence criterion was reduced to 10<sup>-4</sup> due to large convergence instabilities during the simulations caused by the turbulence generated by the gas-phase. Moreover, air mass balance was monitored between the gas inlet and outlet in order to ensure that the simulated system reached steady state (within 1% accuracy).

Different drag models were applied and the results were validated with PIV results. Diluted gas–liquid flow was simulated using the following drag force models: Schiller–Naumann’s model, Morsi–Alexander’s model, Tomiyama’s laminar drag force model in combination with Brucato’s turbulence drag force correction factor, and Schiller–Naumann’s model with Lane’s turbulence correction factor. The correction factors were implemented in the CFD model via user-defined functions (UDF). The profile-based assessment of the performance of the drag force model combinations in the gas–liquid agitated flow is presented in Publication I. However, to be specific, a quantitative comparison of the root mean square (RMS) errors between the CFD and PIV profiles is presented below in Table 4.3. The summarized data shows the quantitative comparison of the various laminar drag force models in combination with the Brucato’s correction factor. The accuracy of the combination of the Schiller–Naumann’s drag model and Lane’s correction factor is not included.

**Table 4.3. The RMS error between the simulated radial and axial velocity components (Laminar drag force + Brucato’s modification factor) and the measured radial and axial velocity components for the sampled radial profiles presented in Publication I**

Operational conditions, mixing speed and superficial gas velocity	Phase		RMS, %					
		Profile vertical coordinate, mm	65		155		365	
		Drag force	$\frac{U_{rad}}{U_{tip}}$	$\frac{U_{ax}}{U_{tip}}$	$\frac{U_{rad}}{U_{tip}}$	$\frac{U_{ax}}{U_{tip}}$	$\frac{U_{rad}}{U_{tip}}$	$\frac{U_{ax}}{U_{tip}}$
5 s <sup>-1</sup> 0.83 mm/s	Liquid	Schiller & Naumann (1933)	70	70	66	65	55	379
		Morsi & Alexander (1972)	70	71	66	65	70	419
		Takamasa & Tomiyama (1999)	70	96	63	103	106	637
	Gas	Schiller & Naumann (1933)	80	86	34	102	67	90
		Morsi & Alexander (1972)	97	85	33	104	71	87
		Takamasa & Tomiyama (1999)	122	91	33	97	106	77

$5 \text{ s}^{-1}$ $1.67 \text{ mm/s}$	Liquid	Schiller & Naumann (1933)	68	78	71	82	60	113
		Morsi & Alexander (1972)	68	78	71	79	59	111
		Takamasa & Tomiyama (1999)	67	82	67	83	144	198
	Gas	Schiller & Naumann (1933)	62	85	38	102	90	87
		Morsi & Alexander (1972)	62	85	38	102	89	87
		Takamasa & Tomiyama (1999)	62	88	34	97	110	81

When performing the plots comparison one should be careful because the RMS error formulation does not take into account misalignments of the plots. Therefore, it should not be used separately from the profile-wise plots to judge the accuracy of the tested models. Nevertheless, in the present example, the RMS errors point to the same conclusion as drawn in Publication 1: the combinations of the Schiller-Naumann's and Morsi-Alexander's laminar drag force models with the Brucato's modification factor produce similar results due to the similarity in the mathematical formulation of the laminar drag force models and the high  $Re$  number of the flow. Additionally, the contours of the gas volume fraction, simulated using the drag force combinations, are presented in Figure 4.2.

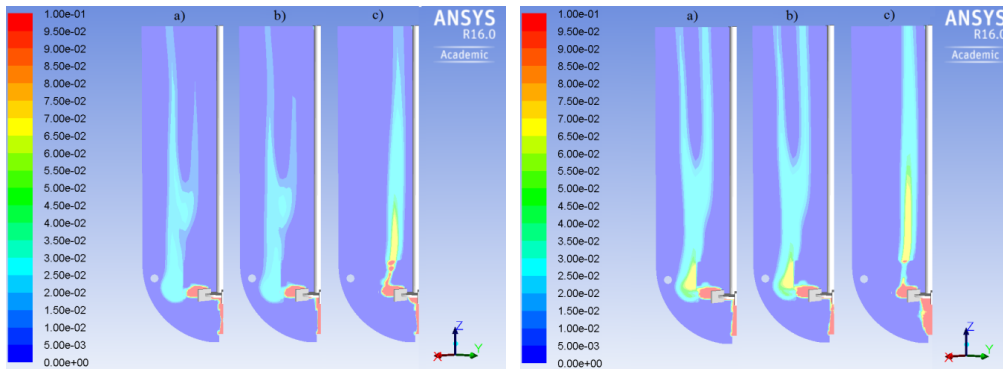


**Figure 4.2. Comparison of gas-volume fractions between the different drag force models at 0.83 mm/s (left) and 1.67 mm/s (right) gas flow rates: (a) Schiller-Naumann's and Brucato's models, (b) Morsi-Alexander's and Brucato's models, and (c) Tomiyama's and Brucato's models**

As can be seen from Figure 4.2, the Tomiyama's model predicts insignificant dispersion of the gas, unlike the other two drag force combinations for both gas flow rates. The smaller gas dispersion resulted in smaller gas hold-up (Table 4.4).

**Table 4.4. Prediction of the gas hold-up (in %) using a combination of different Laminar drag force models and Brucato's modification factor of turbulence with rotation speed  $5 \text{ s}^{-1}$  and different gas flow rates**

Laminar drag force	Superficial velocity of gas, mm/s	
	0.83	1.67
Schiller & Naumann (1933)	0.56	0.75
Morsi & Alexander (1972)	0.53	0.74
Takamasa & Tomiyama (1999)	0.53	0.54

The gas drag force correcting factor for turbulence proposed by Lane et al. (2005) was also tested. The results, presented in Publication I, showed the superiority of the formulation proposed by Lane et al. and the combination of the Schiller-Naumann's model and the Lane's model was used in the further modelling of the drag force.

Depending on the secondary-phase volume fraction, the turbulence of the phase can be calculated differently. At high volume fraction of secondary phase, the turbulence parameters can be found in similar manner as those of primary phase by solving separate transport equations for  $k$  and  $\varepsilon$  using the "per phase" turbulence formulation. However at low volume fraction, the turbulence parameters of the secondary phase can be also evaluated from the mean characteristics of the primary phase and the ratio of the particle relaxation to eddy-particle interaction times (Tchen 1974; Hinze 1975) using the "dispersed" turbulence formulation.

The significance of the dilute gas phase turbulence on the gas-liquid hydrodynamics was assessed by comparing the dispersed and per-phase turbulence models. The results are presented in Figure 4.3 as plots of liquid phase velocity components, sampled at different radial profiles along the vertical axis. The schematic illustration of the radial profiles is shown in Figure 4.5.

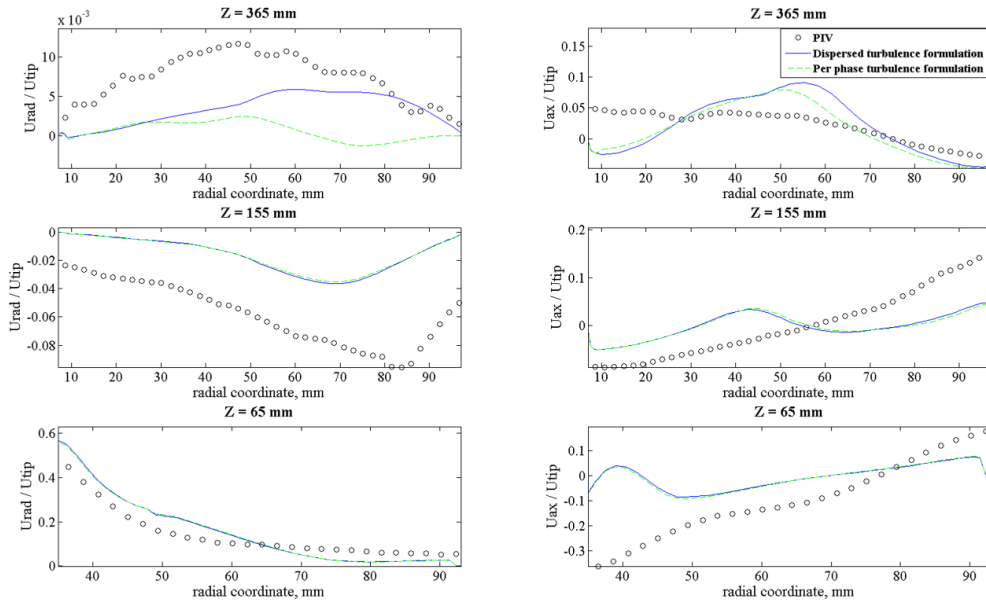


**Figure 4.3. Comparison of radial and axial velocity components of liquid phase, simulated with different gas phase turbulence formulations, against PIV measurements at mixing speed  $5 \text{ s}^{-1}$  and  $0.53 \text{ mm/s}$  gas flow rate. The results are shown as radial profiles sampled at several vertical positions**

The turbulence formulations for the dispersed phase produced very close results, especially in the region of the impeller and in the middle of the tank. It means that the turbulence energy of the gas bubbles is negligible compared to that of the swirling liquid. A bigger deviation can be found in the region next to the liquid surface, which is far from the impeller, where the RANS turbulence models, based on empirical parameters, become less accurate.

The RMS errors calculated for each profile sampled are summarized in Table 4.5, comparing the performance of different formulations of dispersed secondary-phase turbulence.

**Table 4.5. The RMS error (in %) between the profiles of velocity components, measured by PIV and calculated by CFD using dispersed and per-phase turbulence formulations at  $5 \text{ s}^{-1}$  and  $0.83 \text{ mm/s}$**

Phase	Profile vertical coordinate, mm	65		155		365	
	Secondary-phase turbulence formulation	$\frac{U_{rad}}{U_{tip}}$	$\frac{U_{ax}}{U_{tip}}$	$\frac{U_{rad}}{U_{tip}}$	$\frac{U_{ax}}{U_{tip}}$	$\frac{U_{rad}}{U_{tip}}$	$\frac{U_{ax}}{U_{tip}}$
<i>Liquid</i>	Dispersed	68	78	71	82	60	113
	Per phase	86	77	72	87	69	95
<i>Gas</i>	Dispersed	62	85	38	102	90	87
	Per phase	82	87	38	99	92	97

Moreover, gas hold-ups, simulated at two different gas flow rates with different formulation of gas phase turbulence, are presented in Table 4.6.

**Table 4.6. Gas hold-up values (in %) simulated using dispersed and per-phase turbulence formulations at  $5 \text{ s}^{-1}$  and at different gas flow rates**

Secondary-phase turbulence formulation	The superficial velocity of gas, mm/s	
	0.83	1.67
Dispersed	0.56	0.75
Per phase	0.52	0.78

As concluded by Gimbun et al. (2009), Joshi et al. (2011b), Karimi and Akdogan (2012), and Sajjadi et al. (2012), the effect of non-drag forces is negligible in gas–liquid swirling flows in an STR when compared to drag force. Nevertheless, the conclusion was tested in this study. The drag force models (Schiller & Naumann 1933; Lane et al. 2005)—both used alone and in conjunction with the Saffman-Mei’s lift force, Tomiyama’s wall lubrication force, and Burns’ turbulence dispersion force models—were used to simulate the gas–liquid mixing, and the cumulative effect of the non-drag forces was assessed. As a result, the addition of non-drag forces improved the gas-liquid hydrodynamics results insignificantly. However, inclusion of additional forces increased the computational load and made convergence more difficult. Therefore, the non-drag forces do not play a significant role in the gas–liquid mixing flow in an STR and can be safely omitted.

The simulations using the Schiller-Naumann’s drag force model with Lane’s turbulence modification were performed at two gas flow rates:  $0.27 \text{ mm/s}$  and  $0.53 \text{ mm/s}$ .



A qualitative analysis of per-phase velocity contours against PIV data is presented in Figure 4.4.

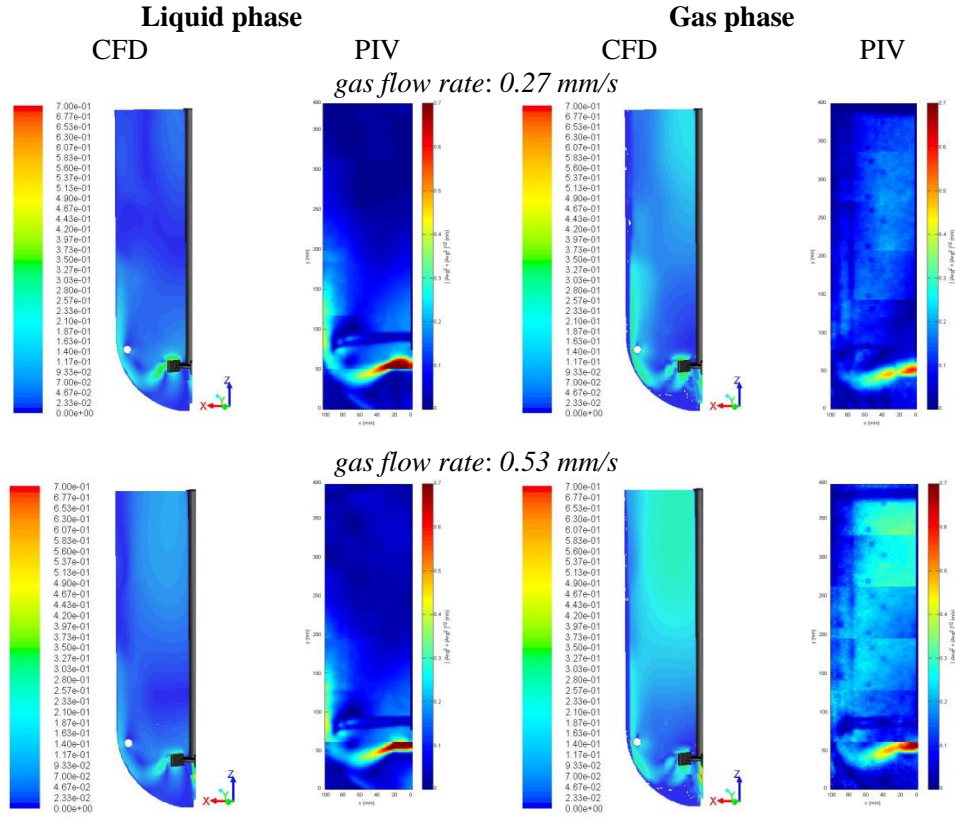


**Figure 4.4. The time-averaged velocity contours of the liquid and gas phases in a round-bottomed STR, agitated at  $5 \text{ s}^{-1}$  and aerated at  $0.27$  and  $0.53 \text{ mm/s}$ , measured by PIV and calculated by CFD**

The general similarity of the overall velocity contours can be seen in the comparison of the simulated and experimental results for the two gas-flow rates. It is important to mention that the reactor has an aspect ratio of 2, which complicates modelling of the top part of the tank.

#### 4.1.3. The outcomes

In the first application (see Publication I), the main model settings were found for simulation of single and dilute gas–liquid flows agitated in an STR with reasonable accuracy. The outcomes of the work can be outlined with the following statements:

1. The RSM turbulence model is the most accurate model among the RANS models for simulating water mixing in an STR.

2. The  $k$ - $\varepsilon$  Realizable model is the most accurate turbulence model among the two-equation models validated by PIV and mixing power experimental data.
3. Dilute gas–liquid flows, with the assumption of constant-sized spherical bubbles, are best modelled by Schiller-Naumann’s laminar drag force model in combination with the turbulence drag force correction factor proposed by Lane et al. (2005).
4. The addition of non-drag forces does not improve the results accuracy regarding the simulated gas–liquid flow, but the increase in both computational time and convergence problems is considerable.
5. The simulated gas-flow rate is rather small for calculating the turbulence characteristics of the gas-phase flow individually, using per-phase turbulence formulation.

#### 4.2. The effect of stirrer turn angle on resolved hydrodynamics in a baffled STR using MRF

##### 4.2.1. The research tasks

Based on the findings achieved in our previous study, the MRF approach was used to simulate the flow induced by mechanical rotation of the stirrer, with the resolved geometry analyzed in liquid and gas–liquid systems. Joshi et al. (2011a) presented a literature review comparing the different mixing techniques used in CFD and concluded that the SM technique is both the most accurate and time-consuming approach. The MRF technique, in turn, is much faster, but less accurate compared to the SM technique. The error originates from the static position of the impeller relative to the baffles. The conclusion fostered a logical question about the sensitivity of multiphase hydrodynamics regarding baffle–impeller interaction. Thus, single and multiphase mixing flows were simulated using the “frozen rotor” method at different angles of rotation. The effect of the impeller position, as well as the effect of partial and full averaging over the positions, was evaluated and compared to PIV data.

**Table 4.7. The summarized conditions of the mixing simulations**

Phase	Agitation rate, s <sup>-1</sup>	Superficial gas velocity, mm/s	Phenomena	Models
Water	5	-	Turbulence	$k$ - $\varepsilon$ Realizable model (Shih et al. 1995)
			Near-wall flow	Standard wall function model
Air–water	5	0.83	Primary phase turbulence	$k$ - $\varepsilon$ Realizable model (Shih et al. 1995)

$(d_b = 1\text{ mm})$		1.67	Near-wall flow	Standard wall function model
			Secondary phase turbulence	Dispersed turbulence model
			Drag force in laminar flow	Model of Schiller & Naumann (1933)
			Drag force in turbulent flow	Model of Lane et al. (2005)

#### 4.2.2. The methods and research progress

Using the optimal models and boundary conditions that were concluded in the previous study (see Publication I), single and multiphase mixing flows in an STR were simulated with  $0^\circ$ ,  $15^\circ$ ,  $30^\circ$ , and  $45^\circ$  angles of Rushton turbine rotation. In addition, more radial profiles were sampled from the round-bottomed tall reactor (Figure 4.5) for more accurate analysis.

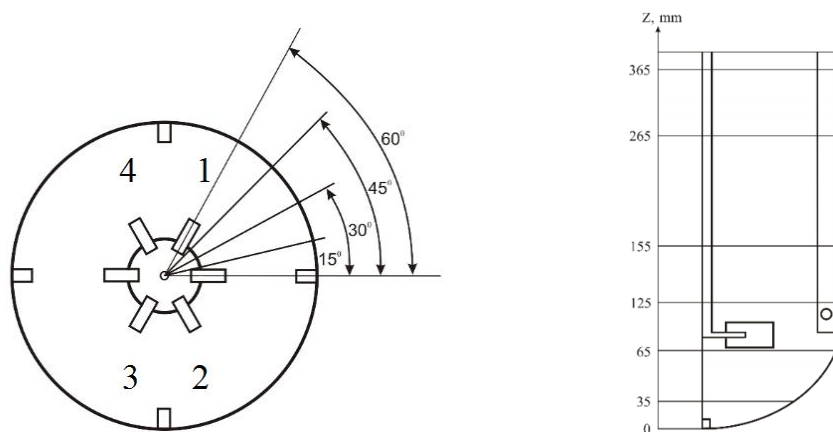


**Figure 4.5. Schematic illustrations of impeller positioning in the “frozen-frame” MRF method (left) and with the sampled radial profiles (right)**

The single-phase results, presented in Publication II, revealed significant variation of the radial and axial velocity components in the profile at 65 mm, representing the area near the impeller with high mixing intensity. The rest of the sampled profiles demonstrated minor velocity deviations at the level of statistical uncertainty. Therefore, the impeller–baffle relative positioning affects mainly the impeller-swept area. In turn, the relative position of the baffles and impeller blades caused larger deviation in the case of gas–liquid mixing for all the sampled profiles. However, the deviation is less than the one caused by the different gas–liquid drag force models studied previously.

To improve the results of single-phase simulations, averaging of the simulation results obtained at 0° and 30° angles of the impeller rotation was performed as well as over all of the four impeller locations. When compared to the measured PIV data, the averaging procedure improved the results. Averaging over all four angle positions benefited the accuracy of the simulated data the most.

#### 4.2.3. The outcomes

In this study (see Publication II), the MRF approach to simulating mixing was assessed in regard to its sensitivity towards the impeller angle of rotation with respect to the baffles. The outcomes can be summarized as follows:

1. The relative baffles–impeller position mainly has an effect on the simulated velocity field in the swept region of the impeller in the case of single-phase mixing.
2. The averaging procedure of the CFD results achieved at several impeller angles of rotation improves the accuracy.
3. Gas–liquid flow is more sensitive to baffle–impeller interaction, but the effect is not critical.

### 4.3. Leaching hydrodynamics in a batch STR

#### 4.3.1. The research tasks

A non-coalescence gas–liquid–solid mixed flow is chosen to describe the complicated hydrodynamics and oxygen mass transfer in a lab-scale stirred tank. Thiosulphate leaching of gold from the concentrate, milled after the flotation stage, uses oxygen to recover copper (II) to copper (I). Hence, gas–liquid mass transfer is critical for the process. Moreover, tiny solids suspended in the primary liquid flow affect rheological characteristics. Being opaque, acquirement of experimental data from the flow is complicated. Therefore, EIT was used to study local gas hold-up in a flat-bottomed STR. The slurry is modelled with a water solution of carboxymethyl cellulose, which shares similar rheology but is optically transparent and suitable for PIV measurement. Global parameters—such as mixing power, gas hold-up, and oxygen mass transfer—are measured and simulated.

**Table 4.8. The summarized conditions of mixing simulations**

Phase	Agitation rate, s <sup>-1</sup>	Gas superficial velocity, mm/s	Phenomena	Models
CMC 50 000 (0.15 w%)–water	6.67	-	Primary phase shear thinning rheology	Power-law model
			Turbulence	<i>k</i> - $\epsilon$ Realizable model (Shih et al. 1995)

			Near-wall flow	Standard wall function model
Aerated slurry ( $d_b = 1.5$ mm)	6.67	0.41	Primary phase shear thinning rheology	Power-law model
			Primary phase turbulence	$k$ - $\varepsilon$ Realizable model (Shih et al. 1995)
			Near-wall flow	Standard wall function model
			Secondary phase turbulence	Dispersed turbulence model
			Drag force in laminar flow	Model of Schiller & Naumann (1933)
			Drag force in turbulent flow	Model of Lane et al. (2005)

#### 4.3.2. The methods and research progress

A water solution of gold concentrate (of 20 w%), studied by Lampinen et al. (2015), was tested in Anton Paar rheometer using cone and blade probes. Both probes measured a shear-thinning rheology for the slurry. A water solution of carboxymethyl cellulose (CMC 30 and CMC 50 000) and Xanthan gum were found to have similar shear-thinning rheology. The Xanthan gum solution had a lower flow index. However, its transparency was insufficient to conduct PIV measurements of mixing hydrodynamics. Therefore, CMC 50 000 was used since it has a longer molecular chain, and hence higher viscosity. The measured rheological parameters, described via power-law model, was used in the CFD simulations.

Global gas hold-up was measured in the CMC solutions over the range of gas superficial velocities (0–3.3 mm/s) at a constant  $6.67 \text{ s}^{-1}$  mixing rate. Measurement of gas hold-up in an STR by level difference method has good accuracy at high gas hold-up levels. The gas hold-up has an almost linear dependence on superficial gas velocity for glass beds suspended in water, as described by Rewatkar et al. (1993) numerically and later confirmed experimentally by Kraume and Zehner (2001), and by Laakkonen (2006) for Xanthan gum solutions. A similar observation was made and presented in Publication III.

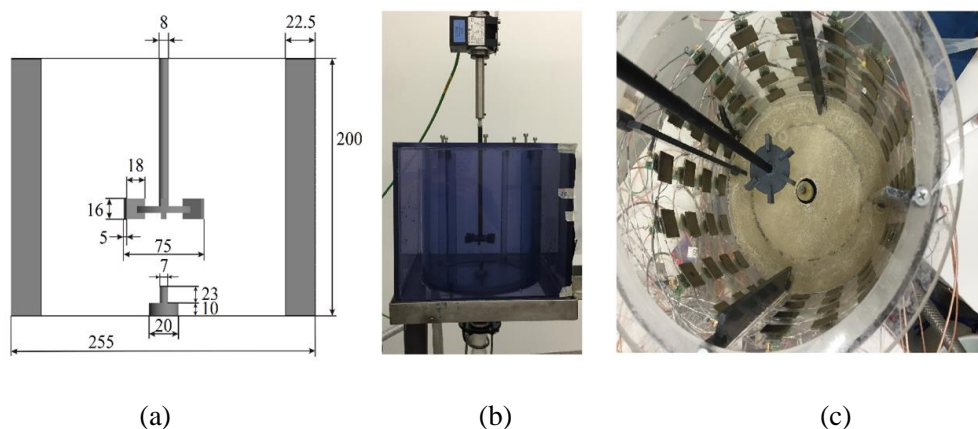


**Figure 4.6. Reactor illustrations: (a) the scheme and sizing (in mm), (b) a photo of the tank encased inside a Plexiglas rectangular container for PIV experiments, and (c) a photo of the vessel equipped with electrodes for EIT experiments**

Oxygen mass transfer from gas to liquid was measured by the dynamic gas-in method both in the CMC 50 000 (0.15 %) and CMC 30 (1.8 %) water solutions with and without salt addition over a range of mixing rates ( $3.33\text{--}10\text{ s}^{-1}$ ) and aeration rates ( $0.02\text{--}0.06\text{ mm/s}$ ). During the tests, an oxygen probe was located in a region of vigor mixing between the baffles where high mixing intensity causes the bulk solution around the probe to be constantly renewed by the flow. Otherwise, the probe might consume all the oxygen around it and cause inaccurate measurements. With increasing aeration rate, mass transfer also increased in CMC 50 000, while it sometimes dropped in CMC 30, especially at  $3.33$  and  $6.67\text{ s}^{-1}$ . This can be explained by reduced turbulence and bubble coalescence in the absence of salt in the solutions. The addition of sodium thiosulphate (1 M) significantly increased the mass transfer rate due to the breakage of the CMC molecular chains, causing a viscosity drop and bubble surface contamination with ions. Thus, both components of the volumetric mass transfer coefficient, namely  $k_L$  and the contact area, were significantly increased.

The hydrodynamics of single-phase mixing of the CMC 50 000 (0.15 %) solution was measured by PIV. The measured results of the time-averaged velocities and velocity components, as well as the calculated shear rate, were used to validate the CFD simulations. The hydrodynamics of the agitated turbulent viscous solution was simulated accurately, meaning that the  $k\text{--}\varepsilon$  Realizable model and the power-law model, supplied with empirical parameters, can reliably predict the flow field in the STR.

EIT was used to provide local gas hold-up measurement data of the mixed CMC 50 000 solution in the STR. For this purpose, gas–liquid mass transfer and mixing power were measured to determine the minimum amount of thiosulphate salt addition due the sensitivity of the EIT technique. The concentration of sodium thiosulphate in the STR (at  $10\text{ s}^{-1}$  and  $0.65\text{ mm/s}$ ) was increased from 0 to 0.4 M with 0.05 M steps. After the very

first portion of the salt, the mixing power increased and this was not changed with further addition of the salt. The mixing power dynamics is explained by the effect of large bubbles surrounding the impeller that decreased the average solution density in the impeller sweep region. Further addition of salt affected bubble-size distribution, but the impact was not strong enough to influence the measured torque. The previous statement is supported by the measured dynamics of the gas–liquid  $k_L a$ , which kept rising as the salt concentration was increased until leveling off at 0.2 M. Thus, the optimal amount of salt (0.1 M), at which the  $k_L a$  reached 91 % of the maximum  $k_L a$  value, was found from the EIT tests. However, the high conductivity (7.9 mSm) at the optimal salt concentration made the EIT set-up blind to local gas hold-up since the current injections bypassed the bubbles resulting in an insignificant change of conductivity distributions at the reference (non-aerated) mixing system and measured (aerated) mixing system.

BSD in an aerated slurry is a result of opposing phenomena. Increased viscosity reduces mixing intensity, while solids increase bubble breakage rate and ions cover the bubble surfaces making them non-coalescing. Bubbles were captured by CCD cameras on the plane of the PIV laser in the mixed CMC 50 000 solution in the presence of salt, aerated at 0.41 mm/s. The mean bubble size was found to be around 1.5 mm, which was then used as the assumed constant bubble size in the CFD simulations of the aerated slurry.

Based on the empirical parameters of the slurry rheology and the mean bubble size, CFD simulations of the thiosulphate slurry, aerated at 0.41 mm/s and mixed at  $6.67 \text{ s}^{-1}$ , were performed, and the local  $k_L$ , contact area and gas–liquid mass transfer were calculated.

#### 4.3.3. The outcomes

In Publication III, the gas–liquid mass transfer was modelled in the aerated slurry in an STR equipped with a Rushton turbine. The outcomes of the research are as follow:

1. A set of empirical parameters of a power-law model can be used to accurately simulate turbulent non-Newtonian fluid mixing in an STR.
2. The addition of salt to an aerated water-based CMC solution in an STR generates a narrow BSD.
3. The high conductivity of the solution prevents the effective measurement of local gas hold-up by EIT in an aerated STR.
4. The calculation of gas–liquid  $k_L a$ , based on the hydrodynamics simulated for the mixed slurry in an aerated STR at steady state, produces realistic results.

#### 4.4. The effect of mixing intensity and feeding locations on semi-batch precipitation in STR

##### 4.4.1. The research tasks

Crystallization has a huge amount of mixed reacting flow applications in STRs in food, pharmaceutical and chemical industries. Precipitation of barium sulphate in a semi-batch STR, widely studied by other researchers (Koralewska et al. 2008; Torbacke 2001; Torbacke & Rasmuson 2004; Uehara-Nagamine & Armenante 2001; Wang et al. 2007), was chosen as a representative crystallization process to study the effect of feeding point location on crystal size. Barium sulphate precipitation in a semi-batch agitated reactor is studied experimentally and the effect of mixing at different scales is analyzed using CFD as a tool. The dynamics of the crystallization process is visualized using EIT and global conductivity monitoring. Crystal size distribution and morphology are measured and analyzed. Based on the results of the current work, the empirical correlation of the TR-number, introduced by Torbacke (2001), is estimated outside the range studied by the authors.

**Table 4.9. Summarized conditions of the mixing simulations**

Phase	Agitation rate, s <sup>-1</sup>	Phenomena	Models
Water	6.67	Turbulence	<i>k-ε</i> Realizable model (Shih et al. 1995)
		Near-wall flow	Standard wall function model

##### 4.4.2. The methods and research progress

The effect of mixing scales on crystals formation was studied by feeding a reagent at different mixing intensities at several spatial locations over a range of stirring speeds. The reactor used in the previous subchapter 4.3 was equipped with stainless steel electrodes of an EIT system in order to visualize the crystallization process dynamics in the reactor domain by measuring local spatial conductivity gradients. Four rows of 16 electrodes in each row produced results of approximately 2 cm<sup>3</sup> of spatial resolution, averaged over two seconds. A peristaltic pump fed the solution of barium chloride into the solution of sodium sulphate at a constant flow rate of 2.55 m/s. The solutions volumes and the reagents concentrations were used in the amounts according to the reaction stoichiometry. Using a glass tube, the barium sulphate solution was injected at different spatial locations, the coordinates of which are specified in Figure 4.7 in mm.

In addition to the EIT electrodes, a conductivity probe was placed into the reactor in order to follow the global conductivity during the crystallization. The measured results were analyzed and used to validate the EIT results.

After each batch test, the crystals size distribution (CSD) was measured by laser diffractometer (LD) while the morphology was analyzed by scanning electronic microscopy (SEM). For convenience, CSD was characterized by  $d_{90}$ .



CFD simulations of the single-phase mixing in the STR were used to calculate local fluid bulk velocity and the turbulent diffusion in the places of injections. That allowed verification of the TR value proposed by Torbacke (2001) versus  $d_{90}$  in the range of  $10^3$ – $10^6$ .

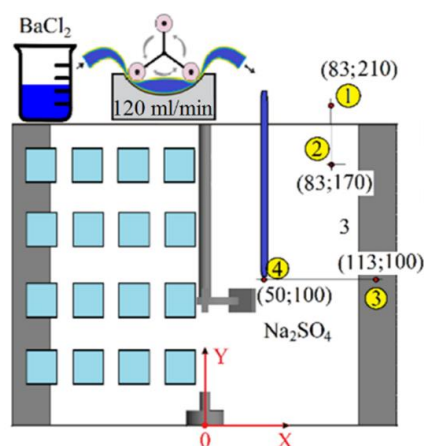


**Figure 4.7. A schematic representation of the batch crystallization set-up with the spatial coordinates, specified in mm, of BaCl<sub>2</sub> (0.1 M) injection points into the water solution of Na<sub>2</sub>SO<sub>4</sub> (0.1 M)**

The effect of local turbulent diffusion in the injection region has a dominating effect over  $d_{90}$ . However, at some points of low local mixing intensity, the  $d_{90}$  values were noticed to be high, which is a result of macromixing timescale. If the supersaturated solution is not dispersed within a critical time, the growth of the resulting crystals is not effective. Therefore, a third coordinate of macromixing timescale was added to a 3D diagram of the local turbulent diffusion and  $d_{90}$  in order to characterize the crystal size dependence on local and global mixing scales.

#### 4.4.3. The outcomes

A combination of experimental and numerical tools was used to investigate the effect of different feeding point locations in a semi-batch STR in this research (see Publication IV), which resulted in the following outcomes:

1. EIT is a powerful tool, capable of visualizing the temporal history of the dynamic precipitation process in a semi-batch STR.
2. A CFD model of single phase STR can provide crucial information on local hydrodynamics.
3. The TR number has been validated both in and outside of the range studied by Torbacke (2001).
4. The effect of the meso- and macromixing on CSD was found and a 3D graphical correlation was presented.

## 4.5. The fermentation process in an industrial draft tube STR

### 4.5.1. The research tasks

The fermentation process of biomass growth in gas–liquid reacting flow, agitated in a draft tube reactor at industrial scale (800 m<sup>3</sup>), is modelled by CFD. Ethanol is produced during the anabolism of *Pichia pastoris* cells. Hence, the gas–liquid system becomes non-coalescing. The results of the simulated liquid mixing are validated by the measured power number at industrial scale. The biomass growth is simulated over the range of superficial gas velocities. A dense population of air bubbles reduces the drag force in turbulent flow (Lau et al. 2011; Roghair et al. 2011). Therefore, the drag force model employed in previous studies is modified to comprise the bubble swarm effect, according to Roghair et al. (2011). The approaches to compensate underpredicted energy dissipation rate in CFD simulations of mixing in an STR due to insufficient spatial discretization of the reactor domain are analyzed for their impact on oxygen  $k_L a$ . Using steady-state multiphase hydrodynamics, the batch fermentation is simulated at different aeration rates, the results of which are compared to lab-scale results. The impact of oxygenation on *P. pastoris* metabolic pathways is considered.

**Table 4.10. Summarized conditions of mixing simulations**

Phase	Agitation rate, s <sup>-1</sup>	Gas superficial velocity, mm/s	Phenomena	Models
Water	1	-	Turbulence	$k$ - $\varepsilon$ Realizable model (Shih et al. 1995)
	3.33 6.67		Near-wall flow	Standard wall function model
Air–water ( $d_b = 2\text{ mm}$ )	1	13.6 27.2 40.8	Primary phase turbulence	$k$ - $\varepsilon$ Realizable model (Shih et al. 1995)
			Near-wall flow	Standard wall function model
			Secondary phase turbulence	Dispersed turbulence model
			Drag force in laminar flow	Model of Schiller & Naumann (1933)
			Drag force increment in turbulent flow	Model of Lane et al. (2005)

			Drag force increment in swarm of bubbles	Model of Roghair et al. (2011)
--	--	--	--	--------------------------------

#### 4.5.2. The methods and research progress

The scale-up process started from the construction of a lab-scale ( $14 \text{ dm}^3$ ) physical model of the OKTOP®9000 reactor (Figure 3.3), which was identical to the reactor used by Tervasmäki et al. (2016, 2018) to investigate mixing hydrodynamics experimentally. A transparent reactor was encased in a Plexiglas box, where the space between the box and the reactor was filled with water in order to match the refractive indexes of the media and thus to prevent optical distortion due to the curvature of the reactor walls. SPIV was applied to measure three velocity components on a two-dimensional plane. Radial and axial components were determined based on orthogonal projections of the tracers shift, while the tangential component was calculated from the difference of the projections captured by each camera (Figure 3.4, on the right). A special 3D calibration plate was used to calibrate the SPIV system. Liquid mixing at  $3.33$  and  $6.67 \text{ s}^{-1}$  was measured by SPIV to gain the experimental data for validation of the hydrodynamics in the reactor at lab scale.

A CFD model of the reactor was built to test the modelling approach used earlier to simulate mixing flow in an STR. The reactor had no geometrical symmetry that would allow symmetrical simplifications of the modelled reactor, which resulted in a high number of elements and thus significant computational time. The simulation results are compared with experimental SPIV data qualitatively in Figures 4.8 and 4.9 and quantitatively with the torque measurements in Table 4.11.

The established approach showed reasonable accuracy when comparing CFD and experimental results. This gives a starting point for the scale-up procedure. The reactor geometry was scaled-up from  $14 \text{ dm}^3$  to  $800 \text{ m}^3$ . The grid size was not changed, which made the real volume of each element equal to approximately  $0.9 \text{ dm}^3$ . However, the  $y^+$  value of the elements adjacent to the reactor walls remained within the limits suitable for applying a standard wall function. The power number of water mixing in the OKTOP®9000 reactor at the scale of  $800 \text{ m}^3$  was provided by Outotec Oy company, which was used to validate the CFD simulation of water mixing. The references for the mixing speed  $1 \text{ s}^{-1}$  were defined based on the volumetric power  $500 \text{ W/m}^3$  that was used in single-phase mixing by Tervasmäki et al. (2018).

The aeration rate was defined so as to cover a range from the superficial velocity used by Tervasmäki et al. (2018) to the flow rate next to flooding point. Therefore, the flooding point was determined first using the empirical correlation proposed by Hudcova et al. (1987) for an STR, and CFD simulations with different gas-flow rates (0.05–0.31 vvm). The flooding was determined to occur around 0.18 vvm at a  $1 \text{ s}^{-1}$  agitation rate. Therefore, the aeration rates were chosen as 0.042, 0.083, and 0.125 vvm. Since the simulated systems are not dilute, the effect of bubble swarms on turbulence, noticed experimentally

by Lau et al. (2011), had to be taken into account. There are two ways to include the phenomenon in a CFD model of gas–liquid flow, namely by modifying the energy dissipation value by an empirical parameter (Li et al. 2017) or using the more mechanistic approach of the correlation of gas–liquid drag force to a local gas volume fraction (Roghair et al. 2011). The latter model was included in the turbulence modification factor via UDF. Since the mesh is large, the mean bubble size was used to calculate gas–liquid mixing hydrodynamics. The mean bubble size of 2 mm was determined from the experimental work of Hu et al. (2005) and Machon et al. (1997), based on volumetric mean mixing power and surface tension. According to Tervasmäki et al. (2018), the stable fermentation process produces 1 % of ethanol in the solution, the surface tension of which was measured as 0.69 N/m. BSD is known to influence the interfacial contact area, therefore bubble  $d_{32}$  was calculated over converged CFD simulation results at a steady state via the empirical equation proposed by Calderbank and Moo-Young (1960) and QMOM. Due to the long computational time required for the QMOM to produce results, the BSD was only calculated at a 0.083 vvm aeration rate.

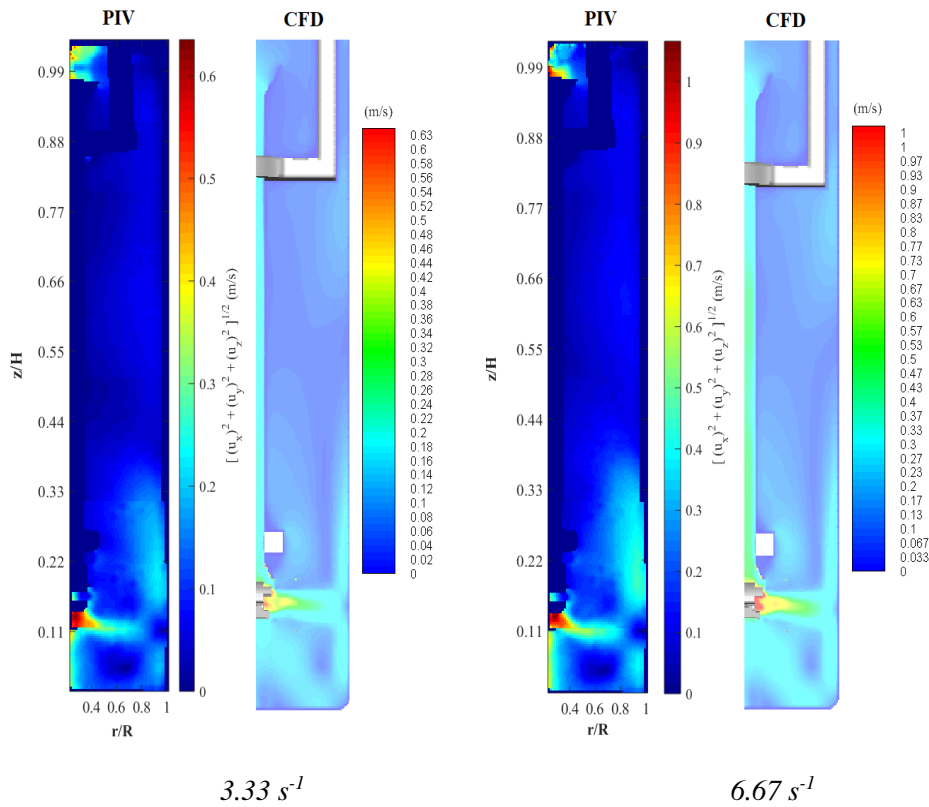


**Figure 4.8.** A qualitative comparison of velocity contours from simulations and SPIV measurements in an OKTOP®9000 reactor of lab scale at different mixing speeds

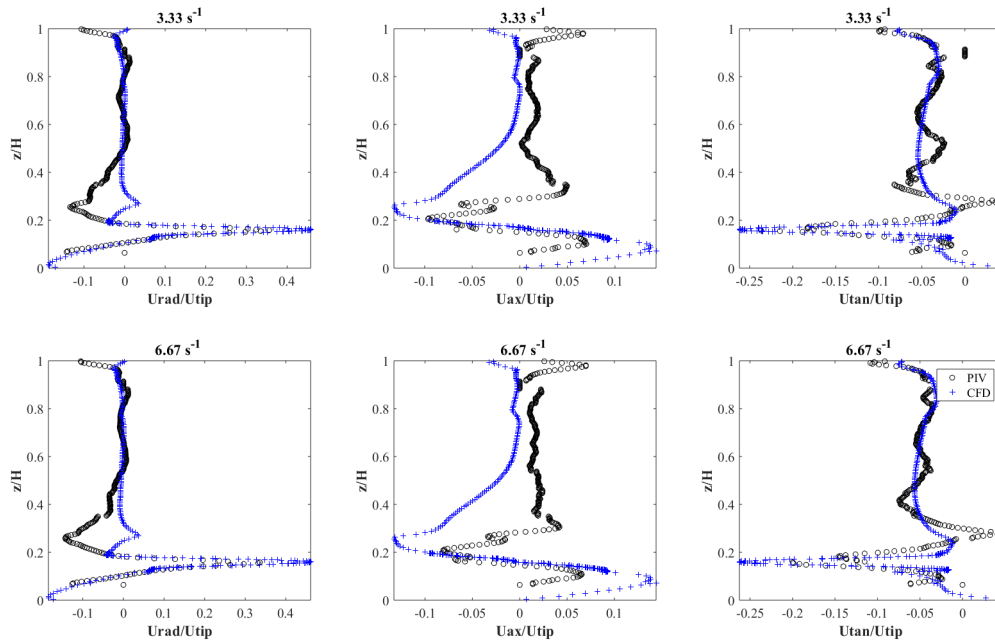


**Figure 4.9. CFD vs PIV: a comparison of the velocity components in vertical profile, sampled at  $r/R = 0.5$  for mixed water in a lab-scale OKTOP®9000 reactor at different mixing speeds**

The established approach showed reasonable accuracy when comparing CFD and experimental results. This gives a starting point for the scale-up procedure. The reactor geometry was scaled-up from 14 dm<sup>3</sup> to 800 m<sup>3</sup>. The grid size was not changed, which made the real volume of each element equal to approximately 0.9 dm<sup>3</sup>. However, the  $y^+$  value of the elements adjacent to the reactor walls remained within the limits suitable for applying a standard wall function. The power number of water mixing in the OKTOP®9000 reactor at the scale of 800 m<sup>3</sup> was provided by Outotec Oy company, which was used to validate the CFD simulation of water mixing. The references for the mixing speed 1 s<sup>-1</sup> were defined based on the volumetric power 500 W/m<sup>3</sup> that was used in single-phase mixing by Tervasmäki et al. (2018).

**Table 4.11. Torque, simulated and measured experimentally**

Mixing speed, s <sup>-1</sup>	Torque, mN·m		
	CFD	Experimental	Difference, %
3.33	10	9	10
6.67	35	35	2

The aeration rate was defined so as to cover a range from the superficial velocity used by Tervasmäki et al. (2018) to the flow rate next to flooding point. Therefore, the flooding point was determined first using the empirical correlation proposed by Hudcova et al. (1987) for an STR, and CFD simulations with different gas-flow rates (0.05–0.31 vvm). The flooding was determined to occur around 0.18 vvm at  $1 \text{ s}^{-1}$  agitation rate. Therefore, the aeration rates were chosen as 0.042, 0.083, and 0.125 vvm. Since the simulated systems are not dilute, the effect of bubble swarms on turbulence, noticed experimentally by Lau et al. (2011), had to be taken into account. There are two ways to include the phenomenon in a CFD model of gas–liquid flow, namely by modifying the energy dissipation value by an empirical parameter (Li et al. 2017) or using the more mechanistic approach of the correlation of gas–liquid drag force to a local gas volume fraction (Roghair et al. 2011). The latter model was included in the turbulence modification factor via UDF. Since the mesh is large, the mean bubble size was used to calculate gas–liquid mixing hydrodynamics. The mean bubble size of 2 mm was determined from the experimental work of Hu et al. (2005) and Machon et al. (1997), based on volumetric mean mixing power and surface tension. According to Tervasmäki et al. (2018), the stable fermentation process produces 1 % of ethanol in the solution, the surface tension of which was measured as 0.69 N/m. BSD is known to influence the interfacial contact area, therefore bubble  $d_{32}$  was calculated over converged CFD simulation results at a steady state via the empirical equation proposed by Calderbank and Moo-Young (1960) and QMOM. Due to the long computational time required for the QMOM to produce results, the BSD was only calculated at a 0.083 vvm aeration rate.

The difference in the calculated mean  $d_{32}$  and its effect on gas–liquid mass transfer decreased as the gas-flow rate increased. As was mentioned in Section 2.3.6, gas–liquid mass transfer depends on the turbulence energy dissipation rate, which is usually underpredicted by RANS models. Therefore, the effect of  $\varepsilon$  compensation approaches was analyzed. Using the assumption of 2 mm mean bubble size at 0.042 vvm and  $1 \text{ s}^{-1}$  mixing speed, 20 % underprediction in  $\varepsilon$ , which was compensated linearly, increased the  $k_L a$  by less than 5 %, while the  $\varepsilon$  compensation, proportional to the resolved  $\varepsilon$ , increased the mass transfer by 2 %. In fact, the latter method of proportional compensation is more accurate. However,  $\varepsilon$  measured experimentally (Delafose et al. 2011) obeys a power-law model that makes the effect of  $\varepsilon$ , compensated by an improved power-law approach, even less significant for  $k_L a$  than the proportional approach used in this work. Nevertheless, the effect of  $\varepsilon$  compensation is case dependent.

The kinetics of the metabolism of *P. pastoris* was coupled with the resolved hydrodynamics of the multiphase mixing via gas–liquid mass transfer, where the effect of hydrostatic pressure on oxygen saturation concentration was included in UDF. Since the  $Da$  number is small for the system in order to cause a significant gradient in the species concentration, the reaction kinetics were solved with the assumption of a perfectly mixed reactor at different aeration rates. The results of the yeast metabolism modelling were in agreement with the results of Tervasmäki et al. (2018) at lab scale and showed that with an insufficient supply rate of oxygen, the cells switch to glucose fermentation, producing ethanol, which is further used as food. This scenario produces lower cell yield

due to carbon loss in CO<sub>2</sub>, which is a by-product in each metabolic reaction. In turn, the increase in aeration rate can raise the cell yield and reduce CO<sub>2</sub> emission.

#### 4.5.3. The outcomes

In this work, described in more details in Publication V, the scale-up of a multiphase OKTOP®9000 reactor was carried out with the help of CFD modelling. Based on the outcomes achieved in our previous studies, the CFD model was updated to incorporate new phenomena and was coupled with the fermentation reactions. The following outcomes can be listed as follow:

1. The  $k$ - $\varepsilon$  Realizable model and standard wall function model can describe single-phase mixing hydrodynamics accurately in a draft tube reactor, agitated by an impeller of special design at the lab and industrial scales.
2. The scale-up of the OKTOP®9000 reactor has been implemented and validated using the same number of elements and set of models used in the lab-scale CFD model without violation of their range of applicability.
3. The effect of bubble swarms on gas–liquid drag force was taken into account in the multiphase mixing simulations at large scale.
4. The effect of  $\varepsilon$  compensation was less significant than the effect of BSD on gas–liquid mass transfer.
5. Given the assumption of perfect mixing, the metabolic reactions were coupled to the hydrodynamics of the multiphase mixing via oxygen  $k_L a$ , including the effect of hydrostatic pressure.

#### 4.6. Discussions

The outcomes of the thesis clearly show the applicability of CFD simulations in resolving important design parameters of multiphase mixing in STRs of various geometry and scale. During the study of mixing hydrodynamics in single phase water mixing, described in Publications I and II, the model combination accurately describing the mixed hydrodynamics was found and validated. Despite the warning given by Marshall & Bakker (2001) about the usage of the  $k$ - $\varepsilon$  Realizable model in combination with the MRF model for mixing, the  $k$ - $\varepsilon$  Realizable model, designed for highly swirling motion, produced the most accurate results among the tested two-equation turbulence models when the MRF and SM approaches were used. The results are in agreement with the conclusions of Gimbun et al. (2009), Haringa (2017), Mendoza-Escamilla et al. (2018); Wu (2012). However, with mesh fine enough to resolve near boundary flow, the  $k$ - $\varepsilon$  SST model can produce accurate results as well, as was shown by Lane (2017).

Accurate resolution of multiphase hydrodynamics in aerated STRs requires that the drag force modification is taken into account to include the effects of turbulence and bubble swarms. In dilute gas-liquid mixing the Lane's model combined with the laminar Schiller-Naumann's drag model was superior over the Brucato's modification model. The results obtained in Publication I and by Evans et al. (2008) and Karimi et al. (2012) prove the

critical assessment given by Lane et al. (2005). The drawback of the “frozen rotor” in the MRF approach can be improved by averaging the simulation results obtained at several angular positions of the impeller.

Slurry mixing can be simulated with known rheological parameters, which was shown in Publication III for the example of CMC-water solution mixing. Such approach, used by Wu (2012a), Craig et al. (2013), reduces the amount of transport equations to be solved at reasonable accuracy of the results. However, the impact of the solids on bubbles must be taken into account.

Simulated multiphase hydrodynamics can be used to evaluate local volumetric mass transfer. However, turbulence cannot be resolved with good accuracy by RANS models at feasible mesh even at lab scale STR (Delafose et al. 2008; Lane, 2017). Turbulence affects local  $k_L a$  in two ways. At microscale, mixing intensity increases the rate of species transport between phases, while at mesoscale turbulent eddies interact with dispersed phase affecting gas hold-up and local contact area. Underpredicted local energy dissipation rate can be compensated based on overall mixing power that can be measured or simulated from wall stress integral over the impeller area with good precision (Joshi et al. 2011a). In the simulated draft tube reactor (see Publication V), the most realistic way to compensate underpredicted  $\varepsilon$  via non-linear distribution (Ben-Nun et al. 2015) affected  $k_L a$  almost ten times less than the resolution of the contact area via PBM. However, the local  $\varepsilon$  has impact on breakage and coalescence that was not considered in this thesis and it remains for future research. Moreover, coarse meshes make the  $\varepsilon$  compensation even more important for accurate evaluation of volumetric mass transfer coefficient.

Effective dispersion of saturation concentration in precipitation promotes crystal growth (Mullin 2001). Therefore, mixing affects the precipitation process at all scales. Simulation of mixing flow can be useful in precipitation analysis as shown in Publication IV. Acting at microscale, turbulence dispersion is the most influencing factor because it disperses the supersaturated concentration fastest (Kilander & Rasmuson 2005; Torbacke 2001). However, mixing intensity distribution is not uniform in STR and injected reagent follows the mixing flow pattern from the region of injection, passing regions of high and low turbulence dispersion. Thus, effective dispersion depends on the injection point through macromixing. Continuing this logic, one should also consider mesomixing scale and take the RTD of the saturated concentration into account as well. Then, crystal size can be correlated to turbulence dispersion and macro scales as the design parameters.

Slow reaction kinetics makes it possible to use the assumption of perfectly mixed CSTR, which significantly reduces computational load. However in the presence of significant concentration gradients (Haringa et al. 2017) during reactions, simultaneous simulation of fluid dynamics and reaction kinetics is required, which drastically increases computational time. To reduce the calculation time, block model can be applied based on CFD simulation results (Bashiri et al. 2016; Nauha et al. 2015, 2018).





## 5. Conclusions

Various turbulent multiphase reacting flows, mixed in STRs of different geometries and scales, were modelled numerically and validated experimentally, showing good accuracy. Models of relevant physical phenomena were successfully included when necessary. The series of considered CFD cases proved that CFD can provide more detailed information on fluid flow and is a powerful tool in reactor design, optimization, and scale-up.

During the work, the combination of basic models that are feasible and accurate, describing the turbulent flow hydrodynamics of single and multiphase flow in an STR, was determined based on experimental validation. A two-equation  $k$ - $\varepsilon$  Realizable turbulence model simulates liquid mixing the most accurately within an acceptable computational time. In dilute gas–liquid, vigorously agitated in STRs, a drag force model in laminar flow should include the effect of turbulence in order to produce reasonable results, while non-drag forces can be omitted.

The rheology of a mixed slurry was described by a power-law model. With the empirical parameters available, the turbulent hydrodynamics of shear-thinning fluid was simulated with reasonable accuracy compared to experimental measurements. Given the assumption of constant bubble size, local oxygen mass transfer was simulated in a gas–liquid–solid STR at steady state.

The EIT-visualized dynamic process of sodium sulphate crystallization in a semi-batch STR was in agreement with the history of measured global conductivity. Information on the mixing pattern and local mixing intensity was gained via the CFD model of a single-phase STR in order to correlate the data with crystal size using a TR number. Agreement in the trend of the TR number was found inside and beyond the range studied by (Torbacke, 2001). The scatter of the TR-number values was explained by the effect of macromixing, which correlated with crystal  $d_{90}$  and presented as a 3D correlation.

Using CFD modelling, a fermentation process was simulated in a draft tube reactor at both lab and industrial scales. The effect of a higher gas volume fraction leading to bubble swarm appearance in gas–liquid hydrodynamics was included in the drag force. The effect of the interfacial contact area, calculated by PBM, was found to have a bigger effect on gas–liquid  $k_L a$  compared to the compensated energy dissipation rate. The slow kinetics of the fermentation was coupled with an industrial-scale reactor and the simulation results were in agreement with experimental measurements carried out at lab scale.

A compromise between the computational power and the accuracy of the modelling results leads to simplification in CFD simulations. More complex phenomena are forced to be solved at a coarser mesh, which produces higher uncertainties in crucial parameters, such as the turbulence dissipation rate in an STR. Being involved in many physical models of breakage and coalescence, nucleation, growth rate, mass transfer coefficient etc.,  $\varepsilon$  is underpredicted in an STR with a coarse mesh. The various empirical parameters that are proposed in literature often depend on  $\varepsilon$ , which makes it a cornerstone value for

reacting flows in an STR. Therefore, the compensation methods that can accurately calculate local  $\varepsilon$  are important and worth studying.

As the power capacity of computers is growing, CFD simulations are to become an inevitable part of reactor design and tackling industrial solutions. Therefore, models and simulation techniques are to be further developed in order to increase the accuracy, flexibility, and applicability of CFD when used in solving practical tasks. Since there are limits to simulation capacity, the precise determination of empirical parameters is crucial and the creation of databases of such coefficients, classified for different applications, is important. Therefore, fundamental work on the measurements of empirical values is a vast area of research. In parallel, tackling the technical issues of STR modelling fills the database of solution receipts that helps others to move forward.

## References

- Adrian, R. J. (1991). Particle-Imaging Techniques For Experimental Fluid Mechanics. *Annual Review of Fluid Mechanics*, 23(1), 261–304. <https://doi.org/10.1146/annurev.fluid.23.1.261>
- Alberini, F., Liu, L., Stitt, H. E., & Simmons, M. J. H. (2017). Comparison between 3-D-PTV and 2-D-PIV for determination of hydrodynamics of complex fluids in a stirred vessel. *Chemical Engineering Science*, 171, 189–203. <https://doi.org/10.1016/j.ces.2017.05.034>
- Aubin, J., Le Sauze, N., Bertrand, J., Fletcher, D. F., & Xuereb, C. (2004). PIV Measurements of Flow in an Aerated Tank Stirred by a Down- and Up-Pumping Axial Flow Impeller. *Experimental Thermal and Fluid Science*, 28, 447–456.
- Aw, S. R., Rahim, R. A., Rahiman, M. H. F., Mohamad, E. J., Yunus, F. R. M., Wahab, Y. A., ... Jamaludin, J. (2015). Simulation study on electrical resistance tomography using metal wall for bubble detection. *Jurnal Teknologi*, 73(6), 31–35. <https://doi.org/10.11113/jt.v73.4403>
- Bach, C., Yang, J., Larsson, H., Stocks, S. M., Gernaey, K. V., Albaek, M. O., & Krühne, U. (2017). Evaluation of mixing and mass transfer in a stirred pilot scale bioreactor utilizing CFD. *Chemical Engineering Science*, 171, 19–26. <https://doi.org/10.1016/j.ces.2017.05.001>
- Baldyga, J., & Pohorecki, R. (1995). Turbulent micromixing in chemical reactors - a review. *Chemical Engineering Journal*, 58, 183–195. [https://doi.org/10.1016/0923-0467\(95\)02982-6](https://doi.org/10.1016/0923-0467(95)02982-6)
- Bao, Y., Yang, J., Wang, B., & Gao, Z. (2015). Influence of impeller diameter on local gas dispersion properties in a sparged multi-impeller stirred tank. *Chinese Journal of Chemical Engineering*, 23(4), 615–622. <https://doi.org/10.1016/j.cjche.2014.12.006>
- Basavarajappa, M., & Miskovic, S. (2016). Investigation of gas dispersion characteristics in stirred tank and flotation cell using a corrected CFD-PBM quadrature-based moment method approach. *Minerals Engineering*, 95(July), 161–184. <https://doi.org/10.1016/j.mineng.2016.06.026>
- Ben-Nun, R., Sheintuch, M., Kysela, B., Konfršt, J., & Fořt, I. (2015). Semianalytical characterization of turbulence from radial impellers, with experimental and numerical validation. *AIChE Journal*, 61(4), 1413–1426. <https://doi.org/10.1002/aic.14723>
- Brucato, A., Grisafi, F., & Montante, G. (1998). Particle drag coefficients in turbulent fluids. *Chemical Engineering Science*, 53(18), 3295–3314.

[https://doi.org/10.1016/S0009-2509\(98\)00114-6](https://doi.org/10.1016/S0009-2509(98)00114-6)

- Burns, A. D., Frank, T., Hamill, I., & Shi, J. M. (2004). The Favre averaged drag model for turbulent dispersion in Eulerian multi-phase flows. *5th International Conference on Multiphase Flow*, (392), 1–17. Retrieved from [http://www.drthfrank.de/publications/2004/Burns\\_Frank\\_ICMF\\_2004\\_final.pdf](http://www.drthfrank.de/publications/2004/Burns_Frank_ICMF_2004_final.pdf)
- Calderbank, P. H., & Moo-Young, M. B. (1960). The continuous phase heat and mass transfer properties of dispersions. *Chemical Engineering Science*, 50(24), 3921–3934. [https://doi.org/10.1016/0009-2509\(96\)81823-9](https://doi.org/10.1016/0009-2509(96)81823-9)
- Cebeci, T., Shao, J. P., Kafyeke, F., & Laurendeau, E. (2005). *Computational Fluid Dynamics for Engineers. Fluid Dynamics*. <https://doi.org/10.1007/3-540-27717-X>
- Celik, I. B., Ghia, U., Roach, P. J., Freitas, C. J., Coleman, H., & Raad, P. E. (2008). Procedure for Estimation and Reporting of Uncertainty Due to Discretization in CFD Applications. *Journal of Fluids Engineering*, 130(7), 78001. <https://doi.org/10.1115/1.2960953>
- Champagnat, F., Cornic, P., Cheminet, A., Leclaire, B., Le Besnerais, G., & Plyer, A. (2014). Tomographic PIV: particles versus blobs. In *10TH INTERNATIONAL SYMPOSIUM ON PARTICLE IMAGE VELOCIMETRY - PIV13* (pp. 1–8). Delft. <https://doi.org/10.1088/0957-0233/25/8/084002>
- Craig, K. J., Nieuwoudt, M. N., & Niemand, L. J. (2013). CFD simulation of anaerobic digester with variable sewage sludge rheology. *Water Research*, 47(13), 4485–4497. <https://doi.org/10.1016/j.watres.2013.05.011>
- Date, A. W. (2005). *Introduction to computational fluid dynamics*. Retrieved from [http://books.google.com/books?hl=en&lr=&id=4lkiP\\_LnJwoC&oi=fnd&pg=PR13&dq=Introduction+to+computational+fluid+dynamics&ots=6qxwW\\_GYbF&sig=oA\\_8gdN5itGO6BNw1Q4fr\\_WvNY](http://books.google.com/books?hl=en&lr=&id=4lkiP_LnJwoC&oi=fnd&pg=PR13&dq=Introduction+to+computational+fluid+dynamics&ots=6qxwW_GYbF&sig=oA_8gdN5itGO6BNw1Q4fr_WvNY)
- Delafosse, A., Collignon, M. L., Crine, M., & Toye, D. (2011). Estimation of the turbulent kinetic energy dissipation rate from 2D-PIV measurements in a vessel stirred by an axial Mixel TTP impeller. *Chemical Engineering Science*, 66(8), 1728–1737. <https://doi.org/10.1016/j.ces.2011.01.011>
- Delafosse, A., Line, A., Morchain, J., & Guiraud, P. (2008). LES and URANS simulations of hydrodynamics in mixing tank: Comparison to PIV experiments. *Chemical Engineering Research and Design*, 86(12), 1322–1330. <https://doi.org/10.1016/j.cherd.2008.07.008>
- Devi, T. T., & Kumar, B. (2015). Design of a gas–liquid unbaffled stirred tank with a concave blade impeller. *Journal of Engineering Physics and Thermophysics*, 88(1), 76–87. <https://doi.org/10.1007/s10891-015-1169-7>

- Escudié, R., & Liné, A. (2003). Experimental analysis of hydrodynamics in a radially agitated tank. *AIChE Journal*, 49(3), 585–603. <https://doi.org/10.1002/aic.690490306>
- Evans, G. M., Doroodchi, E., Lane, G. L., Koh, P. T. L., & Schwarz, M. P. (2008). Mixing and gas dispersion in mineral flotation cells. *Chemical Engineering Research and Design*, 86(12), 1350–1362. <https://doi.org/10.1016/j.cherd.2008.07.006>
- Frössling, N. (1938). On the vaporization of a falling drop. *Gerlands Beitr Geophys*, 52, 170–216.
- Garcia-Ochoa, F., & Gomez, E. (2004). Theoretical prediction of gas-liquid mass transfer coefficient, specific area and hold-up in sparged stirred tanks. *Chemical Engineering Science*, 59(12), 2489–2501. <https://doi.org/10.1016/j.ces.2004.02.009>
- Gimbun, J., Rielly, C. D., & Nagy, Z. K. (2009). Modelling of mass transfer in gas-liquid stirred tanks agitated by Rushton turbine and CD-6 impeller: A scale-up study. *Chemical Engineering Research and Design*, 87(4), 437–451. <https://doi.org/10.1016/j.cherd.2008.12.017>
- Haario, H. (2001). *MODEST User Guide*. ProfMath Oy. Retrieved from [http://www.researchgate.net/publication/229016569\\_Statistical\\_Analysis\\_in\\_Modeling\\_MCMC\\_Methods/file/72e7e528e132575a55.pdf](http://www.researchgate.net/publication/229016569_Statistical_Analysis_in_Modeling_MCMC_Methods/file/72e7e528e132575a55.pdf)
- Haringa, C. (2017). *The interaction between hydrodynamics and metabolic dynamics in industrial-scale fermentation processes*.
- Haringa, C., Deshmukh, A. T., Mudde, R. F., & Noorman, H. J. (2017). Euler-Lagrange analysis towards representative down-scaling of a 22 m<sup>3</sup> aerobic *S. cerevisiae* fermentation. *Chemical Engineering Science*, 170, 653–669. <https://doi.org/10.1016/j.ces.2017.01.014>
- Hashemi, N., Ein-Mozaffari, F., Upreti, S. R., & Hwang, D. K. (2016). Analysis of power consumption and gas holdup distribution for an aerated reactor equipped with a coaxial mixer: Novel correlations for the gas flow number and gassed power. *Chemical Engineering Science*, 151, 25–35. <https://doi.org/10.1016/j.ces.2016.05.003>
- Havelka, P., Moucha, T., Sinkule, J., & Linek, V. (1998). Chemical dynamic method for measuring kLa in gas-liquid dispersions. *Chemical Engineering Communications*, 168, 97–110. <https://doi.org/10.1080/00986449808912709>
- Heikkinen L. (2005). *Statistical Estimation Methods for Electrical Process Tomography*. Kuopio Univeristy.
- Higbie, R. (1935). The rate of absorption of a pure gas into a still liquid. *Transactions of*

- AIChE*, 35, 36–60. <https://doi.org/10.1017/CBO9780511805134.010>
- Hinze J.O. (1975). *Turbulence* (2nd ed.).
- Hu, B., Pacek, A. W., Stitt, H. E., & Nienow, A. W. (2005). Bubble sizes in agitated air-alcohol systems with and without particles: Turbulent and transitional flow. *Chemical Engineering Science*, 60(22), 6371–6377. <https://doi.org/10.1016/j.ces.2005.02.066>
- Hudcova, V., Nienow, A. W., Wang, H. Z., & Liu, H. X. (1987). On the effect of liquid height on the flooding/loading transition. *Chemical Engineering Science*, 42(2), 375–377.
- Joshi, J. B., Nere, N. K., Rane, C. V., Murthy, B. N., Mathpati, C. S., Patwardhan, A. W., & Ranade, V. V. (2011a). CFD simulation of stirred tanks: Comparison of turbulence models. Part I: Radial flow impellers. *Canadian Journal of Chemical Engineering*, 89(1), 23–82. <https://doi.org/10.1002/cjce.20446>
- Joshi, J. B., Nere, N. K., Rane, C. V., Murthy, B. N., Mathpati, C. S., Patwardhan, A. W., & Ranade, V. V. (2011b). CFD simulation of stirred tanks: Comparison of turbulence models (Part II: Axial flow impellers, multiple impellers and multiphase dispersions). *Canadian Journal of Chemical Engineering*, 89(4), 754–816. <https://doi.org/10.1002/cjce.20465>
- Kálal, Z., Jahoda, M., & Fořt, I. (2014). CFD prediction of gas-liquid flow in an aerated stirred vessel using the population balance model. *Chemical and Process Engineering - Inżynieria Chemiczna I Procesowa*, 35(1), 55–73. <https://doi.org/10.2478/cpe-2014-0005>
- Kaneda, Y., & Ishihara, T. (2006). High-resolution direct numerical simulation of turbulence. *Journal of Turbulence*, 7(20), 1–17. <https://doi.org/10.1080/14685240500256099>
- Karimi, M., Akdogan, G., Dellimore, K. H., & Bradshaw, S. M. (2012). Comparison of different drag coefficient correlations in the CFD modelling of a laboratory-scale Rushton-turbine flotation tank. In *Ninth International Conference on CFD in the Minerals and Process Industries CSIRO* (pp. 1–7). Melbourne. Retrieved from [http://www.cfd.com.au/cfd\\_conf12/PDFs/039KAR.pdf](http://www.cfd.com.au/cfd_conf12/PDFs/039KAR.pdf)
- Kasat, G. R., & Pandit, A. B. (2005). Review on mixing characteristics in solid-liquid and solid-liquid-gas reactor vessels. *Canadian Journal of Chemical Engineering*, 83(4), 618–643. <https://doi.org/10.1002/cjce.5450830403>
- Kaskiala, T. (2005). *Studies on gas-liquid mass transfer in atmospheric leaching of sulphidic zinc concentrates*. Helsinki University of Technology.

- Kawase, Y., Halard, B., & Moo-Young, M. (1992). Liquid-Phase mass transfer coefficients in bioreactors. *Biotechnology and Bioengineering*, 39(11), 1133–1140. <https://doi.org/10.1002/bit.260391109>
- Keane, R. D., & Adrian, R. J. (1992). Theory of cross-correlation analysis of PIV images. *Applied Scientific Research*, 49(3), 191–215. <https://doi.org/10.1007/BF00384623>
- Khan, F. R. (2005). *Investigation of Turbulent Flows and Instabilities in a Stirred Vessel using Particle Image Velocimetry*. Loughborough University.
- Khopkar, A. R., & Ranade, V. V. (2006). CFD Simulation of Gas-Liquid Stirred Vessel: VC, S33, and L33 Flow Regimes. *AIChE Journal*, 52(5), 1654–1672. <https://doi.org/10.1002/aic>
- Kilander, J., & Rasmuson, Å. C. (2005). Energy dissipation and macro instabilities in a stirred square tank investigated using an le PIV approach and LDA measurements. *Chemical Engineering Science*, 60(24), 6844–6856. <https://doi.org/10.1016/j.ces.2005.02.076>
- Kocamustafaogullari, G., & Ishii, M. (1995). Foundation of the interfacial area transport equation and its closure relations. *International Journal of Heat and Mass Transfer*, 38(3), 481–493. [https://doi.org/10.1016/0017-9310\(94\)00183-V](https://doi.org/10.1016/0017-9310(94)00183-V)
- Koralewska, J., Piotrowski, K., Wierzbowska, B., & Matynia, A. (2008). Kinetics of barium sulphate reaction crystallization in crystallizers with internal circulation. *Brazilian Journal of Chemical Engineering*, 25(2), 375–387. <https://doi.org/10.1590/S0104-66322008000200015>
- Kourunen J. (2009). *Imaging of Mixing in Selected Industrial Processes Using Electrical Resistance Tomography*. University of Eastern Finland, Kuopio.
- Kumar, S., & Ramkrishna, D. (1996). On the solution of population balance equations by discretization—I. A fixed pivot technique. *Chemical Engineering Science*, 51(8), 1311–1332. [https://doi.org/10.1016/0009-2509\(96\)88489-2](https://doi.org/10.1016/0009-2509(96)88489-2)
- Laakkonen, M., Alopaeus, V., & Aittamaa, J. (2006). Validation of bubble breakage, coalescence and mass transfer models for gas-liquid dispersion in agitated vessel. *Chemical Engineering Science*, 61(1), 218–228. <https://doi.org/10.1016/j.ces.2004.11.066>
- Laakkonen, M., Moilanen, P., & Aittamaa, J. (2005). Local bubble size distributions in agitated vessels. *Chemical Engineering Journal*, 106, 133–143. <https://doi.org/10.1016/j.cej.2004.11.010>
- Lamont, J. C., & Scott, D. S. (1970). A eddy cell model of mass transfer into the surface of a turbulent liquid. *AIChE Journal*, 16(4), 513–519.



<https://doi.org/10.1205/cherd06066>

- Lampinen, M., Laari, A., & Turunen, I. (2015). Ammoniacal thiosulfate leaching of pressure oxidized sulfide gold concentrate with low reagent consumption. *Hydrometallurgy*, 151, 1–9. <https://doi.org/10.1016/j.hydromet.2014.10.014>
- Lane, G. L. (2006). *Computational Modelling of Gas-Liquid Flow in Stirred Tanks*. The University of Newcastle.
- Lane, G. L. (2017). Improving the accuracy of CFD predictions of turbulence in a tank stirred by a hydrofoil impeller. *Chemical Engineering Science*, 169, 188–211. <https://doi.org/10.1016/j.ces.2017.03.061>
- Lane, G. L., & Koh, P. T. L. (1997). CFD Simulation of a Ruston Turbine in a Baffled Tank. In *Inter. Conf. on CFD Mineral & Metal Processing and Power Generation CSIRO* (pp. 377–386).
- Lane, G. L., Schwarz, M. P., & Evans, G. M. (2005). Numerical modelling of gas-liquid flow in stirred tanks. *Chemical Engineering Science*, 60(8–9 SPEC. ISS.), 2203–2214. <https://doi.org/10.1016/j.ces.2004.11.046>
- Lau, Y. M., Roghair, I., Deen, N. G., van Sint Annaland, M., & Kuipers, J. A. M. (2011). Numerical investigation of the drag closure for bubbles in bubble swarms. *Chemical Engineering Science*, 66(14), 3309–3316. <https://doi.org/10.1016/j.ces.2011.01.053>
- Launder, B. E., Reece, G. J., & Rodi, W. (1975). Progress in the development of a Reynolds-stress turbulence closure. *Journal of Fluid Mechanics*, 68(3), 537–566. <https://doi.org/10.1017/S0022112075001814>
- LaVision GmbH. (2006). DaVis FlowMaster Software. LaVision Inc.
- Levins, D. M., & Glastonbury, J. R. (1972). Particle-liquid hydrodynamics and mass transfer in a stirred vessel. Part II—Mass transfer. *Transactions of IChemE*, 50, 32–41.
- Li, D., Gao, Z., Buffo, A., Podgorska, W., & Marchisio, D. L. (2017). Droplet Breakage and Coalescence in Liquid–Liquid Dispersions: Comparison of Different Kernels with EQMOM and QMOM. *AIChE Journal*, 63(6), 2293–2311. <https://doi.org/10.1002/aic>
- Li, L. (2013). *Computational fluid dynamics modelling of complex fluid flow in stirred vessels*. University of Birmingham. Retrieved from [http://etheses.bham.ac.uk/4753/2/Decl\\_IS\\_Liu14PhD.pdf](http://etheses.bham.ac.uk/4753/2/Decl_IS_Liu14PhD.pdf)
- Li, X., Guan, X., Zhou, R., Yang, N., & Liu, M. (2017). CFD Simulation of Gas Dispersion in a Stirred Tank of Dual Rushton Turbines. *International Journal of*

- Chemical Reactor Engineering*, 15(4). <https://doi.org/10.1515/ijcre-2016-0221>
- Lindmark, J., Thorin, E., Bel Fdhila, R., & Dahlquist, E. (2014). Effects of mixing on the result of anaerobic digestion: Review. *Renewable and Sustainable Energy Reviews*, 40, 1030–1047. <https://doi.org/10.1016/j.rser.2014.07.182>
- Lindstedt, M. (2017). Combined Mesh and Frame Motion for Fast Transient CFD Simulation of Rotating Machines. In *NAFEMS World Congress 2017*. Stockholm.
- Liné, A., Gabelle, J. C., Morchain, J., Anne-Archard, D., & Augier, F. (2013). On POD analysis of PIV measurements applied to mixing in a stirred vessel with a shear thinning fluid. *Chemical Engineering Research and Design*, 91(11), 2073–2083. <https://doi.org/10.1016/j.cherd.2013.05.002>
- Linek, V., Beneš, P., & Vacek, V. (1989). Dynamic pressure method for  $k_L a$  measurement in large-scale bioreactors. *Biotechnology and Bioengineering*, 33, 1406–1412.
- Linek, V., Kordač, M., Fijasová, M., & Moucha, T. (2004). Gas-liquid mass transfer coefficient in stirred tanks interpreted through models of idealized eddy structure of turbulence in the bubble vicinity. *Chemical Engineering and Processing: Process Intensification*, 43(12), 1511–1517. <https://doi.org/10.1016/j.cep.2004.02.009>
- Linek, V., Moucha, T., & Sinkule, J. (1996). Gas-liquid mass transfer in vessels stirred with multiple impellers—I. Gas-liquid mass transfer characteristics in individual stages. *Chemical Engineering Science*, 51(12), 3203–3212. [https://doi.org/10.1016/0009-2509\(95\)00395-9](https://doi.org/10.1016/0009-2509(95)00395-9)
- Liu, T. Y., Sheng, Y., Han, L. H., & Liu, Q. (2017). Simulation of the bubble behaviors for gas-liquid dispersion in agitated vessel. *Journal of Chemical Engineering of Japan*, 50(1), 4–14. <https://doi.org/10.1252/jcej.16we023>
- Lubchenko, N., Magolan, B., Sugrue, R., & Baglietto, E. (2018). A more fundamental wall lubrication force from turbulent dispersion regularization for multiphase CFD applications. *International Journal of Multiphase Flow*, 98, 36–44. <https://doi.org/10.1016/j.ijmultiphaseflow.2017.09.003>
- Luo, H. (1993). *Coalescence, Breakup and Liquid Circulation in Bubble Column Reactors*. The University of Trondheim.
- Luo, H., & Svendsen, H. F. (1996). Theoretical model for drop and bubble breakup in turbulent dispersions. *AIChE Journal*, 42(5), 1225–1233.
- Machon, V., Pacek, A. W., & Nienow, A. W. (1997). Bubble sizes in electrolyte and alcohol solutions in a turbulent stirred vessel. *Chemical Engineering Research and Design*, 75(3), 339–348. <https://doi.org/10.1205/026387697523651>

- Malik, S., L  v  que, E., Bouaifi, M., Gamet, L., Flottes, E., Simo  ns, S., & El-Hajem, M. (2016). Shear improved Smagorinsky model for large eddy simulation of flow in a stirred tank with a Rushton disk turbine. *Chemical Engineering Research and Design*, 108, 69–80. <https://doi.org/10.1016/j.cherd.2016.02.035>
- Marchisio, D. L., & Fox, R. O. (2005). Solution of population balance equations using the direct quadrature method of moments. *Journal of Aerosol Science*, 36(1), 43–73. <https://doi.org/10.1016/j.jaerosci.2004.07.009>
- Marshall, E. M., & Bakker, A. (2001). *Computational Fluid Mixing*. Fluent Incorporated.
- McGraw, R. (1997). Description of Aerosol Dynamics by the Quadrature Method of Moments. *Aerospace Science and Technology*, 27, 225–265. <https://doi.org/10.1080/02786829708965471>
- Mena, P. C. (2005). *On gas absorption into a turbulent liquid*. Universidade do Porto.
- Mendoza-Escamilla, V. X., Alonzo-Garc  a, A., Mollinedo, H. R., Gonz  lez-Neria, I., Antonio Y  nez-Varela, J., & Martinez-Delgadillo, S. A. (2018). Assessment of k–  models using tetrahedral grids to describe the turbulent flow field of a PBT impeller and validation through the PIV technique. *Chinese Journal of Chemical Engineering*, 26(5), 942–956. <https://doi.org/10.1016/j.cjche.2018.02.012>
- Menter, F. R. (1993). Zonal Two Equation k-w Turbulence Models for Aerodynamic Flows. In *24th Fluid Dynamics Conference*. Orlando.
- Morsi, S. A. J., & Alexander, A. J. (1972). An investigation of particle trajectories in two-phase flow systems. *Journal of Fluid Mechanics*, 55(2), 193–208.
- Mullin, J. W. (2001). *Crystallization*. *Kirk-Othmer Encyclopedia of Chemical Technology* (4th ed.). <https://doi.org/10.1002/0471238961.0318251918152119.a01.pub3>
- Nauha, E. K., K  lal, Z., Ali, J. M., & Alopaeus, V. (2018). Compartmental modeling of large stirred tank bioreactors with high gas volume fractions. *Chemical Engineering Journal*, 334(November 2017), 2319–2334. <https://doi.org/10.1016/j.cej.2017.11.182>
- Orszag, S. A. (1970). Analytical theories of turbulence. *Journal of Fluid Mechanics*, 41(2), 363–386.
- Orszag, S. A., Yakhot, V., Flannery, W. S., Boysan, F., Choudhury, D., Maruzewski, J., & Patel, B. (1993). Renormalization Group Modeling and Turbulence Simulations. In *International Conference on Near- Wall Turbulent Flows*. Tempe.
- Pinelli, D., Liu, Z., & Magelli, F. (2010). Analysis of kLa Measurement Methods in

- Stirred Vessels: The Role of Experimental Techniques and Fluid Dynamic Models. *International Journal of Chemical Reactor Engineering*, 8(1). <https://doi.org/10.2202/1542-6580.1915>
- Raffel, M., Willert, C. E., Wereley, S. T., & Kompenhans, J. (2007). *Particle Image Velocimetry* (2nd ed., Vol. 79). Springer. <https://doi.org/10.1007/978-3-540-72308-0>
- Ramsey, J. D., Amer, M., & Feng, Y. (2019). Using CFD Simulations and Statistical Analysis to Correlate Oxygen Mass Transfer Coefficient to Both Geometrical Parameters and Operating Conditions in a Stirred-Tank Bioreactor. *Biocatalysts and Bioreactor Design*. <https://doi.org/10.1002/btpr.2785>
- Randolph, A. D., & Larson, M. A. (1971). *Theory of Particulate Processes*. London: Academic Press, Inc.
- Roghair, I., Lau, Y. M., Deen, N. G., Slagter, H. M., Baltussen, M. W., Van Sint Annaland, M., & Kuipers, J. A. M. (2011). On the drag force of bubbles in bubble swarms at intermediate and high Reynolds numbers. *Chemical Engineering Science*, 66(14), 3204–3211. <https://doi.org/10.1016/j.ces.2011.02.030>
- Ruchti, G., Dunn, I. J., & Bourne, J. R. (1981). Comparison of dynamic oxygen electrode methods for the measurement of kLa. *Biotechnology and Bioengineering*, 23, 277–290. <https://doi.org/10.1002/bit.260230204>
- Saffman, P. G. (1965). The Lift on a Small Sphere in a Slow Shear Flow. *Journal of Fluid Mechanics*, 22(2), 385–400.
- Sajjadi, B., Raman, A. A. A., Ibrahim, S., & Shah, R. S. S. R. E. (2012). Review on gas-liquid mixing analysis in multiscale stirred vessel using CFD. *Reviews in Chemical Engineering*, 28(2–3), 171–189. <https://doi.org/10.1515/revce-2012-0003>
- Sarkar, J., Shekhawat, L. K., Loomba, V., & Rathore, A. S. (2016). CFD of mixing of multi-phase flow in a bioreactor using population balance model. *Biotechnology Progress*, 32(3), 613–628. <https://doi.org/10.1002/btpr.2242>
- Scargiali, F., D’Orazio, A., Grisafi, F., & Brucato, A. (2007). Modelling and simulation of gas - liquid hydrodynamics in mechanically stirred tanks. *Chemical Engineering Research and Design*, 85(5 A), 637–646. <https://doi.org/10.1205/cherd06243>
- Schiller, L., & Naumann, Z. (1933). A drag coefficient correlation. *Z.Ver.Deutsch.Ing*, 77(13–14), 318–320. <https://doi.org/10.1016/j.ijheatmasstransfer.2009.02.006>
- Schroeder, A., & Willert, C. E. (2008). *Particle Image Velocimetry. New Developments and Recent Applications. Optics & Laser Technology* (Vol. 9). [https://doi.org/10.1016/0030-3992\(77\)90116-5](https://doi.org/10.1016/0030-3992(77)90116-5)

- Schwartzberg, H. G., & Treybal, R. E. (1968). Fluid and Particle Motion in Turbulent Stirred Tanks. Particle Motion. *Industrial & Engineering Chemistry Fundamentals*, 7(1), 6–12. <https://doi.org/10.1021/i160025a002>
- Shih, T. H., Liou, W. W., Shabbir, A., Yang, Z., & Zhu, J. (1995). A new k- $\epsilon$  eddy viscosity model for high Reynolds number turbulent flows – model development and validation. *Computers Fluids*, 24(3), 227–238.
- Svens, K. (2010). Outotec atmospheric zinc concentrate direct leaching process - Past, present and future. *World of Metallurgy - Erzmetall*, 63(3), 136–144.
- Taghavi, M., Zadghaffari, R., Moghaddas, J., & Moghaddas, Y. (2011). Experimental and CFD investigation of power consumption in a dual Rushton turbine stirred tank. *Chemical Engineering Research and Design*, 89(3), 280–290. <https://doi.org/10.1016/j.cherd.2010.07.006>
- Takamasa, T., & Tomiyama, A. (1999). Three-Dimensional Gas-Liquid Two-Phase Bubbly Flow in a C- Shaped Tube. In *Ninth International Topical Meeting on Nuclear Reactor Thermal Hydraulics (NURETH-9)*. San Francisco, CA.
- Tervasmäki, P., Latva-Kokko, M., Taskila, S., & Tanskanen, J. (2016). Mass transfer, gas hold-up and cell cultivation studies in a bottom agitated draft tube reactor and multiple impeller Rushton turbine configuration. *Chemical Engineering Science*, 155, 83–98. <https://doi.org/10.1016/j.ces.2016.07.048>
- Tervasmäki, P., Latva-Kokko, M., Taskila, S., & Tanskanen, J. (2018). Effect of oxygen transfer on yeast growth kinetic and reactor model to estimate scale-up effects in bioreactors. *Food and Bioprocess Processing*, 129–140. <https://doi.org/https://doi.org/10.1016/j.fbp.2018.08.004>
- Tomiyama, A. (1998). Struggle with computational bubble dynamics. In *Third International Conference on Multiphase Flow* (pp. 8–12). Lyon.
- Torbacke, M. (2001). *On the Influence of Mixing and Scaling-Up in Semi-Batch Reaction Crystallization*. Royal Institute of Technology. [https://doi.org/10.1016/S0009-2509\(00\)00452-8](https://doi.org/10.1016/S0009-2509(00)00452-8)
- Torbacke, M., & Rasmuson, Å. C. (2004). Mesomixing in semi-batch reaction crystallization and influence of reactor size. *AIChE Journal*, 50(12), 3107–3119. <https://doi.org/10.1002/aic.10213>
- Tsamopoulos, J., Dimakopoulos, Y., Chatzidai, N., Karapetsas, G., & Pavlidis, M. (2008). Steady bubble rise and deformation in Newtonian and viscoplastic fluids and conditions for bubble entrapment. *Journal of Fluid Mechanics*, 601, 123–164. <https://doi.org/10.1017/S0022112008000517>

- Uehara-Nagamine, E., & Armenante, P. M. (2001). Effect of Process Variables on the Single-Feed Semibatch Precipitation of Barium Sulphate. *Chemical Engineering Research and Design*, 79(8), 979–988. <https://doi.org/http://dx.doi.org/10.1205/02638760152721226>
- Van't Riet, K. (1979). Review of Measuring Methods and Results in Nonviscous Gas-Liquid Mass Transfer in Stirred Vessels. *Industrial and Engineering Chemistry Process Design and Development*, 18(3), 357–364. <https://doi.org/10.1021/i260071a001>
- Vardar, F., & Lilly, M. D. (1982). The measurement of oxygen -transfer coefficients in fermentors by frequency response techniques. *Biotechnology Advances*, 24, 1711–1719.
- Vasconcelos, J. M. T., Nienow, A. W., Martin, T., Alves, S. S., & McFarlane, C. M. (1997). Alternative ways of applying the hydrogen peroxide steady state method of kLa measurement. *Chemical Engineering Research and Design*, 75(5), 467–472. <https://doi.org/10.1205/026387697523967>
- Versteeg, H. K., & Malalasekera, W. (2007). *An Introduction to Computational Fluid Dynamics* (2nd ed.). Pearson Education Limited. <https://doi.org/10.2514/1.22547>
- Wang, H., & Zhai, Z. J. (2012). Analyzing grid independency and numerical viscosity of computational fluid dynamics for indoor environment applications. *Building and Environment*, 52, 107–118. <https://doi.org/10.1016/j.buildenv.2011.12.019>
- Wang, Z., Zhang, Q., Yang, C., Mao, Z.-S., & Shen, X. (2007). Simulation of Barium Sulfate Precipitation using CFD and FM-PDF Modeling in a Continuous Stirred Tank. *Chemical Engineering & Technology*, 30(12), 1642–1649. <https://doi.org/10.1002/ceat.200700262>
- Westerweel, J. (1993). *Digital Particle Image Velocimetry - Theory and Application*. Delft University Press.
- Wilcox, D. (1994). *Turbulence Modeling for CFD*.
- Witz, C., Treffer, D., Hardiman, T., & Khinast, J. (2016). Local gas holdup simulation and validation of industrial-scale aerated bioreactors. *Chemical Engineering Science*, 152, 636–648. <https://doi.org/10.1016/j.ces.2016.06.053>
- Wu, B. (2012a). CFD simulation of mixing for high-solids anaerobic digestion. *Biotechnology and Bioengineering*, 109(8), 2116–2126. <https://doi.org/10.1002/bit.24482>
- Wu, B. (2012b). Computational Fluid Dynamics study of large-scale mixing systems with side-entering impellers. *Engineering Applications of Computational Fluid*

- Mechanics*, 6(1), 123–133. Retrieved from <http://upcommons.upc.edu/handle/2099.1/16002>
- Wu, B. (2013). Advances in the use of CFD to characterize, design and optimize bioenergy systems. *Computers and Electronics in Agriculture*, 93, 195–208. <https://doi.org/10.1016/j.compag.2012.05.008>
- Yawalkar, A. A., Vishwas, G. P., & Beenackers, A. A. C. M. (2002). Gas Hold-Up in Stirred Tank Reactors. *The Canadian Journal of Chemical Engineering*, 80, 158–166.
- Zhang, Q., Yang, C., Mao, Z., & Mu, J. (2012). Large Eddy Simulation of Turbulent Flow and Mixing Time in a Gas – Liquid Stirred Tank. *Industrial & Engineering Chemistry Research*, 51, 10124–10131. <https://doi.org/10.1021/ie202447n>

## **Publication I**

Gradov, D. V., Laari, A., Turunen, I., and Koiranen, T.

**Experimentally validated CFD model for gas-liquid flow in a round-bottom stirred tank equipped with Rushton turbine**

Reprinted with permission from  
*International Journal of Chemical Reactor Engineering*  
Vol. 15(2), pp. 1-17, 2016  
© De Grutter





Dmitry Vladimirovich Gradov\*, Arto Laari, Ilkka Turunen and Tuomas Koiranen

# Experimentally Validated CFD Model for Gas-Liquid Flow in a Round-Bottom Stirred Tank Equipped with Rushton Turbine

DOI 10.1515/ijcre-2015-0215

**Abstract:** Hydrodynamics of gas-liquid flow in a round-bottom stirred tank is modelled at two gas flow rates, constant bubble size and agitator speed of 300 rpm. A round-bottom tank equipped with four baffles and a Rushton turbine was chosen to represent a typical reactor used in hydrometallurgical processes operating under pressure. The applicability of different momentum interchange models and the Realizable k- $\epsilon$ , SST k- $\omega$ , and RSM turbulence models was studied using CFD software. The results were compared and validated against experimental data from Particle Image Velocimetry measurements by means of liquid and gas velocity distributions. In addition, energy balance between power input and dissipation energy was compared for the different turbulence models. The CFD model was found to be in good agreement with the measurements. Of the turbulence models studied, the Realizable k- $\epsilon$  model showed best agreement with the measured velocity profiles. Popular drag force models proposed in the literature were assessed, as was the influence of inclusion of non-drag forces. Gas flow was found to affect the liquid phase flow in the tank by generating an additional secondary circulation loop in the upper part of the reactor.

**Keywords:** stirred tanks, hydrodynamics, multiphase modelling, CFD, particle image velocimetry

## 1 Introduction

A typical hydrometallurgical unit operation in leaching of metals is a stirred tank reactor equipped with a rotating agitator. Such units are complicated systems that

include mixing and multiphase mass transfer. Thus, reliable simulation and prediction methods are required to be able to design the reactor and optimize reaction conditions. Geometrically distinctive features such as shape and size of the reactor and agitator, impeller clearance, number of baffles and their shape, and design of the gas sparger and its location are just some of the issues that need to be taken into account when designing the mixing system. The round-bottom stirred reactor is a special reactor geometry that is often used in glass-lined reactors or in stirred reactors operating under pressure. The rounded shape of the reactor bottom creates different flow hydrodynamics in the bottom part than found with flat-bottom geometries. In this study, a round-bottom reactor equipped with four baffles and a Rushton turbine was selected to represent a typical reactor used in hydrometallurgical processes operating under pressure.

Mixed suspensions in hydrometallurgical leaching processes are normally three-phase systems consisting of solid, liquid and gas phases. The design and scale-up of multiphase stirred tank reactors require reliable predictions of flow fields, phase volume fractions and turbulence properties. Local flow fields and volume fractions in the reactor are needed to calculate the residence time of the phases to ensure homogeneous mixing, prevent short-circuit flows and bypass accumulation of phases at different regions in the reactor. Evaluation of multiphase mass transfer is another important issue. There are numerous examples in the chemical and metallurgical industry where the production rate is driven by gas-liquid or solid-liquid mass transfer, and evaluation of multiphase mass transfer is a crucial part of reactor design.

In recent decades, Computational Fluid Dynamics (CFD) has emerged as a useful tool to describe hydrodynamics in multiphase systems. The approach allows estimation of fluid velocities, slip velocities, interfacial surface area, phase volume fractions and turbulence properties. These factors determine gas-liquid and solid-liquid mass transfer and should hence be modelled with high accuracy. Turbulence intensity influences multiphase mass transfer by affecting not only the mass

\*Corresponding author: Dmitry Vladimirovich Gradov, School of Engineering Science, Lappeenranta University of Technology, P.O. Box 20, FI-53851 Lappeenranta, Finland, E-mail: dmitry.vladimirovich.gradov@gmail.com  
Arto Laari, Ilkka Turunen, Tuomas Koiranen, School of Engineering Science, Lappeenranta University of Technology, P.O. Box 20, FI-53851 Lappeenranta, Finland, E-mail: arto.laari@lut.fi; ilkka.turunen@lut.fi; tuomas.koiranen@lut.fi

transfer coefficient between the bubbles or particles and the liquid phase but also the bubble size distribution through bubble breakage and coalescence. Turbulence models should therefore be able to predict kinetic turbulence energy and turbulence energy dissipation rate accurately in order to facilitate accurate flow distribution and mass transfer simulation.

Much research has been done on mixing tank modelling of single-phase flow (Vivek 2002; Bai, Wang, and Armenante 2010; Huang and Li 2013; Joshi et al. 2011). Joshi et al. (2011) have recently published a thorough study of the effect of different turbulence models on flow velocity fields and turbulence properties in stirred tanks with radial flow impellers. Considerable differences in the simulated flow profiles were found at different locations in the tank depending on the turbulence model used: standard  $k-\epsilon$  model, modified  $k-\epsilon$  model based on renormalization group method (RNG), and Reynolds Stress model (RSM). The impeller-baffle interaction models studied for stirred tanks were implemented via Impeller Boundary Condition, Multiple Reference Frame (MRF), and Sliding Mesh approaches. In their work, comparison was also made with the Large Eddy Simulation (LES) model. The simulated turbulence properties were compared to experimental values. It was found that when using the MRF impeller model, the standard  $k-\epsilon$  turbulence model underpredicted the power number (integrated from the simulated energy dissipation rate) by 40 %. However, the RNG  $k-\epsilon$  model underpredicted the power number by only 5 %, and the RSM model overpredicted the power number by 45 %. Therefore, it seems that different turbulence models can give dramatically different energy dissipation rates.

Modelling of gas-liquid stirred tanks is further complicated by interactions between the phases. These interactions are generally taken into account by inclusion of different momentum interchange forces in the model. Several forces act on agitated bubbles, for example, drag, lift, turbulence dispersion, and added mass forces. The first numerical CFD simulations of gas-liquid stirred tanks appeared in the literature in the 1980's (Issa and Gosman 1981; Harvey and Greaves 1982). Since then the performance of the resulting gas-liquid models has seen considerable improvement (Tatterson 1991; Gosman et al. 1992; Bakke and Van den Akker 1994; Morud and Hjertager 1996; Lane, Schwarz, and Evans 2000; Deen, Solberg, and Hjertager 2002; Venneker, Derksen, and Van den Akker 2002; Moucha, Linek, and Prokopova 2003; Linek et al. 2004; Laakkonen et al. 2005; Sun, Mao, and Yu 2006; Scargiali et al. 2007; Gimbut, Rielly, and Nagy 2008; Moilanen 2009; Zhang et al. 2009; Gelves,

Benavides, and Quintero 2013). Most of the presented models have assumed constant bubble size, neglecting the effects of bubble size distribution, to find appropriate models for gas-liquid interaction. Despite the remarkable achievements of these models, validation of the results has been carried out mainly based on liquid phase velocity and gas hold up distribution, excluding gas phase velocity distribution. Most authors have concluded that drag force has the greatest influence on phase interaction and hence greatest attention has been paid to modelling this force while other forces, such as lift and the added mass forces, have received less attention (Lane, Schwarz, and Evans 2000; Scargiali et al. 2007; Khopkar et al. 2004). Some stirred tank multiphase modelling has considered local bubble size distribution and its shape (Ishii and Zuber 1979), and recent research work has exploited Population Balance Models (PBM), allowing changes in bubble size distribution to be captured fairly accurately (Venneker, Derksen, and Van den Akker 2002; Laakkonen et al. 2005; Gimbut, Rielly, and Nagy 2008).

Validation of simulation results against experimental data is an essential part of any modelling as it provides information about the reliability of the proposed numerical model. Many techniques are available for validation of CFD models, such as Hot Wire Anemometry (HWA) (Jensen 2004), Laser Doppler Velocimetry (LDA) (Wu and Patterson 1989) and Particle Image Velocimetry (PIV) (Huang and Li 2013; Xinhong et al. 2010). PIV is a well-suited method for the current study and gives spatial resolution of sufficient precision. However, validation of numerical models for three-phase systems using PIV is difficult due to the nontransparent nature of mixed suspensions, which limits direct measurements from the system. One possible strategy to overcome this problem is to start from a two-phase system and then extend the validated two-phase models to three-phase systems. This approach allows development of robust process design for three-phase systems from a hydrodynamics standpoint.

The aim of the current work is to develop an experimentally validated CFD model for gas-liquid flow in a round bottom stirred tank. Different momentum interchange and turbulence models are compared and validated against experimental data using radial profiles of velocity components. The turbulence models are also validated by comparison of the simulated integrated energy dissipation rate to the power input calculated from the momentum source at the impeller. CFD simulations for the selected round-bottom reactor geometry can give valuable information that is applicable to design of semi- and full-scale industrial cases.

## 2 Material and methods

### 2.1 Experimental set-up

A round-bottom stirred tank made of glass was used in the experiments. The tank was equipped with a Rushton turbine and four baffles to prevent circulation and to promote mixing. The reactor dimensions are given in Figure 1. The vessel shape can be considered as a combination of a sphere split in half and a cylinder swept out of the cut to the reactor height to achieve an aspect ratio of 2. At the bottom of the vessel, a gas sparger was mounted at the height of 7 mm from the bottom. The atypical baffle construction is due to the glass material. The baffles comprised four rectangular flow reflectors connected by a ring located at the reactor bottom (see Figure 1). To reduce optical distortions and to facilitate PIV measurements, the tank was fitted inside a rectangular box made of polyacrylate. The space between the box and the glass vessel was filled with tap water.

The agitator rotation speed was maintained at 300 rpm and the liquid height to tank diameter ratio was kept at 2. With this rotation speed, the Reynolds number is almost 24 000, which means that the flow is fully turbulent. Tap water at 20 °C was used as the liquid phase. The agitator clearance was fixed to 50 mm off the bottom of the reactor vessel, which corresponds roughly to one quarter of the vessel width.

### 2.2 Method and criteria of validation

In this study, Particle Image Velocimetry (PIV) was used to validate the simulated flow fields in the stirred tank. The PIV technique is capable of producing direct validation of flow fields by capturing the movement of tracing particles that are small enough not to interfere with the flow. A schematic presentation of the PIV set-up is given in Figure 2. The PIV set-up used included a double-pulsed Nd: Yag laser and two CCD cameras with a resolution of  $1,600 \times 1,200$  pixels. The laser and the cameras were controlled by Davis 7.2 PIV software. By slicing the flow with a thin laser sheet, PIV can produce a two-dimensional picture of the fluid motion in the sheet. A vector velocity field for each phase can be constructed based on the spatial shift of tracer-particles in the time  $\Delta t$  between a pair of laser pulses. Imaging of the tracer shift was carried out using two CCD cameras synchronized

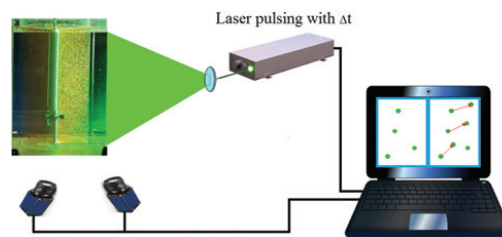


Figure 2: Schematic representation of the PIV set-up.

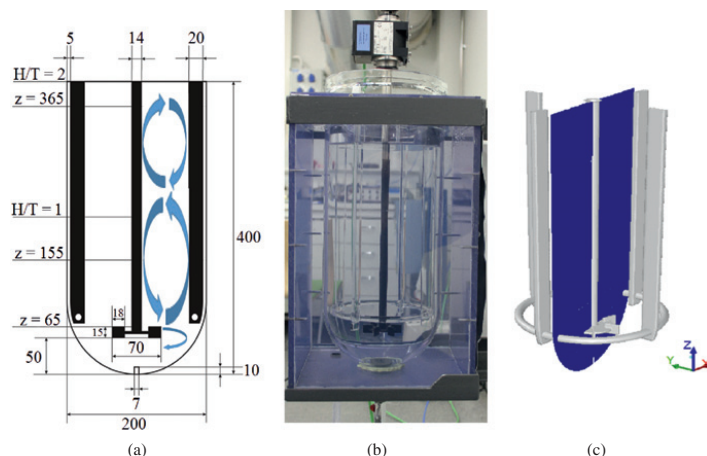


Figure 1: Studied round-bottom reactor. (a) reactor geometry sizing in mm, (b) photographic image of the reactor, (c) sampled plane used in validation.

with the laser pulsing. Thus, the non-stereo PIV system was able to measure velocity vector fields in two-dimensional space, including axial and radial components.

To measure liquid phase flow, fluorescent particles of size 20–50  $\mu\text{m}$ , made of polyamide, were used as tracers in both the single-phase and two-phase PIV experiments. Fluorescent tracer particles have the benefit that they emit light at different wavelength than the laser beam. Therefore, good quality background images can be acquired by using high pass filters mounted on the CCD cameras to separate light of different wavelengths. By employing such preliminary filtering, strong light reflections from parts of the vessel, baffles and impeller with a rotating shaft can be greatly reduced or even totally eliminated. Gas phase tracking was performed using the light reflected from bubbles. In this case, the camera was capped with a grey filter to reduce the reflected light intensity.

The laser sheet in the reactor was positioned vertically, near the baffle, and 3 mm behind the geometrical axes of the shaft, as shown in Figure 1. The reason for this positioning was to remove as many visual obstacles and strong reflections as possible. The size of the single frame taken (measurement window) depends on the camera resolution and the distance of the camera from the laser sheet. A typical measurement window size was 110  $\times$  80 mm. The window was split by the PIV software into interrogation areas of 32  $\times$  32 pixels and processed via cross-correlation. The camera resolution, the size of the interrogation area, and the physical size of the measurement window gave a resolution of 2.2 mm for the PIV results. In order to get a full picture of the reactor, it was necessary to take multiple measurements at different heights and to combine the separate images along the vertical axes with 10 mm overlapping. In addition, the lowest frame at the tank bottom was cropped to remove areas outside the tank (Figure 3). A full image (100  $\times$  400 mm) of the reactor, from the tank walls to the shaft, could be obtained by assembling the captured frames. The post-processed resolution of the vertically

combined frames was 94  $\times$  189 vectors. In order to obtain time-averaged results, 500 frames were taken and processed.

### 3 Numerical model

#### 3.1 Meshing

Four different structured grids were built about the studied geometry with different grid densities, giving a total number of cells of around 400 000, 800 000, 1 100 000 and 1 900 000. Scaling uniformity was maintained for all the grids. The minimum orthogonal quality and maximum aspect ratio of the cells were 0.37 and 30.29, respectively.

In the simulation settings, the best practice of use of a standard wall function was followed to keep the dimensionless distance from the wall in the range of 30–300 (Kalitzin et al. 2005; Chmielewski and Gieras 2013). A standard wall function approach was used and the flow was expected to be in the log-law region of the liquid layer next to the wall. However, for stirred reactors it is hard to predict the dimensionless distance ( $y^+$ ) since mixing in a baffled tank differs from tubular flow and the dimensionless  $y^+$  varies along the wall. In addition to the reactor walls, the  $y^+$  value of the baffles also has to be considered. Therefore, an average value for  $y^+$  (close to 100) was used in the meshing.

#### 3.2 Simulations settings

All simulations were performed as steady state simulations using Fluent 16.0 commercial software. Since the grid was built in a structured manner, it was possible to apply a QUICK (Quadratic Upwind Interpolation for Convective Kinetics) differencing scheme of third order during solution for momentum, volume fraction, kinetic

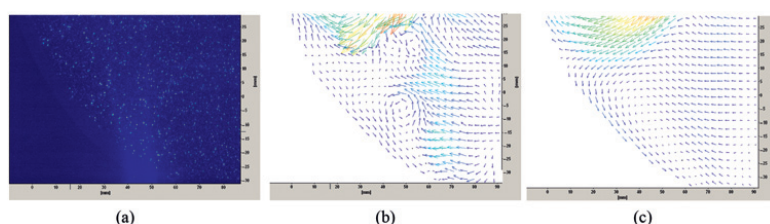


**Figure 3:** Measurement window and calculated velocity vector fields at the bottom part of the tank. (a) horizontal cross-section, (b) instant velocity vector field, (c) averaged velocity vector field.

energy and dissipation rate of turbulence. The pressure-velocity coupling was carried out using the Semi-Implicit (SIMPLE) algorithm.

The Multiple Reference Frame (MRF) approach is a widely used technique to simulate rotating parts such as impellers and shafts within a reactor domain. The rotating parts produce pressure difference, which is the main agitating force when mixing takes place.

In the gas-liquid simulations, the pressure outlet boundary was defined at the top of the tank. The surface tension of air-water at 20 °C equals to 0.0728 N/m ([http://www.engineeringtoolbox.com/water-surface-tension-d\\_597.html](http://www.engineeringtoolbox.com/water-surface-tension-d_597.html)).

The convergence criteria were set to  $10^{-4}$ . However, in the gas-liquid simulations, the computation continues until the balance between air mass flow through the velocity inlet and the pressure outlet is reached within 1% accuracy.

### 3.3 Grid independence test

The effect of grid resolution on the numerical simulation results was tested for the four different grids. The Reynolds number differs significantly within the vessel. Therefore, 14 velocity-sampling points were defined, as presented in Figure 4. A normalized root mean square error index (NRMSE) was employed as a criterion for grid independency testing (Wang and Zhai 2012), whose formulation is as follows:



Figure 4: Sampling points taken for grid independence study.

$$NRMSE = \frac{3}{\left(\frac{N_{fine}}{N_{coarse}}\right)^p - 1} \sqrt{\frac{\sum_{i=1}^n (\phi_1(i) - \phi_2(i))^2}{\sum_{i=1}^n (\phi_2)^2}} \cdot 100\%, \quad (1)$$

where  $N$  is the number of cells in the grid (it is advised to keep the ratio of the number of cells between two grids above 1.3 [Celik et al. 2008]),  $p$  corresponds to the order of discretization,  $n$  is the number of samples, and  $\phi_1$  and  $\phi_2$  are the predictions on the coarse and fine grids respectively.

According to Celik et al. (2008), the difference in results obtained with different grids can be considered negligible if the NRMSE value is less than 10 %. The grid independence test simulations were performed with a second order discretization scheme. In addition to NRMSE, the overall turbulence kinetic energy and energy dissipation were compared by integrating them over the reactor volume. The results presented in Table 1 clearly indicate grid 2 as the optimal grid for the current study.

Table 1: Results of grid independence study.

Grid index	Grid number	NRMSE of velocity magnitude to next finer grid, %	$\int k dV$ , $\frac{m^2}{s^2 m^3} \cdot 10^{-5}$	$\int \epsilon dV$ , $\frac{m^2}{s^2 m^3} \cdot 10^{-5}$
1	428030	38.28	4.32	44.54
2	801266	5.93	4.79	47.88
3	1123506	3.09	4.83	48.41
4	1908526	N/A	4.86	48.67

### 3.4 Single phase flow modelling

In CFD modelling, available computing power and acceptable simulation time also have to be taken into account, for which reason it was decided to apply the RANS models in the current simulations. Turbulence formulation in the RANS models is based on statistical analysis rather than on actual physical phenomena. By contrast, the Large Eddy Simulation (LES) model is based, at least partially, on resolving turbulence fluctuations. Approximations such as the Boussinesq hypothesis can lead to mismatches with real flow behavior due to turbulence isotropy and homogeneity, and due to the numerous empirical constants used to close the model equations. In the current work, it was decided to evaluate the suitability of the most frequently applied RANS models rather than attempt to implement a novel turbulence



model by tuning the model constants for the hydrodynamics of the specific stirred tank.

The main formulations of the RANS models are:

- Conservation equations:

$$\nabla \bar{u} = 0 \quad (2)$$

$$\bar{u} \cdot \nabla \bar{u} = -\nabla \bar{p} + \nabla \cdot [(\mu + \mu_{turb}) \nabla \bar{u}] \quad (3)$$

- Two equation models for k- $\epsilon$  and k- $\omega$ :

$$\bar{u} \cdot \nabla k = P - \epsilon + \nabla \cdot [(\mu + \mu_{turb}/\sigma_k) \nabla k] \quad (4)$$

$$\bar{u} \cdot \nabla \epsilon = C_{\epsilon 1} \frac{\epsilon}{k} P - C_{\epsilon 2} \frac{\epsilon^2}{k} + \nabla \cdot [(\mu + \mu_{turb}/\sigma_\epsilon) \nabla \epsilon], \quad (5)$$

where the production P includes one more constant,  $C_v$ .

Turbulence energy dissipation can be transformed to specific dissipation rate  $\omega$  by the following relationship:

$$\omega = \frac{\alpha \epsilon}{c_\mu k} \quad (6)$$

- Seven equation Reynolds Stress model (RSM):

$$\frac{\partial \overline{u'_i u'_j}}{\partial t} + C_{ij} = P_{ij} + D_{ij} - \epsilon_{ij} + \Pi_{ij} + \Omega_{ij} \quad (7)$$

$$\epsilon_{ij} = \frac{2}{3} \epsilon \delta_{ij}, \quad (8)$$

where  $C_{ij}$  is the Reynolds stress transport by convection,  $P_{ij}$  is the rate of production,  $D_{ij}$  is the transport by diffusion,  $\epsilon_{ij}$  is the rate of dissipation of turbulence kinetic energy,  $\Pi_{ij}$  is the transport due to turbulence pressure-strain interactions, and  $\Omega_{ij}$  is the transport due to rotation.

Three popular models in the RANS family were tested, namely the Realizable k- $\epsilon$  model, the Shear Stress Transport k- $\omega$  model, and the Reynolds Stress Model (RSM). The Realizable k- $\epsilon$  model is a recent model with an improved computational mechanism preventing turbulence energy from being negative. Such energy is not physical (Shih et al. 1995) but can occur using the Standard k- $\epsilon$  model. The Shear Stress Transport k- $\omega$  model has a mechanism for switching into the k- $\epsilon$  formulation at free stream and thereby avoids the common k- $\omega$  problem of being too sensitive to the turbulence properties of free-stream at the inlet (Menter 1993). The Reynolds Stress Model (RSM) is a second order closure model where the Reynolds stresses are found directly (Wallin and Johansson 2000). All three models were first applied in simulation of single phase mixing in order to check their performance against experimental data.

### 3.5 Gas-liquid modelling

In the gas-liquid flow modelling, the gas was introduced into a converged liquid flow field in order to reduce computational instabilities. In the CFD simulation, the stirred tank may be considered as a semi-batch system with gas feed from the bottom through the sparger and exit at the top through the liquid surface. The flow fields were studied at two gas flow rates, 0.5 and 1.0 L/min, which correspond to  $2.653 \cdot 10^{-4}$  m/s and  $5.305 \cdot 10^{-4}$  m/s of superficial velocity, respectively.

Based on analysis carried out from captured PIV frames by manually counting and measuring the bubble size, the average bubble size was around 1 mm in diameter throughout the whole reactor.

In the gas-liquid modelling, an Eulerian multiphase approach was used in which the gas and liquid phases are considered as interpenetrating continua. A dispersed turbulence formulation model was used since the secondary phase is dilute and fluctuating quantities of gaseous phase may be found as the function of the mean terms of the liquid phase. Turbulence terms  $k$  and  $\epsilon$  are first computed for the primary phase, secondary phase turbulence terms are then found (eq. (9)), and exchange of turbulence momentum between phases (eq. (10)) is computed based on Tchen-theory (Hinze 1975).

$$k_p = k_q \left( \frac{\left( (1 + C_V) / \left( \frac{\rho_p}{\rho_q} + C_V \right) \right)^2 + \frac{\tau_{t,pq}}{\tau_{F,pq}}}{1 + \frac{\tau_{t,pq}}{\tau_{F,pq}}} \right), \quad (9)$$

where  $k_q$  and  $k_p$  are the turbulence kinetic energy of primary and secondary phases, respectively,  $C_V$  is the added mass coefficient and equal to 0.5,  $\tau_{t,pq}$  is the Lagrangian integral time scale, and  $\tau_{F,pq}$  is the characteristic particle relaxation time.

$$K_{pq}(\vec{u}_p + \vec{u}_q) = K_{pq}(\vec{U}_p + \vec{U}_q) + K_{pq} \left( \frac{D_p}{\sigma_{pq} \alpha_p} \nabla \alpha_p - \frac{D_q}{\sigma_{pq} \alpha_q} \nabla \alpha_q \right), \quad (10)$$

Where  $K_{pq}$  is the interphase exchange coefficient,  $D_p$  and  $D_q$  are the diffusivities,  $\sigma_{pq}$  is the dispersion Prandtl number, and  $\alpha_p$  and  $\alpha_q$  are the phase fractions.

The momentum conservation equation (eq. (11)) includes the cumulative force acting on the phases. The cumulative force comprises several forces occurring in multiphase interaction, for example, drag, virtual mass, lift, wall lubrication, turbulence diffusion forces etc.

Conservation of momentum for phase  $q$ :

$$\frac{\partial}{\partial t}(\alpha \rho \vec{u})_q + \nabla \cdot (\alpha \rho \vec{u} \vec{u})_q = \nabla \cdot (\alpha \sigma)_q - \alpha_q \nabla p + \vec{F}_q + \alpha_q \rho_q \vec{g} \quad (11)$$

$$\begin{aligned} \vec{F}_q = & \sum_{p=1}^n (K_{pq}(\vec{u}_p - \vec{u}_q) + \dot{m}_{pq}\vec{u}_{pq} - \dot{m}_{qp}\vec{u}_{qp}) \\ & + (\vec{F}_q + \vec{F}_{lift,q} + \vec{F}_{wl,q} + \vec{F}_{vm,q} + \vec{F}_{td,q}), \end{aligned} \quad (12)$$

where  $\vec{F}_q$  is the external body force,  $\vec{F}_{lift,q}$  is the lift force,  $\vec{F}_{wl,q}$  is the wall lubrication force,  $\vec{F}_{vm,q}$  is the virtual mass force, and  $\vec{F}_{td,q}$  is the turbulence diffusion force.

Different drag models have been presented in the literature and the model choice used generally depends on the features and complexity of the case under study. A number of models have been highlighted as being the most effective and they are frequently encountered in scientific research. The most popular model, proposed by Schiller and Naumann in 1935 (eq. (15)), is a model suitable for rigid spherical particles (Azargoshasb et al. 2016; Morchain, Gabelle, and Cockx 2014; Schiller and Naumann 1935). Similar to the previous model but with greater sensitivity to the relative Re is the model suggested by Morsi and Alexander (eq. (16)) (Morsi and Alexander 1972). During experimental work, it was noticed that bubble shape has an effect on the drag force, and a refined model for slightly contaminated systems that takes bubble shape into account via Eötvös number was presented and implemented, first by Ishii and Zuber 1979, and then in modified form by Tomiyama 1998 (eq. (17)) (Ishii and Zuber 1979; Kalal, Jahoda, and Fort 2014; Takamasa and Tomiyama 1999).

$$K_{pq} = \frac{\rho_p C_D \text{Re}}{144 \tau_p} d_p A_i, \quad (14)$$

where  $C_D$  is the drag coefficient, Re is the relative Reynolds number, and  $A_i$  is the interfacial area.

$$C_D = \begin{cases} 24(1 + 0.15\text{Re}^{0.687}) & \text{Re} \leq 1000 \\ 0.44 & \text{Re} > 1000 \end{cases} \quad (15)$$

$$C_D = a_1 + \frac{a_2}{\text{Re}} + \frac{a_3}{\text{Re}^2}, \quad (16)$$

where  $a_i$  is the coefficient based on the relative Reynolds number. The whole Reynolds number range is split into eight ranges to make it more sensitive to the relative Reynolds number.

$$C_D = \max\left(\min\left(\frac{24}{\text{Re}}(1 + 0.15\text{Re}^{0.687}), \frac{72}{\text{Re}}\right), \frac{8E_0}{3(E_0 + 4)}\right), \quad (17)$$

where  $E_0$  is the Eötvös dimensionless number estimating the significance of surface tension and defining the bubble shape.

All the above-mentioned models are based on bubble rise velocity measured in stagnant fluids, which is higher than rise velocity in turbulent flow. A drag force correcting coefficient was proposed by Brucato, Grisafi, and Montante (1998). This turbulence modification factor concept (eq. (18)) changes stagnant fluid drag force to make it suitable for adoption in turbulent multiphase flow simulation. Later, Lane, Schwarz, and Evans (2005) critically considered Brucato's formulation and found that the ratio of slip and terminal velocity as a function of bubble size and Kolmogorov length scale does not take into account particle density or density difference between the phases. Having pointed out this deficiency in Brucato's model, Lane, Schwarz, and Evans (2005) suggested a new correlation (eq. (19)) for slip and terminal velocity to particle relaxation time (eq. (20)) and integral time scale of turbulence (eq. (21)).

$$K_{pq} = \eta K_{pq} = \left(1 + K\left(\frac{d_p}{\lambda}\right)^3\right) K_{pq}, \quad (18)$$

where  $\eta$  is the turbulence modification factor,  $K = 6.5 \cdot 10^{-6}$ ,  $d_p$  is the bubble diameter, and  $\lambda$  is the Kolmogorov length scale.

$$\eta = \left(1 - 1.4\left(\frac{\tau_p}{T_L}\right)^{0.7} e^{\left(\frac{0.6\tau_p}{T_L}\right)}\right)^{-2} \quad (19)$$

$$\tau_p = \frac{\rho_b d_b}{18\mu} \quad (20)$$

$$T_L = 0.135 \frac{k}{\varepsilon}, \quad (21)$$

The Saffman-Mei lift force model (Saffman 1965) takes into account the forces acting on gas bubbles arising from velocity gradients in the liquid phase and from particle rotation. In addition, the wall lubrication force, presented by Tomiyama (1998), and the turbulence dispersion force, presented by Burns et al. (2004), were also applied in the simulations to estimate their input.

## 4 Results and discussion

### 4.1 Water mixing results and discussion

The single-phase simulations and PIV results are presented in Figures 5, 6 and 7, and the simulation



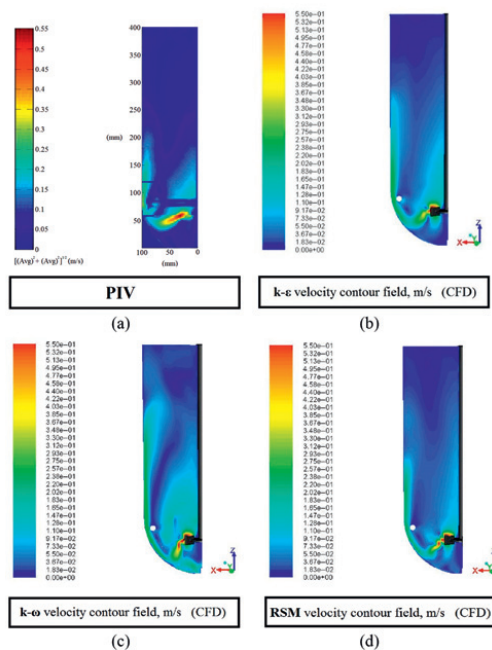


**Figure 5:** Velocity contour fields (CFD vs PIV), (a) average velocity flow field using  $k-\epsilon$  Realizable turbulence model, (b) average velocity flow field obtained from PIV tests, (c) average velocity flow field using  $k-\omega$  SST turbulence model, (d) average velocity flow field using RSM turbulence model.

conditions are briefly summarized in Table 2. There is obvious similarity between the CFD and PIV results, as can be seen from Figure 5. The flow agitated by the impeller moves towards the tank wall, from where the major part of the flow goes upwards, closing the first upper circulation loop and returning to the impeller, attracted by the region of low pressure that appears behind the moving impeller blades. The upwards flow loses its momentum under viscous forces, which results in a weak secondary circulation loop. Of the tested RANS models, the RSM model shows the closest overall match with the flow fields of the PIV results.

The biggest difference in the overall pattern prediction can be observed in the region below the impeller. A strong upward flow motion takes place in all CFD results that is not shown in the PIV experiments. The reason for this upward flow is the presence of a vortex right under the impeller, which is shown as vorticity magnitude in the CFD results in Figure 7. The origin of the strong swirling flow below the impeller can be explained by

the absence of baffles in the bottom part of the reactor, where their dampening effect is negligible. During the experimental tests, it was noticed that the location of the vortex slowly changes position moving around the axis of swirling. Capturing this circulating flow accurately creates difficulties for PIV experiments since a large number of frames are needed for flow averaging, resulting in high computational power and time demands.

An overall vector and contour fields comparison cannot give sufficiently high precision to describe fully the flow behavior in the tank. Therefore, axial and radial components of the velocity vector in the 2D field were extracted along specified lines at different heights, as shown in Figure 1. Three profiles were extracted representing three different regions, namely below the agitator, above the agitator, and the secondary loop regions. The radial profiles of the velocity components are presented in Figure 6 starting from the center of the tank and extending to the tank wall.

In general, all the three models show similar trends. However, in the bottom region, represented by the 65 mm profile, the  $k-\omega$  model shows poor results for both components. By studying the velocity components of the radial profiles, it is clear that the flow is agitated by the low pressure created behind the blades as they move and the jet-wise motion, produced by the impeller, then makes the velocities drop to values close to zero, due to friction and viscous forces, as the flow reaches the wall. While all the turbulence models describe the axial component with the same level of accuracy, the prediction by the  $k-\omega$  model for the radial component is much worse than that of the other two models. For the region above the impeller, the Realizable  $k-\epsilon$  model seems to work with similar accuracy to the Reynolds Stress model.

There is a difference between the PIV and the RANS results in the small area next to the moving shaft because the liquid flow caused by the rotating shaft can hardly be captured by PIV images with the current resolution of 3 mm. The same is true for the region near the wall. Consequently, it can be claimed that the RANS models can capture some flow features that PIV is incapable of depicting due to the lower resolution.

Turbulence properties such as the energy dissipation per unit volume bear information that is crucial for evaluation of multiphase hydrodynamics and local mass transfer rates. Unfortunately, no experimental torque data are available for the current case, neither is there any correlation of  $N_p$  vs  $Re$  available in literature, due to the special reactor geometry and the position of the impeller relative to the baffles. However, following the

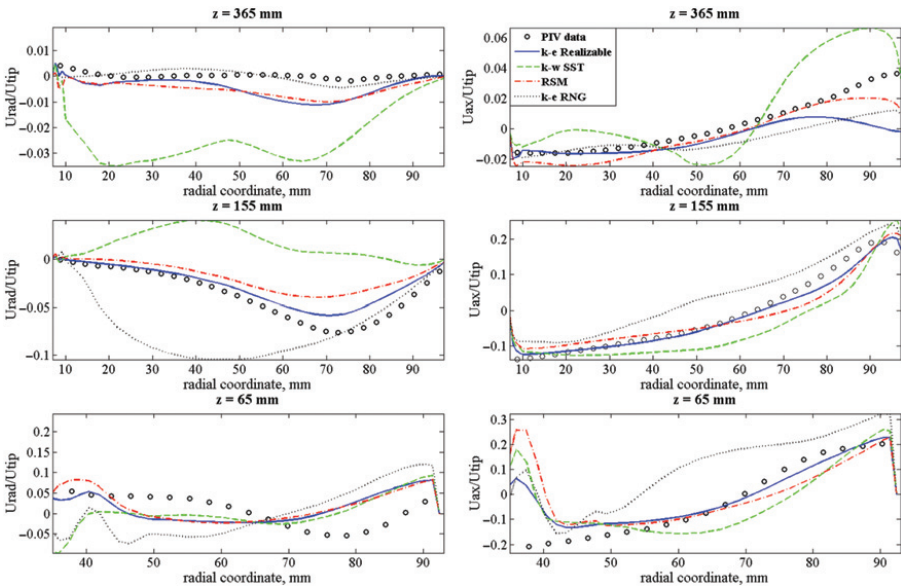


Figure 6: Comparison of velocity components of single phase flow modelling at different height using the k-ε Realizable, k-ω SST, and RSM turbulence models, and the PIV tests

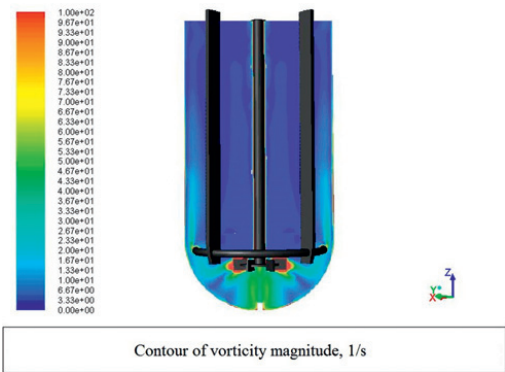


Figure 7: Vortex below the impeller represented by the vorticity magnitude contour modelled with the k-ε Realizable turbulence model.

study of Joshi et al. (2011), the model validation can be done based on energy balance. The amount of energy per time unit applied to the reactor by the rotating stirrer has to be in balance with the total energy dissipation rate. The turbulence models used in the simulations were tested by this criterion. The total power input was

Table 2: Summarized conditions for single phase mixing simulations.

Mixing speed, rpm	Turbulence formulation model	Wall function
300	k-ε Realizable k-ω SST RSM	Standard wall function

estimated based on the wall shear stress integrated over the surface of the impeller by eq. (22). The dissipated energy was found according to eq. (23) by integrating the local energy dissipation rate over the volume. The power derived from the wall shear stress and the energy dissipation rate over the whole reactor and their difference are presented in Table 3.

$$P_{\tau} = 2\pi n \int \tau dA \tag{22}$$

$$P_{\tau} = \rho \int \epsilon dV \tag{23}$$

As the paper published by Joshi et al. (2011) showed, there are differences in energy dissipation rate modelling in different RANS models. Contrary to the overprediction

**Table 3:** Power draw prediction by the RANS models.

Model	Power( $\tau$ ), W	Power( $\varepsilon$ ), W	Difference, %
k- $\varepsilon$ Realizable	1.38	0.96	27
k- $\omega$ SST	1.29	0.75	42
RSM	1.30	0.74	43
Measured experimentally	1.38–1.46		–

of the energy dissipation found by Joshi et al. (2011) for the RSM model, it was found in this study that the RSM model underpredicted the power based on the energy dissipation rate by 43 %. It was also found that the underprediction of the energy dissipation rate is quite similar for all the tested models. The Realizable k- $\varepsilon$  model was in best agreement, while the SST k- $\omega$  model showed the largest deviation. The large underestimation of the power computed from the energy dissipation rate can perhaps be explained by the fact that the turbulence models that are used to calculate energy dissipation assume turbulence isotropy and account only for turbulence eddy dissipation excluding viscous dissipation of unresolved turbulence scales (Lane and Koh 1997; Ducci and Yianneskis 2005).

## 4.2 Two-phase mixing results and discussion

### 4.2.1 General information and turbulence formulation model

For the sake of convenience, the simulation conditions used in this section are summarized in Table 4.

The SST k- $\omega$  model was first tested for gas-liquid mixing and produced asymmetrical results for gas holdup in a steady state after convergence that was not physical.

Therefore, taking of samples and averaging are required for steady-state results. Based on the findings from the single phase modelling and in view of the computational power available, the Realizable k- $\varepsilon$  model should be used for gas-liquid stirred tank simulations as it gives the most accurate predictions of the two-equation models tested and has lower computational power demands than the RSM model.

### 4.2.2 Drag force models

The presence of specific conditions may help in choice of an appropriate model for the drag force. Models in the published literature study reactors with different geometrical parameters and reactions at different conditions, for which reason model comparison is important. In this work, several drag models were tested for a round-bottom tank stirred at 300 rpm with gas flow rate of 0.5 L/min and 1 mm bubble size. As mentioned earlier, the drag force models are designed for stagnant flow, and thus the tested models are supplemented with a turbulence modification factor. In addition, the turbulence modification factors proposed by Brucato, Grisafi, and Montante (1998) and Lane, Schwarz, and Evans (2005) are compared in connection with the Schiller-Naumann drag coefficient model. The results are presented in the Figures 8 and 9.

In the figures, the superior performance of the Schiller-Naumann drag model in conjunction with Lane's turbulence modification factor can be seen clearly for the primary phase and slightly less obviously for the secondary phase. The least accurate results are produced by Tomiyama's model, which can be explained by the small and uniform size of the bubbles. The Schiller-Naumann and Morsi-Alexander models give similar results due to similarities in their formulations. Comparison of the models for drag forces against

**Table 4:** Results of grid independence study.

Mixing speed, rpm	Turbulence model	Wall function	Gas flow rate, L/min	Drag force model	Turbulence modification factor	Non-drag Forces model
300	k- $\varepsilon$ Realizable	Standard wall function	0.5	Schiller-Naumann	Brucato	Lift force (Saffman-Mei)
	k- $\omega$ SST		1	Morsi-Alexander	Lane	Wall lubrication force (Tomiyama)
				Tomiyama		Turbulence dispersion force (Burns et al.)

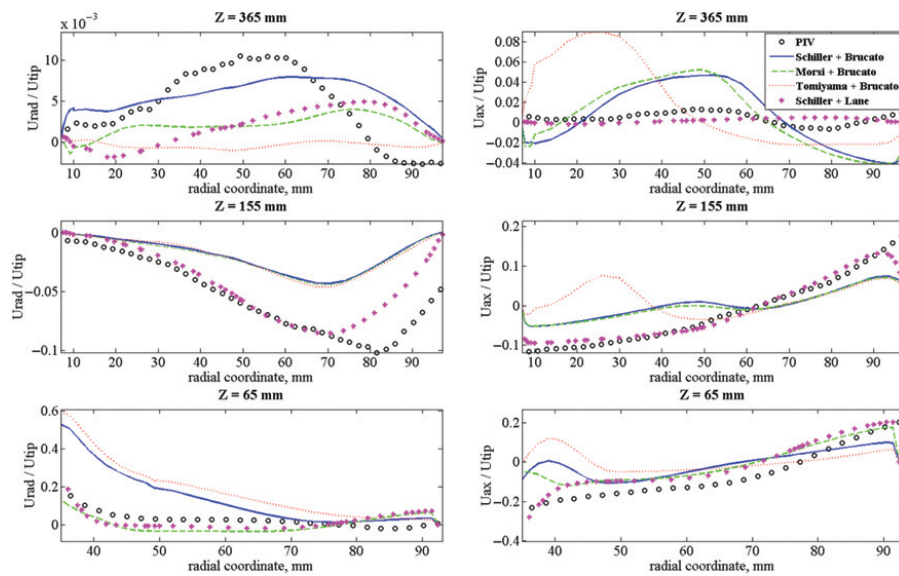


Figure 8: Comparison of liquid velocity components for gas-liquid flow modelling with different drag models at 0.5 L/min gas flow rate.

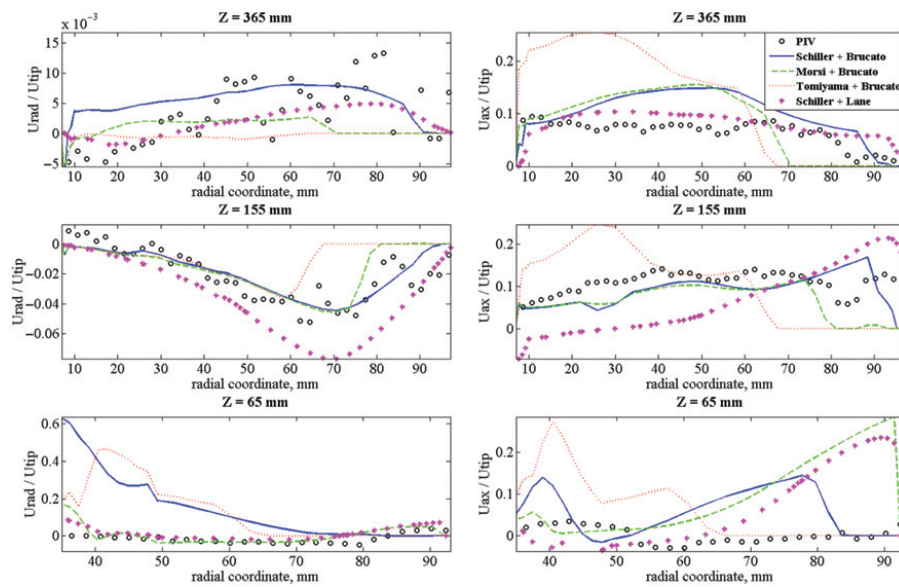


Figure 9: Comparison of gas velocity components for gas-liquid flow modelling with different drag models at 0.5 L/min gas flow rate.

experimental data reveals a similar trend to that found in published literature (Lane, Schwarz, and Evans 2005; Karimi et al. 2012) but contradicts Khopkar and Ranade (2006), where the authors estimated Lane's formulation in a 2D model of "flow through regularly arranged cylindrical objects" and discarded it before carrying out stirred tank simulations in 3D.

#### 4.2.3 Drag force vs non-drag forces

Many researchers have presented that drag force is determinant in multiphase flow and that non-drag forces have minor influence on gas holdup and consequently on the flow (Gimbun, Rielly, and Nagy 2008; Karimi et al. 2012; Sajjadi et al. 2012; Joshi et al. 2011). This work evaluated the cumulative effect of drag, lift, wall lubrication and turbulence dispersion forces on the multiphase hydrodynamics. Results are presented as velocity comparison profiles in Figures 10 and 11. Similar to the published literature, the influence of non-drag forces is found to be minimal. The analysis required considerable computational effort and significant convergence problems were found. It should be noted that available non-drag forces models were

developed based on experimental results conducted in tube flow or bubble columns, where the factor of turbulence and drag force is much less.

#### 4.2.4 Qualitative analysis for gas-liquid mixing modelling

Simulations using the Schiller-Naumann drag force model with Lane's turbulence modification were made for two flow rates, 0.5 L/min and 1 L/min. Qualitative analysis of per phase velocity contours against PIV data is presented in Figure 12. The general similarity of the overall velocity contours can be seen in comparison of the simulated and experimental results for the two gas flow rates. It is important to mention that the reactor has an aspect ratio of 2, which complicates modelling of the top part of the tank. There are several possible reasons for the large deviation in the profiles at 365 mm. In the turbulence model formulation, the velocity components are predicted satisfactorily in relative proximity to the source of the energy, which is an impeller in a stirred vessel. The high aspect ratio of the reactor produces a secondary loop in the mixing pattern above the impeller, as is illustrated in Figure 1, especially when

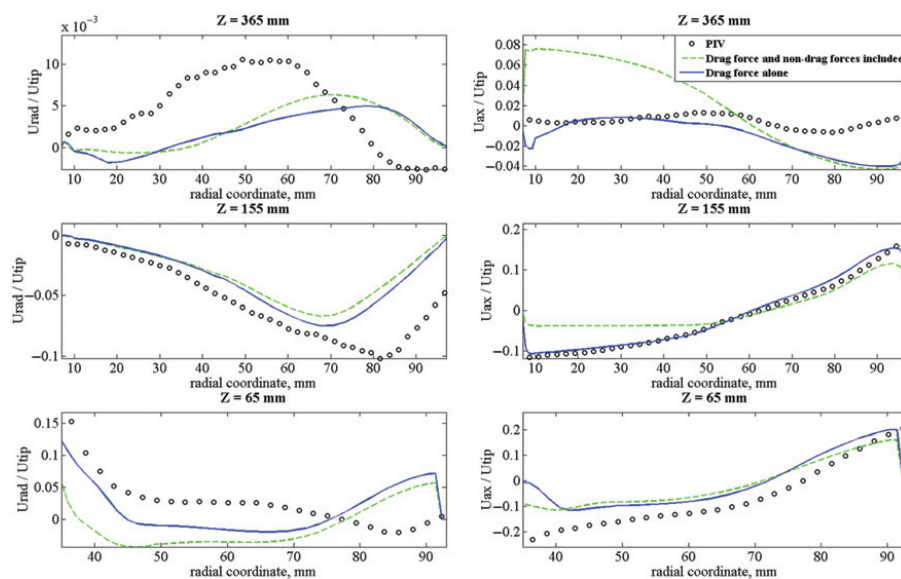


**Figure 10:** Comparison of liquid velocity components for gas-liquid flow modelled with drag force alone and with non-drag forces included at 0.5 L/min gas flow rate.



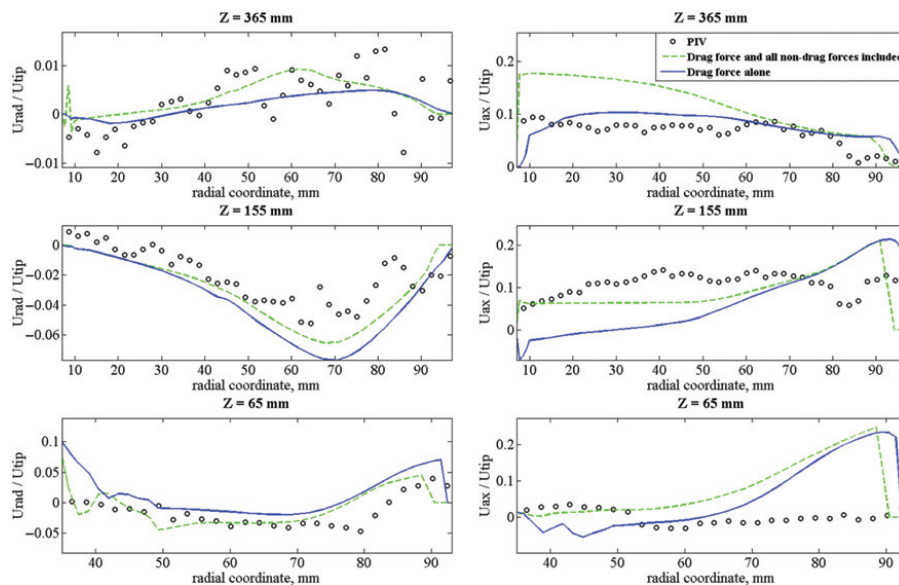


**Figure 11:** Comparison of gas velocity components for gas-liquid flow modelled with drag force alone and with non-drag forces included at 0.5 L/min gas flow rate.

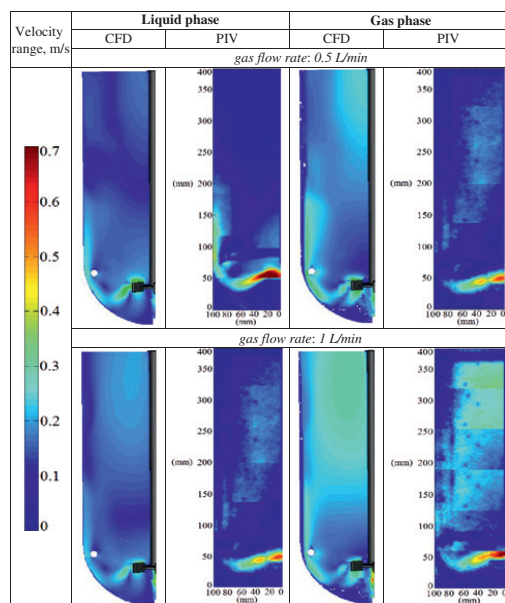


**Figure 12:** Validation of the stirred tank CFD modelling by comparison of the overall velocity contours.

the gas phase is introduced (Figure 13). Even a slight shift of this loop may change the velocity components along the profiles sampled. Another reason for poor predictions in the region close to the surface is the absence of a free surface model. A simple boundary condition as a pressure outlet with a specified back-flow-volume-fraction of 0 is not fully adequate for such complex phenomena, and it does not take movement of the free surface and surface bubbles breakage into account.

A comparison of the liquid phase profiles of the single phase and two-phase mixing at different flow rates is given in Figures 13 and 14. The influence of the gas phase on the flow hydrodynamics of the primary phase can be clearly seen. At 65 mm, in proximity to the stirrer, liquid phase flow dominates, and it is not affected by the gas phase flow. At the same time, the rising gas phase pushes the flow upwards and towards the shaft, promoting the creation of the first circular zone above the impeller. The hindering effect of the drag force of bubbles on the liquid can be seen from the 155 and 365 mm profiles. Starting from a slight change of water velocity in the 155 mm profile, the drag force changes the flow dramatically in the 365 mm profile.

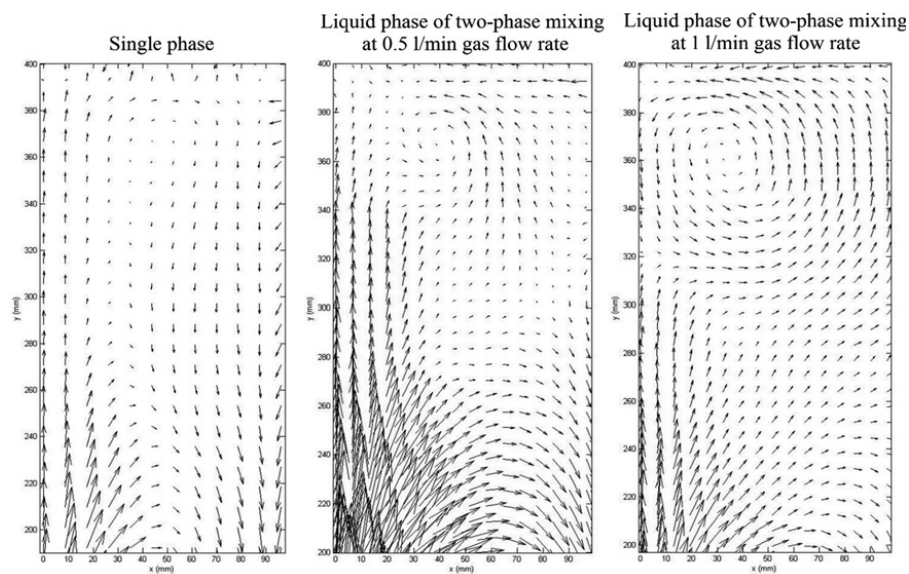


Figure 13: PIV velocity vector contours at three gas flow rates showing the formation of a secondary circulation loop when gas is introduced.

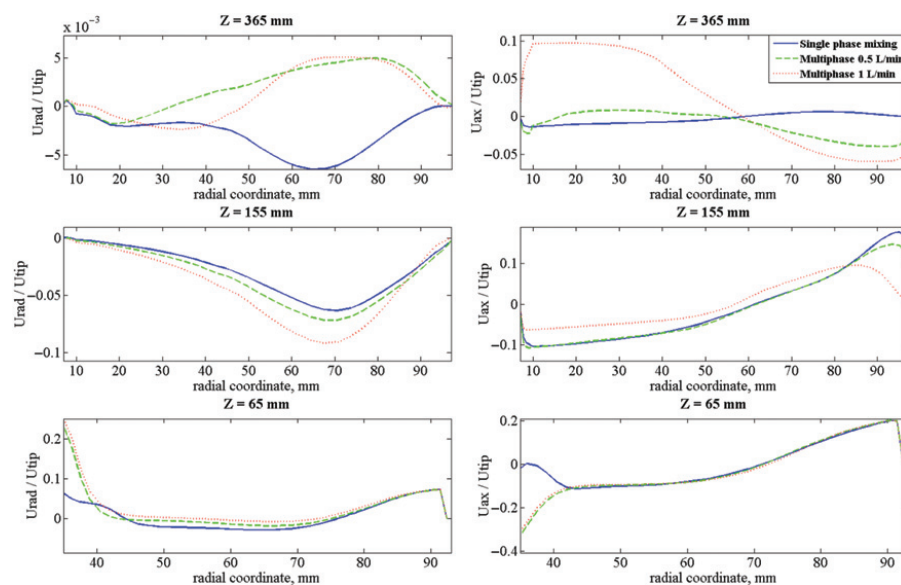


Figure 14: Comparison of the simulated liquid phase velocities at three gas flow rates.

## 5 Conclusions

Gas-liquid flow in a stirred round-bottom reactor of aspect ratio 2 equipped with a Rushton turbine was simulated by commercial CFD software and validated versus unique experimental data from Particle Image Velocimetry. The model is extremely important for stirred tanks of such construction designed to be operated under pressure. The single and multiphase simulations were verified separately. Model validation was carried out by comparing velocity field contours and extracted radial profiles of velocity vector components representing the three main loops in the mixing pattern of the vessel. Three commonly used RANS models were tested for single phase mixing, and their performance was evaluated based on comparison of the profiles of velocity components and the energy balance. Of the RANS models considered, the  $k$ - $\varepsilon$  model was found to be the most accurate and most suitable for multiphase modelling. Gas-liquid flow was implemented in the simulations and popular models for the drag force coefficient were compared against experimental measurements. Comparison of the profiles showed that the Schiller-Naumann drag force model in conjunction with Lane's turbulence modification factor gave the most accurate results. The effect of non-drag forces was also analyzed. It was seen that the inclusion of lift, wall lubrication and turbulence dissipation forces did not result in significant improvement in the simulation results. The effect of the gas on the liquid hydrodynamics was evaluated based on the data acquired. The generally good agreement between the experimental and simulation results illustrates the potential of CFD in stirred reactor modelling of gas-liquid mixing.

## Notation

Symbols	Meaning	Units
$a_i$	Coefficient	–
A	Total area of impeller surface	$m^2$
C	Coefficient	–
$C_D$	Drag coefficient	–
$C_v$	Added mass coefficient	–
$C_{ij}$	Transport by convection	–
d	Secondary phase particle diameter	m
$D_{ij}$	Transport by diffusion	$m^2/s^2$
$E_0$	Eötvös number	–
$\bar{F}$	Force	N
g	Gravity acceleration	$m/s^2$
H	Liquid height	m

$K_{pq}$	Interphase exchange coefficient	–
m	Momentum	N m
N	Number of elements	–
n	Impeller speed	rps
p	Pressure	Pa
p	Order of discretization scheme	–
$P_i$	Power input/dissipated	W
$P_{ij}$	Rate of production of shear stress	$m^2/s^2$
Re	Relative Reynolds number	–
T	Reactor diameter	m
$T_L$	Integral time scale of turbulence	s
t	Time	s
$\bar{u}$	Average velocity	m/s
$\bar{u}$	Velocity vector	m/s
$\overline{u'_i u'_j}$	Shear stress	$m^2/s^2$
V	Reactor volume	$m^3$
$\omega$	Specific dissipation rate	1/s

Greek letters	Meaning	Units
$\alpha$	Phase fraction/constant	–
$C_\mu$	Model constant in the standard k- $\varepsilon$	–
$\varepsilon$	Turbulence energy dissipation rate	$m^2/s^3$
$\varepsilon_{ij}$	Turbulence energy dissipation rate	$m^2/s^3$
$\sigma$	Shear stress	Pa
k	Turbulence energy	J
$\lambda$	Kolmogorov length	m
$\eta$	Modification factor	–
$\rho$	Phase density	$kg/m^3$
$\tau$	Torque	N m
$\tau_p$	Particle relaxation time	s
$\mu$	Dynamic viscosity	Pa s
$\mu_t$	Eddy viscosity	Pa s
$\Omega_{ij}$	Transport due to rotation	$m^2/s^2$
$\Pi_{ij}$	Transport due to turbulence pressure – strain interactions	$m^2/s^2$
$\delta_{ij}$	Kronecker's Delta	–
$\phi_i$	Predicted node value of simulation	–

Acronyms	Transcript
CCD	Charge-coupled device
CFD	Computation fluid dynamics
HWA	Hot wire anemometry
IBC	Impeller boundary conditions
LDA	Laser Doppler anemometry
LES	Large Eddy Simulation
MRF	Multiple reference frame
Nd:Yag	Neodymium-doped yttrium aluminum garnet
PBE	Population balance equation model
PIV	Particle image velocimetry
RANS	Reynolds-averaged Navier-Stokes equation
RSM	Reynolds stress equation turbulence model
SIMPLE	Semi-Implicit method for pressure linked equations
SST	Shear stress transport turbulence model
QMOM	Quadrature-based moment methods for kinetics-based flow models
QUICK	Quadratic upwind interpolation for convective kinetics



**Acknowledgements:** The authors are grateful to the Graduate School of Chemical Engineering, an initiative of the Ministry of Education of Finland and the Academy of Finland, for active supervision and financial support.

## References

1. Azargoshasb, H., Mousavi, S.M., Jamialahmadi, O., Shojasodati, S.A., Mousavi, S.B., 2016. Experiments and a three-phase computational fluid dynamics, CFD simulation coupled with population balance equations of a stirred tank bioreactor for high cell density cultivation. *The Canadian Journal of Chemical Engineering* 94(1), 20–32.
2. Bai, B., Wang, Y., Armenante, P.M., 2010. Velocity profiles and shear strain rate variability in the USP dissolution testing apparatus 2 at different impeller agitation speeds. *International Journal of Pharmaceutics* 403, 1–14.
3. Bakke, A., Van den Akker, H.E.A.A., 1994. Computational model for gas-liquid flow in stirred vessel. *Institution of Chemical Engineers* 72(A4), 594–606.
4. Brucato, A., Grisafi, F., Montante, G., 1998. Particle drag coefficients in turbulent fluids. *Chemical Engineering Science* 53(18), 3295–3314.
5. Burns, A.D.B., Frank, T., Hamill, I., Shi, J.M., 2004. The Favre Averaged Drag Model for turbulent dispersion in Eulerian multi-phase flows. *Fifth International Conference on Multiphase Flow*, Yokohama, Japan.
6. Celik, I.B., Ghia, U., Roach, P.J., Freitas, C.J., Coleman, H., Raad, P.E., 2008. Procedure for estimation and reporting of uncertainty due to discretization in CFD applications. *Journal of Fluids Engineering* 130(7), 78001–78005.
7. Chmielewski, M., Gieras, M., 2013. Three-zonal wall function for  $k-\epsilon$  turbulence models. *Computational Methods in Science and Technology* 19(2), 107–114.
8. Deen, N.G., Solberg, T., Hjertager, B.H., 2002. Flow generated by an aerated Rushton turbine: Two-phase PIV experiments and numerical simulations. *Canadian Journal of Chemical Engineering* 80, 638–652.
9. Ducci, A., Yiannakakis, M., 2005. Direct determination of energy dissipation in stirred vessels with two-point LDA. *American Institute of Chemical Engineers Journal* 51(8), 2133–2149.
10. Gelves, R., Benavides, A., Quintero, J.C., 2013. CFD prediction of hydrodynamic behavior in the scale up of a stirred tank reactor for aerobic processes. *Ingeniare Revista Chilena de Ingenieria* 21, 347–361.
11. Gimbin, J., Rielly, C.D., Nagy, Z.K., 2008. Modelling of mass transfer in gas-liquid stirred tanks agitated by Rushton turbine and CD-6 impeller: A scale-up study. *Chemical Engineering Research and Design* 87(4), 437–451.
12. Gosman, A.D.C., Lekakou, C., Politis, S., Issa, I.R., Looney, M. K., 1992. Multidimensional modelling of turbulent two-phase flows in stirred vessels. *American Institute of Chemical Engineers* 38.
13. Harvey, P.S., Greaves, M., 1982. Turbulent flow in an agitated vessel. A predictive model. *Transactions of the Institution of Chemical Engineers* 60(4), 195–200.
14. Hinze, J.O., 1975. *Turbulence*, McGraw-Hill Publishing Co, New York.
15. [http://www.engineeringtoolbox.com/water-surface-tension-d\\_597.html](http://www.engineeringtoolbox.com/water-surface-tension-d_597.html) cited 23.01.2015
16. Huang, W., Li, K., 2013. CFD simulation of flows in stirred tank reactors. *Nuclear Reactor Thermal Hydraulics and Other Applications*. InTech, Chapter 5.
17. Ishii, M., Zuber, N., 1979. Drag coefficient and relative velocity in bubbly, droplet or particulate flows. *American Institute of Chemical Engineers Journal* 25, 843–855.
18. Issa, R.I., Gosman, A.D., 1981. The computation of three-dimensional turbulent two-phase flows in mixer vessels. *2nd International Conference of Numerical Methods in Laminar and Turbulent Flow*, 829.
19. Jensen, K.D., 2004. Flow measurements. *Journal of the Brazilian Society of Mechanical Science & Engineering* XXVI(4), 400–419.
20. Joshi, J.B., Nere, N.K., Rane, C.V., Murthy, B.N., Mathpati, C.S., Patwardhan, A.W., Ranade, V.V., 2011. CFD simulation of stirred tanks: Comparison of turbulence models. Part I: radial flow impellers. *Canadian Journal of Chemical Engineering* 89, 23–82.
21. Joshi, J.B., Nere, N.K., Rane, C.V., Murthy, B.N., Mathpati, C.S., Patwardhan, A.W., Ranade, V.V., 2011. CFD simulation of stirred tanks: Comparison of turbulence models. Part II: axial flow impellers, multiphase impellers and multiphase dispersions. *Canadian Journal of Chemical Engineering* 89, 754–816.
22. Kalal, Z., Jahoda, M., Fort, I., 2014. CFD prediction of gas-liquid flow in an aerated stirred vessel using the population balance model. *Chemical and Process Engineering* 35(1), 55–73.
23. Kalitzin, G., Medic, G., Iaccarino, G., Durbin, P., 2005. Near-wall behavior of RANS turbulence models and implications for wall functions. *Journal of Computational Physics* 204, 265–291.
24. Karimi, M., Akdogan, G., Dellimore, K.H., Bradshaw, S.M., 2012. Comparison of different drag coefficient correlations in the CFD modelling of a laboratory-scale Rushton-turbine flotation tank. *Ninth International Conference on CFD in the Minerals and Process Industries CSIRO*, Melbourne, Australia.
25. Khopkar, A., Aubin, J., Rubio-Atoche, C., Xuereb, C., Le Sauze, N., Bertrand, J., Ranade, V.V., 2004. Flow Generated by Radial Flow Impellers: PIV Measurements and CFD Simulations. *International Journal of Chemical Reactor Engineering* 2(14), 1–14.
26. Khopkar, A.V., Ranade, V.V., 2006. CFD simulation of gas-liquid stirred vessel: VC, S33 and L33 flow regimes. *American Institute of Chemical Engineers* 52(5), 1654–1672.
27. Laakkonen, M., Moilanen, P., Alopaeus, V., Aittamaa, J., 2005. Local bubble size distributions, gas-liquid interfacial area and gas holdups in stirred vessel with particle image velocimetry. *Chemical Engineering Journal* 109, 37–47.
28. Lane, G.L., Koh, P.T.L., 1997. CFD simulation of a Rushton turbine in a baffled tank. *International Conference on CFD in Mineral and Metal Processing and Power Generation*, 377–385.
29. Lane, G.L., Schwarz, M.P., Evans, G.M., 2000. Modelling of the interaction between gas and liquid in stirred vessels, *10th European Conference on Mixing*, 197–204.
30. Lane, G.L., Schwarz, M.P., Evans, G.M., 2005. Numerical modelling of gas-liquid flow in stirred tanks. *Chemical Engineering Science* 60, 2203–2214.
31. Linek, V., Kordac, M., Fújasová, M., Moucha, T., 2004. Gas-liquid mass transfer coefficient in stirred tanks interpreted

- through models of idealized eddy structure of turbulence in the bubble vicinity. *Chemical Engineering Science* 43, 1511–1517.
32. Menter, F.R., 1993. Zonal two equation  $k-\omega$  turbulence models for aerodynamic flows. *AIAA Paper*, 93–2906.
  33. Moilanen, P., 2009. Modelling Gas-Liquid Flow and Local Mass Transfer in Stirred Tanks, Doctoral thesis. Espoo: Helsinki University of Technology, Chapter 2, 4.
  34. Morchain, J., Gabelle, J., Cockx, A., 2014. A coupled population balance model and CFD approach for the simulation of mixing issues in lab-scale and industrial bioreactors. *American Institute of Chemical Engineers* 60(1), 27–40.
  35. Morsi, S.A., Alexander, A.J., 1972. An investigation of particle trajectories in two-phase flow systems. *Journal of Fluid Mechanics* 55(2), 193–208.
  36. Morud, K.E., Hjertager, B.H., 1996. LDA measurements and CFD modelling of gas-liquid flow in a stirred vessel. *Chemical Engineering Science* 51, 233–249.
  37. Moucha, T., Linek, V., Prokopova, E., 2003. Gas hold-up, mixing time and gas-liquid volumetric mass transfer coefficient of various multiple-impeller configurations: Rushton turbine, pitched blade and techmix impeller and their combinations. *Chemical Engineering Science* 58, 1839–1846.
  38. Saffman, P.G., 1965. The lift on a small sphere in a slow shear flow. *Journal of Fluid Mechanics* 22, 385–400.
  39. Sajjadi, B., Raman, A.A.A., Ibrahim, S., Shah, R.S.S.R.E., 2012. Review on gas-liquid mixing analysis in multiscale stirred vessel using CFD. *Reviews in Chemical Engineering* 28, 171–189.
  40. Scargiali, F., D'Orazio, A., Grisafi, F., Brucato, A., 2007. Modelling and simulation of gas-liquid hydrodynamics in mechanically stirred tanks. *Institution of Chemical Engineers, Part A, Chemical Engineering Research and Design* 85(A5), 647–653.
  41. Schiller, L., Naumann, Z., 1935. A Drag Coefficient Correlation. *Z. Ver. Deutsch. Ing.* 77–318.
  42. Shih, T.H., Liou, W.W., Shabbir, A., Yang, Z., Zhu, J., 1995. A new  $k-\epsilon$  eddy viscosity model for high Reynolds number turbulent flows – model development and validation. *Computers Fluids* 24(3), 227–238.
  43. Sun, H., Mao, Z.S., Yu, G., 2006. Experimental and numerical study of gas hold-up in surface aerated stirred tanks. *Chemical Engineering Science* 61, 4098–4110.
  44. Takamasa, T., Tomiyama, A., 1999. Three-dimensional gas-liquid two-phase bubbly flow in a C-shaped tube. *Ninth International Topical Meeting on Nuclear Reactor Thermal Hydraulics, NURETH-9*. San Francisco, USA,
  45. Tatterson, G.B., 1991. *Fluid Mixing and Gas Dispersion in Agitated Tanks*, McGraw-Hill, Inc., New York, Chapter 1.
  46. Tomiyama, A., 1998. Struggle with computational bubble dynamics. *Third International Conference on Multiphase Flow*, Lyon, France.
  47. Venneker, B.C.H., Derksen, J.J., Van den Akker, H.E.A., 2002. Population balance modelling of aerated stirred vessels based on CFD. *American Institute of Chemical Engineers* 48, 673–685.
  48. Vivek, V.R., 2002. CFD predictions of flow near impeller blades in baffled stirred vessels: Assessment of computational snapshot approach. *Chemical Engineering Communications* 189, 895–922.
  49. Wallin, S., Johansson, A.V., 2000. An explicit algebraic Reynolds stress model for incompressible and compressible turbulent flows. *Journal of Fluid Mechanics* 403, 89–132.
  50. Wang, H., Zhai, Z., 2012. Analyzing grid independency and numerical viscosity of computational fluid dynamics for indoor environment applications. *Building and Environment Journal* 52, 107–118.
  51. Wu, H., Patterson, G.K., 1989. Laser-Doppler measurements of turbulent flow parameters in a stirred mixer. *Chemical Engineering Science* 44(10), 2207–2221.
  52. Xinhong, L., Yuyun, B., Zhipeng, L.L., Zhengming, G., 2010. Analysis of turbulence structure in the stirred tank with a deep hollow blade disc turbine by time-resolved PIV. *Fluid Flow and Transport Phenomena* 18(4), 588–599.
  53. Zhang, Q., Young, Y., Mao, Z., Yang, C., Zhao, C., 2009. Experimental determination and numerical simulation of mixing time in a gas-liquid stirred tank. *Chemical Engineering Science* 64, 2926–2933.



## **Publication II**

Gradov, D. V., Laari, A., and Koiranen, T.

**Influence of the relative position of impeller and baffles in Multiple Reference  
Frame simulation of gas-liquid mixing in stirred tank**

Reprinted with permission from

*International Journal of Chemical Engineering and Applications*

Vol. 18(1), pp. 53-60, 2017

© IACSIT



# Influence of the relative position of impeller and baffles in Multiple Reference Frame simulation of gas-liquid mixing in stirred tank

D. V. Gradov, A. Laari and T. Koironen

**Abstract**— In this paper analysis is carried out on the response of hydrodynamics to the relative position of stirrer and baffles when Multiple Reference Frame (MRF) technique is used to simulate a mixing tank of single and multiphase systems. A typical stirred reactor equipped with four baffles and a six-blade Rushton turbine is studied. Operational conditions of constant speed (5 rps) and  $2.653 \cdot 10^{-4}$  m/s gas superficial velocity with constant bubble size (1 mm) were applied. The simulations were performed in ANSYS Workbench (FLUENT) 16.0 with four different angles of impeller blade with regard to baffles. The results were averaged over two utmost and all four impeller blade positions and validated against experimental data, produced by means of Particle Image Velocimetry. Comparison of the simulated and experimental results was executed using profiles of velocity components along sampled lines, representing various zones in the vessel. The impeller angle of rotation with respect to the position of baffles was found to contribute to the overall reactor hydrodynamics especially in multiphase systems. Averaging of the simulation results over all impeller positions was shown to enhance the accuracy of the simulated results of single phase and multiphase mixing hydrodynamics.

**Index Terms**— stirred tank, multiphase, CFD, PIV, validation

## I. INTRODUCTION

Stirred tank is one of the key unit operations widely utilized in chemical industry. Its performance has direct impact on production quality, yield, and therefore overall effectiveness. That is why it is extremely important to match a certain chemical reaction to a suitable reactor and to operate it under optimal conditions. It is well known that chemical process features and performance can be forecasted and its output estimated via mathematic modeling.

Chemical reaction modeling often employs the assumption of the media to be perfectly mixed. In order to assess the hydrodynamics within a reactor it is possible to take into account different geometries and scales of operation using Computational Fluid Dynamics (CFD). The usage of Reynolds-averaged Navier-Stokes (RANS) equations is a compromise between the needs of engineering, computational time and resources available.

Since 80's stirred tank modeling has been studied in literature by many research groups such as Issa and Gosman, Harvey and Greaves, Lane et al., Vivek et al., Laakkonen et al., Bai et al., and Huang et al among many others [1] – [7]. Liquid mixing is described numerically mainly via two-equation models of RANS family due to affordable computational load. For this reason, the Large Eddy Simulation approach has fewer applications in multiphase mixing regardless the fact that it shows higher accuracy compared to experimental data. Aubin et al. [8] and Vlachakis [9] claim that the impeller interaction with baffles has a periodic character that allows to assume the stirred reactor to be in a steady state. Two main approaches to treat the impeller geometry are generally used when stirred tank is modeled. These are the Sliding Mesh (SM) and the Multiple Reference Frame approaches. The MRF simulation aids in saving time

without losses in accuracy compared to transient SM approach where the actual geometry of agitator is moving. According to Marshal and Bakker in "Computational Fluid Mixing" [10] mixing tank simulations with the "frozen rotor" (MRF) method using the outermost impeller positions and averaging the results should be carried out to produce accurate results. This suggestion has not been usually followed in the published literature. Therefore, the influence of the impeller blade position relative to baffles on the overall hydrodynamics in a vessel equipped with four baffles is studied in this work and evaluated qualitatively and numerically by averaging the simulation data.

There are several experimental methods for validating numerical simulation data of hydrodynamics. They could be grouped as intrusive methods, which are mainly based on Constant Temperature Anemometry, for example Hot Wire Anemometry (HWA) [11], and non-intrusive ones, such as Laser Doppler Velocimetry (LDA) [12] and Particle Image Velocimetry (PIV) [13]. The PIV technique provides velocity vector fields in two-dimensional space that is used in this study.

The present paper is dedicated to baffle-impeller interaction assessment and results averaging procedure for stirred reactor when the Multiple Reference Frame method is applied. The single and multiphase simulation results of averaging are validated against experimental data obtained by means of PIV.

## II. MATERIALS AND METHODS

### A. Object of Study

A round bottom stirred reactor equipped with baffles and a Rushton turbine is the object of study in the current research. The dimensions of the reactor are presented in Table I. The vessel is made of glass and sealed in a plexiglass box for conducting PIV tests. The clearance of the six-blade impeller from the tank bottom was kept the same as its diameter. The gas inlet sparger was mounted in the very center of the vessel bottom. The operational conditions were 300 rpm of rotational speed and 0.12 vvm for gas flow rate. In order to examine the influence of the blades positioning far from the impeller, the liquid height was twice the tank diameter. The schematic view of the reactor together with velocity profile sampling strategy is illustrated in Fig. 1.

### B. Validation Technique

Particle Image Velocimetry is widely used for fluid flow study and its results are frequently used to validate simulation results [1], [9], [11], [14]. It produces instantaneous velocity vector field in 2D or 3D in case of stereographic PIV. By means of fast laser pulsing it is possible to track slight shift of submerged light tracers within an interrogation window of interest. A classical set-up includes cameras installed perpendicular towards a dense laser sheet produced by Nd:Yag laser. In the current research, two CCD cameras with

a resolution of 1600 pixels  $\times$  1200 pixels were used. That allows capturing 2D velocity fields from the whole reactor with the resolution of 188 vectors  $\times$  189 vectors. The main requirements for the tracer particles are that they follow the media without disturbing the flow and reflect intensive light on certain wavelengths. It is also necessary to take into account that the studied reactor has many strongly reflecting parts which prevents the use of standard hollow glass PIV tracer particles. Therefore, 20-50  $\mu$ m particles made of melamine resin covered with fluorescent dye (Rhodamine B) were applied. Their usage in water flow tests has the benefit that a uniform dark background can be obtained with large camera aperture installing wave length filters on the cameras. To detect the movement of gas phase, tests were carried out with only grey filters mounted on the cameras to decrease the reflected light intensity from bubbles to protect the camera.

TABLE I: DIMENSIONS OF THE REACTOR

Reactor dimension	Value, mm
Tank diameter	20
Liquid height	40
Impeller diameter	70
Impeller blade width	15
Impeller clearance	70
Shaft diameter	14
Baffle width	20
Baffle distance from tank wall	5
Sparger height	10
Sparger width	7

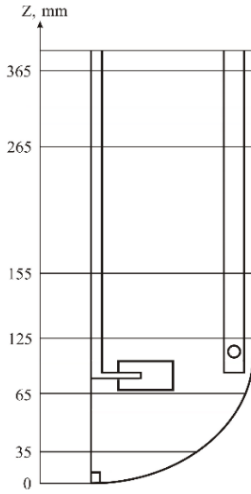


Fig. 1. Mixing reactor and schematic representation of profiles sampling positions

The position of the laser sheet was set to be at a distance of 10 mm in front of a baffle to maximize the area captured in a frame and to eliminate the neighboring baffle from the field of view. Each frame includes half of the reactor from the vessel wall to the agitator shaft in width and 10 cm in height. Therefore, six overlapping frames were taken along the vertical axes in order to capture the whole tank. The

coordinates of the interrogation window were measured to extract the analogue plane from the CFD simulation results. A schematic representation of the PIV set-up is shown in Fig. 2

The detention time between the laser pulses was adjusted individually for each position along the vertical axis so that tracer shift would not exceed the interrogation area when post-processing the data. In total, 500 frames were taken to obtain experimental results at steady state.

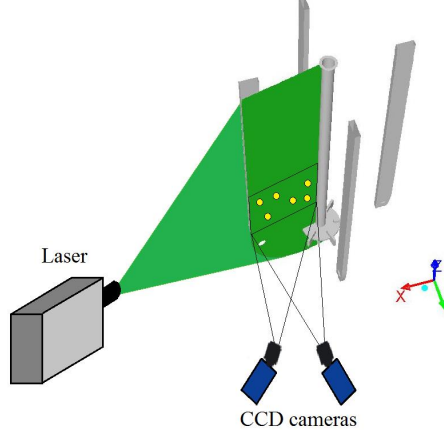


Fig. 2. Conceptual schema of two-phase PIV set-up used in the current work

### C. Simulation Settings

It was decided not to use geometrical symmetry and instead consider complete reactor hydrodynamics to avoid any concerns how the symmetry might affect the overall flow fields. The reactor domain was discretized by structured meshes with a maximum aspect ratio of 30 and high orthogonal quality to reduce numerical errors. Grid independence test carried out over four meshes with increasing resolution. The test showed that there is no sense to use more than 800000 elements because with further increase of mesh density velocity components values stay within 10 % of the normalized root mean square error index (NRMSE) (Eq. 1) that identifies grid difference to be insignificant [15].

$$nrmse = \frac{3}{(n_{fine} / n_{coarse})^p - 1} \sqrt{\frac{\sum_{i=1}^N (\phi_1(i) - \phi_2(i))^2}{\sum_{i=1}^N (\phi_2)^2}} \cdot 100\% \quad (1)$$

$n_{fine}$  and  $n_{coarse}$  are the number of cells in a fine and coarse grids correspondingly,  $p$  represents the order of discretization,  $N$  is the number of samples,  $\phi_1$  and  $\phi_2$  are the predictions on coarse and fine grids accordingly.

Multiphase mixing was simulated in Eulerian-Eulerian model according to which the phases may interpenetrate each other. Five impeller revolutions per second produce fully turbulent flow (24000 Re). The k- $\epsilon$  Realizable model was used for turbulence modeling since it was designed to overcome the difficulties of the Standard k- $\epsilon$  model when rotation and/or swirling are involved via the introduction of turbulence viscosity as a variable instead of being constant [16]. The impeller motion was modelled via the MRF

approach where the fluid in the region surrounding the rotating parts moves around a “frozen” impeller and a shaft. By producing boundary conditions for the interfacing walls between the zones, the motion transfers to the outer stationary zone.

To avoid computational instabilities, mixing of the liquid phase only was simulated first until convergence was reached and then the gas flow rate was activated with a constant bubble size of 1 mm. The reactor top was assigned as pressure outlet with backflow volume fraction of air set to zero, which corresponds to degassing condition. The interphase interaction included only the drag force since the cumulative effect of lift, wall lubrication and turbulence diffusion forces can be considered negligible according to Lane et al. and Scargiali et al. [17], [18]. Scargiali et al. and Brucato et al. [19] showed the superior performance of the Morsi-Alexander drag force in combination with the Brucato modification coefficient included. Originally, the Brucato coefficient was suggested for solid particles being later reduced by two orders of magnitude to adopt it for gas bubbles [14], [19].

Third order differencing QUICK (Quadratic Upwind Interpolation for Convective Kinetics) scheme was used for momentum and turbulence because of its higher accuracy. Coupling of pressure and velocity was performed by using the Semi-Implicit algorithm. The simulations were continued until the residuals of all the variables were lower than  $10^{-4}$ . Two-phase simulations were run until both the convergence and the error in the air mass balance between the inlet and the outlet reached acceptable level of 5 %.

Single phase mixing computation took around 8500 iterations, which corresponds to 14 hours of real time when four cores were involved (Intel(R) Xeon(R) w3565 3.2 GHz and 24 Gb RAM) Multiphase simulations took no more than 18000 iteration and 30 hours of real time.

#### D. Averaging Procedure

The reactor construction and the four baffles against the six blades of Rushton turbine allow positioning the impeller within angles between  $0^\circ$  to  $60^\circ$  with respect to the baffles. The simulations were done at four positions of the impeller  $0^\circ$ ,  $15^\circ$ ,  $30^\circ$ , and  $45^\circ$  correspondingly, as it is depicted in Fig. 3. Then, the velocity profiles representing the different regions of the reactor were sampled from PIV and CFD results and averaged in Matlab over the different combinations of the impeller positions. The resulting data of the single phase and multiphase mixing are plotted versus the PIV tests in Figs. 4 – 10. The major complication in the averaging is to make the data acquisition when the number and the shape of the elements differ as the impeller turns. In this work, all the data correlation was accomplished manually. However, it is recommended that in future automatic CFD tools for averaging should be created.

#### E. Single Phase Averaging Assessment

Before the averaging results are compared to the experimental data, it is interesting to see the velocity component profiles at different positions along the reactor height. The vessel may be split into three regions as follows: the bottom, impeller and reactor upper part regions. The

profiles have been chosen so that all the three parts are tested. The results are gathered in Figs. 4 and 5.

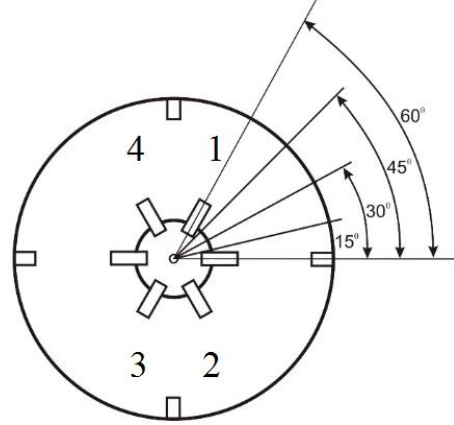


Fig. 3. Impeller positioning diagram

### III. RESULTS

The major difference in the velocity components can be seen at the 35, 65 and 365 mm profiles whereas the 125, 155 and 265 mm ones indicate no dispersion. The rotating zone expectedly produces the highest velocity variation as how in the 125 mm profile. The MRF technique employs averaging at the interface walls before the motion is transferred to the stationary zone. By careful examination of the variation of the velocity components along the sampled profiles, it can be noticed that the biggest deviation is between the angles  $0^\circ$  and  $30^\circ$ , which signify that these two are the extreme impeller positions. In addition, some deviation may be noticed over the distance between the bottom and the top parts of the tank.

The RANS models are known to produce accurate results near the source of energy. In the profiles at 65, 125, 155 mm the simulation results are indeed qualitatively in the best agreement with the experimental ones. The RANS models have difficulties with flow separation and swirling predictions and they are greatly dependent on the domain geometry and grid configuration. The round bottom and the position of the baffles create difficulties for prediction of hydrodynamics in the bottom part, as represented by the 35 mm profile. In the regions that are far from the source of energy, the agreement is very poor.

It is important to know the sufficient number of samples that should be used when averaging the data. Therefore, it was decided to use the two extreme impeller positions, for example  $0^\circ$  and  $30^\circ$ , and all four samples for testing purposes. The outputs are presented in Fig. 6. The biggest deviation can be observed in the close vicinity of the impeller in the rotating zone, which is shown in the 65 mm profile. Therefore, it is recommended to do the averaging of the results over all the four angles of the agitator positions when this particular zone is crucial in the research. What comes to the top and the bottom parts, averaging over all positions is not that necessary and in single phase mixing simulation of the two extreme impeller locations produces similar results.



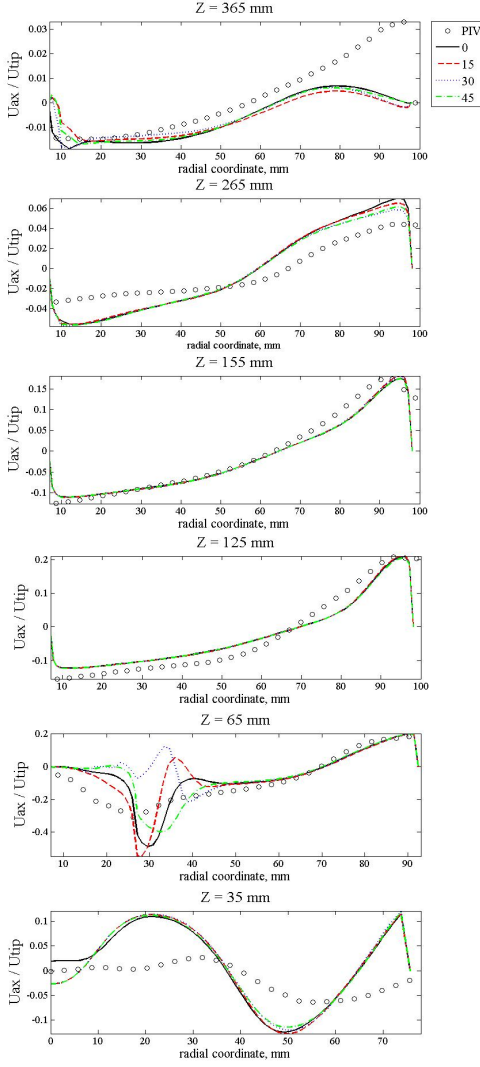


Fig. 4. Comparison of axial velocity profiles at different impeller positions produced by averaged results from CFD and PIV

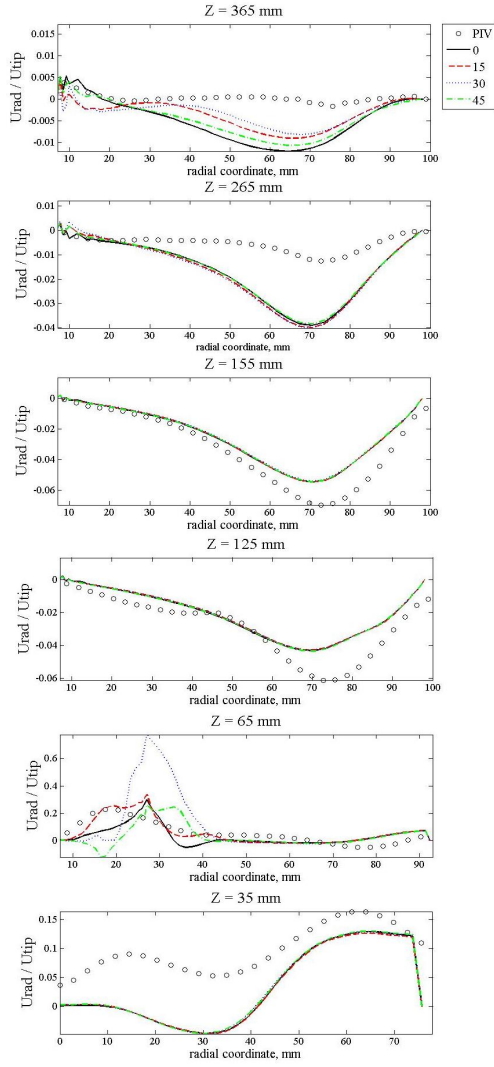


Fig. 5. Comparison of radial velocity profiles at different impeller positions produced by averaged results from CFD and PIV

TABLE II: NORMALIZED ROOT-MEAN-SQUARE DEVIATION OF THE SIMULATIONS RESULTS OF SINGLE PHASE MIXING AGAINST EXPERIMENTAL DATA

Angle of impeller position	Normalized RMS deviation of radial and axial velocity components along the sampled profiles, %											
	35 mm		65 mm		125 mm		155 mm		265 mm		365 mm	
	radial	axial	radial	axial	radial	axial	radial	axial	radial	axial	radial	axial
0°	68.1	194.8	71.1	42.67	26.2	26.0	27.0	20.2	203.5	62.8	609.0	72.3
15°	68.3	202.31	46.6	51.3	26.2	25.2	27.6	19.2	212.5	60.7	428.2	81.3
30°	67.5	201.7	116.6	81.4	26.3	25.6	28.1	19.0	216.3	57.3	383.4	77.3
45°	67.4	194.7	89.9	47.0	25.7	26.1	27.4	20.0	200.6	57.5	531.6	75.7
Averaging over												
0° and 30°	67.9	198.4	76.9	47.3	26.2	25.8	27.5	19.6	209.8	59.7	486.9	78.4
all four angles	67.8	198.2	52.7	32.5	26.1	25.7	27.3	19.5	208.1	59.4	481.0	76.2

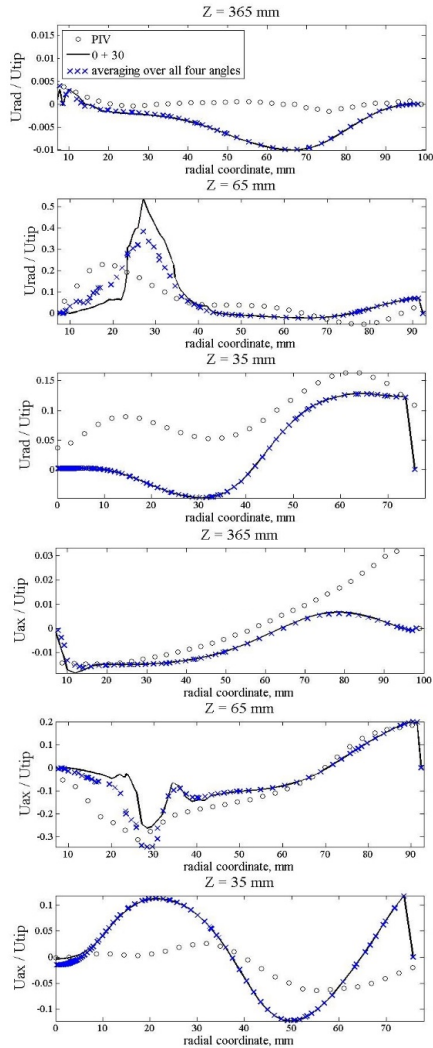


Fig. 6. Axial and radial velocity profiles comparison of the CFD simulations averaged over different impeller positions and the PIV results

Quantitative evaluation of improvement achieved by averaging of simulation results is of great interest and may also give valuable information about how the number of samples taken into account may improve the simulation results in comparison to experimental data. The quantitative analysis for single phase is presented in Table II. The normalized root-mean-square error shows the deviation of the simulation results from the experimental data. It shows the influence of the impeller position on the overall hydrodynamics in the reactor especially in the regions around the stirrer and in the top of the vessel near the gas-liquid surface. The influence would not be that much if the aspect ratio of the vessel would not be high which is clear by considering the profiles at 155 and 265 mm.

Benefits of the averaging procedure can be estimated from Table II. Obviously, a decreasing tendency in deviation can be tracked as more impeller angles are involved. The biggest improvement can be seen at the profiles 65 and 365 mm where the simulation results deviate the most. As it is shown in Figure 3, the six-blade-impeller vs. four-baffle system repeats itself after every  $60^\circ$  of rotation. Thus,  $15^\circ$  plane of rotation in sector 1 where the deviation is at minimum (46.6 %) corresponds to the  $30^\circ$  plane of blade location in sector 4 where the deviation is at maximum (116.6 %).

Nevertheless, averaging of the results at the two extreme positions increases accuracy significantly. As more angles are involved, the deviation from experimental data reduces further but not drastically. Therefore, it is reasonable to perform at least two simulations of stirrer tank with the impeller position at the two utmost locations in order to have more accurate hydrodynamics of single phase mixing.

#### A. Multiphase Averaging Assessment

The averaging procedure is of particular interest and importance for multiphase systems. Gas-liquid mixing was considered next and the influence of the impeller position relative to the baffles was studied by comparing the velocity profiles at different locations. It must be noted that multiphase mixing is a complicated phenomenon that includes multiple counter acting forces and the simulation of its hydrodynamics has greater uncertainty when compared to experimental results than that of the single phase.

The profiles that are shown below in Figs. 7 – 10 represent the complete reactor from the top to bottom and from the vessel center, or agitator shaft, to the tank wall. The whole reactor lay-out is easily visualized in the presented manner when looking at the profiles and assessing qualitatively the hydrodynamics in the reactor. Since the multiphase system is complicated with interfacial forces and turbulence computed per phase, even a slight change in the impeller blade position gives deviation in the velocity components in every sampled profile. As in the case of the single phase, the biggest variation is observed near the impeller.

One may note that the angle of the agitator with respect to baffles has a bigger effect on the gaseous phase. In the current work, the gas flow rate is rather low and therefore, the primary phase turbulence has great impact on the movement of the secondary phase. Thus, it is important to undertake averaging in order to produce results of higher accuracy.

In addition, it could be expected that at higher gas flow rates gas hydrodynamics should be less dependent on the fluctuations in the liquid flow and therefore, averaging over the two extreme positions for gas phase should be enough. However, the number of impeller positions to be involved in the averaging is dictated by the qualitative evaluation of hydrodynamics (see Table III and Table IV).

Analysis of the root-mean square deviation of multiphase mixing is less straightforward due to the complexity of gas-liquid interaction modeling in fully turbulent flow. And as an outcome, the accuracy raise after averaging procedure is less than in single phase mixing.

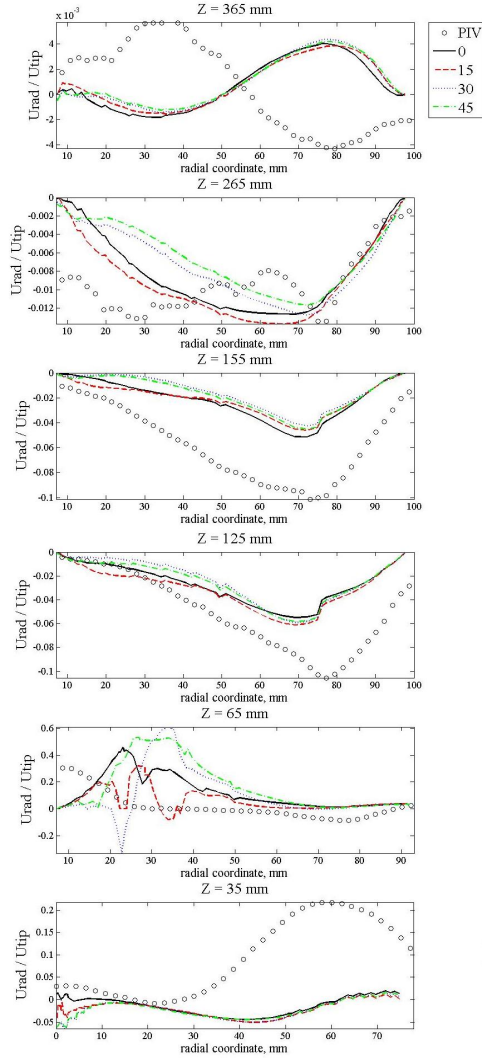


Fig. 7. Radial velocity profiles comparison of the CFD simulations in liquid phase averaged over different impeller positions and the PIV results

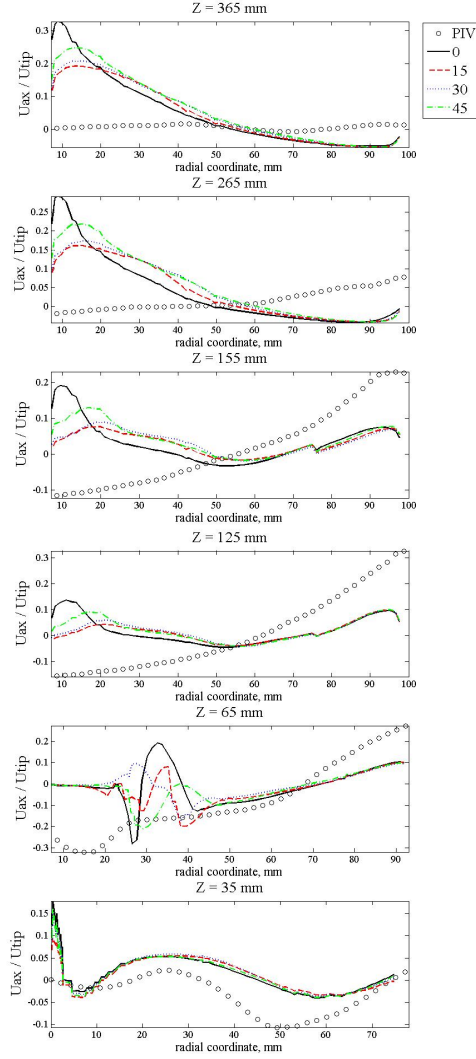


Fig. 8. Axial velocity profiles comparison of the CFD simulations in liquid phase averaged over different impeller positions and the PIV results

TABLE III: NORMALIZED ROOT-MEAN-SQUARE DEVIATION OF THE SIMULATIONS RESULTS OF LIQUID PHASE IN MULTIPHASE MIXING AGAINST EXPERIMENTAL DATA

Angle of impeller position	Normalized RMS deviation of radial and axial velocity components along the sampled profiles, %											
	35 mm		65 mm		125 mm		155 mm		265 mm		365 mm	
	radial	axial	radial	axial	radial	axial	radial	axial	radial	axial	radial	axial
0°	215.7	122.1	71.7	96.7	123.2	111.2	65.5	129.6	39.8	407.3	130.2	1331.5
15°	218.0	111.0	84.4	71.8	136.2	99.1	68.1	117.5	35.0	357.4	130.1	1112.5
30°	223.0	120.4	78.8	73.8	114.1	104.6	72.5	124.2	44.4	377.5	131.3	1171.7
45°	211.8	117.4	70.7	80.7	118.7	111.0	70.4	133.4	50.5	420.0	225.8	206.0
Averaging over												
0° and 30°	218.5	120.1	68.0	73.5	118.2	106.6	68.8	124.9	41.6	385.2	130.6	1235.9
all four angles	216.6	117.4	57.3	71.3	115.6	105.5	68.3	124.5	41.4	385.2	129.8	1102.3

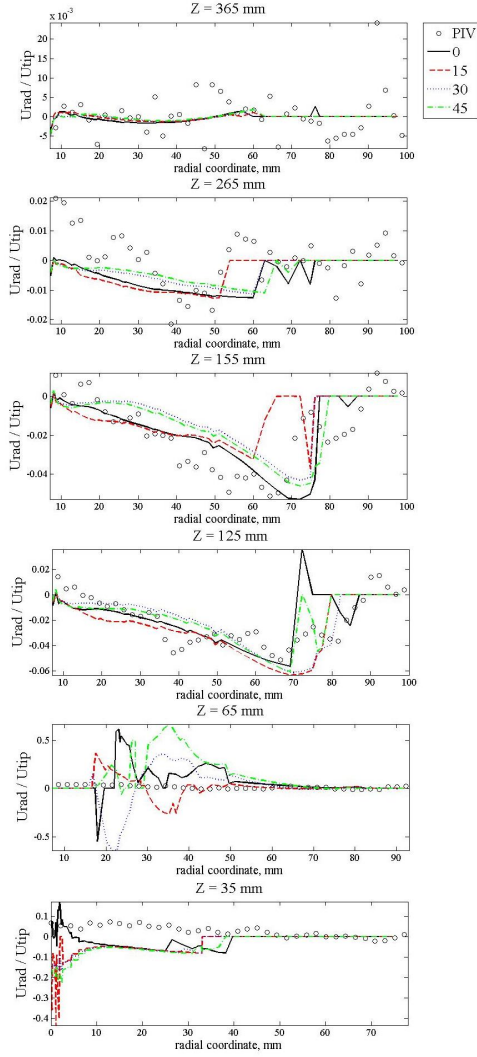


Fig. 9. Radial profiles comparison of the CFD simulations in gas phase averaged over different impeller positions and the PIV results

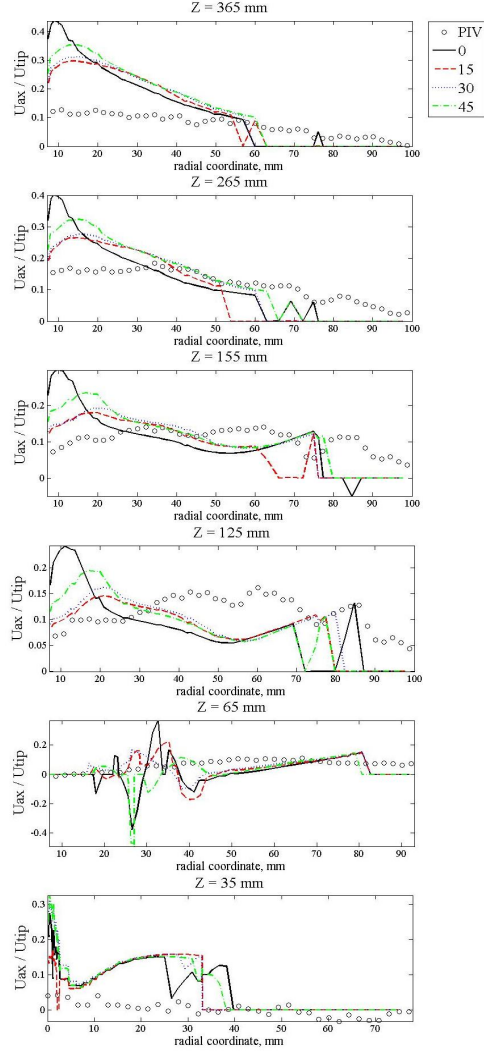


Fig. 10. Axial velocity profiles comparison of the CFD simulations in gas phase averaged over different impeller positions and the PIV results

TABLE IV: NORMALIZED ROOT-MEAN-SQUARE DEVIATION OF THE SIMULATIONS RESULTS OF GAS PHASE IN MULTIPHASE MIXING AGAINST EXPERIMENTAL DATA

Angle of impeller position	Normalized RMS deviation of radial and axial velocity components along the sampled profiles, %											
	35 mm		65 mm		125 mm		155 mm		265 mm		365 mm	
	radial	axial	radial	axial	radial	axial	radial	axial	radial	axial	radial	axial
0°	107.8	112.7	580.4	472.4	44.6	105.6	34.8	97.0	134.5	91.9	84.8	511.5
15°	110.2	122.4	334.3	394.5	58.9	98.2	38.2	81.8	144.6	79.4	85.1	432.6
30°	109.9	122.9	759.6	329.5	47.7	97.1	39.2	80.5	122.7	75.6	83.7	450.9
45°	109.4	116.8	879.9	356.4	48.7	98.6	36.8	81.9	115.9	76.0	154.5	116.0
Averaging over												
0° and 30°	109.8	119.5	546.4	330.0	48.9	100.1	34.9	86.8	128.2	82.5	84.2	475.9
all four angles	109.3	118.6	427.3	328.9	45.2	98.9	34.1	83.8	128.0	79.6	84.0	455.9

In multiphase mixing qualitative analysis of liquid phase shows higher values for root-mean-square deviations at all profiles taken. Analogously to single phase mixing, the biggest deviation of simulation appears near the impeller and, therefore, averaging is important in that region. Deviations in gas phase are slightly less dependent on impeller position in modeling. The profile at 65 mm is an exception due to the radial flow generated by the mixer is dominant in this case.

The amount of impeller position needed to get improved simulation accuracy is similar to single phase mixing modeling. The larger the number of the stirrer positions taken into account, the higher the accuracy in the results one may achieve. However, improvement in accuracy gradually decreases when more impeller positions are added. Therefore, one should find a compromise between the accuracy needed and the affordable computational time.

#### IV. CONCLUSION

The results in the presented work clearly indicate that the averaging of results improves the accuracy of CFD simulations of single and multiphase mixing in a baffled stirred tank when the “frozen rotor” approach is applied. It was observed that the profiles of the velocity components are various depending on the impeller angle relative to the baffles. Such variation is low for single phase and significantly higher when a secondary gaseous phase is introduced. It was proved that averaging over the two utmost impeller positions improves the simulated results of hydrodynamics. As far as the Rushton turbine is concerned, averaging over four impeller positions produces more accurate results than just over the two extreme stirrer positions. Researchers and engineers, who deal with stirred tank modeling, are advised to execute several simulations with the stirrer turned within the sector where stirrer-blade-baffle interaction appears. Such a sector is dictated by the number of impeller blades relative to the quantity and construction of baffles. The proposed above suggestion is just for modeling of single phase mixing as well as for multiphase mixing. Since the “frozen rotor” technique is widely used in mixing simulations, it makes sense to consider developing automatic or semiautomatic methods and tools for averaging procedure.

#### REFERENCES

- [1] V. R. Vivek, “CFD predictions of flow near impeller blades in baffled stirred vessels: assessment of computational snapshot approach,” *Chemical Engineering Communications*, vol. 189, pp. 895-922, 2002
- [2] B. Bai, Y. Wang, and P. M. Armenante, “Velocity profiles and shear strain rate variability in the USP dissolution testing apparatus 2 at different impeller agitation speeds,” *International Journal of Pharmaceutics*, vol. 403, pp. 1-14, 2010
- [3] W. Huang and K. Li, “CFD simulation of flows in stirred tank reactors,” *Nuclear Reactor Thermal Hydraulics and Other Applications*, InTech, 2013, ch. 5
- [4] R. I. Issa and A. D. Gosman, “The computation of three-dimensional turbulent two-phase flows in mixer vessels,” *2nd International Conference of Numerical Methods in Laminar and Turbulent Flow*, pp. 829, 1981
- [5] P. S. Harvey and M. Greaves, “Turbulent-flow in an agitated vessel.1. A predictive model,” *Transactions of the Institution of Chemical Engineers*, vol. 60(4), pp. 195-200, 1982
- [6] G. L. Lane, M. P. Schwarz and G. M. Evans “Modeling of the Interaction between gas and liquid in stirred vessels,” *10th European Conference on Mixing*, pp. 197-204, 2000
- [7] M. Laakkonen, P. Moilanen, V. Alopaeus and J. Aittamaa, “Local bubble size distributions, gas-liquid interfacial area and gas holdups in stirred vessel with particle image velocimetry,” *Chemical Engineering Journal*, vol. 109, pp. 37-47, 2005
- [8] J. Aubin, S. M. Kresta, J. Bertrand, C. Xuere and D. F. Fletcher, “Alternate Operating Methods for Improving the Performance of a Continuous Stirred Tank Reactor,” *Trans IChemE*, vol. 84, pp. 569-582, 2006
- [9] V. N. Vlachakis, “Turbulent Characteristics in Stirring Vessels: A Numerical Investigation,” M.S. Thesis in Mech. Eng., Blacksburg, Virginia, June 16, 2006
- [10] M. Marshall and A. Bakker, “Computational Fluid Mixing,” Fluent Inc., Lebanon, 2002
- [11] K. D. Jensen, “Flow Measurements,” *Journal of the Brazilian Society of Mechanical Science & Engineering*, Vol. XXVI, No. 4, pp. 400-419, 2004
- [12] H. Wu and G. K. Patterson, “Laser-Doppler measurements of turbulent flow parameters in a stirred mixer,” *Chemical Engineering Science*, vol. 44(10), pp. 2207-2221, 1989
- [13] L. Xinhong, B. Yuyun, L. I. Zhipeng and G. Zhengming, “Analysis of turbulence structure in the stirred tank with a deep hollow blade disc turbine by time-resolved PIV,” *Fluid Flow and Transport Phenomena*, vol. 18(4), pp. 588-599, 2010
- [14] M. Laakkonen, “Development and validation of mass transfer models for the design of agitated gas-liquid reactors” PhD Thesis in Tech., Espoo, Finland, 2006
- [15] H. Wang and Z. Zhai, “Analyzing grid independency and numerical viscosity of computational fluid dynamics for indoor environment applications,” *Building and Environment journal*, vol. 52, pp. 107-118, 2012
- [16] T. H. Shih, W. W. Liou, A. Shabbir, Z. Yang and J. Zhu, “A New k-ε Eddy Viscosity Model for High Reynolds Number Turbulent Flows - Model Development and Validation,” *Computers Fluids*, vol. 24(3), pp. 227-238, 1995
- [17] G. L. Lane, M. P. Schwarz and G. M. Evans, “Modeling of the Interaction between gas and liquid in stirred vessels,” *10th European Conference on Mixing*, pp. 197-204, 2000
- [18] F. Scargiali, A. D’Orazio, F. Grisafi and A. Brucato, “Modeling and simulation of gas-liquid hydrodynamics in mechanically stirred tanks,” *Chemical Engineering Research and Design*, vol. 85(A5), pp. 647-653, 2007
- [19] A. Brucato, F. Grisafi and G. Montante, “Particle drag coefficients in turbulent fluids,” *Chemical Engineering Science*, vol. 53(18), pp. 3295-3314, 1998



**Dmitry Gradov** is a doctoral student at Lappeenranta University of Technology (LUT). He received his first MSc (2010) in mineral processing from Saint-Petersburg State Mining University and second MSc (2011) from LUT in the field of product and process development. He has been a doctoral student since 2012. Current research is related to numerical modeling and experimental study of multiphase hydrodynamics in batch stirred tank.



**Arto Laari** is a research scientist at Lappeenranta University of Technology (LUT). He received his PhD (2005) and the title of Docent (2010) from LUT in the field of product and process development. He has been working as an associate professor in the same department in 2010-2014. His current scientific interests are in the development of sustainable metal leaching processes and in the storage and transformation of renewable energy.



**Tuomas Koironen** is a professor at Lappeenranta University of Technology (LUT). He received his PhD (1998) in Helsinki University of Technology, and the title of Docent (2004) from Lappeenranta University of Technology. After having 12 years industrial experience in pharmaceutical R&D as research scientist, he started the professorship at Lappeenranta University of Technology in 2013. His current scientific and teaching interests are fluid dynamics in chemical engineering applications, liquid droplet behavior in reactive flows, process development and intensified processes.

## **Publication III**

Gradov, D. V., González, G., Vauhkonen, M., Laari, A., and Koiranen, T.  
**Experimental and numerical study of multiphase mixing hydrodynamics in batch stirred tank applied to ammoniacal thiosulphate leaching of gold**

Reprinted with permission from  
*Journal of Chemical Engineering and Process Technology*  
Vol. 8(3), pp. 1-17, 2017  
© OMICS Publishing Group







## Experimental and Numerical Study of Multiphase Mixing Hydrodynamics in Batch Stirred Tank Applied to Ammoniacal Thiosulphate Leaching of Gold

Dmitry Vladimirovich Gradov<sup>1\*</sup>, Gerardo González<sup>2</sup>, Marko Vauhkonen<sup>2</sup>, Arto Laari<sup>1</sup> and Tuomas Koironen<sup>1</sup>

<sup>1</sup>School of Engineering Science, Lappeenranta University of Technology, Lappeenranta, Finland

<sup>2</sup>Department of Applied Physics, University of Eastern Finland, Kuopio, Finland

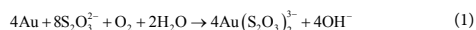
### Abstract

Hydrodynamics of aerated slurry is studied experimentally and numerically using the example of thiosulphate leaching of gold concentrate. The studied milled concentrate has shear-thinning fluid rheology and it was imitated by water-based solutions of CMC. Presence of electrolytes, as in the case of the leaching slurry, has great influence on bubble size distribution. Primary phase flow is measured by Particle Image Velocimetry. Local gas hold-up in aerated CMC 50000 (0.15 w%) solution is measured by Electrical Impedance Tomography. Volumetric mass transfer is measured by dynamic method in different CMC solutions over a range of operational conditions in absence and presence of electrolytes. The experimental data was used in CFD modelling of the aerated slurry. Single phase hydrodynamics of shear-thinning fluid (CMC 50000 (0.15 w%)) have been modelled and validated against experimental data with reasonable agreement. Multiphase mixing of the thiosulphate slurry was modelled with the assumption of constant bubble size. The results of the simulations and measurements are presented and discussed.

**Keywords:** Multiphase flow; Slurry mixing; PIV; EIT; CFD

### Introduction

Thiosulphate leaching is a promising alternative to cyanidation, which is frequently used for selective dissolution of gold from ores and concentrates. Slow kinetics of thiosulphate leaching is often boosted by addition of copper (II). The copper oxidizes metallic gold transforming it to ionic form, which reacts with thiosulphate ligands producing stable gold-thiosulphate complexes. Ammoniacal media is required to prevent passivation by sulfur that might appear from the decomposition of thiosulphate when it reacts with ore [1]. It is suggested that ammonia transports gold ions to bulk solution by being more strongly adsorbed on gold surface [2]. Oxygen is needed to recover copper (II) from copper (I) at a little expense of slow thiosulphate oxidation by molecular oxygen [3]. Overall mechanism of gold leaching with thiosulphate can be briefly summarized by the following reaction [4]:



Selective dissolution of gold with the above-described reaction usually takes place in aerated stirred tanks. Continuous stirred-tank reactors (CSTR) of various types are frequently used in mining, chemical and biochemical industries to promote reaction by providing intensive mixing and high rate of mass transfer. In many cases, mixing affects conversion and yield of product. Poor mixing might result in stagnant zones. It is important to predict locations of stagnant zones. Providing good mixing benefits rate of mass transfer via effective renewal of fluids contact.

As computational power is constantly growing, numerical simulation of mixing tanks may efficiently reveal stagnant zones and help saving resources and time. In the last two decades, Computational Fluid Dynamics (CFD) has been successfully applied for modelling of multiphase hydrodynamics in stirred reactors of different types and shapes. Promising results in resolving flow fields as well as phase interaction parameters are well-described and analyzed in the review article of Joshi et al. [5]. Even though fluid dynamics modelling has been applied successfully to solve engineering tasks, CFD models of multiphase flows involve numerous empirical coefficients caused by spatial discretization and lack of knowledge about phenomena. This leads to uncertainties limiting application area. Tuning of empirical

coefficients is a “compulsory measure” that requires validation procedure against experimental data.

There are many methods that have been designed to study fluid flow experimentally. Intrusive techniques such as Hot Wire Anemometry (HWA) are trustworthy and they can produce accurate results of high temporal and spatial resolution. However, they interfere flow and cannot measure many points synchronously [6]. Visual observations and measurements of hydrodynamics has taken significant place in hydrodynamics studies all along. Optical methods such as point-wise Laser Doppler Anemometry (LDA) and field-wise Particle Image Velocimetry (PIV) methods are extensively used in scientific studies dealing with optically transparent flows in stirred tanks [7-10]. For turbid and non-transparent flows Doppler Ultrasonic Velocimetry (DUV) has been developed. The operating principle of DUV is somewhat similar to PIV and it measures flow characteristics by means of ultrasonic beams reflected from seeding particles [11]. Measurements of Bubble Size Distribution (BSD) in mixed multiphase solution by tomographic PIV is challenging since images, taken in two-dimensional space and illuminated by laser pulse, give information on bubble size that is limited to particular area of laser sheet. In addition, local gas hold-up remains unknown in whole reactor. Application of Electrical Impedance Tomography (EIT), which is based on voltage measurements, has shown great potential in studies of multiphase flows for phase visualization in 3D [12-14]. Since conductivity is a function of gas hold-up, it is possible to obtain local void fraction of secondary phase by measuring voltages difference between primary phase alone and multiphase flow. Measuring voltage at several electrodes simultaneously

**\*Corresponding author:** Dmitry Vladimirovich Gradov, School of Engineering Science, Lappeenranta University of Technology, Lappeenranta, Finland, Tel: +358465470573; E-mail: [dmitry.gradov@lut.fi](mailto:dmitry.gradov@lut.fi)

**Received** July 09, 2017; **Accepted** July 13, 2017; **Published** July 22, 2017

**Citation:** Gradov DV, González G, Vauhkonen M, Laari A, Koironen T (2017) Experimental and Numerical Study of Multiphase Mixing Hydrodynamics in Batch Stirred Tank Applied to Ammoniacal Thiosulphate Leaching of Gold. J Chem Eng Process Technol 8: 348. doi: [10.4172/2157-7048.1000348](https://doi.org/10.4172/2157-7048.1000348)

**Copyright:** © 2017 Gradov DV, et al. This is an open-access article distributed under the terms of the Creative Commons Attribution License, which permits unrestricted use, distribution, and reproduction in any medium, provided the original author and source are credited.



reconstruction of conductivity difference distribution and hence local gas hold-up is possible [15,16].

Studying of mixing hydrodynamics facilitates finding local  $k_L$ , which is needed to evaluate specific volumetric interfacial mass transfer rate in CSTR. Based on Higbie's penetration theory Kawase et al. [17,18] showed that mass transfer coefficient in liquid film for viscous fluids can be expressed through local energy dissipation:

$$k_L = C \sqrt{D_L} \left( \frac{\varepsilon \rho}{K} \right)^{\frac{1}{2(1+n)}}, \quad (2)$$

where  $\varepsilon$  is the turbulence energy dissipation rate,  $\text{m}^2/\text{s}^3$ ,  $D_L$  is the gas diffusivity in liquid,  $\text{m}^2/\text{s}$ ,  $\rho$  is the liquid density,  $\text{kg}/\text{m}^3$ ,  $K$  is the consistency index,  $\text{Pa}\cdot\text{s}^n$ ,  $n$  is the dimensionless flow behavior index,  $C$  is the proportionality coefficient. The effect of gas bubbles to the mass transfer coefficient is taken into account with the proportionality coefficient. The value of 0.301 for the coefficient, proposed by Kawase [18], has been tested by Garcia-Ochoa and Gomez [19] and was found to produce accurate results for gas-liquid mass transfer in stirred reactors.

In addition to local mass transfer coefficient, local interfacial area is also needed to evaluate local  $k_L a$ . Measured locally distributions of bubble sizes and gas void fraction can provide information about local interfacial area between gas and liquid.

The idea of the current work is to acquire sufficient experimental data in order to be able to connect hydrodynamics of stirred multiphase flow to reaction kinetics. Thiosulphate leaching of gold in ammoniacal solution with the presence of copper (II) in stirred reactor was studied experimentally first and then simulated by means of CFD in order to get distribution of local mass transfer rate of oxygen into solution. The data presented in this study are useful for multiphase flows of finely-milled concentrate as well as for shear-thinning fluids agitated by Rushton turbine in aerated baffled reactors.

## Materials and Methods

### Object of study

The process of gold leaching with thiosulphate in ammoniacal solution, studied earlier [20] in a lab-scale batch STR, was taken as an example of typical multiphase pulp mixing process frequently encountered in mining and pharmaceuticals industries. The reaction

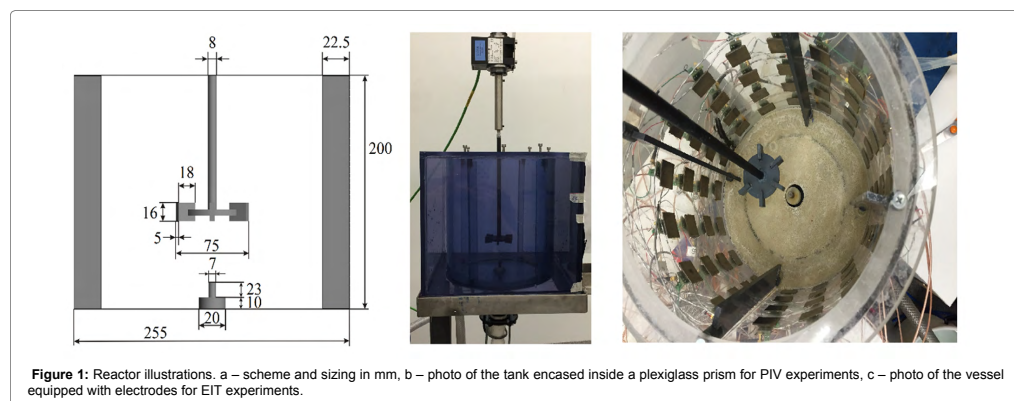
proceeds under almost ambient conditions (atmospheric pressure and  $30^\circ\text{C}$ ).

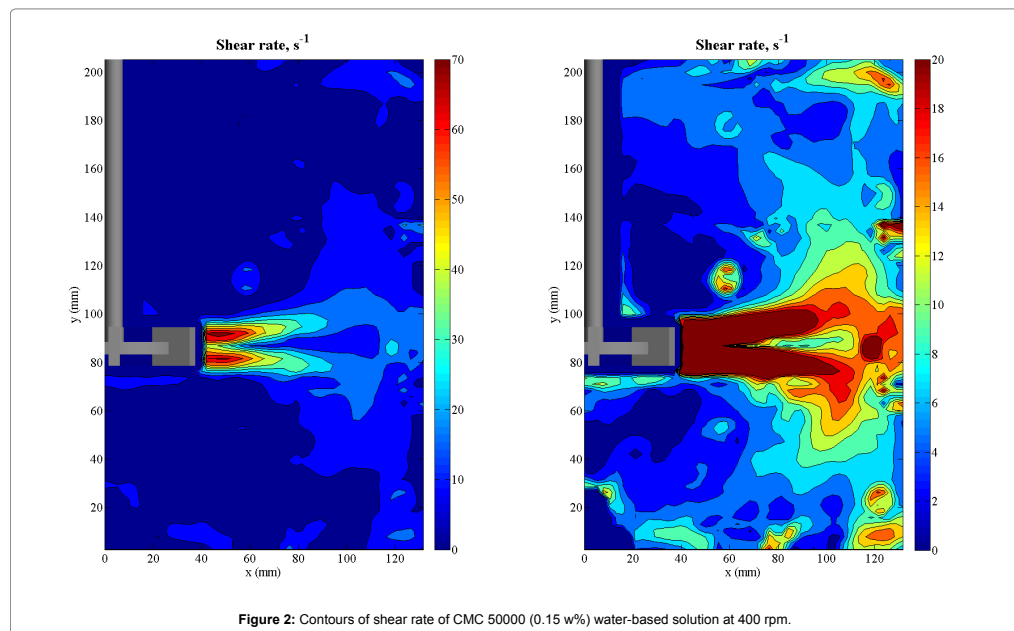
A lab-scale baffled stirred reactor, equipped with standard six-blade Rushton turbine, was investigated in the current research. A schematic representation of the vessel geometry and its dimensional parameters are presented in Figure 1. The impeller clearance was set at the distance equal to its diameter from the bottom of the tank. The gas sparger is a perforated metal pipe mounted at the bottom of the tank. The tank, made out of plexiglass, was designed and constructed in two versions. EIT uses controlled current injections to measure responding voltages at electrodes placed around the flow. Therefore, the vessel, meant to be used in EIT experiments, was equipped with electrodes on the walls arranged in rows. In particular, an arrangement of 4 rows consisting of 16 electrodes, made out of stainless steel, was mounted on perimeter of the reactor wall. Thus, approximate resolution of the spatial reconstruction is roughly  $2\text{ cm}^3$ . Another tank of the same size was encased inside a rectangular plexiglass container to be filled with liquid of the same refractive index as the studied solution in order to eliminate visual distortions.

The power input per volume of fluid that was used in the reaction kinetics research was scaled via the known power number of the dual impeller to the reactor scale used in the current work. The scaled power input corresponds to the mixing rate of around 400 rpm.

### Experimental techniques

**Rheology study:** The mean diameter of the gold concentrate particles used by Lampinen et al. [20] was  $7\text{ }\mu\text{m}$ . [21] Having measured the total heat production in calorimeter (universal Calvet calorimeter C80 CS Evolution of SETARAM Instrumentation with reversing mechanism) as the function of solids content, and the maximum value corresponded to 30% of solids content, which was suggested to be optimal in the leaching solution. The range of the shear rate in the pulp mixing with the four different impeller speeds was roughly estimated using the PIV data (Figure 2) and the CFD model. Single phase mixing of the above-mentioned reactor was simulated in Fluent 16 and the results are summarized in Table 1. Looking ahead, rheological measurements of the gold concentrate suspended in water revealed shear-thinning behavior (Figure 3). The suspension used in the leaching experiments is non-transparent. Therefore, it is not suitable for hydrodynamics study by PIV. Suspended solids may also cause some bias when measured by





EIT due to conductivity difference between solids and liquid. For that reason, it was decided to imitate the solution experimentally by using Sodium Carboxy Methyl Cellulose (CMC) dissolved in water. Water solutions of CMC also have shear-thinning behavior and effect of CMC to rheological properties depends on molecular length. Two CMC powders were tested: CMC 30 and CMC 50000. The number going after CMC denotes viscosity of 2 % water-based solution measured at 25°C [22].

Dynamic Mechanical Analysis of the leaching pulp and water-based CMC solutions was performed using Anton Paar Modular Compact Rheometer 302. By means of swirling cone-analyzer (standard measuring cylinder CC27/T200/AL) the effective viscosity was measured in the shear rate range from 1 to 200 s<sup>-1</sup>. Suspended solids in the leaching pulp had a tendency to sedimentate. Therefore, the pulp viscosity was measured additionally with a stirrer-sensor (ST24-2D/2V/2V-30/109). Measurements made by the cone and the blade analyzers produced similar results meaning that sedimentation for such tiny particles is a relatively slow process. Thus, the cone mixer-sensor was used alone in all the experiments in further.

**Overall gas hold-up measurements:** Gas hold-up measurements were made based on visual observation of liquid surface level of the agitated solutions. The reliability of the measurements was compromised by surface fluctuations and appearance of foam. In order to reduce uncertainties, the rise of the surface level  $\Delta h$  was measured at two positions: between the baffles next to the vessel wall. In each experiment, the agitated solution was allowed to reach equilibrium and then 10 readings from each point were made and averaged. The overall gas hold-up was computed based on the following equation:

$$\varepsilon_{\Delta h} = \frac{h_{\text{gassed}} - h_{\text{ungassed}}}{h_{\text{gassed}}}, \quad (3)$$

where  $\varepsilon_{\Delta h}$  the overall gas hold-up,  $h_{\text{gassed}}$  and  $h_{\text{ungassed}}$  are the heights of the mixed solutions with and without gas introduction correspondingly.

**EIT:** The EIT set-up used in the experiments involved a signal generator, receiver, controller, and computer. The purpose of the signal generator is to produce current pulses of constant voltage to the solution according to a predefined scheme of pulses order. There are two different scenarios for the order of current injections that can be applied. Voltage injections can be sent pair-wise e.g., adjacent pairs of electrodes or multiple electrodes simultaneously. In both scenarios, voltages are measured at all electrodes. Then, obtained signal goes to demodulation process, where input voltage is decomposed into real and imaginary parts that are needed to get phase and amplitude according to the following formulations [23]:

$$v_{\text{real}} = \frac{2}{N} \sum_{i=0}^{N-1} v(i) \sin \frac{2\pi i}{N} \quad (4)$$

$$v_{\text{image}} = \frac{2}{N} \sum_{i=0}^{N-1} v(i) \cos \frac{2\pi i}{N} \quad (5)$$

$$A = \frac{2}{N} \sqrt{v_{\text{real}}^2 + v_{\text{image}}^2} \quad (6)$$

$$\varphi = \tan^{-1} v_{\text{image}} / v_{\text{real}}, \quad (7)$$

where N is the number of electrodes, v(i) is the measured voltage

Impeller speed, rpm	$\dot{\gamma}$ , $s^{-1}$			Method of determination
	Minimum	Maximum	Volume averaged	
100	0.002	350	2	CFD
200	0.005	708	5	CFD
400	0.012	1443	12	CFD
400	0	70	8	2D PIV plane (Figure 2)
600	0.024	2186	19	CFD

**Table 1:** Range of shear rate in the reactor.

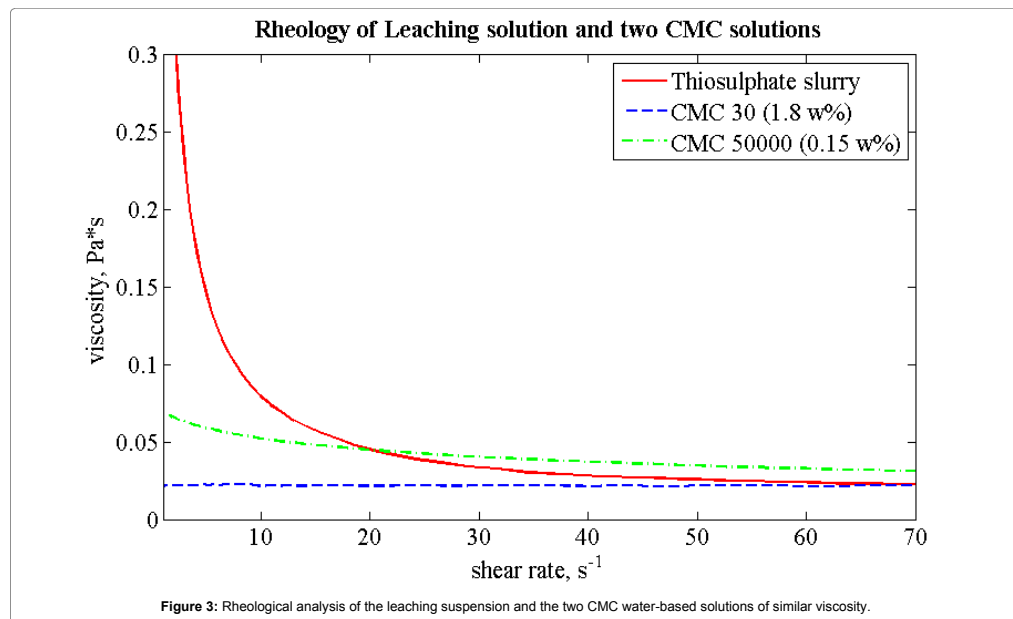


**Figure 3:** Rheological analysis of the leaching suspension and the two CMC water-based solutions of similar viscosity.

at  $i$ -th electrode,  $V$ ,  $v_{\text{real}}$  is the real part of measured voltage,  $V$ ,  $v_{\text{image}}$  is the imaginary part of measured voltage,  $V$ ,  $\phi$  and  $A$  are the signal phase and amplitude correspondingly.

Finding a conductivity distribution out of measured voltage outcomes of preset current injections represents itself an inverse problem. Computation of conductivity distribution is a challenging task to solve, since even a slight shift of voltages may be a result of significant change of conductivity distribution in solution, meaning that the "equation" might have several solutions. Therefore, some additional information about object of study is needed to solve the inverse problem. Prior information on conductivity distribution may be achieved statistically and used as a reference [23,24].

The difference method exploits measurements of non-gassed mixed solution as a reference in order to get gas void fraction distribution in the reactor. The conductivity distribution is the function of fluid resistance, and hence, local gas hold-up could be found as follows [23]:

$$\varepsilon_{\text{LH}} = \frac{2(\sigma_1 - \sigma_2)}{2\sigma_1 + \sigma_2}, \quad (8)$$

where  $\sigma_1$  is the conductivity distribution of liquid phase, S/m,  $\sigma_2$  is the conductivity distribution of dispersed gas phase, S/m. Thereby,

the difference method automatically removes the influence of non-conductive parts of the vessel such as baffles and impeller.

Many researches describe successful applications of the technique for stirred tanks to measure local gas hold-up [13,14,25-28]. Value of current injections value is dictated by conductivity of the studied solution. The higher the solution conductivity, the higher the current injections are required in order to increase sensitivity of the system.

**PIV:** Particle Image Velocimetry was used to study the hydrodynamics of the liquid phase agitated in multiphase mixing. The PIV technique measures velocity flow fields by capturing the movement of tracing particles, which are small enough not to interfere the flow. By slicing the flow with a laser sheet, PIV can produce a two-dimensional picture of the fluid motion within the laser sheet of illumination. A vector velocity field is constructed based on spatial shift of tracer-particles between a pair of laser pulses emitted consecutively in accordance with a preset time delay. The PIV set-up included a double-pulsed Nd:Yag laser and two Charge-Coupled Device (CCD) cameras of the following resolution  $1600 \times 1200$  pixels. The laser and the cameras were managed by Davis 7.2 PIV software. The imaging of tracers shift was carried out by two CCD cameras which were

synchronized with laser pulsing. Thus, velocity vector fields of axial and radial components were measured in 2D space.

In order to measure liquid phase flow, fluorescent particles of size 20 – 50  $\mu\text{m}$ , made of polyamide, were used as tracers. The fluorescent tracers emit light at different wavelength than the laser. This property facilitates getting images with uniformly illuminated background. High bandpass filters (Light red bandpass filter: BP635) were installed on the CCD cameras to separate light within the wavelength range 615 – 645 nm to filter out the green light coming from light-reflecting surfaces of the reactor [29]. Gas bubbles pictures were made using the light reflected from bubbles. In this case, a camera was capped with a grey filter (B+W, 52 103 ND 0.9 8x) only to reduce intensity of the reflected light.

The laser sheet in the reactor was positioned vertically near the baffle and 2 mm behind the vertical axis of the shaft. The reason for this positioning was to remove as many visual obstacles and strong reflections as possible. Size of single frame taken (measurement window) depends on camera resolution and focal length of objective. A typical size of the measurement frame was  $127 \times 100$  mm. Such frames were processed twice via cross-correlation algorithm. At first, the frame square is split by the PIV software into interrogation areas of  $128 \times 128$  pixels to search vectors. Then, interrogation areas were decreased to  $64 \times 64$  pixels with 50% overlap and the frame was treated in similar

way to search for tracers shift with higher precision. The final PIV results have resolution of 2.2 mm. A sample of the taken frames and the resulting vector field of instantaneous and average velocities are presented in Figure 4. In order to get a full picture of the reactor, it was necessary to take three frames at different heights along the vertical axis with 50 mm overlapping (Figure 5). Thus, when the captured frames were assembled, a full image of the reactor, from the tank wall to the shaft, of size  $127 \times 200$  mm could be obtained. The resolution of post-processed and vertically combined frames was  $51 \times 79$  vectors. Totally 1000 frames were taken and processed in order to obtain time-averaged results.

**$k_L a$  measurements:** Volumetric mass transfer coefficient was measured via “gassing-out” dynamic method by using dissolved oxygen meter MARVET BASIC. All the experiments were performed at  $20^\circ\text{C}$ . The reactor was at first bubbled with nitrogen until dissolved oxygen concentration reached its minimum. Then a valve of nitrogen pipe line was closed and air was introduced. The evolution of the changing oxygen concentration was recorded until it reached its maximum value. The data was analyzed by parameter estimation software MODEST [30] and the volumetric mass transfer rate was calculated using Eq. 9.

$$\frac{c_{\text{sat}} - c_{\text{liquid}}(t_1)}{c_{\text{sat}} - c_{\text{liquid}}(t_2)} = \frac{e^{(-k_L a t_1)} - k_L a \tau_p e^{-t/\tau_p}}{1 - k_L a \tau_p}, \quad (9)$$

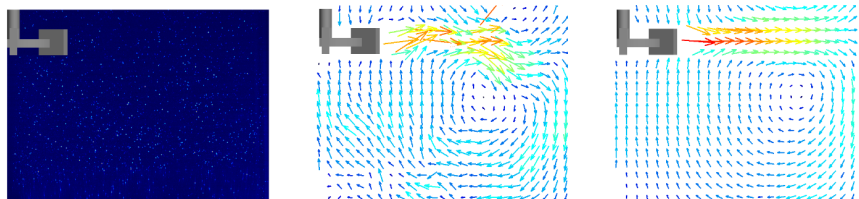


**Figure 4:** Measurement window and the calculated velocity vector fields near the impeller. a – PIV frame, b – instant velocity vector field, c – averaged velocity vector field.

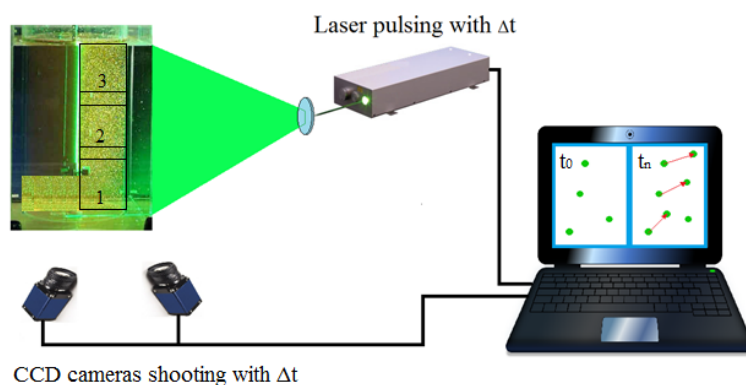


**Figure 5:** Schematic representation of PIV set-up

where  $c_{sat}$  is the saturated oxygen concentration in water, mol/m<sup>3</sup>,  $c_{liquid}$  is the oxygen concentration in liquid, mol/m<sup>3</sup>, at  $t_1$  and  $t_2$ .

Time constant shows how quickly a measuring probes responses to a sudden step change of oxygen concentration. In order to expect accurate results the value of the time constant should be lower than  $k_1 a^{-1}$  [31,32]. The response time constant  $\tau$  of the probe was measured separately for each solution studied. In the experiments, the oxygen probe was placed between baffles where the mixing is vigorous and the bulk solution around the probe is constantly renewed by the flow. Otherwise, the probe might consume all the oxygen presented in the bulk around at some moment and further measurements become inaccurate.

### Modelling theory

**Multiphase fluid flow:** The Stoke's number (Eq. 10) for the studied system is more than 1, meaning that the secondary phase influence onto the primary phase is not negligible and it has to be taken into account.

$$St = \frac{\tau_p}{\tau_q} = \frac{d_p^2 \rho_p \epsilon^{0.5}}{36 \nu^{1.5}}, \quad (10)$$

where  $\tau_p$  and  $\tau_q$  are the relaxation time of primary phase and bubble,  $s$ ,  $d_p$  is the bubble diameter,  $m$ ,  $\epsilon$  is the energy dissipation,  $m^2/s^3$ ,  $\nu$  is the kinematic viscosity,  $m^2/s$ .

Therefore, in the gas-liquid modelling, Eulerian-Eulerian multiphase approach was used, in which gas and liquid phases are considered as interpenetrating continua. A set of conservation equation is solved for each phase (Eq. 12 and 13). Additionally, volume fraction is introduced (Eq. 11).

$$\sum_i \alpha_i = 1 \quad (11)$$

$$\nabla \cdot \bar{u} = 0 \quad (12)$$

$$\bar{u} \cdot \nabla \bar{u} = -\nabla \cdot [(\mu + \mu_{turb}) \nabla \bar{u}], \quad (13)$$

where  $\alpha_i$  is the phase volume fraction,  $\bar{u}$  - phase velocity,  $m/s$ ,  $\bar{p}$  is the pressure,  $Pa$ ,  $\mu_{turb}$  is the turbulent viscosity,  $Pa \cdot s$ .

**Suspended solids:** The tiny milled concentrate was used in the original leaching tests with mean size of  $7 \mu m$ . Pulp flow can be modeled via effective viscosity [33]. Rheology of the leaching slurry has been measured experimentally and modelled via power-law model (Eq. 23).

**Turbulence:** In CFD modelling, available computing power and acceptable simulation time were limited, for which reason it was decided to apply a Reynolds-Averaged Navier-Stokes (RANS) turbulence model in the current simulations. Turbulence formulation in RANS models are based on statistical analysis rather than on actual physical phenomena. By contrast, the Large Eddy Simulation (LES) model is based, at least partially, on resolving turbulence fluctuations. Approximations such as the Boussinesq hypothesis can lead to mismatches with real flow behavior due to turbulence isotropy and homogeneity. As a result, empirical constants are introduced to tune the model (Eq. 14 and 15). In the current work, it was decided to evaluate the suitability of the most frequently applied RANS models rather than attempt to implement a novel turbulence model by tuning the model constants for the hydrodynamics of the specific stirred tank. In our previous work [34], three popular models in the RANS family were tested, namely the Realizable k- $\epsilon$  model, the Shear Stress Transport k- $\omega$  model, and the Reynolds Stress Model (RSM). The Realizable k- $\epsilon$  model produce the most accurate results for single and

multiphase mixing in round bottom STR. The Realizable k- $\epsilon$  model is a recent model with an improved computational mechanism preventing turbulence energy from being negative. Such energy is not physical but can occur using the Standard k- $\epsilon$  model.

$$\bar{u} \cdot \nabla k = P - \epsilon + \nabla \cdot \left[ \left( \mu + \frac{\mu_{turb}}{\sigma_k} \right) \nabla k \right] \quad (14)$$

$$\bar{u} \cdot \nabla \epsilon = C_{\epsilon 1} \frac{\epsilon}{k} P - C_{\epsilon 2} \frac{\epsilon^2}{k} + \nabla \cdot \left[ \left( \mu + \frac{\mu_{turb}}{\sigma_\epsilon} \right) \nabla \epsilon \right], \quad (15)$$

where  $k$  is the turbulence kinetic energy,  $m^2/s^2$ . Production  $P$  includes one more constant.

Dispersed turbulence formulation model was used since the secondary phase is dilute and fluctuating quantities of the gaseous phase may be found as the function of the mean terms of the liquid phase. At first, turbulence terms  $k$  and  $\epsilon$  are first computed for primary phase. Then, secondary phase turbulence terms are found and exchange of turbulence momentum between phases is computed based on Tchen-theory [35].

**Phase interaction:** Momentum conservation equation (Eq. 16)

includes cumulative force  $\bar{F}_i$  (Eq. 17) acting on primary phase. The cumulative force comprises several forces occurring in multiphase interaction, including drag, virtual mass, lift, wall lubrication, turbulence diffusion forces etc.

$$\frac{\partial}{\partial t} (\alpha \bar{p})_q + \nabla \cdot (\alpha \bar{p} \bar{u})_q = \nabla \cdot (\alpha \sigma)_q - \alpha_q \nabla p + \bar{F}_q + \alpha_q p_q \bar{g} \quad (16)$$

$$\bar{F}_q = \sum_p (K_{pq} (\bar{u}_p - \bar{u}_q) + \dot{m}_{pq} \bar{u}_p - \dot{m}_{qp} \bar{u}_q) + (\bar{F}_{d,p,q} + \bar{F}_{l,p,q} + \bar{F}_{m,p,q} + \bar{F}_{w,p,q}) \quad (17)$$

where  $\bar{F}_i$  is the external body force,  $\bar{F}_{d,i}$  the lift force,  $\bar{F}_{l,i}$  is the wall lubrication force  $\bar{F}_{m,i}$  is the virtual mass force, and  $\bar{F}_{w,i}$  is the turbulence diffusion force.

Different drag models can be found in published literature. The most popular model, proposed by Schiller and Naumann [36] in Eq. 19, is a drag model suitable for rigid spherical particles.

$$K_{pq} = \frac{\rho_p C_D Re}{144 \tau_p} d_p A_i \quad (18)$$

where  $\rho_p$  is the particle density,  $kg/m^3$ ,  $C_D$  is the drag coefficient,  $A_i$  is the relative Reynolds number, and  $A_i$  is the interfacial area,  $m^2$ . The drag force coefficient is the function of  $Re$  according to the following formulation:

$$CD = \begin{cases} 24(1 + 0.15 Re^{0.687}) & Re \leq 1000 \\ 0.44 & Re > 1000 \end{cases} \quad (19)$$

The drag force model is based on bubble rise velocity measured in stagnant fluids, which is higher than rise velocity in turbulent flow. A model correcting drag force coefficient for turbulence was proposed by Brucato et al. [37]. This turbulence modification factor concept (Eq. 20) changes stagnant fluid drag force to make it suitable for adoption in turbulent multiphase flow simulation. Later, Lane et al. [24] critically considered Brucato's formulation and found that ratio of slip and terminal velocity as a function of bubble size and Kolmogorov length scale does not take into account particle density or density difference between phases. Having pointed out this deficiency in Brucato's model, Lane et al. suggested a new correlation (Eq. 21) for turbulence modification factor that is based on ratio of stagnant to turbulent terminal velocity  $\frac{U_{t,s}}{U_{t,r}}$  to be correlated with ratio of particle relaxation time to integral time scale of turbulence (Eq. 22).

$$K'_{pq} = \eta K_{pq} = \left( 1 + K \left( \frac{d_p}{\lambda} \right)^3 \right) K_{pq}, \quad (20)$$

where  $\eta$  is the turbulence modification factor,  $K = 6.5 \cdot 10^{-6}$ ,  $\lambda$  is the Kolmogorov length scale, m.

$$\eta = \left( 1 - 1.4 \left( \frac{\tau_p}{\tau_c} \right)^{0.7} e^{\left( \frac{0.6\tau_p}{\tau_c} \right)} \right)^{-2} \quad (21)$$

$$T_i = 0.135 \frac{k}{\varepsilon} \quad (22)$$

Gradov et al. showed that the Schiller-Naumann drag force model in conjunction with Lane's turbulence modification factor gave the most accurate results for air-water mixing in stirred tank at the assumption of constant bubble diameter equal 1 mm. Also, the effect of non-drag forces was found to be insignificant air-water mixing simulations. Therefore, in order to reduce computational complexity and promote solution stability the above mentioned combination of models was used to simulate drag force, while other forces models were ignored [34].

**Modelling strategy:** In the gas-liquid flow simulations, the gas was introduced into converged liquid flow field in order to reduce computational instabilities. In the CFD simulations, the stirred tank can be considered as a semi-batch system with gas is supplied via sparger and exit through liquid surface. The gas phase was introduced in a transient manner at 0.02 s time step until mass flow rate balance was reached and stabilize within 5% deviation. Under relaxation factors for pressure and velocity were reduced up to 0.15 and 0.35 correspondingly to facilitate convergence. Second order discretization scheme was applied to all the parameters. Convergence criterion was set at  $10^{-4}$  for all the variables to be simulated. When multiphase flow hydrodynamics have been computed, mass transfer was calculated on top of multiphase results according to Eq. 2. The operational conditions simulated and models used in single phase and multiphase mixing simulations are summarized in Tables 2 and 3.

## Results and Discussion

### Experimental results

**Rheology:** The rheology of the leaching suspension as well as the water solutions of CMC 50000 (0.15 w%) and CMC 30 (1.8 w%) were measured and shown in Figure 3. The presented data was plotted in log-log scale, and the rheological parameters were found from the Ostwald-de Waele power law [38]:

$$\mu_{\text{eff}} = K (\dot{\gamma})^{n-1}, \quad (23)$$

where  $\mu_{\text{eff}}$  is the effective viscosity, Pa·s,  $K$  is the consistency index, Pa·s<sup>n</sup>,  $n$  is the flow behavior index.

The viscosity of all the solutions approach constant level as the shear rate is increased. However, only the solution of short molecular chain CMC 30 shows insignificant shear-thinning rheology. Therefore, only CMC 50000 has been used in further as an imitation model of leaching suspension. It is advisable to set limits for the effective viscosity when modelling non-Newtonian hydrodynamics in order to avoid numerical errors. Calculated power law parameters are summarized in Table 4.

**Gas hold-up:** Measurement of gas hold-up in STR by level difference has better accuracy at high gas hold-ups. Gas hold-up has linear dependence on superficial velocity as described by Rewatkar et al. [39] numerically and approved experimentally experimentally later by Kraume and Zehner [40] for glass beds suspended in water and by Laakkonen [41] for Xanthan solutions. In the current study, gas hold-up was measured over the range of gas flow rates from 1 to 10 L/min at

constant impeller speed of 400 rpm. The results are plotted in Figure 6.

The obtained results show almost linear dependence of gas hold-up from gas flow rate. It is necessary to use relatively low gas flow rate in PIV measurements to ensure good optical transparency of solution and reduce impact of gas bubbles onto laser intensity. Therefore, gas flow rate could be safely reduced to 1.25 L/min.

**EIT:** Increased viscosity promotes growth of bubble size due to increased coalescence rate. However, it is also known that presence of electrolytes in solution inhibits bubble coalescence [42]. At sufficiently high salt concentrations, bubbles, covered by ion layer, repel each other. The total optimal concentration of salts for thiosulphate leaching was found to be 0.4 mol/L [20]. Unfortunately, the EIT set-up loses its sensitivity at high conductivity of solution since the maximum current was limited to 6.5 mA. For that reason, the salt concentration had to be reduced to lower value, where a compromise between the similarity in the multiphase solution properties compared to the original solution and the set-up limits could be met. It can be concluded, that significant amount of ions in liquid suppresses the bubble-growing effect generated by higher viscosity. The influence of the salt concentration on gas phase can also be tested indirectly by measuring the power draw of the impeller. Impeller torque was measured as salts were added stepwise (0.05 mol/L per step). The results (Figure 7) show that 0.05 mol/L of salts was enough to effectively cover the major part of the bubbles surface in the solution. Further addition of salts has insignificant effect on the mixing power and hence on the gas hold-up. However, the power draw is mainly driven by the average density of the multiphase solution, and it is little influenced by the distribution of bubble size which has, however, significant influence on the contact surface area between the phases. Therefore, the overall  $k_a$  was also measured at different salt concentrations, as depicted in Figure 7 (left plot). The slow increase of the overall mass transfer is an evidence of the ongoing shift in the BSD towards small bubbles. At concentration 0.1 mol/L, with a conductivity of 7.9 mS/m (which is within the maximum conductivity limit of the EIT), the  $k_a$  value is 91% of the maximum  $k_a$  value at concentration 0.4 mol/L. Therefore, this concentration was selected as a reasonable compromise and was used in all the experiments.

In order to evaluate the performance of the EIT set-up, several experiments were made at three gas flow rates without mixing. The

Operational conditions	Modelled phenomenon	Model used
400 rpm	Turbulence	k-ε Realizable
	Shear-thinning rheology of mixed fluid	Power-law model
	Flow near the solid walls	Standard wall function

**Table 2:** Summarized conditions for single phase mixing simulations.

Operational conditions	Modelled phenomenon	Model used
400 rpm	Turbulence	k-ε Realizable
	Shear-thinning rheology of mixed fluid	Power-law model
1.25 L/min of air flow rate	Flow near the solid walls	Standard wall function
	Bubble size	Constant $d_b = 1.5$ mm

**Table 3:** Summarized conditions for multiphase mixing simulations.

Solution	n	K, Pa·s <sup>n</sup>	$\mu_{\text{min}}$ , Pa·s	$\mu_{\text{max}}$ , Pa·s
Thiosulphate slurry	0.200	0.044	0.02	0.40
CMC 50000 (0.15 w%)	0.746	0.086	0.02	0.09

**Table 4:** Power law model parameters.

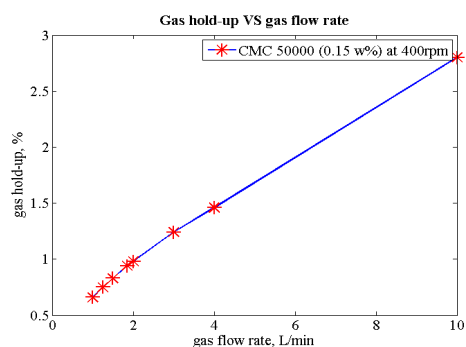


**Figure 6:** Gas hold-up vs superficial gas velocity in CMC 50000 (0.15 %) water-based solution at 400 rpm.

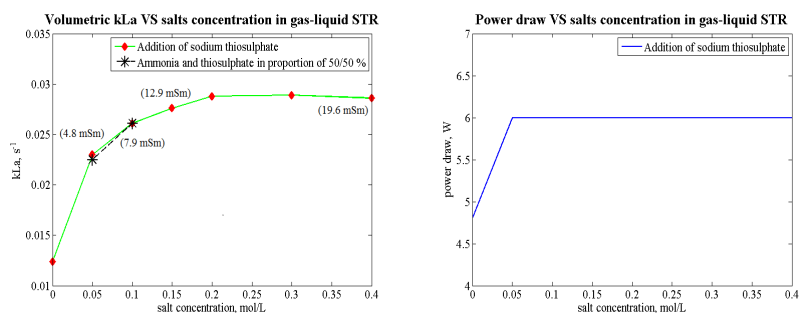


**Figure 7:** Overall  $k_L a$  (right) and power draw (left) with conductivity of CMC 50000 (0.15 %) water-based solution at 600 rpm and 2 L/min gas flowrate vs salt concentration

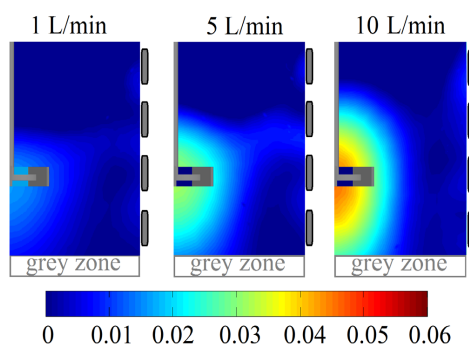


**Figure 8:** Local gas hold-up in CMC 50000 (0.15 %) and 0.1 mol/L of sodium thiosulphate in 2D plane (middle plane positioned between the baffles) measured by EIT without mixing.



obtained local gas hold-ups are illustrated in Figure 10. The resolution of the resulting images was around 2 cm<sup>3</sup>. It is clear that at large flow rates, the contrast in gas-liquid conductivity is high and the EIT results of gas-liquid mixing become more reliable.

The local gas hold-ups of the water-based solution of CMC 50000 mixed at 200, 400 and 600 rpm over the range of gas flow rates from 1 to 2 L/min are presented in Figures 10-11.

The overall gas hold-ups increase as the gas flow rate is increased with all the impeller speeds tested. Unfortunately, the poor resolution of the EIT set-up does not capture small bubbles present in high quantities in the most agitated region around the impeller. At low gas flow rates and high impeller speeds conditions are challenging when bubbles are smaller and distributed more uniformly in the volume of the reactor. Decreased and evenly distributed gas void fraction allows electrical current bypassing small bubbles especially at high loads of electrolytes in the solution. The measured zero value of gas hold-up around the impeller indicates narrow size distribution of small bubbles. The bubbles become traceable only in the region of low turbulence intensity where bubble coalescence takes place. The regions of bubble growth are most distinct at low ratio of impeller speed to gas superficial

velocity. It can be noticed that bubble size grows in radial direction towards the wall. Below the impeller, a down pumping circulation loop generates a stagnant zone where the retention time of bubbles is bigger. Meanwhile, bubbles, escaping the loop, gravitate to the free surface and move into less turbulent region where they coalesce. In addition, intensive foaming takes place when the CMC-water-thiosulphate solution is mixed which facilitates accumulation and growth of bubbles near the free surface. As a result, high local gas hold-up next to the surface is formed which is also presented in all the figures.

**PIV:** PIV results of CMC 50000 (0.15 w%), showing contours of the averaged velocity vector field and the r.m.s instantaneous velocity field, are shown in Figure 12. The averaged velocity vector field is a great source of information. The spatial velocity gradients may give information about the range of shear rate in the 2D slice of the flow (Figure 2). That information was used to define the range of shear rate in the rheology study of the suspension and the CMC water-based solutions. When studying the shear rate distribution in the PIV plane more closely one may notice that the agitated flow is rapidly attenuated in the viscous solution. It can be clearly seen that the visible stable streams which have shear rates of 70 s<sup>-1</sup> are pushed by the agitator and dissipated into the bulk solution where the initial shear rate is reduced

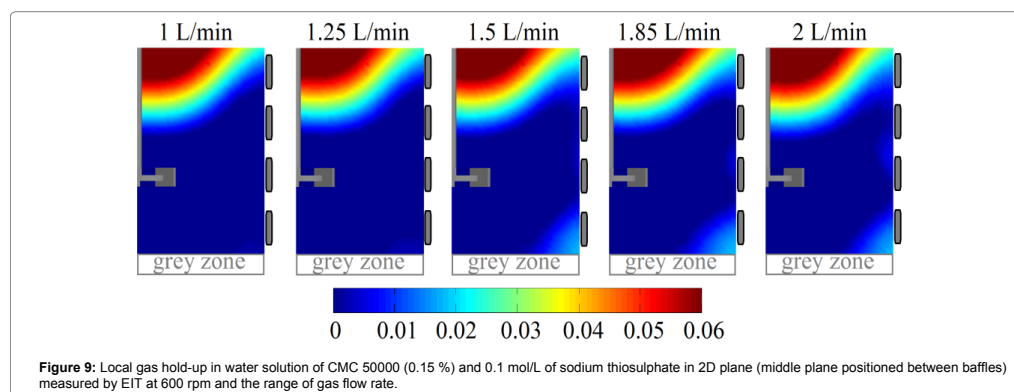


**Figure 9:** Local gas hold-up in water solution of CMC 50000 (0.15 %) and 0.1 mol/L of sodium thiosulphate in 2D plane (middle plane positioned between baffles) measured by EIT at 600 rpm and the range of gas flow rate.

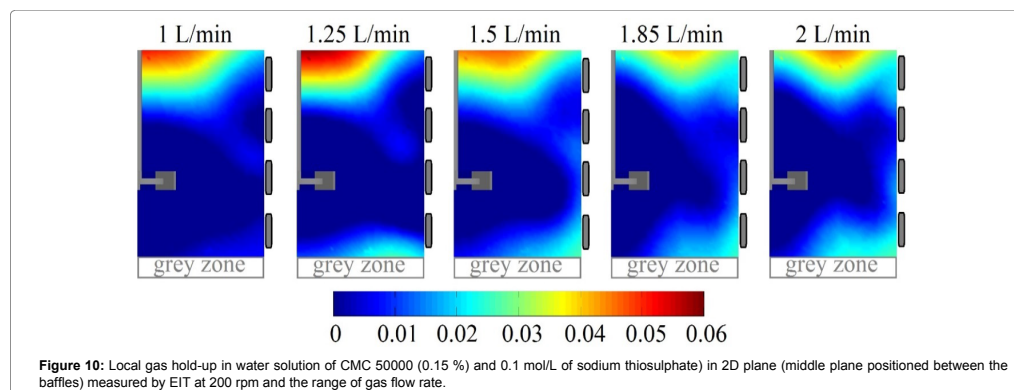
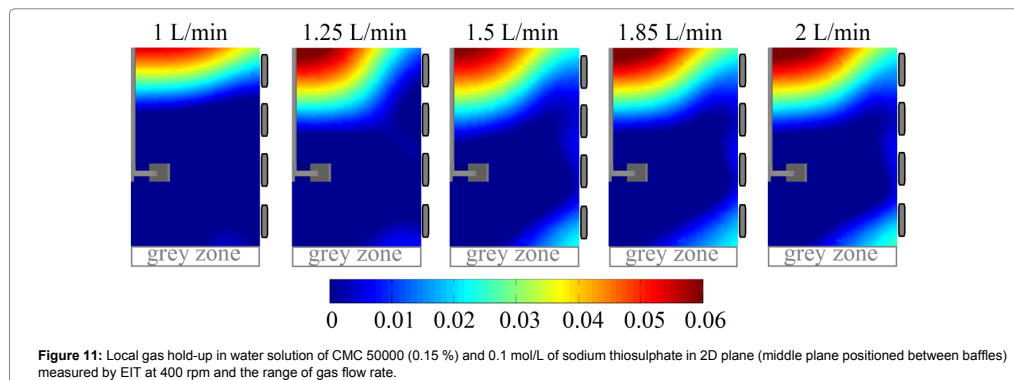


**Figure 10:** Local gas hold-up in water solution of CMC 50000 (0.15 %) and 0.1 mol/L of sodium thiosulphate in 2D plane (middle plane positioned between the baffles) measured by EIT at 200 rpm and the range of gas flow rate.





to around  $10 \text{ s}^{-1}$ .

Salts free single phase mixing of the CMC solution at 400 rpm (Figures 2 and 6) at 1.25 L/min were measured by the PIV and used for validation of CFD results.

As it was stated earlier, the leaching solution used in the original tests of thiosulphate leaching of gold [20] had high salts concentration. In the PIV tests, CMC 50000 (0.15 w%) solution with 0.1 mol/L concentration of sodium thiosulphate was used to study gas bubbles. Presence of salts has significant impact onto BSD. Ions of the same sign cover surface of gas bubbles and block coalescence rate by repelling mechanism. As a result, one may notice narrow distribution of gas bubbles in Figure 13.

Bubble size distribution is almost uniform in the most turbulent region next to the impeller as well as also elsewhere in the image. Bubble size varies from 1 mm to 1.8 mm as it is seen in the zoomed picture. The bubbles are densely populated in the plane of measurement. However, it should be mentioned that only those bubbles that are in focus were considered when evaluating the bubble size.

Such a narrow range of BSD may be approximated as a constant bubble size (1.5 mm) throughout the reactor under the current conditions. Considering CFD modelling this approximation greatly simplifies modelling and use of Population Balance Model (PBM) can be avoided.

**Overall  $k_L a$ :** Two water-based solutions of CMC 30 (1.8%) and CMC 50000 (0.15%) were used to measure the volumetric mass transfer coefficient at three impeller speeds and the range of gas flow-rates with and without addition of salts. The results are presented in Figure 14.

The volumetric mass transfer rate is proportional to interfacial contact area and mixing intensity. At mixing speed 600 rpm  $k_L a$  grows as gas flow rate is increased. However, at lower mixing speeds  $k_L a$  increases up to some point and then goes down with the increase of gas input. The reason for this behavior is the contact area that drops if mixing intensity is not enough to keep the bubble size small. Without salts both CMC solutions have similar mass transfer due to similar apparent viscosity. Presence of ions in water-based solution of CMC 30 does not lead to significant drop of viscosity and the similar mass transfer can be observed. However, ion presence affects CMC 50000 so that the long chain molecules are broken and the apparent viscosity

of solution is decreased. Low viscosity and high content of ions in the solution give nearly constant and small bubble size that results in high values for  $k_L a$ .

## Numerical results

**Grid independence test:** Spatial discretization influences results of numerical simulation. Five different grids have been tested. Water mixing simulations were used in grid independence study. Reactor geometry was meshed with almost doubling factor relatively one another and scaling uniformity was maintained as well. Re number differs significantly within the vessel therefore 14 sampling points of velocity have been defined in the reactor domain. A normalized root mean square error index (NRMSE) was employed as a criterion for grid independency validation [43]. Its formulation is as follows:

$$\text{NRMSE} = \frac{3}{\left( \frac{N_{\text{fine}}}{N_{\text{coarse}}} \right)^2 - 1} \sqrt{\frac{\sum_{i=1}^n (\varphi_1(i) - \varphi_2(i))^2}{\sum_{i=1}^n (\varphi_2(i))^2}} \cdot 100\%, \quad (24)$$

where N is number of cells in a grid (it is advised to keep grid size ratio above 1.3 corresponds to order of discretization, n is number of samples,  $\varphi_1$  and  $\varphi_2$  are predictions on coarse and fine grids accordingly.

According to the authors, grid difference might be considered negligible if NRMSE value is less than 10%. During mesh sizing independence tests simulations were performed with second order discretization scheme. Results presented in Table 5 clearly indicate grid 4 to be optimal one for the needs of the current study.

**Shear-thinning fluid mixing:** To reduce numerical instability the gas-liquid multiphase simulation strategy included two steps. The gas-liquid simulations were made in two-way coupling. At first,

Grid name	Number of elements	Torque, mNm	$\int k_d V, \text{m}^2/\text{s}^2 \cdot 10^{-5}$	$\int \epsilon_d V, \text{m}^2/\text{s} \cdot 10^{-5}$	NRMSE $\bar{u}$ %
1	108 276	54.0	9.9	139.2	20
2	269 654	56.0	10.8	161.2	13
3	464 532	56.6	10.7	166.4	15
4	754 056	65.6	13.0	209.1	9
5	1 969 376	64.4	12.6	208.5	NaN
Measured experimentally	65 $\pm$ 3				

Table 5: Grid test results of water mixing at 400 rpm in STR.

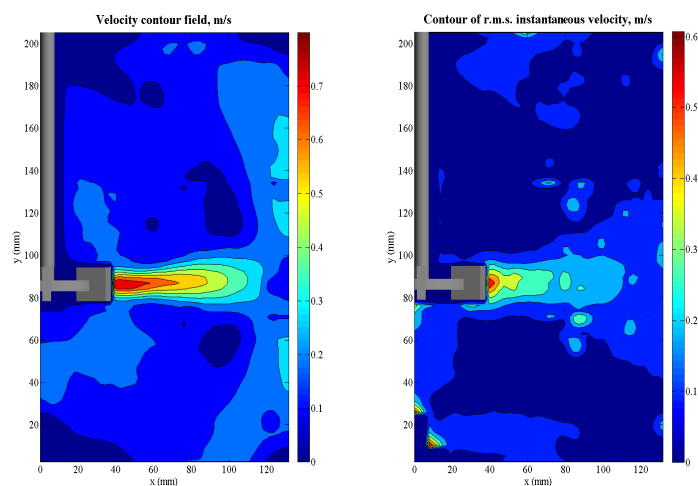


**Figure 12:** Velocity field contour (left) and contour of r.m.s. instantaneous velocity (right) for CMC 50000 (0.15 w%) water-based solution at 400 rpm.

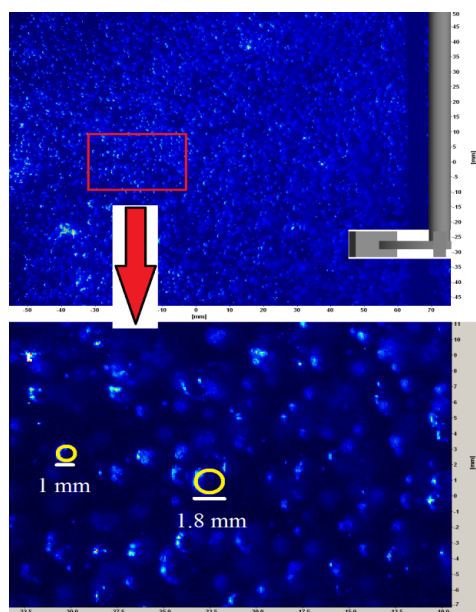


**Figure 13:** PIV frame with measured bubble sizes in CMC 50000 (0.15 %) water-based solution with salt addition (1 mol/L) at 400 rpm and 1.25 L/min gas flow rate.

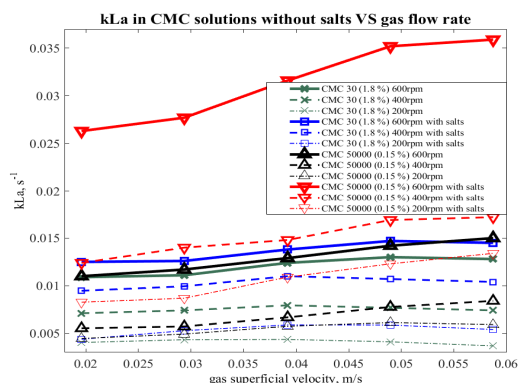


**Figure 14:** Measured overall  $k_L a$  via dynamic method for water-based solutions of CMC 50000 (0.15 %) and CMC 30 (1.8 w%) in gas-liquid STR alone and in presence of salts (1 mol/L).

primary phase flow has been resolved, converged solution results of which were used as initial data before activation of secondary phase. It is important to resolve primary phase accurately because primary phase hydrodynamics has great impact onto secondary phase. Before gas phase introduction in a transient manner, the simulation results of mixed non-Newtonian solution were validated against experimental results.

Qualitative analysis was performed by comparison of the velocity contour fields in vertical 2D plane sampled at the identical spatial position and it is shown in Figure 15. Particle Image Velocimetry used in this work measured only two velocity components out of three. Therefore, the velocity contour of CFD simulation results was adjusted for qualitative comparison and includes only radial and axial components. The tip speed of the Rushton turbine rotating at 400 rpm is 1.57 m/s. Radial and tangential at the tip of impeller can be equaled. However, accurate measurements of impeller jet-stream are complicated by rotating blades of the turbine and slight swinging of the shaft. That makes slight underprediction of maximum radial velocity component in the impeller region in PIV measurements.

Overall velocity distribution profiles look quite similar between CFD and PIV results. Both circulations taking place above and below jet-stream are captured at the same locations and in similar manner. However, jet-stream velocity field profile is a bit thicker in CFD contour. It could be explained by isotropic turbulence being used by the turbulence model, while the flow turbulence produced by a Rushton turbine is anisotropic [44,45].

Since velocity field contours comparison might be biased, the velocity components normalized with the tip speed were validated against experimental results in radial profiles (Figure 16). In order to sample hydrodynamics at different regions of the reactor, the profiles were taken at three vertical positions 30, 80 and 150 mm starting from the bottom. The simulation of shear-thinning flow agitated by the Rushton turbine describes the flow accurately.

Power draw was found experimentally by measuring torque via on-shaft torque transducer. The measured and simulated torque of

single phase mixing of CMC 50000 (0.15 w%) and the leaching slurry are presented in Table 6. As expected, the reduction of power draw is observed in case of gas-liquid mixing, because average density of multiphase solution is lower than of single phase. The torque of mixed CMC 50000 was simulated accurately.

**Aerated slurry mixing:** When the solution of the leaching slurry mixing has reached convergence, air has been introduced via velocity inlet in transient manner with 0.02 s as time step. The simulation lasted until the balance of air mass flow rate was observed. Average density of the suspension (30 w%) is 1570 kg/m<sup>3</sup>.

Average velocity field of the mixed slurry is presented in Figure 17. Maximum value of velocity magnitude is around tip speed. One may notice velocity contour of the air jet supplied via sparger.

As it was found during the gas bubbles study in PIV section, the BSD is very narrow in presence of electrolytes (0.1 mol/L). Therefore, 1.5 mm bubble size was used in the simulations. Specific volumetric surface area of secondary phase can be found as follows:

$$A_p = \frac{6\epsilon_p}{d_p}, \quad (25)$$

where  $\epsilon_p$  is the volume fraction of secondary phase, fraction.

The volume fraction and specific surface area of gas phase in the mixed slurry are shown in Figure 18. On one hand, high apparent viscosity of the leaching slurry increases dissipation rate of energy and power draw growth as a result. On other hand, higher viscosity hinders rise velocity of gas bubbles that leads to higher gas hold up almost twice up to 1.35% (Figure 6). Being small the bubbles follow the flow of the primary phase. The flow pattern of the radial impeller has two loops

Flow type		Torque, mN·m	
		Experimental	CFD
Single phase	CMC 50000 (0.15 w %)	68 ± 3	65.6
	Thiosulphate slurry	-	103.0
Multiphase	Thiosulphate slurry	-	101.2

**Table 6:** Simulated VS experimental torque.

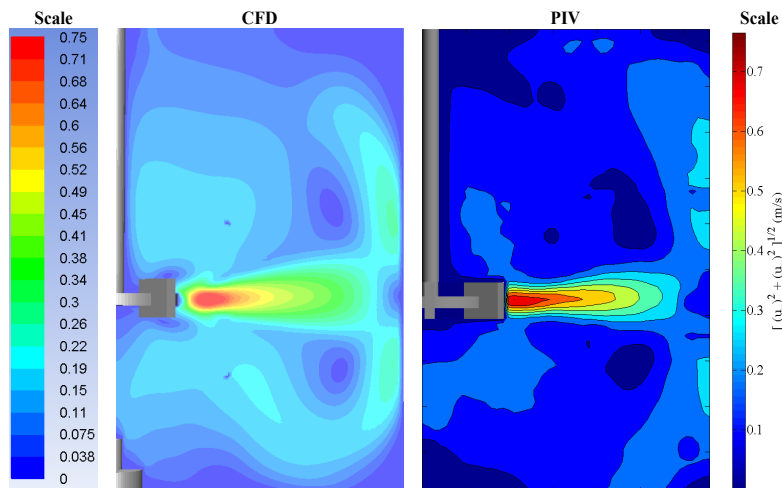


**Figure 15:** Average velocity field contours of water-based CMC 50000 (0.15 %) mixing at 6.67 rps modeled by CFD and measured by PIV.

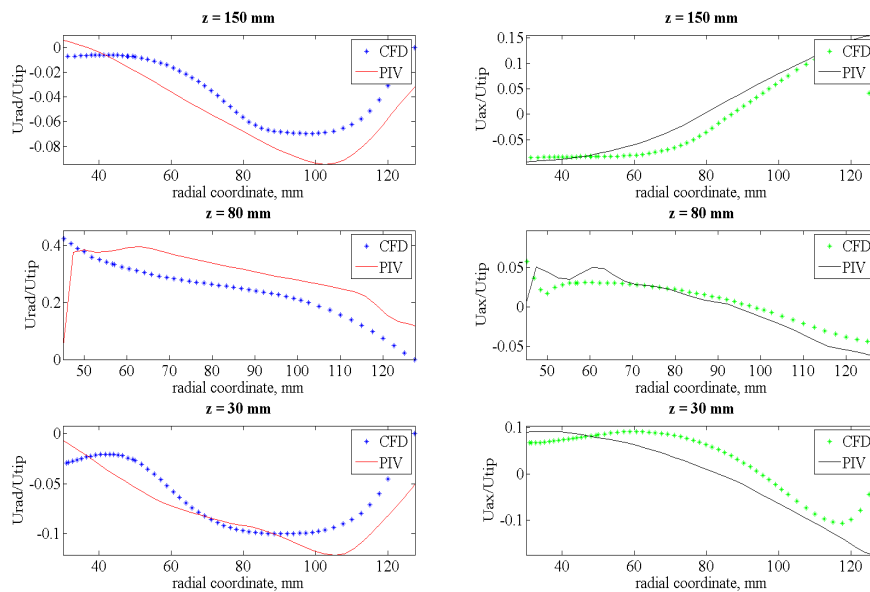


**Figure 16:** Comparison of normalized mean velocity components, measured by PIV and simulated by CFD of water-based CMC 50000 (0.15 %) mixing at 400 rpm, sampled at different vertical positions.

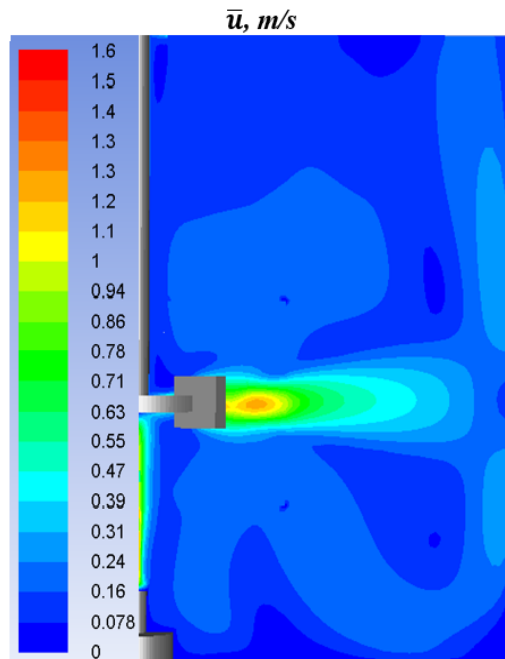


**Figure 17:** Average velocity contour fields of the slurry mixed at 400 rpm and aerated at 1.25 L/min ( $d_b=1.5$  mm).

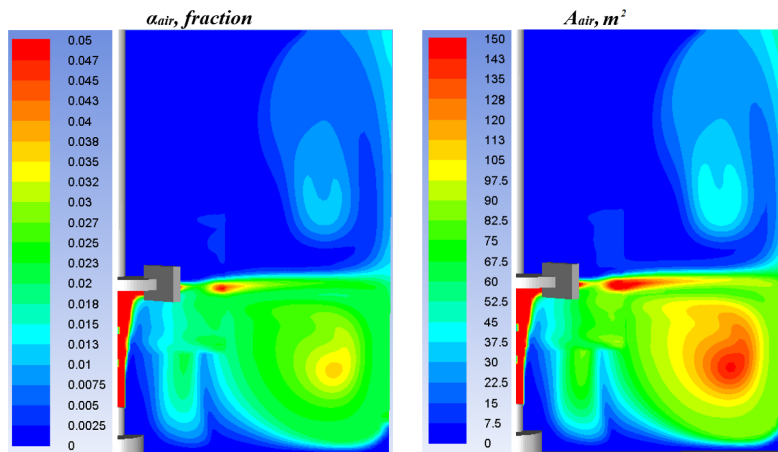


**Figure 18:** Contour of air volume fraction and specific surface area of the slurry mixed at 400 rpm and aerated at 1.25 L/min ( $d_b = 1.5$ mm).

of circulation. Following radial jet-flow of Rushton turbine they are dragged into down circulation while only small portion of gas goes up. The upper loop can also be distinguished since some amount of air bubbles are accumulated there. Total interfacial area is 0.26 m<sup>2</sup>.

**Mass transfer:** Mass transfer has been modelled using Eq. 2. Diffusivity of oxygen in liquid depends on physical properties of solution. According to Hung and Dinius [46], an increase of electrolytes concentration drops oxygen diffusivity. Diffusion coefficient of oxygen was calculated based on measured values of  $D_L(O_2)$  in water with presence of sodium sulphate. Linear interpolation from the above mentioned work resulted in  $D_L(O_2)=1.65 \times 10^{-9}$  m<sup>2</sup>/s. Influence of suspended solids interaction with gas bubbles onto diffusion coefficient is unknown and neglected in this work since particles are finely milled. Theoretically, tiny particles can partially cover gas-liquid interface and cause some decrease of oxygen mass transfer into the liquid phase. However, overall  $k_L a$  reduction should not be significant since interfacial area was increased drastically due to small bubbles. The distributions of specific volumetric mass transfer coefficient and mass transfer rate of oxygen are presented in Figure 19.

As it can be noticed from the distribution of specific mass transfer, the rate of mass transfer is higher in the regions where gas hold-up and energy dissipation rate are high. Therefore, the most intensive mass transfer is in the radial jet created by Rushton turbine. However, high gas hold-up of small bubbles, which do not coalesce, in the lower loop promotes mass transfer. Also, the region of moderate  $k_L a$  value, caused by bubble retention in the upper circulating loop can be seen. Overall simulated mass transfer in mixed thiosulphate slurry is 0.0183 s<sup>-1</sup>, which is 30% higher compared to the mass transfer measured in the mixed CMC 50000 (0.15%) solution under analogous operational conditions [47,48].

## Conclusions

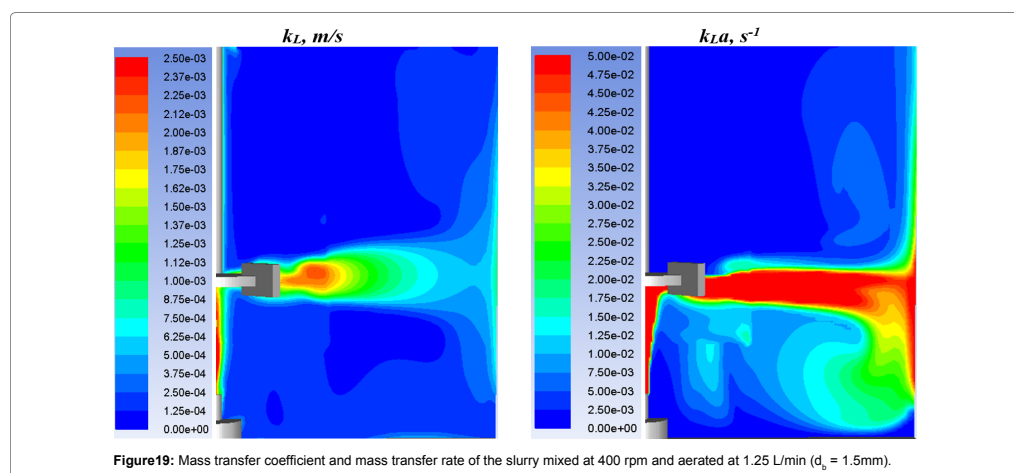
During this work mixing of aerated slurry on the example of thiosulphate leaching has been studied experimentally and simulated numerically. Rheology of the suspended solids was measured and found similar to those of shear-thinning fluids, which can be described

by power-law model. Therefore, the slurry was imitated with water-based Carboxy Methyl Cellulose solutions (CMC 30 and CMC 50000) in order to study mixing hydrodynamics experimentally. Velocity vectors and shear rate fields of CMC 50000 (0.15 w%), mixed at 400 rpm were measured by stereoscopic PIV in vertical 2D plane.

Volumetric mass transfer was measured by dynamic method in the CMC solutions over the range of operational conditions in absence and presence of electrolytes. Presence of electrolytes promotes mass transfer of oxygen. Electrolytes decrease viscosity by breaking molecular chains of CMC that increases mass transfer coefficient. Bubbles coalescence blockage causes significant growth of surface area. Measurements of volumetric mass transfer at constant operational conditions were made with stepwise addition of electrolytes. The study revealed that decrease of bubble size is dominating factor upon  $k_L a$  because viscosity drop takes place at lower salt amount. When level of electrolytes saturation is reached slight decrease of mass transfer was found at stable power draw. It could be due to contamination of the gas-liquid interfacial area.

Local gas hold-up in the aerated CMC 50000 (0.15 w%) solution was measured by EIT. Potentially the technique is capable to measure local gas hold-up in slurry. However, the sensitivity of the set-up was not enough to measure gas hold-up distribution of dispersed phase in electrolyte solution accurately.

The achieved experimental data was used in CFD modelling of the aerated slurry. Single phase non-Newtonian fluid mixing, modelled via effective viscosity, was validated against the PIV measurements of velocity components in vertical plane. Simulated and measured power consumptions of the CMC mixing at 400 rpm were in reasonable agreement. In the presence of electrolytes (0.1 mol/L) the bubble size in the CMC solution (400 rpm and 1.25 L/min) was found to be almost constant (1.5 mm). Multiphase mixing hydrodynamics of the thiosulphate slurry was modeled at the assumption of constant bubble size. Results of the simulation were presented and discussed. The simulated  $k_L a$  in the leaching pulp was compared to the measured one



in CMC 50000 (0.15 w%) under analogous operating conditions. It was found that bigger density of the leaching slurry caused higher global gas hold-up and hence oxygen mass transfer rate [49].

#### Acknowledgements

The authors are grateful to the Finnish Funding Agency TEKES and, in particular, to Outotec Finland Oy collaborating under FERMATRA project (908/31/2016 and 958/31/2016), for active supervision and financial support. Also, the work of Marko Vauhkonen and Gerardo González was supported by the Academy of Finland (Project 250215 Finnish Center of Excellence in Inverse Problems Research).

#### Nomenclature

Symbols	Meaning	Units
A	Signal amplitude	-
$A_i$	Interphase surface area	m <sup>2</sup>
$C_i$	Empirical coefficient	-
$C_D$	Drag force coefficient	-
$c_{\text{gas}}$	Oxygen concentration in gas phase	mol/m <sup>3</sup>
$C_{\text{liquid}}$	Oxygen concentration in liquid phase	mol/m <sup>3</sup>
$d_b$	Bubble diameter	m
$D_L$	Diffusivity in liquid phase	m <sup>2</sup> /s
$F_i$	Force	N
$h_{\text{gassed}}$	Surface level in gassed reactor	m
$h_{\text{ungassed}}$	Surface level in non-gassed reactor	m
K	Consistency index	Pa·s <sup>n</sup>
$K_{pq}$	Interphase exchange coefficient	-
k	Turbulence kinetic energy	m <sup>2</sup> /s <sup>2</sup>
$k_i$	Mass transfer coefficient in liquid phase	m/s
$k_a$	Volumetric mass transfer coefficient	s <sup>-1</sup>
$N_{\text{fine}}$	Number of cells in fine grid	-
$N_{\text{coarse}}$	Number of cells in coarse grid	-
n	Dimensionless flow behavior index	-
NRMSE	Normalized root mean square error	%
$\bar{p}$	Pressure	Pa
$P'$	Order of discretization	-
Re	Reynold's number	-
St	Stoke's number	-
$T_L$	Turbulence length scale	m
t	Time	s
$U_t$	Particle terminal velocity in turbulent flow	m/s
$U_s$	Particle terminal velocity in stagnant flow	m/s
$\bar{U}$	Mean velocity	m/s
$u_r$	Radial velocity component	m/s
$u_z$	Axial velocity component	m/s
V	Volume of reactor	m <sup>3</sup>
$v_{\text{image}}$	Imaginary part of measured voltage	V
$v_{\text{real}}$	Real part of measured voltage	V

Greek letters	Meaning	Units
$\alpha_i$	Phase volume fraction	-
$\epsilon$	Turbulence kinetic energy dissipation rate	m <sup>2</sup> /s <sup>3</sup>
$\epsilon_{\text{EIT}}$	Global gas hold-up measured by EIT	-
$\epsilon_{\Delta h}$	Global gas hold-up measured by level differencing	-
$\epsilon_{i,\text{EIT}}$	Local gas hold-up in element i, measured by EIT	-
$\mu$	Dynamic viscosity	Pa·s
$\mu_{\text{eff}}$	Effective viscosity	Pa·s
$\mu_{\text{turb}}$	Turbulent viscosity	Pa·s
$\eta$	Turbulence modification factor for drag force	-

$\rho$	Density	kg/m <sup>3</sup>
$\sigma_1$	Conductivity distribution of non-gassed mixing	S/m
$\sigma_2$	Conductivity distribution of gas-liquid mixing	S/m
$\tau$	Time constant	s
$\tau_b$	Relaxation time of bubble	s
$\tau_p$	Relaxation time of primary phase	s
$\nu$	Kinematic viscosity	m <sup>2</sup> /s
$\gamma$	Shear rate	s <sup>-1</sup>
$\lambda$	Kolmogorov length scale	m
$\phi$	Signal phase	-
$\phi_i$	Prediction of property value on grid i	-

Acronyms	Transcript
CCD	Charged-Couple Device
CFD	Computational Fluid Dynamics
CISTR	Continuous Ideally Stirred-Tank Reactor
CMC	Carboxy Methyl Cellulose
FEM	Finite Element Method
HWA	Hot Wire Anemometry
LDA	Laser Doppler Anemometry
MCR	Modular Compact Rheometer
Nd:Yag	Neodymium-doped yttrium aluminum garnet
PIV	Particle Image Velocimetry
UDV	Ultrasonic Doppler Anemometry
vvm	Volume of gas per volume of mixed solution per minute

#### References

- Jiang T, Chen J, Xu S (1993) A kinetic study of gold leaching with thiosulfate. Hydrometallurgy, Fundamentals, Technology and Innovations. AIME, pp: 119-126.
- Chen J, Deng T, Zhu G, Zhao J (1996) Leaching and recovery of gold in thiosulfate based system research summary at ICM. Transactions of Indian Institute of Metallurgy 49: 841-884.
- Naito K, Sheh C, Okabe T (1970) The chemical behaviour of low valence sulfur compounds. Decomposition and oxidation of tetrathionate in aqueous ammonia solution. Bulletin of the Chemical Society of Japan 43: 1372-1376.
- Groose AC, Dicoski GW, Shaw MJ, Haddad PR (2003) Leaching and recovery of gold using ammoniacal thiosulfate leach liquors (a review). Hydrometallurgy 69: 1-21.
- Joshi JB, Nere NK, Rane CV, Murthy BN, Mathpati CS, et al. (2013). CFD simulation of stirred tanks: comparison of turbulence models. Part II: axial flow impellers, multiple impellers and multiphase dispersions. Canadian Journal of Chemical Engineering 89: 754-816.
- Jensen K (2004) Flow measurements. 10th Brazilian Congress of Thermal Sciences and Engineering 26: 400-419.
- Khopkar A, Aubin J, Rubio-Atoche C, Xuereb C, Le Sauze N, et al. (2004) Flow Generated by Radial Flow Impellers: PIV Measurements and CFD Simulations. International Journal of Chemical Reactor Engineering 2: 1-14.
- Möilanen P (2009) Modelling gas-liquid flow and local mass transfer in stirred tanks. Helsinki, PhD, Finland: Helsinki University of Technology.
- Xinhong L, Yuyun B, Zhipeng LI, Zhengming G (2010) Analysis of turbulence structure in the stirred tank with a deep hollow blade disc turbine by time-resolved PIV. Fluid Flow and Transport Phenomena 18: 588-599.
- Busciglio A, Grisafi F, Scargiali F, Brucato A (2013) On the measurement of local gas hold-up, interfacial area and bubble size distribution in gas-liquid contactors via light sheet and image analysis: Imaging technique and experimental results. Chemical Engineering Science 102: 551-566.
- Takeda Y (1986) Velocity Measurement by Ultrasonic Doppler Shift Method. International Journal Heat and Fluid Flow 7: 313-318.
- Mann R, Dickin FJ, Wang M, Dyakowski T, Williams RA, et al. (1997) Application of electrical resistance tomography to interrogate mixing process at plant scale. Chemical Engineering Science 52: 2087-2097.

**Citation:** Gradov DV, González G, Vauhkonen M, Laari A, Koironen T (2017) Experimental and Numerical Study of Multiphase Mixing Hydrodynamics in Batch Stirred Tank Applied to Ammoniacal Thiosulphate Leaching of Gold. J Chem Eng Process Technol 8: 348. doi: [10.4172/2157-7048.1000348](https://doi.org/10.4172/2157-7048.1000348)

Page 17 of 17

13. Wang M, Dorward A, Vlaev D, Mann R (2000) Measurements of gas-liquid mixing in a stirred vessel using electrical resistance tomography (EIT). Chemical Engineering Journal 46: 93-98.
14. Kourunen J, Niiti T, Heikkinen LM (2011) Application of three-dimensional electrical resistance tomography to characterize gas hold-up distribution in laboratory flotation cell. Minerals Engineering 24: 1677-1686.
15. Arizmendi-Morquero AM, Perez-Garibay R, Uribe-Salas A, Nava-Alonso F (2002) On-line solids hold-up measurement in mineral slurries by the standard addition method. Minerals Engineering 15: 61-64.
16. Gomez CO, Finch JA (2007) Gas dispersion measurements in flotation cells. International Journal of Mineral Processing 84: 51-58.
17. Higbie R (1935) The rate of absorption of a pure gas into a still liquid during short periods of exposure. Institution of Chemical Engineers 35: 36-60.
18. Kawase Y, Halard B, Moo-Young M (1992) Liquid-phase mass transfer coefficients in bioreactors. Biotechnology and Bioengineering 93: 1133-1140.
19. Garcia-Ochoa F, Gomez E (2004) Theoretical prediction of gas-liquid mass transfer coefficient, specific area and hold-up in sparged stirred tanks. Chemical Engineering Science 59: 2489-2501.
20. Lampinen M, Laari A, Turunen I (2015) Ammoniacal thiosulfate leaching of pressure oxidized sulfide gold concentrate with low reagent consumption. Hydrometallurgy 151: 1-9.
21. Sharikov FY, Zhukov VV, Lampinen M (2012) Investigation of Gold Oxidized Leaching Process from Concentrate of Base Ore by Utilization Calve Calorimetry. Problem Definition and First Results, Material Investigation by Utilization Methods of Thermal Analysis, Calorimetry and Gas Trapping. International Conference Reports. Saint-Petersburg: Poltorak: 59-61.
22. Wuestenberg T (2014) Cellulose and Cellulose Derivatives in the Food Industry: Fundamentals and Applications. Germany: Wiley-VCH.
23. Kourunen J (2009) Imaging of Mixing in Selected Industrial Processes Using Electrical Resistance Tomography. Kuopio, PhD Thesis, Finland: University of Eastern Finland.
24. Heikkinen L (2005) Statistical Estimation Methods for Electrical Process Tomography. Kuopio, PhD Thesis, Finland: University of Kuopio.
25. Holden PJ, Wang M, Mann R, Dicki FJ, Edwards RB (1999) On Detecting Mixing Pathologies Inside a Stirred Vessel Using Electrical Resistance Tomography. Chemical Engineering Research and Design 77: 709-712.
26. Tarkiff MS, Hamzah AA, Karnarudin SK, Abdullah J (2009) Electrical Resistance Tomography Investigation of Gas Dispersion in Gas-Liquid Mixing in an Agitated Vessel. Journal of Applied Science 9: 3110-3115.
27. Bawadi A, Chirag D, Nguyen T, Cooper CG, Adesoji AA (2011) Electrical resistance tomography-assisted analysis of dispersed phase hold-up in a gas-inducing mechanically stirred vessel. Chemical Engineering Science 66: 5648-5662.
28. Montante G, Paglianti A (2015) Gas hold-up distribution and mixing time in gas-liquid stirred tanks. Chemical Engineering Journal 279: 648-658.
29. Adrian R (2011) Bibliography of particle image velocimetry using imaging methods: 1917 - 1995. University of Illinois. Illinois: TAM Report 817.
30. Haario H (1994) MODEST User's guide. ProfMath Oy, Helsinki, Finland.
31. Van't Riet K (1979) Review of measuring methods and results in non-viscous gas-liquid mass transfer in stirred tanks. Industrial and Engineering Chemistry Process Design and Development 18: 357-364.
32. Rucht G, Dunn IJ, Bourne JR (1981) Comparison of dynamic oxygen electrode methods for the measurement of kLa. Biotechnology and Bioengineering 23: 277-290.
33. Bhutani G, Cilliers JJ, Brito-Parada PR (2017) A three-dimensional numerical framework for the modeling of the pulp phase in froth flotation Computational Modeling 17: 1-8.
34. Gradov DV, Laari A, Turunen I, Koironen T (2016) Experimentally Validated CFD Model for Gas-Liquid Flow in a Round-Bottom Stirred Tank Equipped with Rushton Turbine. International Journal of Chemical Reactor Engineering 15: 1-20.
35. Holden J (1955) Fundamentals of the hydrodynamics mechanism of splitting in dispersion processes. American Institute of Chemical Engineers Journal 289-295.
36. Schiller L, Naumann Z (1935) A Drag Coefficient Correlation. Z. Ver. Deutsch. Ing 77: 318-320.
37. Brucato A, Grisafi F, Montante G (1998) Particle drag coefficients in turbulent fluids. Chemical Engineering Science 53: 3295-3314.
38. Scot Blair GW (1939) An Introduction to Industrial Rheology. Journal of Physical Chemistry 43: 853 - 864.
39. Rewatkar VB, Deshpande AJ, Pandit AB, Joshi JB (1993) Gas hold-up behaviour of mechanically agitated gas-liquid reactors using pitched blade down flow turbines. Canadian Journal of Chemical Engineering 71: 226-237.
40. Kraume M, Zehner P (2001) Experience with Experimental Standards for Measurements of Various Parameters in Stirred Tanks. Chemical Engineering Research and Design 79: 811-818.
41. Laakkonen M (2006) Development and Validation of Mass Transfer Models for the Design of Agitated Gas-Liquid Reactors. Helsinki, PhD, Finland: Helsinki University of Technology.
42. Prince MJ, Blanch HW (1990) Transition Electrolyte Concentration for Bubble Coalescence. American Institute of Chemical Engineers Journal 36: 1425-1429.
43. Wang H, Zhai Z (2012) Analyzing grid independency and numerical viscosity of computational fluid dynamics for indoor environment applications. Building and Environment 52: 107-118.
44. Lee KC, Yianneskis M (1998) Turbulence Properties of the Impeller Stream of a Rushton Turbine. American Institute of Chemical Engineering 44: 13-24.
45. Fentiman NJ, Lee KC, Paul GR, Yianneskis M (1999) On the trailing vortices around hydrofoil impeller blades. Chemical Engineering Research and Design 77: 731-740.
46. Hung GW, Dinius RH (1972) Diffusivity of oxygen in electrolyte solutions. Journal of Chemical & Engineering Data 17: 449-451.
47. Busciglioni A, Grisafi F, Montante G (1998) Particle drag coefficients in turbulent fluids. Chemical Engineering Science 53: 3295-3314.
48. Hugo P, Steinbach J (1986) A comparison of the limits of safe operation of a SBR and a CSTR. Chemical Engineering Science 41: 1081-1087.
49. Lasa HI (1986) Chemical Reactor Design and Technology. Ontario, Canada: University of Western Ontario.

**Citation:** Gradov DV, González G, Vauhkonen M, Laari A, Koironen T (2017) Experimental and Numerical Study of Multiphase Mixing Hydrodynamics in Batch Stirred Tank Applied to Ammoniacal Thiosulphate Leaching of Gold. J Chem Eng Process Technol 8: 348. doi: [10.4172/2157-7048.1000348](https://doi.org/10.4172/2157-7048.1000348)

#### OMICS International: Open Access Publication Benefits & Features

##### Unique features:

- Increased global visibility of articles through worldwide distribution and indexing
- Showcasing recent research output in a timely and updated manner
- Special issues on the current trends of scientific research

##### Special features:

- 700+ Open Access Journals
- 50,000+ editorial team
- Rapid review process
- Quality and quick editorial, review and publication processing
- Indexing at major indexing services
- Sharing Option: Social Networking Enabled
- Authors, Reviewers and Editors rewarded with online Scientific Credits
- Better discount for your subsequent articles

Submit your manuscript at: <http://www.omicsonline.org/submit>





## **Publication IV**

Gradov, D. V., González, G., Vauhkonen, M., Laari, A., and Koiranen, T.  
**Experimental investigation of reagent feeding point location in a semi-batch  
precipitation process**

Reprinted with permission from  
*Chemical Engineering Science*  
Vol. 190, pp. 361-369, 2018  
© Elsevier





Contents lists available at ScienceDirect

## Chemical Engineering Science

journal homepage: [www.elsevier.com/locate/ces](http://www.elsevier.com/locate/ces)

# Experimental investigation of reagent feeding point location in a semi-batch precipitation process

Dmitry Vladimirovich Gradov<sup>a,\*</sup>, Gerardo González<sup>b</sup>, Marko Vauhkonen<sup>b</sup>, Arto Laari<sup>a</sup>, Tuomas Koiranen<sup>a</sup><sup>a</sup> School of Engineering Science, Lappeenranta University of Technology, P.O. Box 20, FI-53851 Lappeenranta, Finland<sup>b</sup> Department of Applied Physics, Eastern University of Finland, P.O. Box 1627, FI-70211 Kuopio, Finland

## H I G H L I G H T S

- Study of the effect of reagent feeding point location in STR on BaSO<sub>4</sub> crystallization.
- Visualization of temporal history of BaSO<sub>4</sub> precipitation by EIT.
- CFD model of the crystallization hydrodynamics in a batch STR.
- Validation of Rasmuson's TR-number.
- The effect of macro and mesomixing on d<sub>90</sub>, CSD and morphology of BaSO<sub>4</sub> crystals.

## A R T I C L E I N F O

## Article history:

Received 20 January 2018

Received in revised form 22 April 2018

Accepted 15 June 2018

Available online 18 June 2018

## Keywords:

Crystallization

Precipitation

Mixing

EIT

CFD

## A B S T R A C T

This research is dedicated to a study of BaSO<sub>4</sub> crystallization process in a batch stirred reactor. The temporal development of the precipitation process is measured by conductivity at global and local levels. The effect of the macromixing on temporal evolution of local conductivity is shown in the experimental results obtained by EIT. The effects of the mixing intensity and the BaCl<sub>2</sub> feed location on the CSD and morphology are considered. Morphology of the crystals was found to be independent from mixing intensity in the studied range. The CFD simulations of the mixing hydrodynamics were used to estimate the influence of turbulent dispersion on crystal size. The correlation of mean crystal size and TR number proposed by (Torbacke and Rasmuson, 2001) has been checked against d<sub>90</sub> in the range of 10<sup>3</sup>–10<sup>5</sup> and showed reasonable agreement. The scatter of the results plotted can be explained by the macromixing scale and critical time of the crystallization not included into TR number. The combined effect of mixing at meso and macro scales onto crystal size is proposed.

© 2018 Elsevier Ltd. All rights reserved.

## 1. Introduction

Precipitation plays an important role in chemical and pharmaceutical industry. Crystallization process of reaction products facilitates solid liquid separation, characteristics of which affect quality of final product. Batch wise crystallization has lower production capacity compared to continuous one. Nevertheless, it was actively studied by numerous researchers due to Stirred Tank Reactor (STR) simplicity, isolation from upstream process and transient manner.

Main parameters, controlling crystallization process, have been the objects of intensive research. The mechanism of crystallization is described comprehensively by Mullin (2001). Influence of

mixing speed onto Crystal Size Distribution (CSD) has been studied earlier (Kim and Tarbell, 1999; Torbacke and Rasmuson, 2004; Wang et al., 2009; Steyer et al., 2012). Precipitation of barium sulphate was used as a typical crystallization process to investigate influence of mixing at all scales by Torbacke and Rasmuson (2001). They proposed a dimensionless number (TR-number Eq. (1)) evaluating ratio of reagent feeding time and specific spatial mesomixing time scale. This dimensionless number correlates well with mean weight particle size within the studied range 10<sup>4</sup> to 10<sup>6</sup>. However, there is a scatter of particle sizes at close TR values, which tells that the number proposed is useful but doesn't take into account some parameters affecting crystallization.

$$TR = \frac{t_{feed}}{t_{meso}} = \frac{U_{bulk}}{d} t_{feed}, \quad (1)$$

where  $t_{feed}$  is the time of reagent feed, s;  $t_{meso}$  is the mesomixing time scale, s;  $U_{res}$  is the bulk velocity, m/s;  $d$  is the hydraulic

\* Corresponding author.

E-mail addresses: [dmitry.gradov@lut.fi](mailto:dmitry.gradov@lut.fi) (D.V. Gradov), [gerardo.delmuro@uef.fi](mailto:gerardo.delmuro@uef.fi) (G. González), [marko.vauhkonen@uef.fi](mailto:marko.vauhkonen@uef.fi) (M. Vauhkonen), [arto.laari@lut.fi](mailto:arto.laari@lut.fi) (A. Laari), [tuomas.koiranen@lut.fi](mailto:tuomas.koiranen@lut.fi) (T. Koiranen).

<https://doi.org/10.1016/j.ces.2018.06.042>

0009-2509/© 2018 Elsevier Ltd. All rights reserved.

Notation			
Symbols	meaning, units		
A	signal amplitude, –	$\sigma_1$	conductivity distribution of homogeneous mixing, Sm/m
d	hydraulic diameter of injection pipe, m	$\sigma_2$	conductivity distribution of non-homogeneous mixing, Sm/m
$D_t$	turbulent dispersion, $m^2/s$	$\Delta\sigma$	resulting conductivity distribution of gas-liquid mixing, Sm/m
n	number of samples, –	$\tau$	torque, N-m
N	mixing speed, rps	$v(i)$	voltage at <i>i</i> -th electrode, V
$N_{el}$	number of electrodes, –	$v_{image}$	imaginary part of measured voltage, V
$N_i$	number of grid cells in <i>i</i> th grid, –	$v_{real}$	real part of measured voltage, V
$N_q$	dimensionless pumping number of impeller, –	$\phi$	signal phase, V
$p^*$	order of discretization, –	$\phi_1$	CFD simulation results on coarse grid, –
P	mixing power, W	$\phi_2$	CFD simulation results on fine grid, –
St	Stoke's number, –	Acronyms	Transcript
$t_{feed}$	time of reactant injection, s	CFD	computational fluid dynamics
$t_{macro}$	macromixing time scale, s	STR	stirred-tank reactor
$t_{meso}$	mesomixing time scale, s	CSD	crystal size distribution
$t_D$	turbulence dispersion time scale, s	EIT	electric impedance tomography
TR	TR-number, –	NRMSE	normalized root mean square error
$U_{bulk}$	velocity of local bulk flow, m/s	PIV	particle image velocimetry
V	volume of reactor, $m^3$	SEM	scanning electronic microscopy
Greek letters	Meaning, units		
$\varepsilon$	turbulence energy dissipation rate, $m^2/s^3$		
k	turbulence kinetic energy, $m^2/s^2$		

diameter of the feeding pipe, m. This formulation does not take into account several important factors such as bulk flow direction relative to the feed flow, feed velocity magnitude, global flow pattern in reactor, and cumulative time of chemical reaction and crystallization, which is critical.

Overall flow pattern of agitated Newtonian liquid in STR has been simulated accurately using Computational Fluid Dynamics (CFD) modelling (Yeoh et al., 2004; Bakker and Oshinowo, 2004; Joshi et al., 2011; Gradov et al., 2016; Lane, 2017). Barrett et al. (2011) performed CFD simulations to assess the influence of meso and micromixing onto premature nucleation of benzoic acid in a batch reactor. In their research, different time scales were estimated and compared in order to define effect of mixing scales. The macromixing (Eq. (2)) as well as turbulent dispersion (Eq. (4)) time scales were found to have major influence on the crystallization process while the effect of micromixing and mesomixing due to internal convection is negligible.

$$t_{macro} = \frac{V}{N_q N D^3} \quad (2)$$

$$D_t = 0.1 \frac{k^2}{\varepsilon} \quad (3)$$

$$t_D = \frac{Q_{feed}}{U_{bulk} D_t}, \quad (4)$$

where  $V$  is the reactor volume,  $m^3$ ,  $N_q$  is the impeller pumping number (0.72 for Rushton turbine),  $N$  is the mixing speed, rps,  $D$  is the impeller diameter, m,  $k$  is the turbulence kinetic energy,  $m^2/s^2$ ,  $\varepsilon$  is the energy dissipation rate,  $m^2/s^3$ ,  $Q_{feed}$  is the volumetric flow rate of fed reagent,  $m^3/s$ .

Visualization of crystallization process can be done with a help of non-intrusive technique Electrical Impedance Tomography (EIT). Research group from The University of Manchester described successful applications of EIT technique for stirred tanks to visualize precipitation process (Wabo et al., 2004; Kagoshima and Mann,

2005; Stanley et al., 2005; Mann, 2009). They demonstrated that EIT is a suitable technique to study conductive fluid systems that are opaque. Reaction visualization pattern as well as local conductivity readings were in reasonable agreement with independent measurements.

The purpose of this research is to consider effect of macro and mesomixing on crystal size and morphology by studying an example of classical precipitation process of barium sulphate in a batch STR at lab scale. EIT instrument is applied to measure temporal local conductivities in the batch STR to reveal the spreading pattern of chemical reaction and precipitation of  $BaSO_4$ . Numerical simulation is used to estimate local mesomixing via fluid flow hydrodynamics modelling. The effect of turbulent mesomixing is considered and discussed.

## 2. Materials and methods

### 2.1. Batch crystallization set-up

A lab-scale baffled stirred reactor, made of plexiglass, with standard six-blade Rushton turbine was investigated in the current research. A schematic representation of the vessel geometry and its dimensional parameters are presented in Fig. 1a. The impeller clearance was set at the distance equal to its diameter from the bottom of the tank. Power draw was measured by on-shaft torque meter.

Barium sulphate precipitation was arranged as a batch process where barium chloride (0.1 M) is injected into predissolved water solution of sodium sulphate (0.1 M) at a constant flow rate in several spatial points as it is illustrated in Fig. 1b. A peristaltic pump Masterflex L/S was used to maintain stable 2 mL/s flowrate of the reagent through a glass pipet ( $d = 1$  mm) during 50 s. The experimental time line is presented in Fig. 2. The batch process has been performed at different volumetric power inputs: 19, 63 and 500 W/ $m^3$  that correspond to 2.5, 5 and 7.5 rps of the stirring speed. The global conductivity has been tracked during each

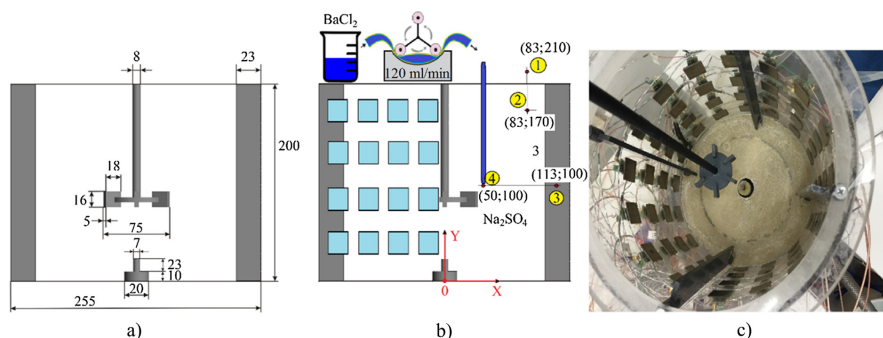


Fig. 1. Batch crystallization set-up. a – reactor sizing, mm, b – schematic representation of crystallization set-up with spatial coordinates of  $\text{BaCl}_2$  (1 M) injection points, specified in mm, into water solution of  $\text{Na}_2\text{SO}_4$  (0.01 M), c – photo of reactor equipped with electrodes for EIT experiments.

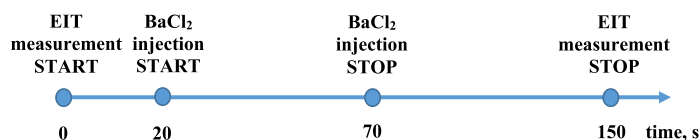


Fig. 2. Temporal sequence of actions in EIT precipitation tests.

experiment by a conduct meter Consort C3010. All the 12 experiments were carried out at constant temperature 20 °C.

At the end of each test, samples were taken from homogeneous outflow for analyzing barium sulphate crystals. Crystal size distribution was measured by Laser Diffraction method in a particle size analyzer MasterSizer 3000 produced by Malvern company. Barium sulphate crystals (refractive index 1.637) have irregular shape, therefore Mie's theory was applied to find CSD using non-spherical option. Crystal morphology has been studied by Scanning Electron Microscopy (SEM) Hitachi SU 3500.

## 2.2. EIT

EIT technique employs current injections to measure responding voltages at electrodes placed around flow. Therefore, the reactor was equipped with electrodes on the walls arranged in rows. In particular, 4 rows of 16 electrodes made of stainless steel were mounted around the tank perimeter (Fig. 1b, c). Thus, approximate resolution of the spatial reconstruction is roughly 2 cm<sup>3</sup>. The EIT set-up, used in the experiments, consisted of a signal generator, receiver, controller, and computer. The purpose of the signal generator is to produce current pulses of constant voltage to the solution according to a predefined scheme of pulses order. There are two possible scenarios for the order of current injections to be applied. The voltage injections can be sent pair-wise e.g. adjacent pairs of electrodes or by multiple electrodes simultaneously. In both cases, voltages are measured at all electrodes. Then, the obtained signal goes to demodulation process, where the input voltage is decomposed into the real and imaginary parts that are needed to get the phase and amplitude according to the following formulations (Kourunen, 2009):

$$v_{\text{real}} = \frac{2}{N_{\text{el}}} \sum_{i=0}^{N-1} v(i) \sin \frac{2\pi i}{N_{\text{el}}} \quad (5)$$

$$v_{\text{image}} = \frac{2}{N_{\text{el}}} \sum_{i=0}^{N-1} v(i) \cos \frac{2\pi i}{N_{\text{el}}} \quad (6)$$

$$A = \frac{2}{N_{\text{el}}} \sqrt{v_{\text{real}}^2 + v_{\text{image}}^2} \quad (7)$$

$$\varphi = \tan^{-1} v_{\text{image}} / v_{\text{real}} \quad (8)$$

where  $N_{\text{el}}$  is the number of electrodes,  $v(i)$  is the measured voltage at  $i$ -th electrode,  $V$ ,  $v_{\text{real}}$  is the real part of measured voltage,  $V$ ,  $v_{\text{image}}$  is the imaginary part of measured voltage,  $V$ ,  $\varphi$  and  $A$  are the signal phase and amplitude correspondingly.

Finding the conductivity distribution out of the measured voltage outcomes of the preset current injections represents itself an inverse problem. Computation of conductivity distribution is a challenging task to be solved since even a slight shift of voltages may be the result of a significant change of the conductivity distribution in the solution, meaning that the equation might have several solutions. Therefore, some additional information about the object of study is needed to solve the inverse problem. Prior information on homogeneous conductivity distribution may be achieved statistically and then used as reference (Heikkinen, 2005, Kourunen, 2009).

The difference method exploits measurements of homogeneous mixed solution as a reference in order to get background conductivity distribution. Non-homogeneous conductivity distribution caused by ions concentration gradients in the reactor when a reagent is introduced can be found as follows (Heikkinen, 2005):

$$\Delta\sigma = \frac{2(\sigma_1 - \sigma_2)}{2\sigma_1 + \sigma_2} \quad (9)$$

where  $\sigma_1$  and  $\sigma_2$  are the conductivity distributions of homogeneous and non-homogeneous solutions correspondingly, Sm/m. Thereby, the difference method automatically removes the influence of the

non-conductive parts presented in the tank such as baffles, impeller etc.

Current injections values are dictated by conductivity of the studied solution. The higher the solution conductivity, the higher the current injections are required in order to increase sensitivity of the measuring system.

### 2.3. CFD model of mixing hydrodynamics

Mesomixing time scale can be estimated using local turbulence kinetic energy and the energy dissipation rate and it is known to have an impact onto CSD of  $\text{BaSO}_4$  (Zauner and Jones, 2000). Therefore, RANS CFD simulations of the mixing in the STR were performed to study the correlation of CSD and the turbulent dispersion in the local regions of barium chloride injections. The CFD model is based on the assumption of crystals-liquid interaction being negligible so that the crystals follow the flow ( $St_{max} \approx 0.01 \ll 1$ ). The turbulence has been simulated using  $k-\epsilon$  Realizable model, which is designed for strong swirling flows (Shih et al. 1995). Multiple Reference Frame approach was used to simulate the impeller motion in steady state manner. Ansys Fluent 18.0 CFD software was used.

In order to minimize the influence of the spatial discretization onto the results of the numerical simulations, a grid test has been made using five different grids. The simulations of water mixing at 6.67 rps were used in the grid independence study. The reactor geometry was meshed with doubling factor and the scaling uniformity was maintained as well. The flow differs significantly in the STR, therefore 14 points of velocity have been sampled in the reactor domain. Normalized Root Mean Square Error (NRMSE) index (Eq. (10)) was employed as a criterion for the grid independency estimation (Wang and Zhai, 2012). According to the authors, grid difference might be considered negligible if NRMSE value is less than 10%.

$$NRMSE = \frac{3}{\left(\frac{N_1}{N_2}\right)^{p^*} - 1} \sqrt{\frac{\sum_{i=1}^n (\varphi_1(i) - \varphi_2(i))^2}{\sum_{i=1}^n (\varphi_1(i))^2}} \cdot 100\%, \quad (10)$$

where  $N_i$  is the number of cells in a grid (advised to keep grid size ratio above 1.3 (Celik et al. 2008)),  $p^*$  is the order of discretization,  $n$  is the number of samples,  $\varphi_1$  and  $\varphi_2$  are the predictions on fine and coarse grids accordingly.

During the mesh size independence test, simulations were performed with second order discretization scheme. Results, presented in Table 1, clearly indicate grid 4 to be optimal one for the needs of the current study.

Second order discretization scheme was used in the mixing tank simulations at the preset convergence level of  $10^{-5}$  for all variables. Each simulation took around 6 h of real computing time on a computer with 4 processors and 16 Gb RAM.

## 3. Results and discussion

### 3.1. Global conductivity

Barium sulphate precipitation process takes place when reacting ions are mixed, therefore, temporal history of global conductivity can describe mixing of a solution of contacting electrolytes such as those used in the current research. A conductivity probe, placed in the most turbulent zone in front of the stirrer, was tracking the global conductivity dynamics, the example of which is presented in Fig. 3.

The solutions of the predissolved sodium sulphate had the conductivity at the same level during the first 20 s until barium chloride has been introduced. Two processes occurred simultaneously accompanying the reagent feeding that affected the global conductivity value. The raise of the ions concentration in the solution caused the growth of the conductivity. The  $\text{BaSO}_4$  precipitation acted opposite since vacant ions were bound and crystalized. Nevertheless, the overall conductivity jump was clearly observed. The injected electrolytes followed through several flow circulation loops until the solution has become homogeneous. Detection of mixing circulations depends on conductivity probe location and two circles can be noticed clearly in Fig. 3. The mixing intensity is proportional to the height of the first pike and vice versa to the second one denoting logical correlation between stirring speed and mixing time.

### 3.2. Spatial specific conductivity distribution

Global conductivity cannot give detailed information on local conductivity characterizing the development of the reaction and precipitation processes in time and space. The results of EIT measurements are presented in Table 2. The contours of conductivity spatial distribution were sampled at a mid-plane crossing the

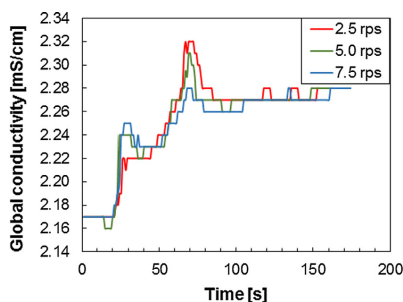


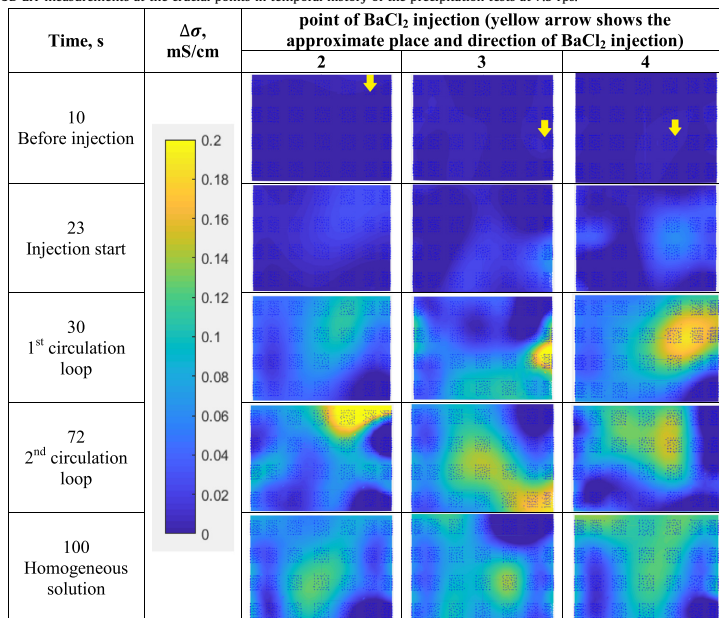
Fig. 3. Temporal history of global conductivity over the range of mixing speeds during  $\text{BaSO}_4$  precipitation at impeller injection of  $\text{BaCl}_2$ .

Table 1  
Grid test results of water mixing at 6.67 rps in STR.

Grid name	Number of elements	Torque, mN·m	$\int kdV, \text{m}^2/\text{s}^2 \cdot 10^{-5}$	$\int \epsilon dV, \text{m}^2/\text{s}^3 \cdot 10^{-5}$	NRMSE ( $\bar{u}$ ), %
1	108 276	54.0	9.9	139.2	20
2	269 654	56.0	10.8	161.2	13
3	464 532	56.6	10.7	166.4	15
4	754 056	65.6	13.0	209.1	9
5	1 969 376	64.4	12.6	208.5	0
Measured experimentally		65 ± 3			

**Table 2**

Cross sectional slices of 3D EIT measurements at the crucial points in temporal history of the precipitation tests at 7.5 rps.



feeding pipe. The temporal progress of the conductivity distributions in the vertical mid-section is split into five main stage namely: the initial stage, the start of injection, the first and the second mixing loops captured by the temporal history of the global conductivity dynamics, and the final homogeneous stage. It must be mentioned, that all the results presented have been achieved by averaging process over 2–3 s of real time to exclude phantom readings. In order to present the process development in time, all the contours were adjusted by the same color bar. The common color bar denotes conductivity difference so that 0 corresponds to the conductivity level at the initial stage and equal to 2.17 mS/cm. Yellow arrows show the locations of the reagent injections. Squares, made of blue crosses, are placed regularly and represent spatial positions of the EIT electrodes to ease the contours reading.

The initial stage is characterized by the stable conductivity level except for the regions where the feeding pipe was placed and some small leakage of barium chloride occurred. At the second stage, one can observe the areas of introduced electrolytes spreading after 1–4 s after the injection. Mainly, they locate near the feeding points, however the circulation loop they follow can be identified. The ions injected at point 3 clearly got into the lower loop created by the radial impeller, while points 2 and 4 stayed in the upper one. In 7 s the first mixing circle has been detected by the global conductivity. The analogous jump in local conductivity can be detected at the locations corresponding to the reagent plumes. The second mixing circle is characterized by high concentration of ions since the reagents have been injecting during 50 s but the areas of high concentration are bigger. Since the start of the BaCl<sub>2</sub> injection until the end of feeding, the influence of the mixing loop onto the reaction progressing can be observed. More homogeneous conductivity distributions can be observed at the last stage. However, some regions of local extremes denote that the precipitation process was not over.

### 3.3. Crystal size distribution

Figs. 4 and 5 describe the influence of the mixing intensity and BaCl<sub>2</sub> feeding location onto CSD.

As it can be seen in Fig. 4, an increase of the mixing intensity pushes the CSD to the right hand side towards bigger size classes that supports the theoretical crystallization mechanism described earlier. Similar trend is observed in Fig. 5.

Barium sulphate have been distributed equally in the domain of the reactor after some period of time in all the tests. Therefore, the supersaturation concentrations have been mainly affected by the mesomixing in the areas of the reagent introductions where the primary stable nuclei have been formed. Similar shapes of the CSDs denote that further crystals growth was also identical.

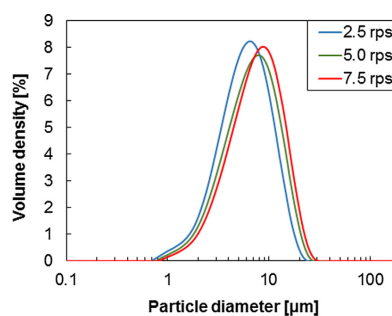


**Fig. 4.** Effect of mixing speed onto CSD of BaSO<sub>4</sub> at BaCl<sub>2</sub> injections near the impeller at point 1 (specific spatial position of point 1 is shown in Fig. 1).



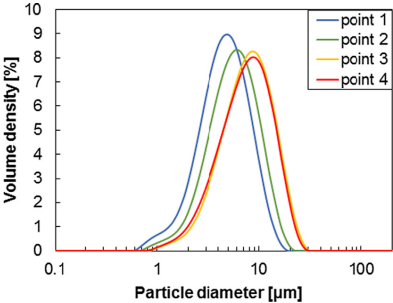


Fig. 5. CSD of BaSO<sub>4</sub> at different spatial locations of BaCl<sub>2</sub> injections (spatial locations of the injection points are shown in Fig. 1) at 7.5 rps.

3.4. Crystals morphology

The results of SEM analysis of the crystals, formed at different mixing intensities when BaCl<sub>2</sub> was injected near impeller, are presented in Table 3. The crystals were scanned at 100, 20 and 5 μm scale.

All the photos clearly show similar shapes of crystals regardless the mixing intensity applied. The formed crystals can be described as flakes of irregular shape and form with torn edges and holes. At the scale of 20 μm, the agglomerates are obvious. Similar in morphology crystals were found by Phillips et al., 1999, Wong et al., 2001, Stanley, 2006.

3.5. Effect of mesomixing

Crucial data for the mesomixing time scale have been obtained with the help of CFD modelling. The simulation and experimental

results of the single phase mixing hydrodynamics at several impeller speeds are presented in Table 4.

The spatial discretization used in the CFD simulations caused the underprediction of local  $\epsilon$  that decreases as the mixing intensity falls. Therefore, the major lump of the underestimated energy dissipation locates in the area of the radial jet flow created by the

Table 4  
Simulation and experimental results of water mixing in STR.

Mixing speed, rps	CFD			Experiments	
	P( $\epsilon$ ), W	P( $\tau$ ), W	Error, %	P( $\tau$ ), W	$\bar{\epsilon}$ , W/kg
2.5	0.12	0.15	23	0.13	0.013
5	0.92	1.24	25	1.18	0.118
7.5	3.12	4.10	25	3.90	0.390

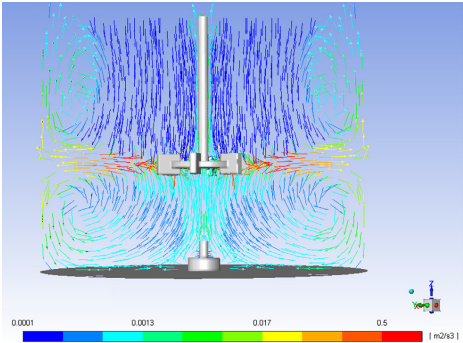


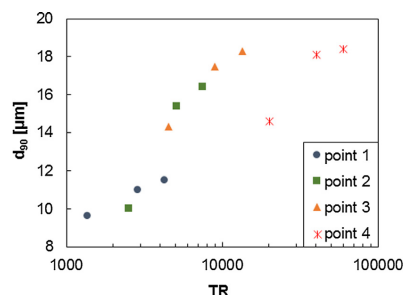
Fig. 6. Velocity vectors field of water mixing at 2.5 rps colored by specific energy dissipation rate.

Table 3  
SEM analysis of the BaSO<sub>4</sub> crystals formed at different mixing intensity.

Scale	Impeller speed, rps		
	2.5	5	7.5
100			
20			
5			

**Table 5**  
Simulation results of energy dissipation rate at the points of  $\text{BaCl}_2$  injections,  $\text{m}^2/\text{s}^3$ .

Mixing speed, rps	Points of $\text{BaCl}_2$ injections, spatial locations of which are shown in Fig. 1			
	1	2	3	4
2.5	5e-08	4e-04	2e-02	4e-01
5	4e-07	4e-03	1e-01	3e+00
7.5	1e-06	1e-02	4e-01	1e+01



**Fig. 7.** Correlation between TR-number and crystal size  $d_{90}$ . The spatial locations of the injection points are shown in Fig. 1.

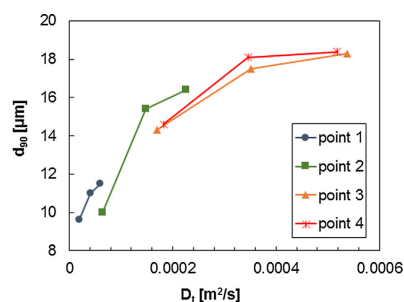


**Fig. 8.** Correlation between spatial specific turbulence dispersion and crystal size  $d_{90}$ . The spatial locations of the injection points are shown in Fig. 1.

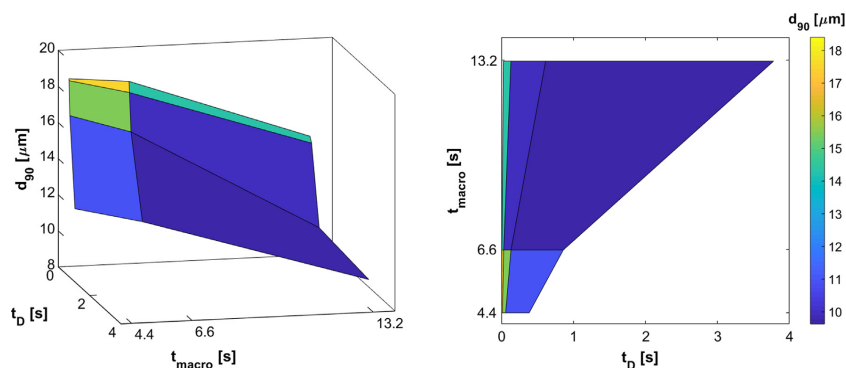


**Fig. 9.** Surface plot of  $d_{90}$  against time scales of macro mixing and specific spatial turbulence dispersion at the locations of  $\text{BaCl}_2$  injection in 3 (left plot) and 2 (right plot) dimensional views. The surface tissue is colored by  $d_{90}$ .

impeller (Fig. 6). The mesomixing time scale in the areas of the reagent introduction is important, however the residence time in the area is short and the overall flow pattern in the reactor plays a role in the supersaturation distribution and thus, in the precipitation process.

Mixing intensity influences the reagents dispersion and can be characterized by local energy dissipation rate. Table 5 summarizes the local energy dissipation rate in the points of injections at different mixing speeds. Based on  $\epsilon$  values, the points can be separated into two groups, namely low (1 and 2) and high intensity mixing (3 and 4).

As it was discovered before, the residence time of the initial supersaturation concentration is of great influence onto the mean size of the crystals while it is less important for the shape of the CSD curve. At higher supersaturation levels, such as low mixing intensity points 1 and 2, the stable nuclei are smaller. Therefore, TR-number (Eq. (1)), taking into account ratio of the feeding time to the mesomixing time has been plotted against  $d_{90}$  in Fig. 7. Analogous plot has been presented by Torbacke and Rasmuson (2001) in the vast range of TR, however the range below  $10^5$  was not covered.

The correlation presented by Torbacke and Rasmuson (2001) is fair in the range of low TR value as well. When the mesomixing in the bulk of the reactor handles the reagent feeding rate and distributes it quickly enough the supersaturation of the barium sulphate decreases and the stable nuclei are bigger. In case of low bulk mixing intensity or long feeding rate the local supersaturation is high and stable nuclei are smaller. By studying Fig. 7, one may notice that some points of the lower TR value correspond to the bigger crystal sizes. Dispersion mechanism due to turbulence has great influence in the reagent mixing occurred in the STR (Barrett et al., 2011). Therefore,  $d_{90}$  has been plotted against the local  $D_t$  (Fig. 8).

One may notice that the turbulence dispersion level in the points 3 and 4 is similar at all the mixing speeds studied. The points from high mixing intensity area have similar behavior, which means that the local turbulent dispersion handled effectively the reagent feeding rate by reducing the supersaturation concentration. On contrary, points 1 and 2 have significant difference in  $D_t$  and produce crystals of different size. As in the case of the local bulk flow velocity level, the higher local turbulence dispersion value does not always correspond to the bigger crystals. The drastic change in  $d_{90}$  of point 2 denotes that the macromixing affected the supersaturation concentration when turbulent dispersion was not sufficient. The injected at point 2 ions got into a circulating loop and

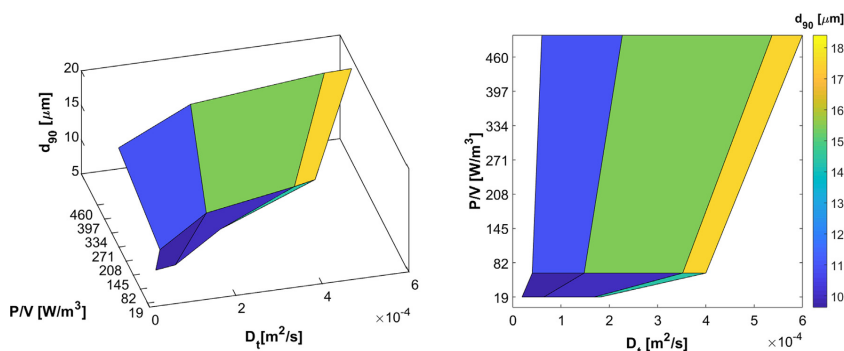


Fig. 10. Surface plot of  $d_{90}$  against volumetric power and specific spatial turbulence dispersion at the locations of  $\text{BaCl}_2$  injection in 3 (left plot) and 2 (right plot) dimensional views. The surface tissue is colored by  $d_{90}$ .

reached the area of higher mixing intensity until critical time for crystallization process has been reached. The reagents, introduced on surface (point 1), were held there longer than the critical time, which resulted in smaller  $d_{90}$ . The influence of the macromixing is evident; therefore, the surface plot of  $d_{90}$  against time scale of macro (Eq. (2)) and mesomixing (Eq. (4)) time scales is presented in Fig. 9.

The surface plot reveals the effect of the macromixing scale. The faster the mixing process, the bigger the crystals are formed and vice versa. The correlation of crystal size ( $d_{90}$ ), volumetric power and local spatial turbulent dispersion was visualized as a surface plot in Fig. 10 to analyze the crystallization system.

The surface plot can be used for optimization purposes to reach target crystal size at lowest energy costs. Thus, under current operational conditions, the supersaturation concentration is dispersed effectively already at 5 rps mixing speed when the barium chloride is injected in the impeller sweep area, if the bigger crystals are desired, while further increase of the mixing speed has insignificant effect. When the shift of CSD towards small particles is a purpose, the most stagnant zone of the reagent injection at the lowest mixing speed is favorable.

#### 4. Conclusions

In this work, the barium sulphate crystallization process was studied in a batch STR at lab scale using experimental and numerical methods. The global conductivity dynamics described the overall process of the chemical reaction and the precipitation processes. The mixing loops and the logical step change in the global conductivity between the homogeneous stages were observed.

The batch crystallization was measured by the EIT technique. The temporal progress of the process has been presented through the samples of vertical cross sections at different times representing four stages of the precipitation. The effect of the feed location and the overall flow pattern in the reactor were considered.

The effect of mixing of macro and mesomixing scales was estimated using CFD simulations of single phase flow in the STR. The plotted TR number versus  $d_{90}$  showed the basic agreement of the trend found by Torbacke and Rasmuson (2001) in the overlapping range as well as beyond. However, the scatter from the trend was observed as well meaning that the effect of macro scale mixing has not been taken into account. The cumulative effect of the macro and mesomixing scales onto  $d_{90}$  was observed and their potential usage for optimization purposes was discussed.

#### Acknowledgements

The authors are grateful to the Finnish Funding Agency TEKES and, in particular, to Outotec Finland Oy collaborating under FERMATRA project (908/31/2016 and 958/31/2016), for active supervision and financial support. The work of Marko Vauhkonen and Gerardo González was also supported by the Academy of Finland (Project 250215 Finnish Center of Excellence in Inverse Problems Research).

#### References

- Bakker, A., Oshinowo, L.M., 2004. Modelling of turbulence in stirred vessels using large eddy simulation. *Chem. Eng. Res. Des.* 82, 1169–1178. <https://doi.org/10.1205/cerd.82.9.1169.44153>.
- Barrett, M., Grady, D.O., Casey, E., Glennon, B., 2011. The role of meso-mixing in anti-solvent crystallization processes. *Chem. Eng. Sci.* 66, 2523–2534. <https://doi.org/10.1016/j.ces.2011.02.042>.
- Celik, I.B., Ghia, U., Roach, P.J., Freitas, C.J., Coleman, H., Raad, P.E., 2008. Procedure for estimation and reporting of uncertainty due to discretization in CFD applications. *J. Fluids Eng.* 130, 78001–78005.
- Gradov, D.V., Laari, A., Turunen, I., Koiranen, T., 2016. Experimentally validated CFD model for gas-liquid flow in a round-bottom stirred tank equipped with Rushton turbine. *Int. J. Chem. React. Eng.* 15. <https://doi.org/10.1515/ijcre-2015-0215>.
- Heikkinen, L., 2005. Statistical Estimation Methods for Electrical Process Tomography.
- Joshi, J.B., Nere, N.K., Rane, C.V., Murthy, B.N., Mathpati, C.S., Patwardhan, A.W., Ranade, V.V., 2011. CFD simulation of stirred tanks: comparison of turbulence models (Part II: Axial flow impellers, multiple impellers and multiphase dispersions). *Can. J. Chem. Eng.* 89, 754–816. <https://doi.org/10.1002/cjce.20465>.
- Kagoshima, M., Mann, R., 2005. Effects of convection, feed-separation and macromixing on particle size distributions for double-jet semi-batch precipitation in a stirred vessel. *Chem. Eng. Sci.* 60, 2155–2165. <https://doi.org/10.1016/j.ces.2004.10.037>.
- Kim, W.-S., Tarbell, J.M., 1999. Micromixing effects on barium sulfate precipitation in a double-jet semi batch reactor. *Chem. Eng. Commun.* 176, 89–113. <https://doi.org/10.1080/00986449908912148>.
- Kourunen, J., 2009. Imaging of Mixing in Selected Industrial Processes Using Electrical Resistance Tomography. University of Eastern Finland, Kuopio.
- Lane, G.L., 2017. Improving the accuracy of CFD predictions of turbulence in a tank stirred by a hydrofoil impeller. *Chem. Eng. Sci.* 169, 188–211. <https://doi.org/10.1016/j.ces.2017.03.061>.
- Mann, R., 2009. ERT imaging and linkage to CFD for stirred vessels in the chemical process industry. In: 2009 IEEE Int. Work. Imaging Syst. Tech. IST 2009 – Proc. 223–228. <https://doi.org/10.1109/IST.2009.5071637>.
- Mullin, J.W., 2001. Crystallization. Reed Elsevier, Oxford.
- Phillips, R., Rohani, S., Baldyga, J., 1999. Micromixing in a single-feed semi-batch precipitation process. *AIChE J.* 45, 82–92. <https://doi.org/10.1002/aic.690450108>.
- Shih, T.H., Liou, W.W., Shabbir, A., Yang, Z., Zhu, J., 1995. A new k-ε eddy viscosity model for high Reynolds number turbulent flows – model development and validation. *Comput. Fluids* 24, 227–238.

- Stanley, S.J., 2006. Tomographic imaging during reactive precipitation in a stirred vessel: mixing with chemical reaction. *Chem. Eng. Sci.* 61, 7850–7863. <https://doi.org/10.1016/j.ces.2006.09.029>.
- Stanley, S.J., Mann, R., Primrose, K., 2005. Interrogation of a precipitation reaction by electrical resistance tomography (ERT). *AIChE J.* 51, 607–614. <https://doi.org/10.1002/aic.10359>.
- Steyer, C., 2012. Precipitation of barium sulfate in a semi-batch stirred tank reactor : influence of feeding policy on particle size and morphology.
- Torbacke, M., 2001. On the influence of mixing and scaling-up in semi-batch reaction crystallization. *Eng. Technol.* 56, 2459–2473. [https://doi.org/10.1016/S0009-2509\(00\)00452-8](https://doi.org/10.1016/S0009-2509(00)00452-8).
- Torbacke, M., Rasmuson, A.C., 2004. Mesomixing in semi-batch reaction crystallization and influence of reactor size. *AIChE J.* 50, 3107–3119. <https://doi.org/10.1002/aic.10213>.
- Wabo, E., Kagoshima, M., Mann, R., 2004. By Visualized Reactive Tracers and 82, 1229–1236.
- Wang, H., Zhai, Z., 2012. Analyzing grid independency and numerical viscosity of computational fluid dynamics for indoor environment applications. *Build. Environ.* 52, 107–118.
- Wang, Z., Mao, Z.S., Yang, C., Zhang, Q., Cheng, J., 2009. Numerical investigation of the influence of kinetics and shape factor on barium sulfate precipitation in a continuous stirred tank. *Front. Chem. Eng. China* 3, 272–281. <https://doi.org/10.1007/s11705-009-0023-x>.
- Wong, D.C.Y., Jaworski, Z., Nienow, A.W., 2001. Effect of ion excess on particle size and morphology during barium sulphate precipitation: an experimental study. *Chem. Eng. Sci.* 56, 727–734. [https://doi.org/10.1016/S0009-2509\(00\)00282-7](https://doi.org/10.1016/S0009-2509(00)00282-7).
- Yeoh, S.L., Papadakis, G., Yianneskis, M., 2004. Numerical simulation of turbulent flow characteristics in a stirred vessel using the LES and RANS approaches with the sliding/deforming mesh methodology. *Chem. Eng. Res. Des.* 82, 834–848. <https://doi.org/10.1205/0263876041596751>.
- Zauner, R., Jones, A.G., 2000. Mixing effects on product particle characteristics from semi-batch crystal precipitation. *Chem. Eng. Res. Des.* 78, 894–902. <https://doi.org/10.1205/026387600527969>.



## **Publication V**

Gradov, D. V., Han, M., Tervasmäki, P., Latva-Kokko, M., Vaittinen, J.,  
Pihlajamäki, A., and Koiranen, T.

**Numerical simulation of biomass growth in OKTOP®9000 reactor at industrial  
scale**

Reprinted with permission from  
*Industrial and Engineering Chemistry Research*  
Vol. 57(40), pp. 13300–13311, 2018  
© American Chemical Society





# Numerical Simulation of Biomass Growth in OKTOP®9000 Reactor at Industrial Scale

Dmitry Vladimirovich Gradov,<sup>\*,†,‡</sup> Mei Han,<sup>†</sup> Petri Tervasmäki,<sup>‡</sup> Marko Latva-Kokko,<sup>§</sup> Johanna Vaittinen,<sup>||</sup> Arto Pihlajamäki,<sup>†</sup> and Tuomas Koironen<sup>†</sup>

<sup>†</sup>School of Engineering Science, Lappeenranta University of Technology, P.O. Box 20, FI-53851 Lappeenranta, Finland

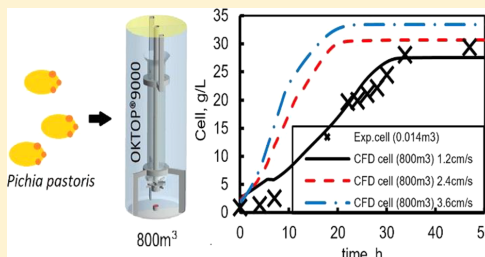
<sup>‡</sup>Chemical Process Engineering, University of Oulu, P.O. Box 4000, FI-90014 Oulu, Finland

<sup>§</sup>Outotec (Finland) Oy, Outotec Research Center, P.O. Box 69, FI-23101 Pori, Finland

<sup>||</sup>Neste Engineering Solutions, NAPCON, P.O. Box 310, FI-06101 Porvoo, Finland

## Supporting Information

**ABSTRACT:** Computational fluid dynamics is a powerful method for scale-up of reactors although it is still challenging to fully embrace hydrodynamics and biological complexities. In this article, an aerobic fermentation of *Pichia pastoris* cells is modeled in a batch OKTOP®9000 reactor. The 800 m<sup>3</sup> industrial scale reactor is equipped with a radial impeller, designed by Outotec Oy for gas dispersion in the draft tube reactor. Measured  $N_p$  of the impeller is used in hydrodynamics validation. The resolved energy dissipation rate is compensated, and its influence on mass transfer is analyzed and discussed. Gas–liquid drag force is modified to simulate effects of liquid turbulence and bubble swarms. Resolved steady state multiphase hydrodynamics is used to simulate the fermentation process. Temporal evolution of species concentrations is compared to experimental data measured in a small copy of the reactor at lab scale (14 L). The effect of oxygenation on the *P. pastoris* cells cultivation is considered.



## 1. INTRODUCTION

Microbial cells are used to produce a wide range of products. In a majority of the production processes, microbes are aerobic and require oxygen for respiration and the cultivation is carried out in aqueous medium. Therefore, efficient oxygen transfer from gas to liquid phase is essential.<sup>1</sup> The industrially relevant reactor scales are tens or hundreds cubic meters, and these reactors cannot be approximated by an ideally mixed approach. As pointed out by Nauha et al.,<sup>2,3</sup> the gas handling capacity of stirred tank reactors (STR) often becomes one of the limiting factors in the large scale. Furthermore, flow patterns in STR with high aspect ratio—typical for large scale applications—often exhibit compartmentalization of the overall dispersion flow and limited axial recirculation throughout the reactor volume.<sup>4</sup>

The OKTOP®9000 reactor was originally developed for direct leaching of zinc concentrate during the 1990s. Today they are in use at some of the largest zinc production plants in the world with reactor volumes ranging around 1000 m<sup>3</sup>. Gas-to-liquid mass transfer is an important issue also in hydrometallurgy due to low oxygen solubility and high oxygen demand. Several hydrometallurgical operations are controlled by the rate of oxygen transfer from gas to aqueous phase. Therefore, the OKTOP®9000 reactor is designed to have high gas-to-liquid mass transfer capacity and good oxygen utilization

efficiency at relatively low agitation power costs. Thus, this type of reactor is also suitable for fermentation processes that require high gas–liquid mass transfer capacity. Gas–liquid mass transfer studies in this type of reactor have been published by Kaskiala<sup>5</sup> and Tervasmäki et al.<sup>6</sup>

For modeling the fermentation process, an accurate description of oxygen mass transfer is vital. Development of mass transfer formulation proposed in the literature can be followed since 1904, as it includes more features of physical mechanism and less assumptions.<sup>7</sup> Interfacial mass transfer is often described by surface renewal models out of which two groups can be distinguished, namely slip-velocity and eddy-cell models.<sup>7–9</sup> In turbulent flows, volumetric power describes the mass transfer more adequately than slip-velocity models.<sup>9</sup> However, the influence of ratio between available energy in fluid and contact surface area of bubbles is unknown<sup>8</sup> and given by empirical coefficient.

Computational fluid dynamics (CFD) has been widely used by researchers to simulate complicated multiphase systems with coupled chemical reactions.<sup>10–15</sup> Models describing gas–

Received: June 21, 2018

Revised: September 6, 2018

Accepted: September 10, 2018

Published: September 10, 2018



liquid hydrodynamics are capable of predicting agitated fluid flow with fair accuracy. At a compromise of time and computational power available, multiphase reactor performance can be evaluated. Simulating of industrial-scale applications (hundreds of m<sup>3</sup>) in a reasonably short time is not common; therefore, only a few relevant published works were found. The effect of spatial discretization on simulated results has to be mentioned here. Typically, reactor geometry does not require a high number of elements to resolve main flow features and simulation time is moderate. Unfortunately, this is not valid for energy dissipation rate which is known to be affected greatly by mesh size.<sup>16</sup> Lane<sup>16</sup> tested several turbulence models in lab scale stirred tank (72 L) at different grids and found that energy dissipation rate is resolved up to 90% at the grid of around 20 million mesh nodes that is not feasible in multiphase mixing simulations at industrial scale.

The local hydrodynamics and gas–liquid mass transfer rate from numerically resolving mass, momentum, and energy balance equations allow one to obtain more insight into assessing the reactor performance compared with empirical correlations for scale-up process of multiphase reactors. The empirical correlations are usually derived from laboratory or pilot-scale experiments where the characteristics of the substrate gradient and the gas–liquid mass transfer are different from the large scale mainly due to mixing heterogeneity.<sup>17,18</sup>

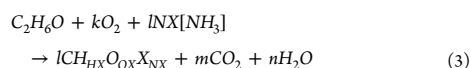
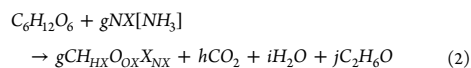
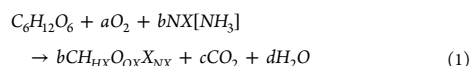
Lapin et al.<sup>19,20</sup> developed an Euler–Lagrange approach to characterize the lifeline/history of an individual cell and performed the simulations of fed-batch cultivations in stirred tank reactors for *Saccharomyces cerevisiae* (0.07 m<sup>3</sup>) and *Escherichia coli* (0.9 m<sup>3</sup>). The modeling work concentrated, among other things, on the detailed description of the sugar uptake of the cells as both of the example organisms are sensitive to glucose concentration in the environment, and concentration gradients are typically expected in fed-batch reactors with high glucose concentration in the feed. Morchain et al.<sup>10</sup> performed the simulation of STR fermenters with volume of 0.07 and 70 m<sup>3</sup>, applying a Euler–Euler approach for gas–liquid flow and the population balance model (PBM) for microorganism heterogeneity. Haringa et al.<sup>14</sup> simulated the aerobic *S. cerevisiae* fermentation in a 22 m<sup>3</sup> fermenter where a large scale substrate concentration gradient existed due to competition between the mixing and the substrate uptake. In their work, the Eulerian–Eulerian approach was used for gas–liquid fluid flow, coupling with PBM to account for bubble size distribution. The discrete phase model with one-way coupling was employed for tracking the cell population and describing the bioreaction. They found that substrate was well mixed within each circulation zone originating from the individual Rushton turbine. The concentration gradient was noticed to be compartmentalized along the reactor. However, the scale of the industrial reactor very often needs to be hundreds of cubic meters to achieve a profitable bioprocess, which leads to a significant computational power requirement.<sup>2</sup> Therefore, accurate resolving of turbulence characteristics becomes challenging at large scale, which has a significant effect on the gas–liquid hydrodynamics and mass transfer. The interactions between microbial metabolism and environmental factors such as oxygen and/or substrate concentrations and mass transfer conditions may be complex. Therefore, the suitability of a certain reactor type and operational conditions for microbial cultivation should be estimated by using

information on the microbial growth—not solely based on the information on the hydrodynamic conditions.

The aim of this research is to develop a CFD model for simulating cell cultivation in an industrial-scale OKTOP®9000 reactor. Using process equipment sizing data, a model was developed that is able to provide accurate results efficiently with respect to computing power and simulation time within feasible limits. Gas–liquid hydrodynamics, oxygen mass transfer, and yeast metabolism reactions are considered in the model. The effect of compensated volumetric power on gas–liquid mass transfer is studied. The aerobic cultivation of *Pichia pastoris* is simulated in batch mode. The effect of oxygen supply on the cells metabolism is considered.

## 2. MATERIALS AND METHODS

**2.1. Metabolism of *Pichia Pastoris* Yeast.** The description of growth kinetics is based on the model presented by Tervasmäki et al.<sup>21</sup> The model recognizes three different metabolic routes, which may be present when the yeast is grown on glucose. Glucose is utilized as the primary carbon source either by a respirative (eq 1) or fermentative (eq 2) route depending on the oxygen availability. Ethanol, which may be present as a product from alcoholic fermentation, can be utilized by respirative metabolism (eq 3) in the absence of the primary carbon source, glucose. The model has been developed and its parameters have been estimated based on literature sources. The specific reaction rates ( $q$ ) and growth rates ( $\mu$ ) are presented by eqs 4–11.



$$q_{g^{ox1}} = \frac{\mu_{max}^{ox}}{Y_{xg}^{ox}} \frac{c_g}{c_g + K_g} \frac{c_o}{c_o + K_o} \quad (4)$$

$$q_g^{ferm} = \frac{\mu_{max}^{ferm}}{Y_{xg}^{ox}} \frac{c_g}{c_g + K_g} \left( 1 - \frac{c_o}{c_o + K_o} \right) \quad (5)$$

$$q_e^{ox2} = \frac{\mu_{max}^e}{Y_{xe}^{ox}} \frac{c_e}{c_e + K_e} \frac{K_i}{c_g + K_g + K_i} \frac{c_o}{c_o + K_o} \quad (6)$$

$$\mu_g^{ox} = q_g^{ox} Y_{xg}^{ox} \quad (7)$$

$$\mu_g^{ferm} = q_g^{ferm} Y_{xg}^{ferm} \quad (8)$$

$$\mu_e^{ox} = q_e^{ox} Y_{xe}^{ox} \quad (9)$$

$$q_o^g = q_g^{ox} Y_{og}^{ox} \quad (10)$$

$$q_o^e = q_e^{ox} Y_{oe}^{ox} \quad (11)$$

where  $q_i$  is the specific rate of component  $i$  (g<sub>i</sub>/(g<sub>x</sub>·h)) and subscripts  $x$ ,  $g$ ,  $e$ , and  $o$  denote cells, glucose, ethanol, and oxygen, respectively. Superscripts  $ox$  and  $ferm$  in eqs 4–9



**Figure 1.** Industrial scale OKTOP@9000 reactor (left) (Outotec Plc., n.d.<sup>23</sup>) and CAD geometry for large-scale reactor and impeller (right). Credit line: Adapted with permission from <http://www.outotec.com/products/leaching-and-solution-purification/zinc-concentrate-direct-leaching>. Copyright Outotec Oyj 2018.

denote respirative and fermentative metabolism, and superscripts  $g$  and  $e$  in eqs 10–11 denote oxygen consumption due to glucose and ethanol utilization, respectively. Parameters  $\mu_{\max}$ ,  $Y$ , and  $K$  are listed in Table S1. Details of the model and validation with laboratory scale experiments are presented in Tevasmäki et al.<sup>21</sup>

**2.2. OKTOP@9000 Reactor.** The OKTOP@9000 reactor has been developed for direct leaching of zinc concentrate in atmospheric conditions. This proven technology applied in industry globally provides the following positive features: high oxygen mass transfer capacity and oxygen utilization efficiency, moderate mixing power requirement, and low mixing time. The OKTOP@9000 reactor is presented at industrial scale in Figure 1. Three baffles are mounted to the vessel walls in the down part of the reactor in order to prevent flow circulation and promote mixing. Designed by Outotec, the stirrer is a combination of a hydrofoil impeller and a radial turbine. The upper parts of the blades are rounded to create high flow and fluid circulation inside the reactor whereas the down parts are made straight to disperse and distribute gas radially. The outer corners of the blades are trimmed to fit the draft tube and reduce the power number of the impeller. The stirrer clearance is 0.33T. A ring-sprayer is mounted below the impeller. The ring has a square profile with replaceable upper lid that is

perforated as needed. The lid surface ( $\approx 0.9 \text{ m}^2$ ) of the ring-sprayer is perforated uniformly with holes of 1 mm in diameter. The dimensions of the reactor are presented in Table S2. The liquid aspect ratio is set around 3.

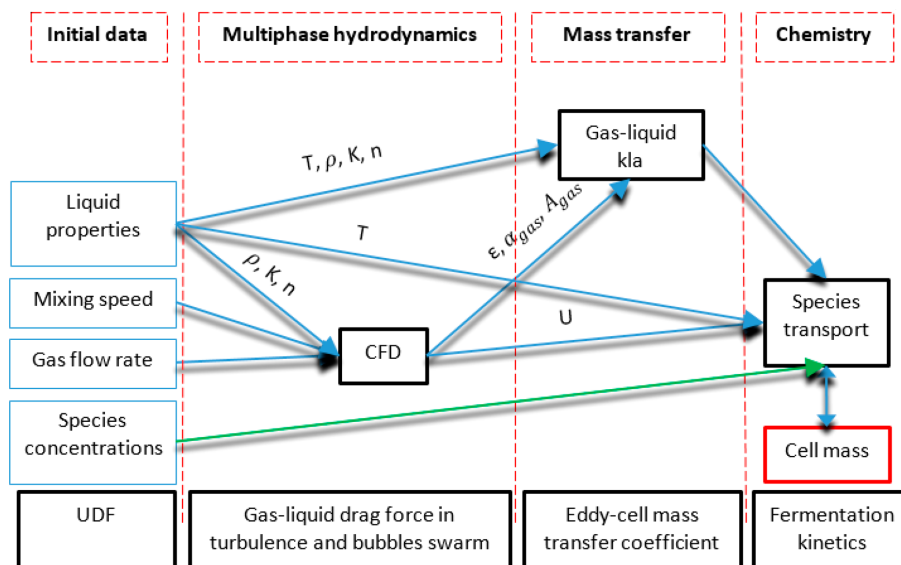
For the model validation purposes, the computational domain of the large-scale reactor is built based on scale-up of an existing laboratory scale test device. The main constructive differences between the industrial device and CFD model are in shaft orientation (bottom versus top entry) and draft tube support frames arrangement. These changes are not supposed to affect the overall hydrodynamics.

**2.3. Operational Conditions of Batch Cultivation of *P. pastoris*.** The batch cultivation of the yeast has been performed experimentally at the lab scale OKTOP@9000 reactor by Tevasmäki et al.<sup>21</sup> The volumetric power and aeration rate used in the lab scale tests were maintained when scaling-up the process to a  $800 \text{ m}^3$  reactor. The operational conditions during the cultivation are summarized in Table S3.

In CFD simulations, the aeration rate was varied to study the effect of oxygenation on the bacteria metabolism. Maximum air flow rate was limited by the flooding at the chosen mixing speed.

**2.4. Numerical Approach.** **2.4.1. Simulation Strategy.** The modeling was carried out in ANSYS Fluent 18 by a

Scheme 1. Block Scheme of Numerical Approach Used in This Work



standard tool kit of the software package with partial usage of user defined function (UDF) when customization was needed. Scheme 1 presents a block-scheme of the simulation strategy used in this work. The overall strategy is divided in four parts entitled by names in red dashed squares. Initial properties of the solution of the cell cultivation process are used to calculate multiphase mixing hydrodynamics in the reactor. Gas–liquid mass transfer is found via postcalculation from the results of the resolved hydrodynamics at steady state. Biological activities are then simulated using data from the simulated hydrodynamics, oxygen mass transfer, and initial species concentrations.

**2.4.2. Multiphase Fluid Flow.** The volume averaged Stoke's number (eq 12) for the studied system is around 11, meaning that the gas phase influence on the liquid phase is not negligible and it has to be taken into account.

$$St = \frac{\tau_p}{\tau_q} = \frac{d_p^2 \varepsilon^{0.5}}{36\nu^{1.5}} \quad (12)$$

where  $\tau_p$  and  $\tau_q$  are the relaxation time of the primary phase and bubble,  $s$ ,  $d_p$  is the bubble diameter,  $m$ ,  $\varepsilon$  is the energy dissipation,  $m^2/s^3$ , and  $\nu$  is the kinematic viscosity,  $m^2/s$ .

Therefore, the Eulerian–Eulerian multiphase approach was used to simulate gas–liquid flow, in which gas and liquid phases are considered as interpenetrating continua expressed via volume fraction per phase and the mass balance is controlled by eq 13. A set of conservation equations is solved for each phase (eqs 14–15).

$$\sum_i \alpha_i = 1 \quad (13)$$

$$\nabla \cdot \bar{u} = 0 \quad (14)$$

$$\bar{u} \cdot \nabla \bar{u} = -\nabla \bar{p} + \nabla \cdot [(\mu + \mu_{turb}) \nabla \bar{u}] \quad (15)$$

where  $\alpha_i$  is the phase volume fraction,  $\bar{u}$  a phase velocity,  $m/s$ ,  $\bar{p}$  is the pressure,  $Pa$ , and  $\mu$  and  $\mu_{turb}$  are the laminar and turbulent viscosities,  $Pa \cdot s$ .

**2.4.3. Turbulence.** It was desired to develop a model that is able to provide results efficiently with respect to computing power and time, for which reason it was decided to apply a Reynolds-averaged Navier-Stoke's (RANS) turbulence model in the current simulations. Turbulence formulations in RANS models are based on statistical analysis rather than on actual physical phenomena. In our previous work<sup>23</sup> three popular models in the RANS family were tested, namely the Realizable  $k$ - $\varepsilon$  model, the shear stress transport  $k$ - $\omega$  model ( $k$ - $\omega$  SST), and the Reynolds stress model (RSM). The Realizable  $k$ - $\varepsilon$  model produced the most accurate results for single and multiphase mixing in round-bottom STR and has therefore been applied in this work.

$$\bar{u} \cdot \nabla k = P - \varepsilon + \nabla \cdot \left[ \left( \mu + \frac{\mu_{turb}}{\sigma_k} \right) \nabla k \right] \quad (16)$$

$$\bar{u} \cdot \nabla \varepsilon = C_{\varepsilon 1} \frac{\varepsilon}{k} P - C_{\varepsilon 2} \frac{\varepsilon^2}{k} + \nabla \cdot \left[ \left( \mu + \frac{\mu_{turb}}{\sigma_\varepsilon} \right) \nabla \varepsilon \right] \quad (17)$$

where  $k$  is the turbulence kinetic energy,  $m^2/s^2$ .

The dispersed turbulence formulation model was used since the secondary phase is dilute and fluctuating quantities of the gaseous phase may be found as the function of the mean terms of the liquid phase. At first, turbulence terms  $k$  and  $\varepsilon$  are computed for the primary phase. Then, secondary phase turbulence terms are found and exchange of turbulence momentum between phases is computed based on Tchen-theory.<sup>24</sup>

**2.4.4. Phase Interaction.** Gradov et al.<sup>23</sup> showed that the Schiller–Naumann's drag force model in conjunction with

Lane's turbulence modification factor gave the most accurate results for air–water mixing in a stirred tank at the assumption of constant bubble diameter equal to 1 mm. Also, the effect of nondrag forces was found insignificant. Therefore, in order to reduce computational complexity and promote solution stability, the above-mentioned combination of models was used to simulate drag force, while other force models were ignored. The momentum conservation eq (eq 18) includes the cumulative force  $\vec{F}_q$  (eq 19) acting on the primary phase.

$$\frac{\partial}{\partial t}(\alpha \rho \vec{u})_q + \nabla \cdot (\alpha \rho \vec{u} \vec{u})_q = \nabla \cdot (\alpha \sigma)_q - \alpha_q \nabla p + \vec{F}_q + \alpha_q \rho_q \vec{g} \quad (18)$$

$$\vec{F}_q = \sum_{p=1}^n (K_{pq}(\vec{u}_p - \vec{u}_q) + \dot{m}_{pq}\vec{u}_{pq} - \dot{m}_{qp}\vec{u}_{qp}) \quad (19)$$

Different drag models can be found in published literature. The most popular model, proposed by Schiller and Naumann<sup>25</sup> in eq 21, is a drag model suitable for rigid spherical particles.

$$K_{pq} = \frac{\rho_p C_D \text{Re}}{144 \tau_p} d_p A_i \quad (20)$$

where  $\rho_p$  is the particle density, kg/m<sup>3</sup>,  $C_D$  is the drag force coefficient,  $\text{Re}$  is the relative Reynolds number, and  $A_i$  is the interfacial area, m<sup>2</sup>. The drag force coefficient is the function of  $\text{Re}$  according to the following formulation:

$$C_D = \begin{cases} 24(1 + 0.15 \text{Re}^{0.687}) & \text{Re} \leq 1000 \\ 0.44 & \text{Re} > 1000 \end{cases} \quad (21)$$

The drag force model is based on bubble rise velocity measured in stagnant fluids, which is higher than rise velocity in turbulent flow. A model correcting drag force coefficient for turbulence was proposed by Brucato et al.<sup>26</sup> at first. This turbulence modification factor concept (eq 22) changes stagnant fluid drag force to make it suitable for adoption in turbulent multiphase flow simulation. Later, Lane et al.<sup>27</sup> suggested a new correlation (eq 23) for turbulence modification factor that is based on ratio of stagnant to turbulent terminal velocity  $\frac{U}{U_r}$  to be correlated with ratio of particle relaxation time to integral time scale of turbulence.

$$K'_{pq} = \eta K_{pq} = \left(1 + K \left(\frac{d_p}{\lambda}\right)^3\right) K_{pq} \quad (22)$$

where  $\eta$  is the turbulence modification factor,  $K = 6.5 \times 10^{-6}$  and  $\lambda$  is the Kolmogorov length scale, m.

$$\eta = \left(1 - 1.4 \left(\frac{\tau_p}{T_L}\right)^{0.7} e^{(0.6\tau_p/T_L)}\right)^{-2} \quad (23)$$

$$T_L = 0.135 \frac{k}{\varepsilon} \quad (24)$$

The presence of a bubbles swarm reduces liquid flow energy increasing drag force between phases. The effect of gas volume fraction (0.01–0.45) of dispersed gas onto gas–liquid drag force has been modeled by Roghair et al.<sup>28</sup> in the flows of intermediate and high Reynolds number as

$$C_{D,swarm} = C_D \left(1 + \alpha_p \left(\frac{18}{E\ddot{o}}\right)\right) (1 - \alpha_p) \quad (25)$$

where  $E\ddot{o}$  is the Eötvös number, which is a dimensionless number to characterize the shape of bubbles or drops moving in a surrounding fluid.

**2.4.5. Mass Transfer.** According to the eddy-cell model, mass transfer is described as a function of energy dissipation rate and rheological parameters defining micromixing.<sup>9</sup> With the assumption of constant temperature, local energy dissipation determines the mass transfer coefficient according to eq 26 as suggested by Kawase and Moo-Young:<sup>29</sup>

$$k_L = C \sqrt{D_L} \left(\frac{\varepsilon \rho}{K}\right)^{1/[2(1+n)]} \quad (26)$$

where  $D_L$  is the gas diffusivity in liquid, m<sup>2</sup>/s ( $2.26 \times 10^{-9}$ , Han and Bartels<sup>30</sup>),  $\rho$  is the liquid density, kg/m<sup>3</sup>,  $K$  is the consistency index, Pa·s<sup>*n*</sup>,  $n$  is the dimensionless flow behavior index, and  $C$  is the proportionality coefficient. The effect of gas bubbles on the mass transfer coefficient is taken into account with the proportionality coefficient. The value of 0.301 for the coefficient, proposed by Kawase and Moo-Young,<sup>29</sup> has been tested by Garcia-Ochoa and Gomez<sup>31</sup> and was found to produce accurate results for gas–liquid mass transfer in stirred bioreactors.

The specific volumetric surface area of the secondary phase is found as follows:

$$A_p = \frac{6\alpha_p}{d_p} \quad (27)$$

Calderbank et al.<sup>32</sup> proposed a correlation for Sauter mean diameter of bubbles in alcohol solutions:

$$d_{32} = 1.9 \left(\frac{\sigma^{0.6}}{\varepsilon^{0.4} \rho^{0.6}}\right) \left(\frac{\mu_{\text{gas}}}{\mu_L}\right) \alpha_p^{0.65} + 0.0009 \quad (28)$$

where  $\sigma$  is the surface tension, N/m. The surface tension of the water–ethanol (1%) solution was measured and resulted in 0.069 N/m.

Machon et al.<sup>33</sup> tested solutions of various gas–liquid surface tension in a stirred tank at three different vertical locations by recording bubble sizes. They concluded mean bubble size as a function of surface tension and specific volumetric mixing power. Based on the results presented, mean bubble size is 2 mm in 1% water–ethanol solution. Later, Hu et al.<sup>34</sup> tested gas–liquid solutions of various surface tensions in turbulent flow and proposed a correlation for Sauter mean bubble size, predicting similar bubble size (2 mm) in OKTOP@9000.

**2.4.6. Bacterial Activity.** The conservation equation of species transport in turbulent flow is as follows:

$$\frac{\partial}{\partial t}(\rho Y_i) + \nabla \cdot (\rho \vec{u} Y_i) = \nabla \cdot (\rho(D_{i,m} + D_i) \cdot \nabla Y_i) + R_i \quad (29)$$

where  $Y_i$  is the mass fraction of component  $i$ ,  $D_{i,m}$  and  $D_i$  are the diffusivities due to laminar and turbulence diffusion correspondingly, m<sup>2</sup>/s, and  $R_i$  is the net rate of production of species  $i$  by chemical reaction kg/(m<sup>3</sup>·s).

Haringa et al.<sup>14,15,35</sup> found significant concentration gradients at  $Da \approx 50$  along the tall reactor equipped with four Rushton turbines, compartmentalized them, and performed a scale-down simulator design from CFD data.

However, such concentration gradients are negligibly small ( $Da \approx 5$ ) in OKTOP@9000 at the studied operational conditions. Therefore, the method is not feasible in this work. Net reaction rates of the species are modeled via UDF as a source term.

$$R_i = -(q_i^{ox1} + q_i^{ferm} + q_i^{ox2})c_x \quad (30)$$

$$R_x = -(\mu_g^{ox1} + \mu_g^{ferm} + \mu_g^{ox2})c_x \quad (31)$$

$$R_o = k_L a (c_o^{sat} - c_o) - (q_o^{ox1} + q_o^{ox2})c_x \quad (32)$$

$$c_o^{sat} = \frac{M_o w_o (p_h - p_{vapor})}{k_H} \quad (33)$$

where  $i$  denotes a species,  $c_o^{sat}$  is the oxygen saturation concentration in the liquid phase, g/L;  $c_o$  is the oxygen concentration in the liquid phase, g/L;  $c_x$  is the biomass concentration, g/L;  $p_h$  is the hydrostatic pressure, atm;  $p_{vapor}$  is the vapor pressure (0.0419 at 30 °C according to Lide et al.<sup>36</sup>), atm;  $k_H$  is the Henry's constant (770), atm·L/mol;  $w_o$  is the mass fraction of oxygen, and  $M_o$  is the molar weight of oxygen, g/mol.

**2.4.7. Boundary Conditions, Solver Settings, and Convergence Criteria.** Mixing in the draft tube reactor was modeled using the multiple reference frame (MRF) method where the rotor is fixed, around which the fluid in the mixing zone is rotated. The method allows steady state simulation at accuracy comparable to the sliding mesh (SM) method as proved by Joshi et al.<sup>37</sup> In the works published previously,<sup>23,38</sup> the MRF approach in combination with the Realizable k- $\epsilon$  turbulent model simulated flow characteristics in a STR accurately close to PIV measurements. Moreover, the results of the sliding mesh approach are not sufficiently verified in turbulent and multiphase mixing flows.<sup>37</sup>

Near wall flow was modeled using a standard wall function due to simplicity and varying  $y^+$  value along the walls of the draft tube reactor. Therefore, the grids were made such that the elements next to the wall fell into the range 30–300 of  $y^+$  value.<sup>39</sup>

In the CFD simulations, the stirred tank can be considered as a semibatch system where gas, supplied via sparger, exits through the liquid surface. The boundary conditions are schematically presented in Figure 2.

At first, the liquid phase mixing flow field has been simulated. Then, in order to reduce computational instabilities, the simulation was switched to transient state (time step is 0.02 s) and gas was fed until mass balance criteria (5% deviation) was met and gas–liquid hydrodynamics stabilized. Under relaxation factors of pressure and velocity were reduced up to 0.15 and 0.35 correspondingly to facilitate convergence. A second order discretization scheme was applied to all the solved variables. The convergence criterion was set at  $10^{-4}$  for all the calculated variables. When multiphase flow hydrodynamics have been computed, mass transfer was calculated on top of multiphase results according to eqs 26–27. Species transport equations were solved at frozen gas–liquid hydrodynamics.

**2.4.8. Spatial Resolution.** Spatial discretization is known to affect simulation results as mentioned earlier in section 1. At feasible grid size, energy dissipation, which is an important parameter influencing bubble size, mass transfer coefficient etc., is underestimated in STRs already at lab scale, not

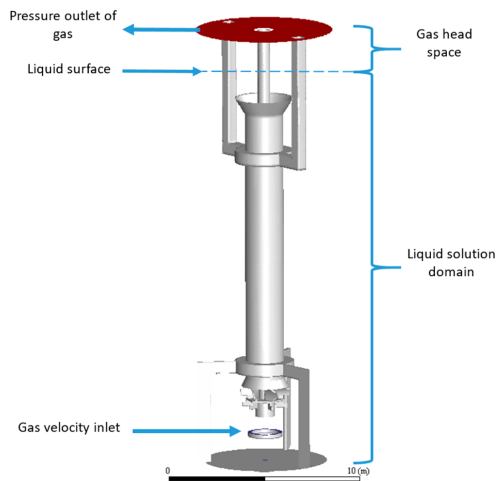


Figure 2. Schematic presentation of boundary conditions to simulate gas–liquid mixing.

mentioning pilot and industrial ones.<sup>16,37</sup> Therefore, refining a grid of the reactor of large scale would result in an enormous number of cells, which is not practical. The computational grid test carried out in this study had a purpose to preserve the main flow field features resolved such as liquid velocity and surface stress on the impeller. The mesh in the stationary zone was meshed by structured elements while the region around the impeller composed unstructured ones (Figure 3). Four grids were produced by doubling the number of elements.

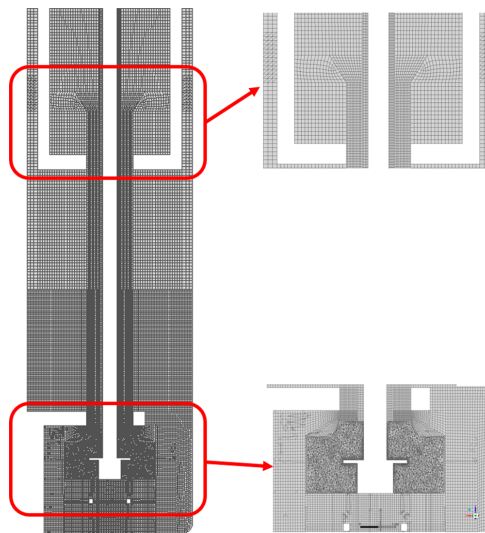


Figure 3. Example of spatial discretization (grid 3) in vertical slice.



The grid test (Table S4) was performed using single phase mixed at 60 rpm. Out of the results, grid 3 with 2 million elements was chosen as an optimal one in further simulations.

**2.4.9. Post Processing of Simulation Results.** Power number ( $N_p$ ) measured at an industrial OKTOP®9000 reactor was shared by Outotec Co for validating the large-scale CFD model (see section 2.2). The simulated power number was within 8% difference to  $N_p$  measured in the large scale reactor. From the model, the power draw can be expressed via energy dissipation integrated over the vessel volume according to the following expression:

$$P_\tau = 2\pi N \int \tau dA_{imp} \quad (34)$$

$$P_e = \rho \int \epsilon dV \quad (35)$$

where  $P$  is the power draw,  $W$ ,  $N$  is the mixing speed,  $s^{-1}$ ,  $\tau$  is the stress, Pa,  $A_{imp}$  is the impeller area,  $m^2$ , and  $V$  is the volume of reactor,  $m^3$ .

Due to the usage of a head space in the simulations (see Figure 3), the global values of mixing power, gas hold-up, and gas–liquid mass transfer were calculated from the iso-surface based on the gas hold-up range 0–0.5. It is worth mentioning that a small region of high gas fraction in the vicinity of the gas sparger is not included into the iso-surface.

### 3. RESULTS

The used models and boundary conditions in the current multiphase mixing simulations are summarized in Table S5.

The simulations were performed using 8 cores of Intel(R) Core(TM) i7-7700 CPU @3.60 GHz and 16Gb operational memory. The strategy comprised three steps, namely: single phase mixing in steady state (7 eq-s–10 s/iteration), transient gas–liquid mixing (14 eq-s–20 s/iteration), and fermentation (5 eq-s–6s/iteration), which took 10 days of calculations for a set of operational conditions.

**3.1. Reactor Hydrodynamics.** In Figure 4, the velocity vector field in a vertical plane is presented where all vectors are of the same size and in-plane to show the overall flow field in single phase mixing at  $1 s^{-1}$ .

The draft tube enlarges the upper circulation loop, produced by a radial impeller. This effect combines benefits of airlift and stirred tank reactors. With a single mixer, aerated gas is well-distributed in the OKTOP®9000 reactor producing a large gas–liquid contact area while the raiser part provides a longer contact time. Depending on mixing speed, supplied gas can be trapped longer, being dragged into the draft tube near the reactor top. At strong enough agitation, solution can be aerated also through vortex appeared on the liquid surface. Global  $Da$  is smaller in single radial impeller draft tube reactors compared to multiple impeller reactors equipped with several Rushton turbines, which prevents compartmentalization of the species concentration gradient.<sup>14</sup>

The reactor aeration was simulated transiently and the global parameters such as volumetric power, gas–liquid contact area, and mass transfer were followed to ensure stable multiphase flow is achieved. Temporal evolution of global parameters traced was noticed to approach a stable level at 40 s of simulation time.

It is known that the mixing power estimated from simulations is calculated more accurately via torque (eq 34) than via the energy dissipation rate (eq 35).<sup>16</sup> The difference at

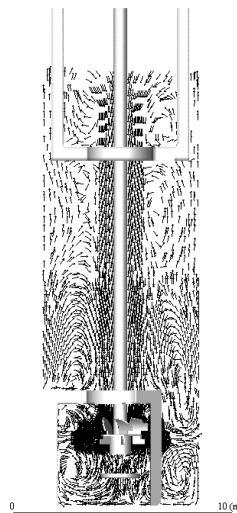


**Figure 4.** Velocity vector field of single phase water mixing at steady state in a vertical plane in the OKTOP®9000 reactor at  $1 s^{-1}$  agitation speed.

steady state is around 20%, which goes along with the observations made by Joshi et al.<sup>37</sup> and Lane.<sup>16</sup> The underpredicted  $\epsilon$  can be compensated linearly by the coefficient as follows:<sup>40</sup>

$$\beta = \frac{\epsilon_{CFD,i}}{\sum_{i=1}^{NB} \epsilon_{CFD,i} w_i} \quad (36)$$

$$\epsilon^* = \beta \frac{P_\tau}{m_q} \quad (37)$$

where  $\epsilon_{CFD,i}$  is the local average energy dissipation rate calculated by CFD,  $m^2/s^3$ ,  $w_i$  is the mass fraction of liquid in cell  $i$ ,  $\epsilon^*$  is the compensated energy dissipation rate,  $m^2/s^3$ , and  $m_q$  is the mass of liquid in cell  $i$ , kg.

At the assumption of constant bubble size, the  $k_L a$  values in the rotating and stationary zones of the reactor obtained in this work are 26 and 74% of total mass transfer. The linearly compensated energy dissipation rate as  $(1.2\epsilon)^{0.25}$  increases the overall mass transfer coefficient less than 5%. One may debate that linear compensation is quite a guess and it should be performed rather via power law.<sup>41,42</sup> Checking this statement is worth separate research, and it is left out of the scope in this work. However, at the assumption that the underpredicted energy is located in the rotating zone, the linear compensation of  $\epsilon$  in that zone only contributes to the overall  $k_L$  just around 2%. Thus, the mass transfer underprediction within 2–5% is negligible for the case under consideration at the assumption of constant bubble size.

More detailed information on the performance of the OKTOP®9000 reactor can be achieved from the contours of velocity field,  $d_{32}$ , and specific mass transfer, presented in Figures 5–7. The effect of gas onto liquid phase hydrodynamics can be seen in Figure 5 where single and multiphase mixing hydrodynamics is presented in vertical midsection.

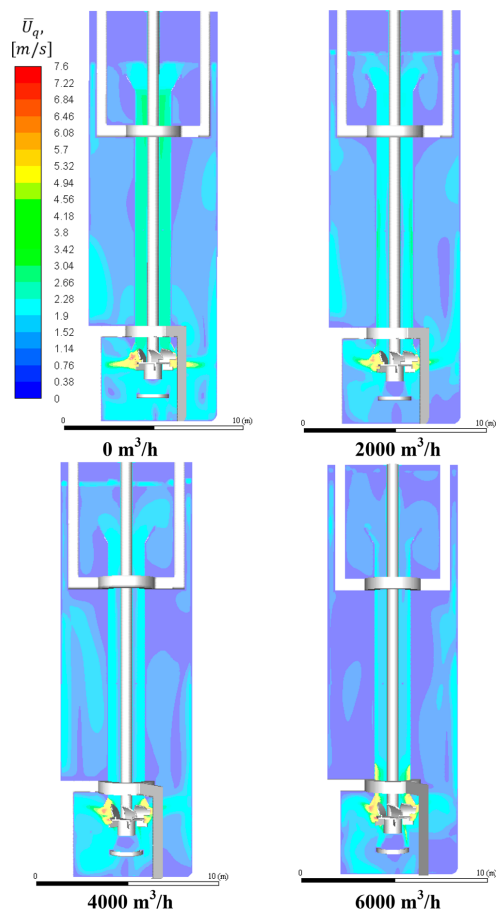


Figure 5. Steady state liquid phase velocity contours in vertical plane gas-liquid mixing in OKTOP@9000 reactor at different air flow rates.

The radial jets coming from the impeller are mainly pushed upward by gas, which reduces the mean velocity of the flow below the impeller. The mean velocity field in the riser part of the reactor is almost unaffected while it is reduced in the draft tube due to the presence of gas. Near the solution surface, fluid is more agitated by gas escaping the liquid.

Gas-liquid hydrodynamics have been simulated with the assumption of constant bubble size, which is acceptable in the case of narrow BSD. However, mass transfer is much more sensitive toward bubble size. Therefore, eq 28 has been applied to get the Sauter mean diameter of bubbles in computational cells (Figure 6). Mean volumetric bubble size was around 1.7 mm in the case of 4000 m<sup>3</sup>/h of gas flow rate, which produced 15% higher  $k_L a$ . The calculated  $d_{32}$  has its minimum in the most turbulent region of radial flow created by the impeller while maximum values can be found in the regions of high local gas hold-ups and low mixing intensity that are located under impeller radial jet and in the central area close to the reactor top. Having left the mixing zone, the bubbles are

moving spirally to the top staying distributed, which keeps relatively constant local gas volume fraction. As a result, no active coalescence can be seen in the middle of the reactor. At the top of the reactor, lowered mixing intensity in combination with increased gas hold-up results in coalescence rate increase and bubbles growth.

Additionally, the bubble size distribution was calculated at 4000 m<sup>3</sup>/h to assess the prediction found by eq 28. For this purpose, the population balance equation for four moments represented the total number  $m_0$ , length  $m_1$ , surface area  $m_2$ , and volume  $m_3$  of the population. The bubble size was limited in the range of 0.1–10 mm. Breakage frequency and daughter bubble distribution have been simulated using Laakkonen's models.<sup>43</sup> Coalescence was calculated via Luo's model.<sup>44</sup> The moments were calculated at frozen hydrodynamics using QUICK scheme and converged at 10<sup>−4</sup>. The results of the calculated mean bubble size are summarized in Table S6.

The results state that the value of mean bubble size predicted by different methods produced close results. The higher the gas flow rate, the smaller the effect of the global mass transfer. Bubble size distribution, calculated via eq 28, was used further to get local mass transfer (Figure 7) and during the fermentation simulations.

Comparing the contours of specific mass transfer (Figure 7), similarity in distribution can be found; however, mixing at micro scale promoted by turbulence, where oxygen is transported from bubble to liquid, is higher in the down part of the reactor. The highest mass transfer is in the vicinity of the impeller. Few words should be said about gas-liquid mass transfer in the draft tube. During experimental tests of gas-liquid mixing in the OKTOP@9000 reactor, gas was noticed to separate from the liquid phase and stick to the shaft in the draft tube under the Coriolis forces. Thus, gas-liquid mass transfer can only take place via the slip-velocity mechanism and considering gas phase as dispersed in the draft tube is not justified. However, the input to  $k_L a$  in the draft tube is insignificantly small as well as in the area near the liquid surface.

Tervasmäki et al.<sup>21</sup> studied lab scale version of OKTOP reactor over the range of gas flow rate and impeller speeds. In Chart 1, the comparison of the global gas-liquid mass transfer measured experimentally in the small scale reactor against simulated results at the industrial scale is presented.

Large reactors provide higher specific interfacial area as bubble size distribution remains similar to smaller reactors when scale-up is done based on constant volumetric power. As a result, the efficiency of oxygen transfer grows along with the scale of the OKTOP reactor at similar specific power input.

The industrial scale reactor is more than 20 m in height and operates under atmospheric pressure. High hydrostatic pressure increases oxygen saturation concentration in the reactor (Figure 8).

Microorganisms are sensitive to high shear strain of fluid media; therefore, the safety of *P. pastoris* bacteria was verified in the reactor at large scale. According to the electronic database of Harvard University,<sup>45</sup> the *P. pastoris* dimension is of 5 μm. In mixed flow, the turbulent eddies of size smaller than the bacteria can be of potential damage. Therefore, the ratio of the bacteria length to Kolmogorov's length scale is presented as a contour in a vertical plane (Figure 9) at 4000 m<sup>3</sup>/h.

The areas of  $\lambda_x/\eta_K$  higher than 1 are potentially dangerous to the microorganisms. As can be seen, the flow strength is not

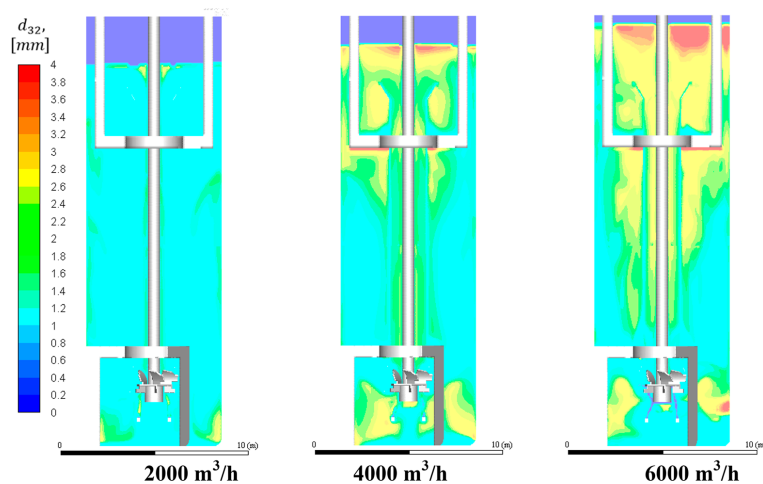


Figure 6. Contour of  $d_{32}$  in vertical plane in OKTOP@9000 reactor at different air flow rates and  $1 \text{ s}^{-1}$  calculated via eq 28.

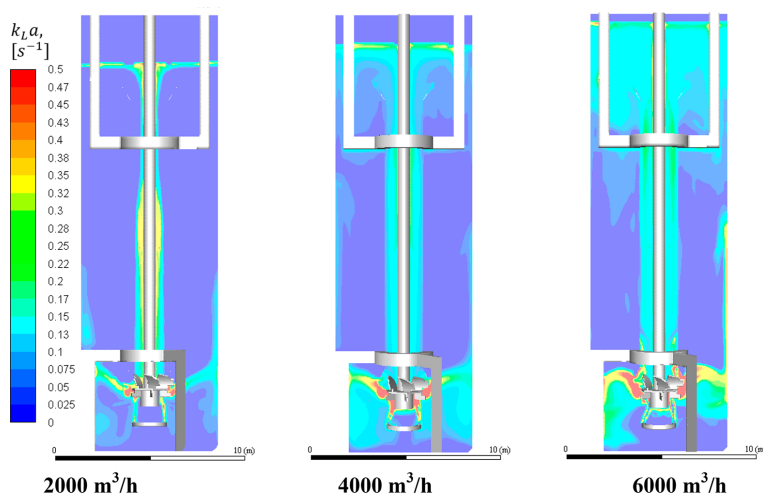


Figure 7. Contours of gas-liquid mass transfer in an OKTOP@9000 reactor at different air flow rates.

enough to harm the bacteria. However, further increase of mixing speed may affect the microorganisms.

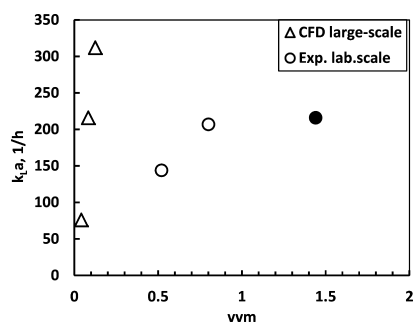
**3.2. Bio Reaction. 3.2.1. Batch Mode.** In this work, the cell cultivation process in the OKTOP@9000 reactor, initially enriched with oxygen, has been simulated in batch mode at 80 g/L of glucose and 2 g/L of cells. To verify the large-scale CFD results, experimental data was taken from the lab scale tests carried out by Tervasmäki et al.<sup>21</sup> for a similar but smaller setup. The concentrations of the glucose, ethanol, and cells are presented in Chart 2 as a function of time. The reported large-scale data points from CFD simulations were calculated as volume averaged.

The simulated results of the fermentation taking place in the reactor at large-scale (800 m<sup>3</sup>) are in a reasonable agreement

with those obtained during the experimental tests on the fermentation carried out in the OKTOP reactor at lab scale (14 L). Since the reaction rate is very low, the main difference between the reactors at lab and large scales is the oxygen transfer rate and oxygen saturation concentration. Following the ethanol production, the effect of oxygen transfer rate can be observed. Excess of available dissolved oxygen promotes glucose oxidation and inhibits fermentative reaction. Being converted to ethanol and then oxidized, the glucose loses part of its mass to CO<sub>2</sub>, resulting in the reduction of cell yield. The conversion is faster at higher oxygen mass transfer rate as well. In addition, minor uncertainties in measurements and maintenance of operational conditions took place as well and



Chart 1. Mass Transfer in OKTOP Reactors at Different Scales in Ethanol 1% Solution at  $P/V \approx 500 \text{ W/m}^3$ <sup>a</sup>



<sup>a</sup>Filled symbol corresponds to the experimental fermentation case in the lab-scale OKTOP reactor. Experimental data is from Tervasmäki et al.<sup>21</sup>

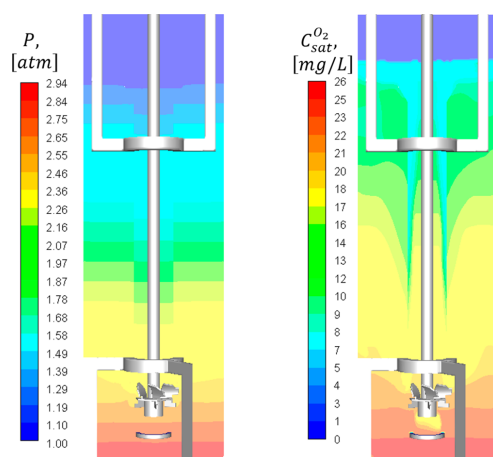


Figure 8. Contours of hydrostatic pressure (left) and oxygen saturation concentration (right) in the OKTOP@9000 reactor.

caused the deviation between simulated and experimental results.

#### 4. CONCLUSIONS

This work presents an aerobic fermenter modeled at industrial scale. Multiphase mixing flow hydrodynamics was simulated at steady state in the draft-tube OKTOP@9000 reactor. Gas–liquid drag force, comprising effects of laminar, turbulent regimes and bubble swarms, was applied to model the behavior of gas bubbles in ethanol containing fluid. Power number was measured at large scale in single phase mixing tests, and it was used for the model validation.

The effect of linearly compensated energy dissipation ( $\epsilon$ ), caused by spatial discretization, onto gas–liquid mass transfer at narrow BSD is considered and found below 5% in the stirred reactor. However, compensated dissipated energy would have greater effect in cases of wide BSD as gas–liquid contact area grows and bubble size gets smaller in the regions of high  $\epsilon$  and

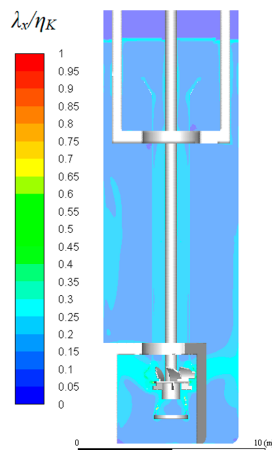
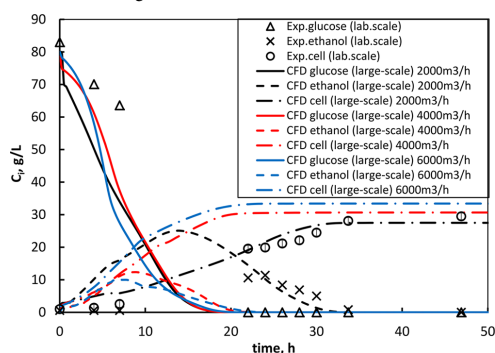


Figure 9. Contour of  $\lambda_x/\eta_K$  in a vertical plane in an OKTOP@9000 reactor at  $1 \text{ s}^{-1}$  and  $4000 \text{ m}^3/\text{h}$ .

Chart 2. Temporal Evolution of Normalized Concentration of Species in Batch OKTOP@9000 Reactor at 80 g/L of Glucose and 2 g/L of Cells<sup>a</sup>



<sup>a</sup>Experimental data is from Tervasmäki et al.<sup>21</sup>

opposite trends take place in the regions of low dissipated energy.

The large scale OKTOP reactor provides higher oxygen mass transfer rate at similar volumetric power consumption as in the lab scale reactor due to higher specific interfacial area. BSD contributes up to 15% of total  $k_L a$  compared to constant bubble size in 1% ethanol solution in the large scale OKTOP reactor.

Fermentation kinetics, describing metabolism of *Pichia pastoris* bacteria, is presented. The batch fermentation process of the cell cultivation was simulated in the draft tube stirred-tank reactor of industrial scale at different air supply rates. The results were compared with experimental data measured at similar reactor of lab scale, and a good match was found. At higher aeration rate, glucose fermentation is avoided, which cuts the carbon losses in  $\text{CO}_2$  and increases the yield of the cells. The metabolism is pushed toward glucose oxidation that

reduces retention time. The CFD modeling was proved to be a reliable tool for design of industrial aerobic fermenters.

## ■ ASSOCIATED CONTENT

### Supporting Information

The Supporting Information is available free of charge on the ACS Publications website at DOI: 10.1021/acs.iecr.8b02765.

Table 1. *Pichia pastoris* cultivation kinetics parameters. Table 2. Sizing of OKTOP@9000 reactor at industrial scale. Table 3. Operational conditions of protein growth in lab scale OKTOP@9000 reactor. Table 4. Results of grid test of single phase mixing in OKTOP@9000 at 1 s<sup>-1</sup>. Table 5. Summarized conditions for gas–liquid mixing in OKTOP@9000. Table 6. Volumetric mean  $d_{32}$  of bubbles found with different approaches and the corresponding mass transfer values (PDF)

## ■ AUTHOR INFORMATION

### Corresponding Author

\*Tel.: +358 46 5470573. E-mail addresses: dmitry.gradov@lut.fi, gradov-dmitrii@inbox.ru, dmitry.vladimirovich.gradov@gmail.com (D.V. Gradov).

### ORCID

Dmitry Vladimirovich Gradov: 0000-0003-4222-0354

### Notes

The authors declare no competing financial interest.

## ■ ACKNOWLEDGMENTS

The authors are grateful to the Finnish Funding Agency TEKES and, in particular, to Outotec Finland Oy and Neste Engineering Solutions Oy collaborating under FERMATRA project (908/31/2016 and 958/31/2016), for active supervision and financial support.

## ■ REFERENCES

- (1) Garcia-Ochoa, F.; Gomez, E. Bioreactor Scale-up and Oxygen Transfer Rate in Microbial Processes: An Overview. *Biotechnol. Adv.* **2009**, *27* (2), 153–176.
- (2) Nauha, E. K.; Visuri, O.; Vermasvuori, R.; Alopaeus, V. A New Simple Approach for the Scale-up of Aerated Stirred Tanks. *Chem. Eng. Res. Des.* **2015**, *95* (October), 150–161.
- (3) Nauha, E. K.; Käläl, Z.; Ali, J. M.; Alopaeus, V. Compartmental Modeling of Large Stirred Tank Bioreactors with High Gas Volume Fractions. *Chem. Eng. J.* **2018**, *334*, 2319–2334.
- (4) Vrábel, P.; van Der Lans, R. G. J. M.; Luyben, K. C. A. M.; Boon, L.; Nienow, A. W. Mixing in Large-Scale Vessels Stirred with Multiple Radial or Radial and Axial up-Pumping Impellers: Modelling and Measurements. *Chem. Eng. Sci.* **2000**, *55* (23), 5881–5896.
- (5) Kaskiala, T. *Studies on Gas-Liquid Mass Transfer in Atmospheric Leaching of Sulphidic Zinc Concentrates*; Helsinki University of Technology, 2005.
- (6) Tervasmäki, P.; Latva-Kokko, M.; Taskila, S.; Tanskanen, J. Mass Transfer, Gas Hold-up and Cell Cultivation Studies in a Bottom Agitated Draft Tube Reactor and Multiple Impeller Rushton Turbine Configuration. *Chem. Eng. Sci.* **2016**, *155*, 83–98.
- (7) Askew, W. S.; Beckmann, R. B. Heat and Mass Transfer in an Agitated Vessel. *Ind. Eng. Chem. Process Des. Dev.* **1965**, *4* (3), 311–318.
- (8) Prasher, B. D.; Wills, G. B. *Ind. Eng. Chem. Process Des. Dev.* **1973**, *12* (3), 351–354.
- (9) Linek, V.; Kordač, M.; Fijasová, M.; Moucha, T. Gas-Liquid Mass Transfer Coefficient in Stirred Tanks Interpreted through Models of Idealized Eddy Structure of Turbulence in the Bubble Vicinity. *Chem. Eng. Process.* **2004**, *43* (12), 1511–1517.
- (10) Morchain, J.; Gabelle, J. C.; Cockx, A. A Coupled Population Balance Model and CFD Approach for the Simulation of Mixing Issues in Lab-Scale and Industrial Bioreactors. *AIChE J.* **2014**, *60* (1), 27–40.
- (11) Schwarz, M. P.; Koh, P. T. L.; Verrelli, D. I.; Feng, Y. Sequential Multi-Scale Modelling of Mineral Processing Operations, with Application to Flotation Cells. *Miner. Eng.* **2016**, *90*, 2–16.
- (12) Nikolic, D. D.; Frawley, P. J. Application of the Lagrangian Meshfree Approach to Modelling of Batch Crystallisation: Part I-Modelling of Stirred Tank Hydrodynamics. *Chem. Eng. Sci.* **2016**, *145*, 317–328.
- (13) Duan, X.; Feng, X.; Yang, C.; Mao, Z. CFD Modeling of Turbulent Reacting Flow in a Semi-Batch Stirred-Tank Reactor. *Chin. J. Chem. Eng.* **2018**, *26*, 675–683.
- (14) Haringa, C.; Deshmukh, A. T.; Mudde, R. F.; Noorman, H. J. Euler-Lagrange Analysis towards Representative down-Scaling of a 22 m<sup>3</sup> Aerobic *S. Cerevisiae* Fermentation. *Chem. Eng. Sci.* **2017**, *170*, 653–669.
- (15) Haringa, C.; Tang, W.; Wang, G.; Deshmukh, A. T.; van Winden, W. A.; Chu, J.; van Gulik, W. M.; Heijnen, J. J.; Mudde, R. F.; Noorman, H. J. Computational Fluid Dynamics Simulation of an Industrial *P. Chrysogenum* Fermentation with a Coupled 9-Pool Metabolic Model: Towards Rational Scale-down and Design Optimization. *Chem. Eng. Sci.* **2018**, *175*, 12–24.
- (16) Lane, G. L. Improving the Accuracy of CFD Predictions of Turbulence in a Tank Stirred by a Hydrofoil Impeller. *Chem. Eng. Sci.* **2017**, *169*, 188–211.
- (17) Enfors, S. O.; Jahic, M.; Rozkov, A.; Xu, B.; Hecker, M.; Jürgen, B.; Krüger, E.; Schweder, T.; Hamer, G.; O'Beirne, D.; et al. Physiological Responses to Mixing in Large Scale Bioreactors. *J. Biotechnol.* **2001**, *85* (2), 175–185.
- (18) Paul, E. L.; Atiemo-obeng, V.; Krestra, S. M. *Handbook of Industrial Mixing Science and Practice*; 2004.
- (19) Lapin, A.; Müller, D.; Reuss, M. Dynamic Behavior of Microbial Populations in Stirred Bioreactors Simulated with Euler–Lagrange Methods: Traveling along the Lifelines of Single Cells <sup>†</sup>. *Ind. Eng. Chem. Res.* **2004**, *43* (16), 4647–4656.
- (20) Lapin, A.; Schmid, J.; Reuss, M. Modeling the Dynamics of *E. Coli* Populations in the Three-Dimensional Turbulent Field of a Stirred-Tank Bioreactor-A Structured-Segregated Approach. *Chem. Eng. Sci.* **2006**, *61* (14), 4783–4797.
- (21) Tervasmäki, P.; Latva-Kokko, M.; Taskila, S.; Tanskanen, J. Effect of Oxygen Transfer on Yeast Growth Kinetic and Reactor Model to Estimate Scale-up Effects in Bioreactors. *Food Bioprod. Process.* **2018**.
- (22) Outotec. Outotec ® Reactor technologies OKTOP Reactor – the complete solution for your process needs <http://www.outotec.com/en/Search-material/Search-material-by-categories/?quicksearchquery=reactor&excludeimages=true&categories=68,75>.
- (23) Gradov, D. V.; Laari, A.; Turunen, I.; Koironen, T. Experimentally Validated CFD Model for Gas-Liquid Flow in a Round-Bottom Stirred Tank Equipped with Rushton Turbine. *Int. J. Chem. React. Eng.* **2016**, *15* (2).
- (24) Hashemi, N.; Ein-Mozaffari, F.; Upreti, S. R.; Hwang, D. K. Analysis of Power Consumption and Gas Holdup Distribution for an Aerated Reactor Equipped with a Coaxial Mixer: Novel Correlations for the Gas Flow Number and Gassed Power. *Chem. Eng. Sci.* **2016**, *151*, 25–35.
- (25) Schiller, L.; Naumann, Z. A Drag Coefficient Correlation. *Z. Ver. Deutsch. Ing.* **1933**, *77* (13–14), 318–320.
- (26) Brucato, A.; Grisafi, F.; Montante, G. Particle Drag Coefficients in Turbulent Fluids. *Chem. Eng. Sci.* **1998**, *53* (18), 3295–3314.
- (27) Lane, G. L.; Schwarz, M. P.; Evans, G. M. Numerical Modelling of Gas-Liquid Flow in Stirred Tanks. *Chem. Eng. Sci.* **2005**, *60* (8–9 SPEC. ISS.), 2203–2214.
- (28) Roghair, I.; Lau, Y. M.; Deen, N. G.; Slagter, H. M.; Baltussen, M. W.; Van Sint Annaland, M.; Kuipers, J. A. M. On the Drag Force of Bubbles in Bubble Swarms at Intermediate and High Reynolds Numbers. *Chem. Eng. Sci.* **2011**, *66* (14), 3204–3211.

- (29) Kawase, Y.; Halard, B.; Moo-Young, M. Liquid-Phase Mass Transfer Coefficients in Bioreactors. *Biotechnol. Bioeng.* **1992**, *39* (11), 1133–1140.
- (30) Han, P.; Bartels, D. M. Temperature Dependence of Oxygen Diffusion in H<sub>2</sub>O and D<sub>2</sub>O. *J. Phys. Chem.* **1996**, *100* (13), 5597–5602.
- (31) Garcia-Ochoa, F.; Gomez, E. Mass Transfer Coefficient in Stirred Tank Reactors for Xanthan Gum Solutions. *Biochem. Eng. J.* **1998**, *1*, 1–10.
- (32) Calderbank, P. H.; Moo-Young, M. B. The Continuous Phase Heat and Mass Transfer Properties of Dispersions. *Chem. Eng. Sci.* **1995**, *50* (24), 3921–3934.
- (33) Machon, V.; Pacek, A. W.; Nienow, A. W. Bubble Sizes in Electrolyte and Alcohol Solutions in a Turbulent Stirred Vessel. *Chem. Eng. Res. Des.* **1997**, *75* (3), 339–348.
- (34) Hu, B.; Pacek, A. W.; Stitt, H. E.; Nienow, A. W. Bubble Sizes in Agitated Air-Alcohol Systems with and without Particles: Turbulent and Transitional Flow. *Chem. Eng. Sci.* **2005**, *60* (22), 6371–6377.
- (35) Haringa, C.; Tang, W.; Deshmukh, A. T.; Xia, J.; Reuss, M.; Heijnen, J. J.; Mudde, R. F.; Noorman, H. J. Euler-Lagrange Computational Fluid Dynamics for (Bio)reactor Scale down: An Analysis of Organism Lifelines. *Eng. Life Sci.* **2016**, *16* (7), 652–663.
- (36) Lide, D. R. *CRC Handbook of Chemistry and Physics*, 84th Edition, 2003–2004; Vol. 53, p. 2616.
- (37) Joshi, J. B.; Nere, N. K.; Rane, C. V.; Murthy, B. N.; Mathpati, C. S.; Patwardhan, A. W.; Ranade, V. V. CFD Simulation of Stirred Tanks: Comparison of Turbulence Models. Part I: Radial Flow Impellers. *Can. J. Chem. Eng.* **2011**, *89* (1), 23–82.
- (38) Gradov, D. V.; González, G.; Vauhkonen, M.; Laari, A.; Koironen, T. Experimental and Numerical Study of Multiphase Mixing Hydrodynamics in Batch Stirred Tank Applied to Ammoniacal Thiosulphate Leaching of Gold. *J. Chem. Eng. Process Technol.* **2017**, *8* (3), 1–17.
- (39) Kalitzin, G.; Medic, G.; Iaccarino, G.; Durbin, P. Near-Wall Behavior of RANS Turbulence Models and Implications for Wall Functions. *J. Comput. Phys.* **2005**, *204* (1), 265–291.
- (40) Li, D.; Gao, Z.; Buffo, A.; Podgorska, W.; M, D. L. Droplet Breakage and Coalescence in Liquid–Liquid Dispersions: Comparison of Different Kernels with EQMOM and QMOM. *AIChE J.* **2017**, *63* (6), 2293–2311.
- (41) Delafosse, A.; Collignon, M. L.; Crine, M.; Toye, D. Estimation of the Turbulent Kinetic Energy Dissipation Rate from 2D-PIV Measurements in a Vessel Stirred by an Axial Mixel TTP Impeller. *Chem. Eng. Sci.* **2011**, *66* (8), 1728–1737.
- (42) Ben-Nun, R.; Sheintuch, M.; Kysela, B.; Konfrst, J.; Fořt, I. Semianalytical Characterization of Turbulence from Radial Impellers, with Experimental and Numerical Validation. *AIChE J.* **2015**, *61* (4), 1413–1426.
- (43) Moilanen, P.; Laakkonen, M.; Aittamaa, J. CFD Modelling of Local Bubble Size Distributions in Agitated Gas-Liquid Vessels - Verification against Experiments, 2004, Vol. 18.
- (44) Luo, H. Coalescence, Breakup and Liquid Circulation in Bubble Column Reactors, 1993.
- (45) Milo, R.; Jorgensen, P.; Moran, U.; Weber, G.; Springer, M. BioNumbers The Database of Key Numbers in Molecular and Cell Biology. *Nucleic Acids Res.* **2010**, *38* (SUPPL.1), 750–753.

# Numerical simulation of biomass growth in OKTOP®9000 reactor at industrial scale

*Dmitry Vladimirovich Gradov<sup>1\*</sup>, Mei Han<sup>1</sup>, Petri Tervasmäki<sup>2</sup>, Marko Latva-Kokko<sup>3</sup>, Johanna  
Vaattinen<sup>4</sup>, Arto Pihlajamäki<sup>1</sup>, Tuomas Koiranen<sup>1</sup>*

## Supporting Information for Publication - TABLES

**Table S1.** *Pichia pastoris* cultivation kinetics parameters

Parameter	Dimension	Value	Reference
$\mu_{\max}^{\text{ox}}$	$\text{h}^{-1}$	0.18	Solà et al. <sup>22</sup>
$\mu_{\max}^{\text{ferm}}$	$\text{h}^{-1}$	0.058	Tervasmäki et al. <sup>21</sup>
$\mu_{\max}^{\text{c}}$	$\text{h}^{-1}$	0.15	Tervasmäki et al. <sup>21</sup>
$Y_{\text{xg}}^{\text{ox}}$	$\text{g}_\text{x}/\text{g}_\text{g}$	0.49	Sonnleitner and Käppeli <sup>23</sup>
$Y_{\text{xg}}^{\text{ferm}}$	$\text{g}_\text{x}/\text{g}_\text{g}$	0.05	Sonnleitner and Käppeli <sup>23</sup>
$Y_{\text{xe}}^{\text{ox}}$	$\text{g}_\text{x}/\text{g}_\text{e}$	0.57	Sonnleitner and Käppeli <sup>23</sup>
$K_{\text{g}}$	$\text{g}_\text{g}/\text{L}$	0.1	Sonnleitner and Käppeli <sup>23</sup>
$K_{\text{o}}$	$\text{mg}_\text{o}/\text{L}$	0.109	Tervasmäki et al. <sup>21</sup>
$K_{\text{e}}$	$\text{g}_\text{e}/\text{L}$	0.1	Sonnleitner and Käppeli <sup>23</sup>

$K_i$	$\text{g}_\text{g}/\text{L}$	0.1	Sonnleitner and Käppeli <sup>23</sup>
HX	$\text{mol}_\text{H}/\text{mol}_\text{C}$	1.69	Carnicer et al. <sup>24</sup>
OX	$\text{mol}_\text{O}/\text{mol}_\text{C}$	0.592	Carnicer et al. <sup>24</sup>
NX	$\text{mol}_\text{N}/\text{mol}_\text{C}$	0.139	Carnicer et al. <sup>24</sup>

**Table S2.** Sizing of OKTOP®9000 reactor at industrial scale

Reactor dimensions	m
Tank diameter	7.6
Liquid height	20
Impeller diameter	2.6
Draft tube diameter	2.1
Draft tube height	13.2
Draft tube clearance	3.3
Ring-sparger vertical position	1.3
Ring-sparger diameter	1.9
Baffles height	4.6

**Table S3.** Operational conditions of protein growth in lab scale OKTOP®9000 reactor

Operational conditions	Value	Units
Stirring speed	1	$\text{s}^{-1}$
Volumetric mean mixing power	500	$\text{W}/\text{m}^3$
Superficial gas velocity	1.36	$\text{cm}/\text{s}$
$\text{C}_6\text{H}_{12}\text{O}_6$ concentration	80	$\text{g}/\text{L}$
Initial concentration of cells in reactor	2	$\text{g}/\text{L}$
Temperature	30	$^\circ\text{C}$

Solution dynamic viscosity	0.798	mPa·s
Solution density	996	kg/m <sup>3</sup>
Air dynamic viscosity	0.0186	mPa·s
Air density	1.164	kg/m <sup>3</sup>
Air-water surface tension in water-ethanol (1 %) solution	0.069	N/m

**Table S4.** Results of grid test of single phase mixing in OKTOP®9000 at 1 s<sup>-1</sup>

Grid label	Mesh size, 10 <sup>6</sup>	k, m <sup>2</sup> /s <sup>2</sup>	ε, m <sup>2</sup> /s <sup>3</sup>	τ, kN·m
1	0.5	257	286	74
2	1	300	421	87
3	2	312	452	87
4	4	317	459	88

**Table S5.** Summarized conditions for gas-liquid mixing in OKTOP®9000

Operational condition	Modelled phenomenon	Model used
60 rpm	Mixing	MRF
	Turbulence	k-ε Realizable, dispersed
	Near wall flow	Standard wall function
2000 4000 6000 m <sup>3</sup> /h of air	Gas-liquid flow	Eulerian-Eulerian
	Bubble size	Constant $d_b = 2\text{ mm}$
	Drag force in laminar flow	Schiller-Naumann <sup>28</sup>
	Drag force modification due to turbulent flow	Lane et al. <sup>30</sup>
	Drag force modification due to bubble swarm	Roghair et al. <sup>31</sup>
	Oxygen mass transfer	Kawase et al. <sup>32</sup>

2 g of yeast 80 g of glucose	Cell cultivation	Tervasmäki et al. <sup>21</sup>
---------------------------------	------------------	---------------------------------

**Table S6.** Volumetric mean  $d_{32}$  of bubbles found with different approaches and the corresponding mass transfer values

Air flow rate, m <sup>3</sup> /h	$d_{32}$ , mm			$k_L a$ , s <sup>-1</sup>		
	Measured <sup>33,34</sup>	Eq. 28 <sup>32</sup>	QMOM	2 mm	Eq. 28 <sup>32</sup>	QMOM
2000	2	1.1	-	54	76	-
4000	2	1.6	1.8	191	216	205
6000	2	1.9	-	302	312	-

#### Notation

Symbols	Meaning	Units
$A_i$	Interfacial area	m <sup>2</sup>
$A_{imp}$	Surface of impeller	m <sup>2</sup>
$C$	Proportionality coefficient	-
$C_D$	Drag force coefficient	-
$c_i$	Specie $i$ concentration	g/L
$d_p$	Bubble size	m
$d_{32}$	Sauter mean diameter	m
$D_L$	Diffusivity	m <sup>2</sup> /s
$D_{i,m}$	Laminar diffusivity of specie $i$	m <sup>2</sup> /s
$D_{i,t}$	Turbulent diffusivity of specie $i$	m <sup>2</sup> /s
$Eö$	Eötvös number	-

$K$	Consistency index	$\text{Pa}\cdot\text{s}^n$
$K_i$	Saturation coefficient of specie $i$ uptake	$\text{g/L}$
$K_{in}$	Inhibition constant	$\text{g/L}$
$k_H$	Henry's constant	$\text{atm}/(\text{L/mol})$
$k_L$	Mass transfer coefficient	$\text{m/s}$
$k_L a$	Volumetric mass transfer coefficient	$\text{s}^{-1}$
$n$	Dimensionless flow behavior index	-
$N$	Mixing speed	$\text{s}^{-1}$
$P$	Power draw	$\text{W}$
$q_i$	Specific rate of component $i$	$\text{g}_i/(\text{g}_{\text{cell}}\cdot\text{s})$
$R_i$	Net rate of production of species $i$	$\text{kg}/(\text{m}^3\cdot\text{s})$
$Re$	Reynolds number	-
$T$	Temperature	$^{\circ}\text{C}$
$T_L$	Turbulence time scale	$\text{s}$
$U_s$	Terminal velocity of gas bubble in stagnant flow	$\text{m/s}$
$U_T$	Terminal velocity of gas bubble in turbulent flow	$\text{m/s}$
$u$	Velocity	$\text{m/s}$
$V$	Reactor volume	$\text{m}^3$
$Y_i$	Species concentration	$\text{g/L}$
$Y_i^{Rj}$	Yield coefficient for species $i$ and $j$ in reaction $R$	$\text{g}_i/\text{g}_j$

Greek letters	Meaning	Units
$\alpha$	Phase volume fraction	-
$\beta$	Coefficient of linearly compensated energy	-
$\varepsilon$	Turbulence energy dissipation rate	$\text{m}^2/\text{s}^3$
$\varepsilon^*$	Linearly compensated turbulence energy dissipation rate	$\text{m}^2/\text{s}^3$



$k$	Turbulence Kinetic Energy	$\text{m}^2/\text{s}^2$
$m_q$	Mass of liquid in a cell	kg
$\mu$	Dynamic viscosity	$\text{kg}/(\text{m}\cdot\text{s})$
$\mu_{max}^R$	Growth rate of cells in reaction R	$\text{s}^{-1}$
$\eta$	Turbulence modification factor	-
$\lambda$	Kolmogorov length scale	m
$\pi$	Mathematical constant	-
$p$	Pressure	Pa
$p_h$	Hydrostatic pressure	Pa
$p_{vapor}$	Vapor pressure	Pa
$\rho$	Phase density	$\text{kg}/\text{m}^3$
$\tau$	Torque	$\text{N}\cdot\text{m}$
$\tau_i$	Time scale	s
$\sigma$	Surface tension	N/m
$\nu$	Kinematic viscosity	$\text{m}^2/\text{s}$
$w_i$	Mass fraction of liquid in cell	-

Acronyms	Transcript
BSD	Bubble Size Distribution
CFD	Computational Fluid Dynamics
CSTR or STR	Continuous Stirred-Tank Reactor
MRF	Multiple Reference Frame approach
PIV	Particle Image Velocimetry
RANS	Reynolds-Averaged Navier-Stokes
RSM	Reynolds Stress Model
SM	Sliding Mesh approach

SST	Shear Stress Transport k- $\omega$ model
UDF	User Defined Function



## ACTA UNIVERSITATIS LAPPEENRANTAENSIS

- 809. HERALA, ANTTI. Benefits from Open Data: barriers to supply and demand of Open Data in private organizations. 2018. Diss.
- 810. KÄYHKÖ, JORMA. Erityisen tuen toimintaprosessien nykytila ja kehittäminen suomalaisessa oppisopimuskoulutuksessa. 2018. Diss.
- 811. HAJIKHANI, ARASH. Understanding and leveraging the social network services in innovation ecosystems. 2018. Diss.
- 812. SKRIKO, TUOMAS. Dependence of manufacturing parameters on the performance quality of welded joints made of direct quenched ultra-high-strength steel. 2018. Diss.
- 813. KARTTUNEN, ELINA. Management of technological resource dependencies in interorganizational networks. 2018. Diss.
- 814. CHILD, MICHAEL. Transition towards long-term sustainability of the Finnish energy system. 2018. Diss.
- 815. NUTAKOR, CHARLES. An experimental and theoretical investigation of power losses in planetary gearboxes. 2018. Diss.
- 816. KONSTI-LAAKSO, SUVI. Co-creation, brokering and innovation networks: A model for innovating with users. 2018. Diss.
- 817. HURSKAINEN, VESA-VILLE. Dynamic analysis of flexible multibody systems using finite elements based on the absolute nodal coordinate formulation. 2018. Diss.
- 818. VASILYEV, FEDOR. Model-based design and optimisation of hydrometallurgical liquid-liquid extraction processes. 2018. Diss.
- 819. DEMESA, ABAYNEH. Towards sustainable production of value-added chemicals and materials from lignocellulosic biomass: carboxylic acids and cellulose nanocrystals. 2018. Diss.
- 820. SIKANEN, EERIK. Dynamic analysis of rotating systems including contact and thermal-induced effects. 2018. Diss.
- 821. LIND, LOTTA. Identifying working capital models in value chains: Towards a generic framework. 2018. Diss.
- 822. IMMONEN, KIRSI. Ligno-cellulose fibre poly(lactic acid) interfaces in biocomposites. 2018. Diss.
- 823. YLÄ-KUJALA, ANTTI. Inter-organizational mediums: current state and underlying potential. 2018. Diss.
- 824. ZAFARI, SAHAR. Segmentation of partially overlapping convex objects in silhouette images. 2018. Diss.
- 825. MÄLKKI, HELENA. Identifying needs and ways to integrate sustainability into energy degree programmes. 2018. Diss.
- 826. JUNTUNEN, RAIMO. LCL filter designs for parallel-connected grid inverters. 2018. Diss.
- 827. RANAEI, SAMIRA. Quantitative approaches for detecting emerging technologies. 2018. Diss.

828. METSO, LASSE. Information-based industrial maintenance - an ecosystem perspective. 2018. Diss.
829. SAREN, ANDREY. Twin boundary dynamics in magnetic shape memory alloy Ni-Mn-Ga five-layered modulated martensite. 2018. Diss.
830. BELONOGOVA, NADEZDA. Active residential customer in a flexible energy system - a methodology to determine the customer behaviour in a multi-objective environment. 2018. Diss.
831. KALLIOLA, SIMO. Modified chitosan nanoparticles at liquid-liquid interface for applications in oil-spill treatment. 2018. Diss.
832. GEYDT, PAVEL. Atomic Force Microscopy of electrical, mechanical and piezo properties of nanowires. 2018. Diss.
833. KARELL, VILLE. Essays on stock market anomalies. 2018. Diss.
834. KURONEN, TONI. Moving object analysis and trajectory processing with applications in human-computer interaction and chemical processes. 2018. Diss.
835. UNT, ANNA. Fiber laser and hybrid welding of T-joint in structural steels. 2018. Diss.
836. KHAKUREL, JAYDEN. Enhancing the adoption of quantified self-tracking wearable devices. 2018. Diss.
837. SOININEN, HANNE. Improving the environmental safety of ash from bioenergy production plants. 2018. Diss.
838. GOLMAEI, SEYEDMOHAMMAD. Novel treatment methods for green liquor dregs and enhancing circular economy in kraft pulp mills. 2018. Diss.
839. GERAMI TEHRANI, MOHAMMAD. Mechanical design guidelines of an electric vehicle powertrain. 2019. Diss.
840. MUSIIENKO, DENYS. Ni-Mn-Ga magnetic shape memory alloy for precise high-speed actuation in micro-magneto-mechanical systems. 2019. Diss.
841. BELIAEVA, TATIANA. Complementarity and contextualization of firm-level strategic orientations. 2019. Diss.
842. EFIMOV-SOINI, NIKOLAI. Ideation stage in computer-aided design. 2019. Diss.
843. BUZUKU, SHQIPE. Enhancement of decision-making in complex organizations: A systems engineering approach. 2019. Diss.
844. SHCHERBACHEVA, ANNA. Agent-based modelling for epidemiological applications. 2019. Diss.
845. YLIJOKI, OSSA. Big data - towards data-driven business. 2019. Diss.
846. KOISTINEN, KATARIINA. Actors in sustainability transitions. 2019. Diss.





ISBN 978-952-335-352-7  
ISBN 978-952-335-353-4 (PDF)  
ISSN-L 1456-4491  
ISSN 1456-4491  
Lappeenranta 2019